The Dissertation Committee for Luke Howard Macfarlan Certifies that this is the approved version of the following dissertation:

PREDICTIONS OF THE MASS TRANSFER IN STRUCTURED PACKINGS USING COMPUTATIONAL FLUID DYNAMICS

Committee:

Roger T. Bonnecaze, Co-Supervisor

R. Bruce Eldridge, Co-Supervisor

Paul W. Belanger

Benny D. Freeman

Gary T. Rochelle

Subhashini Vashisth

PREDICTIONS OF THE MASS TRANSFER IN STRUCTURED PACKINGS USING COMPUTATIONAL FLUID DYNAMICS

by

Luke Howard Macfarlan

Dissertation

Presented to the Faculty of the Graduate School of

The University of Texas at Austin

in Partial Fulfillment

of the Requirements

for the Degree of

Doctor of Philosophy

The University of Texas at Austin

August 2021

Dedication

For my Father and my family

Acknowledgements

This project would not have been possible without significant support from others. Firstly, I am grateful to Bruce Eldridge for his guidance and support. He was a continual source of encouragement and helped me communicate my work well. His insight on real-world separation processes was greatly welcomed. I also appreciated the conversations on our shared Arkansan roots.

I am also grateful for the support and friendship of my friends and lab mates. Mikey Phan always provided wonderful fresh perspectives, and his encouragement to avoid assumptions increased the rigor of the project. Jeff Weinfeld was a great reminder of the benefits of being assertive and provided healthy study breaks with his conversations. I appreciated Melissa Donahue welcoming me into her office when I was a new graduate student and showing me how technical factors often depend on each other. I have and will continue to value the relationships with all of them.

I am thankful for input and guidance of my committee members. Dr. Bonnecaze offered helpful suggestions and research strategies. Dr. Belanger and Dr. Vashisth provided meaningful insight on vapor-liquid contactors and encouraged big-picture considerations of the project. Dr. Freeman provided training on the fundamentals of mass transfer, and Dr. Rochelle often sparked new research ideas to test, which increased the quality of the work.

Many individuals from the Separations Research Program (SRP) assisted as well. I appreciated Frank Seibert's upbeat personality and his experimental expertise. Denzil Smith was a continual source of technical support. Susan McCoy helped with any and all

purchasing needs. I am grateful for the patience of Jarett Spinhirne, Jaime Church, and JR Campos with all my questions about operating the pilot plant.

I am very grateful for the encouragement from my family. Mom, Dad, Kara, and Craig, you were always understanding when I was discussing my research project and motivated me to keep on chugging. Mom and Dad, thanks for the care and training you provided for me growing up – you ensured I had a great education, and you also motivated me to set high goals for myself.

I am extremely grateful to my wife, Emilee. You were understanding when I worked long nights and weekends, and you reminded me of life outside of research. You always helped me explain my work more simply. I also appreciated your patience listening to my ramblings about my technical research challenges of the day. I cannot imagine completing this project without your care and support.

Lastly, I am very grateful for the funding and support from multiple organizations. Praxair/Linde and Eastman provided technical advice as well as financial resources for this project. Individuals from those organizations include Paul Belanger, Subhashini Vashisth, Scott Owens, Arya Ayaskanta, Di Song, and Kirk Larson. I am also grateful for funding from the National Science Foundation and the University of Texas Cockrell School of Engineering. I appreciate Siemens for the Simcenter STAR-CCM+ software and the Texas Advanced Computing Center (TACC) for computational resources.

This material is based upon work supported by the National Science Foundation Graduate Research Fellowship Program under Grant No. DGE-1610403. Any opinions, findings, and conclusions or recommendations expressed in this material are those of the authors and do not necessarily reflect the views of the National Science Foundation.

Abstract

Predictions of the Mass Transfer in Structured Packings Using Computational Fluid Dynamics

Luke Howard Macfarlan, Ph.D.

The University of Texas at Austin, 2021

Supervisors: Roger T. Bonnecaze, R. Bruce Eldridge

Chemical separations are widely performed in industry, with vapor-liquid contactors often accomplishing these separations and providing high-purity products. Structured packings are commonly employed in vapor-liquid contactors and exhibit low pressure drops, high throughputs, and excellent chemical separation performance. Despite the widespread use of these packings, the transport phenomena occurring within them are incompletely understood, inhibiting improvement efforts. Computational fluid dynamics (CFD) is a promising approach to predict the transport phenomena occurring inside the packings and to guide packing innovation.

In this work, CFD predicted the gas-phase mass transfer performance of structured packings, and several key observations resulted. After a model for turbulence-aided mass transfer was identified with pipe flow simulations, the gas-phase mass transfer performance of a traditional structured packing was predicted. The mass transfer coefficients from CFD showed a five percent deviation compared to experimental data, validating the simulations. A geometry investigation determined the impact of three fundamental structured packing parameters on the packing performance. Improved mass transfer performance often

occurred at the cost of hydrodynamic performance. Turbulence had a large impact on the gas-phase predictions.

The liquid-phase mass transfer in structured packings was also simulated. A novel simulation methodology enabled the structured packing performance predictions. To validate the hydrodynamic predictions from the CFD simulations, the predicted liquid holdup was compared to experimental liquid holdup data and showed a deviation of six percent. Comparisons of the predicted liquid flow angle and friction factor to analytical expressions further validated the hydrodynamic CFD predictions. The liquid mass transfer coefficient predictions were validated with experimental data, having a deviation of eight percent, as well as with semi-empirical models. A structured packing geometry study was conducted for the liquid-phase performance, and liquid upheaval near packing crimps significantly contributed to the chemical separation.

A novel interfacial mass transfer model was developed for multiphase CFD simulations. This model can handle concentration jumps of multiple orders of magnitude across the gas-liquid interface. An analytical solution to a two-dimensional system validated the CFD predictions, producing an error of less than one percent. The model was adapted for turbulent conditions and was demonstrated on a structured packing system.

Table of Contents

List of Tables

List of Figures

Chapter 1: Project Motivation and Scope

1.1. PROJECT MOTIVATION

Before discussing the progress and challenges of modeling the mass transfer in structured packings using computational fluid dynamics, a review of chemical separations, the use of structured packings, and computational fluid dynamics is needed.

1.1.1. Chemical Separations

Chemical separation processes account for 10-15 percent of the energy consumed globally and half of the energy consumed industrially in the United States (Sholl and Lively, 2016). Distillation alone is responsible for nearly half of the energy consumption in chemical and petrochemical plants, and a large portion of this power originates from fossil fuels (Bumbac et al., 2009; Owens et al., 2013; Sholl and Lively, 2016; Weinfeld et al., 2018). As a result, decreased energy consumption in just the petroleum, chemical, and paper industries could save $4 billion each year (Sholl and Lively, 2016). Additionally, reduced energy use for chemical separations could lower carbon dioxide emissions by as much as 100 million metric tons annually, which is a global environmental impact (Sholl and Lively, 2016).

1.1.2. Vapor-Liquid Contactors

Vapor-liquid contactors are a promising target for improved performance within the chemical separations field. As the name implies, these vapor-liquid contactors promote interaction between vapor and liquid phases. Contactor internals, which include random packings, structured packings, and trays, are involved in distillation, absorption, and

stripping, three of the most common chemical separation methods. Figure 1-1 demonstrates the distillation and absorption processes that contactor internals often support. Because these contactors are ubiquitous in chemical separation processes, any improvements in their performance would greatly impact the entire field of chemical separations (Erasmus, 2004).

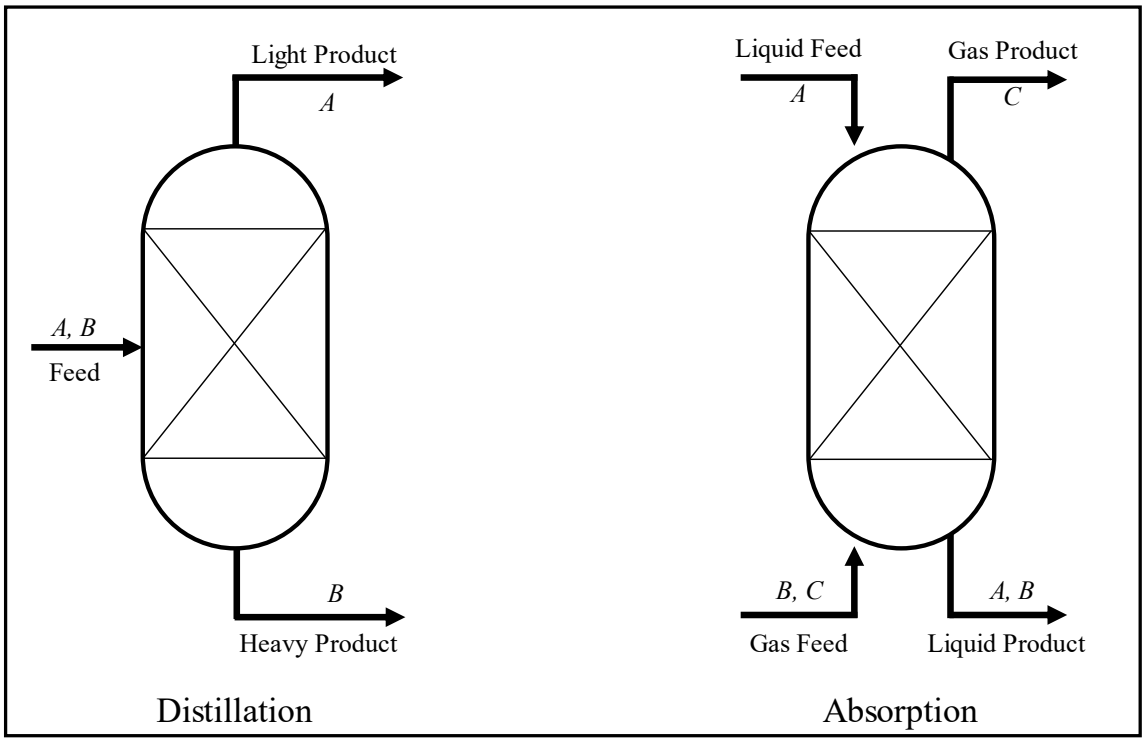

Figure 1-1: Flow diagrams for distillation and absorption chemical separation processes performed by vapor-liquid contactors for generic chemical species A, B, and C.

1.1.3. Structured Packings

Structured packings are the most advanced contactor internals presently available, allowing high gas and liquid flow rates through the column, high mass transfer rates, and low pressure losses (Boot-Handford et al., 2014; Dai et al., 2012; Dong et al., 2017; Erasmus, 2004; Fernandes et al., 2008). In fact, an 80-90 percent reduction in pressure drop has been reported for structured packings compared to a trayed column (Agrawal and Herron, 2000). Figure 1-2 provides a representative depiction of structured packings. The decreased pressure drop of structured packings compared to other vapor-liquid contactors leads to higher energy efficiency because pressure losses often stem from energy losses (Lautenschleger et al., 2015). However, within the structured packing classification, different geometries exhibit a variety of pressure drops for the same chemical separation. This variety reveals efficiency differences among structured packing types and suggests future packing improvements could reduce pressure losses even further (Lautenschleger et al., 2015).

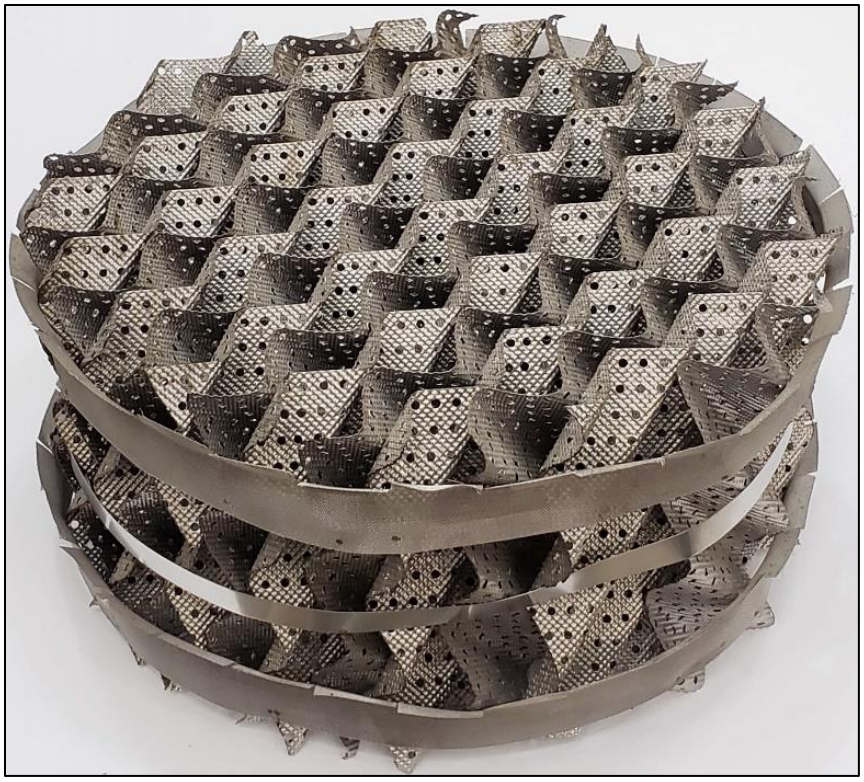

Figure 1-2: Mellapak 125Y structured packing, representative of structured packing geometry.

As an example of this research area's application, improvements in structured packings are especially critical for carbon sequestration efforts. Carbon dioxide emissions can be substantially reduced by absorbing carbon dioxide from post-combustion flue gas (from a coal power plant, for example) and reacting it with an aqueous amine solution (Boot-Handford et al., 2014; Sebastia-Saez et al., 2014). This carbon capture requires absorber and stripper contactors. Structured packings are often used in these contactors due to the contactor internals' exceptional performance. Because 60-80 percent of the total operating costs resides in the stripping process, an efficiency improvement for structured packings would greatly impact carbon sequestration expenses (Sebastia-Saez et al., 2013).

1.1.4. Modeling Transport Phenomena in Structured Packings

Fundamental flow measurements are difficult to obtain for structured packing systems, inhibiting insight into the mechanisms underpinning performance in structured packing (Owens et al., 2013; van Gulijk, 1998). In response, researchers developed semi-empirical correlations based on phenomena which are thought to occur (Wang et al., 2005). For example, the Rocha-Bravo-Fair model uses wetted-wall theory based on the assumption that the liquid forms a film on the surface of the packings while traveling downward (Wang et al., 2005). The Delft model treats the gas flow as undergoing a zigzag path because of the typical shape of structured packings (Wang et al., 2005). Pilot-scale data informed the empirical parameters implemented in many of these models (Raynal et al., 2009; Wang et al., 2005).

While these models offer insight into the operation of vapor-liquid contactors, inadequate support for novel packing design is provided. The reliance on empirical parameters causes complications for structured packing innovation. To use these correlations in novel packing design, researchers must construct and test the novel packing for each design iteration, substantially slowing innovation (Raynal et al., 2004). The models are often only applicable to the structured packing types used in their development (Lautenschleger et al., 2015). The traditional models also show deviations from experimental values, as errors of 20 percent are common for structured packing models (Billet and Schultes, 1993; Fair et al., 2000; Song et al., 2018). This magnitude of error demonstrates the uncertainty of contactor operation and reveals the need for further research.

1.1.5. Effectiveness

The purpose of a vapor-liquid contactor is a chemical separation (Van Winkle, 1967). This separation occurs through mass transfer, particularly interfacial mass transfer. A pressure difference across the column is essential for a bulk movement of the gas phase, but an excess pressure drop reflects an energy loss (Lautenschleger et al., 2015). In general, mass transfer is the desired outcome of a vapor-liquid contactor, and the pressure drop is a required input for the device.

With this input and output, two pathways to improve the efficiency of vapor-liquid contactors emerge. The first pathway is to increase the interfacial mass transfer in the column while maintaining the pressure drop, effectively improving the chemical separation while maintaining the energy requirement (Lautenschleger et al., 2015). This approach would allow for a scale-down of the column, likely producing a subsequent decrease in capital cost and energy input (Khosravi Nikou et al., 2008). The second pathway is to decrease the pressure drop while holding the mass transfer constant, maintaining the chemical separation while reducing the energy requirement (Lautenschleger et al., 2015). This approach would reduce the energy dissipation in the column during operation. In both cases, for successful innovation that advances structured packing performance, considerations of both the mass transfer and the pressure drop are essential (Haroun et al., 2010a).

1.1.6. Computational Fluid Dynamics

Computational fluid dynamics (CFD) has the potential to predict both the mass transfer and the pressure drop. The approach illuminates the underlying physics of a system; the software decomposes the system of interest into a myriad of small cells and

numerically solves equations governing the conservation of mass, momentum, or energy, depending on the relevant physics. Through this process, CFD can predict small-scale phenomena occurring in a system.

Largely because of its ability to predict small-scale phenomena, CFD is a powerful tool to model flow patterns in structured packings (Sun et al., 2013). While structured packings were developed in the 1970s, the first reference to using CFD for studying structured packings appeared in 1994, and the research field has since blossomed with the availability of computational resources (Kister, 1992; Suess et al., 1994). Since 1994, the insight from this computational method into the hydrodynamics and mass transfer within structured packings has already induced improvements in structured packing design, pointing to the power of CFD for future packing optimization (Hodson, 1997; Hodson et al., 1997; Lautenschleger et al., 2015; Shilkin et al., 2010). CFD in general has been, and will likely continue to be, a key tool for the improvement of structured packings (Khosravi Nikou et al., 2008; Sebastia-Saez et al., 2013). Sensitivity studies of parameters are faster to conduct and less expensive with CFD than via experimental efforts (Raynal et al., 2009; Singh et al., 2018). Lastly, this approach is less invasive than experimental methods, not requiring measurement equipment that could impede and alter the flow (Owens et al., 2013).

Because a CFD simulation on an entire column would have a huge computational expense, researchers have developed alternative computational approaches. Significantly reducing computational expense, representative elementary units (REUs) are a common technique used to simplify the analysis of structured packings. This REU is effectively the building block of a packing's shape. Figure 1-3 shows a sample REU. Because many of the packing's physical characteristics are encapsulated in the REU, results from a single REU simulation will reflect the performance of the entire packing, allowing for

extrapolation of the REU results to the entire vapor-liquid contactor (Erasmus, 2004; Petre et al., 2003; Said et al., 2011). An additional benefit of the REU approach involves the scale of the investigated vapor-liquid contactor. REUs typically have periodic boundary conditions on the left and right faces as well as on the top and bottom faces. These boundary conditions force the flow exiting one face to enter the opposite face. The periodic boundary conditions on the left and right faces remove wall effects, so the performance of an REU is comparable to the performance of an infinitely wide column. Unlike most experimental equipment with diameters less that one meter, industrial structured packing column diameters can easily reach 10 meters (Raynal et al., 2009). With REUs, CFD can investigate this larger-scale equipment with fewer wall effects, allowing for more industry-applicable results (Raynal et al., 2009).

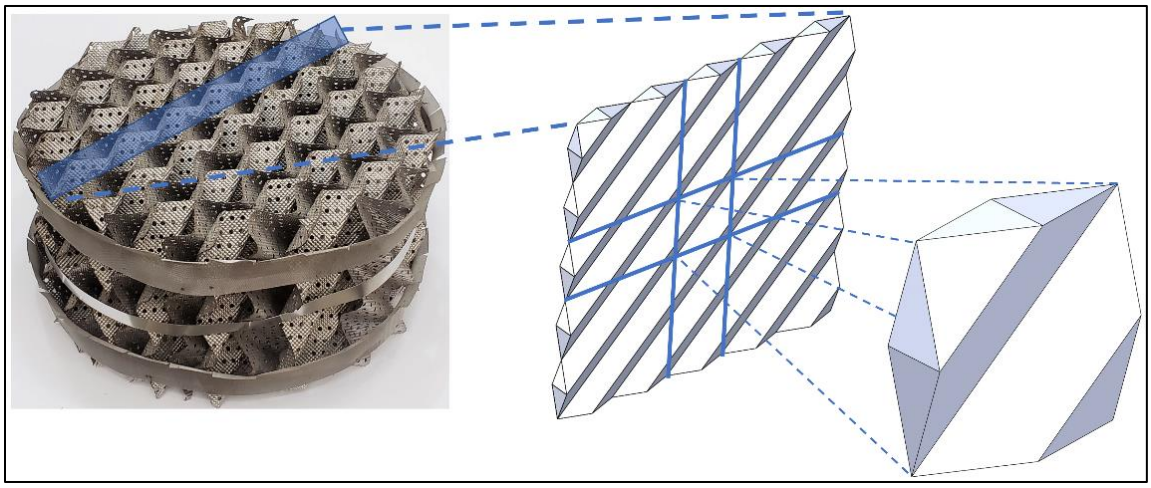

Figure 1-3: Sample representative elementary unit (REU) geometry.

1.2. PROJECT SCOPE

The research in this dissertation focuses on computational fluid dynamics (CFD) predictions of mass transfer in structured packings. This work showed that the gas mass transfer coefficient, liquid mass transfer coefficient, liquid holdup, liquid flow angle, and interfacial mass transfer in structured packings can be accurately predicted using CFD. The ability to utilize CFD to test novel structured packings was also demonstrated, and trends were identified.

A CFD-based investigation of structured packing geometry was conducted for the gas-phase hydrodynamic and mass transfer performance. A robust mass transfer methodology for the gas-phase resistance was identified through pipe flow simulations. The methodology was then applied to structured packing simulations for a variety of industrially relevant geometries. The mass transfer predictions agreed to within five percent of pilot-scale experimental data for standard commercial packings. The influence of structured packing geometry on the overall performance was studied by systematically changing the specific packing area, channel inclination angle, and channel opening angle to determine the geometry which produced a high degree of mass transfer or a low pressure drop.

An investigation on the geometry of structured packings was conducted using CFD to determine its impact on the liquid-phase hydrodynamic and mass transfer performance. Three variables validated the CFD hydrodynamic simulations: the liquid holdup, the liquid flow angle, and the Fanning friction factor. The hydrodynamic CFD predictions demonstrated excellent agreement with experimental holdup data, having a six percent average deviation. The CFD-predicted liquid mass transfer coefficient for the structured packing matched experimental data to within eight percent and also compared favorably with predictions from four industry-accepted semi-empirical correlations. To determine the

dependence of the liquid-phase performance on the geometry of structured packings, the channel inclination angle and the channel opening angle varied. The liquid flow angle impacted the liquid mass transfer coefficient by increasing the upheaval as the film crossed each crimp in the structured packing.

A novel CFD model was developed to predict interfacial mass transfer. This model is capable of simulating a concentration jump of several orders of magnitude and is equipped to predict processes with mass transfer resistances in both phases. The mathematical foundation of the models was established. After a mesh sensitivity investigation, a validation study was conducted, comparing the CFD predictions for the average mass transfer coefficient to an analytical solution. The CFD predictions showed strong agreement with the analytical solution, exhibiting an average error of less than one percent. The interfacial mass transfer model was adapted for turbulent conditions and implemented in structured packing simulations.

1.3. SUMMARY

The focus of this project was to accurately predict the mass transfer in structured packings using CFD. This project on structured packings 1) developed a CFD methodology to predict the hydrodynamic and mass transfer performances asynchronously, 2) uncovered a tradeoff between the hydrodynamic and mass transfer performance in the gas-phase, 3) created a novel simulation strategy for predicting the liquid-phase performance, 4) revealed the impact of the liquid flow angle on the liquid mass transfer coefficient, 5) developed a new interfacial mass transfer methodology, and 6) predicted the overall mass transfer performance for a gas-film-controlled system, a liquid-film-controlled system, and a system with mass transfer resistances in both phases. Together, these contributions show

that CFD can predict the transport phenomena in structured packings and streamline the packing innovation process. The methodologies developed through this work will aid future efforts to better understand and model the transport phenomena in structured packings.

Chapter 2: Literature Review

2.1. INTRODUCTION

CFD offers a predictive methodology to understand the transport phenomena in structured packings. This computational approach can model transport phenomena at the microscopic level, and these microscopic phenomena impact the operation of the entire vapor-liquid contactor. For example, by modeling the diffusion of mass at the microscopic level in structured packings, mass transfer rates can be predicted and applied to the performance of the entire packed column. Multiple strategies exist in the literature to predict these microscopic transport phenomena in structured packings, including mass transfer phenomena.

This chapter summarizes the research methodologies and results for CFD structured packing mass transfer studies. In structured packings, molecules can diffuse both across the interface and within each phase. To address the first mechanism, predictive interfacial mass transfer approaches applicable to CFD structured packing studies are summarized. For the second mechanism, the subsequent section addresses predictive CFD strategies for simulating mass transfer within a phase, including in turbulent flow. Finally, the last section summarizes CFD approaches employing semi-empirical models to account for microscopic mass transfer processes. It should be noted that studies employing a porous medium methodology are outside the scope of this review.

2.2. PREDICTIVE INTERFACIAL MASS TRANSFER APPROACHES

Structured packings provide significant interfacial area for species to move from one phase to the other. To predict the performance of a packing generically, without limiting the study to gas-phase or liquid-phase controlled systems, a CFD mass transfer

approach must allow for the exchange of a chemical species across the interface. Two conditions exist at a typical interface: continuity of the mass flux across the interface and thermodynamic equilibrium. The first condition stems from mass conservation, assuming no species accumulation at the interface. Henry's law can predict the second condition, as Equation (2-1) shows.

$$c_G^* = \mathrm{He}\, c_L^* \tag{2-1}$$

In this equation, c_G^* is the concentration in the gas phase at the interface, c_L^* is the concentration in the liquid phase at the interface, and He is the Henry's constant.

To date, there have been few interfacial mass transfer approaches implemented in structured packing CFD studies. However, several models have been implemented in the broader CFD mass transfer literature that show promise for application in structured packing investigations. The interfacial mass transfer approaches can be broken into two categories: single-field and two-field approaches. In a single-field approach, the solver is superficially indifferent to the phase where the species resides. In a two-field approach, the solver distinguishes between the concentrations in the individual phases. These two mass transfer approaches are analogous to the one-fluid (e.g. volume of fluid or VOF) and two-fluid (e.g. Eulerian-Eulerian) approaches for the hydrodynamics. Table 2-1, Table 2-2, and Table 2-3 list the interfacial mass transfer models previously used to study structured packings as well as the models that could potentially be used for that purpose in the future. The subsequent sections of this paper provide further details on those models.

Author(s)	*Year*	*Single-Field Approach?*	*Structured Packing?*	*Interfacial Mass Transfer Approach*
Petera & Weatherley	2001	Yes	No	Recasting of concentration field
Bothe et al.	2003a	Yes	No	Recasting of concentration field
Bothe et al.	2003b	Yes	No	Recasting of concentration field
Bothe et al.	2004	Yes	No	Recasting of concentration field
Bothe & Warnecke	2005	Yes	No	Recasting of concentration field
Yang & Mao	2005	Yes	No	Recasting of concentration field
Onea	2006	Yes	No	Adjusted flux term
Haghshenas Fard et al.	2007	No	Yes	Mass transfer coefficients from the Rocha-Bravo-Fair model (Rocha et al., 1996)
Kroger et al.	2007	Yes	No	Recasting of concentration field
Banerjee	2008	No	No	Computed flux from concentration gradient
Khosravi Nikou et al.	2008	No	Yes	Mass transfer coefficients from Delft model (Olujić, 2002)
Khosravi Nikou & Ehsani	2008	No	Yes	Mass transfer coefficients from Rocha-Bravo-Fair model (Rocha et al., 1996) and Gualito et al. (1997)
Wang et al.	2008	Yes	No	Recasting of concentration field
Alke et al.	2009	No	No	Redistribution of concentration to impose equilibrium; Calculated gradient across interface and thus a flux using a distribution coefficient
Bothe et al.	2009	Yes	No	Recasting of concentration field
Onea et al.	2009	Yes	No	Adjusted flux term
Xu et al.	2009	No	Yes	Higbie penetration theory
Alke et al.	2010	No	No	Calculated gradient across interface and thus a flux using a distribution coefficient; Subgrid-scale model

Table 2-1: Summary of interfacial mass transfer studies used or potentially used to study structured packings.

Author(s)	*Year*	*Single-Field Approach?*	*Structured Packing?*	*Interfacial Mass Transfer Approach*
Francois & Carlson	2010	Yes	No	Recasting concentration field
Haelssig et al.	2010	No	No	Iteratively enforced equilibrium and mass flux continuity conditions
Haroun et al.	2010a	Yes	No	Adjusted flux term
Haroun et al.	2010b	Yes	Yes	Adjusted flux term; Higbie penetration theory
Bothe et al.	2011	No	No	Calculated gradient across interface and then the flux using Henry's law
Ganguli & Kenig	2011	No	No	Interfacial boundary conditions included as source terms in convection-diffusion equations at the interface
Hayashi & Tomiyama	2011	Yes; No	No	Recasting of concentration field; Computed flux for standard concentration field using gradient of recast concentration field
Haroun et al.	2012	Yes	Yes	Adjusted flux term; Higbie penetration theory
Marschall et al.	2012	Yes	No	Adjusted flux term
Bothe & Fleckenstein	2013	No	No	Redistribution of concentration to impose equilibrium; Calculated gradient and thus a flux across interface
Francois & Carlson	2013	Yes	No	Recasting of concentration field
Sebastia-Saez et al.	2013	No	Yes	Higbie penetration theory
Sun et al.	2013	No	Yes	Higbie penetration theory
Hayashi et al.	2014	No	No	Recasting of concentration field; Computed flux for standard concentration field using gradient of recast concentration field
Fleckenstein & Bothe	2015	No	No	Calculated gradient across interface and then the flux using Henry's law
Sebastia-Saez et al.	2015a	No	Yes	Higbie penetration theory
Deising et al.	2016	Yes	No	Adjusted flux term
Gründing et al.	2016	No	No	Calculated gradients using subgrid-scale model

Table 2-2: Summary of interfacial mass transfer studies used or potentially used to study structured packings (continued).

Author(s)	*Year*	*Single-Field Approach?*	*Structured Packing?*	*Interfacial Mass Transfer Approach*
Soh et al.	2017	No	No	Experimentally measured mass transfer coefficient; Bothe & Fleckenstein (2013) model; Haelssig et al. (2010) model
Weber et al.	2017	Yes	No	Iteratively enforced equilibrium and mass flux continuity conditions
Weiner & Bothe	2017	No	No	Calculated gradients using subgrid-scale model
Falcone et al.	2018	Yes	No	Iteratively enforced equilibrium and mass flux continuity conditions
Hill et al.	2018	Yes	No	Adjusted flux term
Maes & Soulaine	2018	Yes	No	Adjusted flux term
Rieks & Kenig	2018a	No	No	Iteratively adjusted species source term until time derivative of the equilibrium condition was enforced
Rieks & Kenig	2018b	No	No	Iteratively adjusted species source term until time derivative of the equilibrium condition was enforced
Sotoodeh et al.	2018	No	Yes	Mass transfer coefficient from modified Delft model (Behrens, 2006)
Yu et al.	2018	No	Yes	Higbie penetration theory
Amini et al.	2019	No	Yes	Mass transfer coefficients from the Rocha-Bravo-Fair model (Rocha et al., 1996)
Hill et al.	2019	Yes	Yes	Adjusted flux term
Xu et al.	2019	No	Yes	Rayleigh-Plesset equation for spherical bubble growth or shrinkage
Basha et al.	2020	No	Yes	Mass transfer coefficients from the Rocha-Bravo-Fair model (Rocha et al., 1996)
Maes & Soulaine	2020	Yes	No	Adjusted flux term
Manh et al.	2020	No	Yes	Mass transfer coefficients from the Rocha-Bravo-Fair model (Rocha et al., 1996)
Yang et al.	2020	Yes	No	Adjusted flux term
Hassanvand et al.	2021	No	Yes	Mass transfer coefficients from the Rocha-Bravo-Fair model (Rocha et al., 1996)

Table 2-3: Summary of interfacial mass transfer studies used or potentially used to study structured packings (continued).

2.2.1. Single-Field Approaches

2.2.1.1.Recasting the Concentration Field

Substituting the Henry's law equality into the convection-diffusion equations for each phase's concentration field eliminates one of the species variables and simultaneously provides a scalar field valid in the entire multiphase system. The convection-diffusion equation is the governing equation for mass transfer, and Equation (2-2) presents its non-discretized form (Deen, 2012).

$$\frac{\partial c_A}{\partial t} + \nabla \cdot c_A \mathbf{v} = -\nabla \cdot \mathbf{j}_A + S_A \tag{2-2}$$

In this equation, c_A is the concentration, $\mathbf{v}$ is the velocity vector, $\mathbf{j}_A$ is the diffusive flux, and S_A is the sum of the source terms. Figure 2-1 graphically represents a hypothetical recasting of the concentration field. This method was extensively utilized in early interfacial mass transfer studies, primarily for bubble columns, likely because of its simple implementation (Bothe et al., 2003a, 2003b, 2004, 2009; Bothe and Warnecke, 2005; Francois and Carlson, 2013, 2010; Hayashi et al., 2014; Hayashi and Tomiyama, 2011; Kroger et al., 2007; Petera and Weatherley, 2001; Wang et al., 2008; Yang and Mao, 2005). However, this method is challenged by spurious interfacial fluxes computed during the computational advection step, as the flow in one phase can carry away species from the bulk of the opposite phase (Hayashi and Tomiyama, 2011). Additionally, this approach does not strictly ensure mass conservation, although mass conservation errors decrease with increasing mesh fineness (Bothe et al., 2011, 2009).

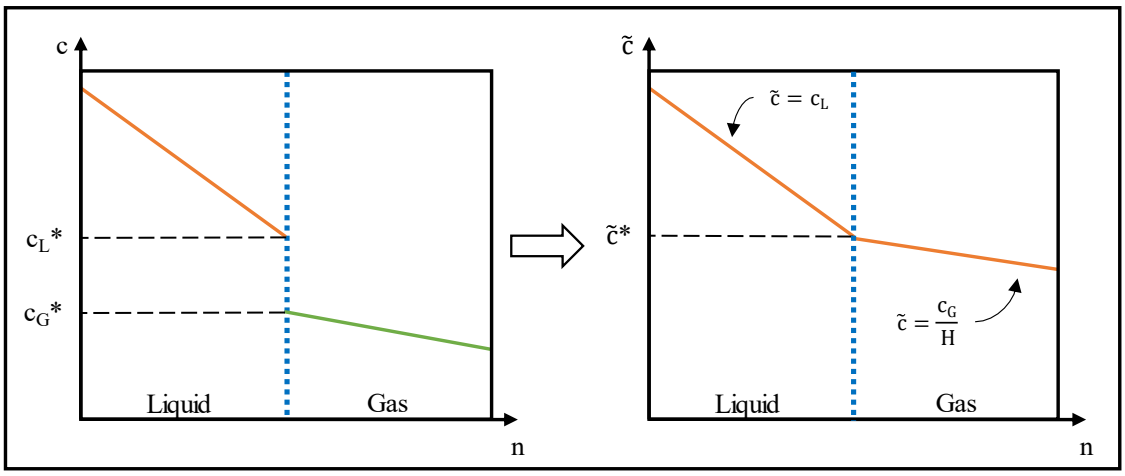

Figure 2-1: Graphical representation of a recasting approach, where n is the coordinate normal to the interface, the * superscript denotes values at the interface, and c̃ denotes the recast concentration.

2.2.1.2.Adjusted Flux Term

Several models increase the flux from advection and diffusion between computational cells to account for the interfacial mass transfer. One common approach uses Henry's law and the gradient of the liquid volume fraction in a solubility flux term, which is then added to the standard diffusive flux prediction by Fick's law. Figure 2-2 illustrates the solubility flux approach. This approach has been tested on both bubble systems and simple one-dimensional diffusion systems (Deising et al., 2016; Haroun et al., 2010a; Marschall et al., 2012; Onea et al., 2009; Onea, 2006) as well as on structured packing systems (Haroun et al., 2012, 2010b). Hill et al. (2018) expanded this method by tracking the molar fraction rather than the molar concentration. By using the relative rather than the absolute velocities of the phases at the interface, Maes and Soulaine (2020, 2018) extended the solubility flux approach to reduce spurious numerical diffusion for systems

with large Péclet numbers. Yang et al. (2020) implemented this approach with a convective flux calculation scheme consistent with the calculation for the liquid volume fraction.

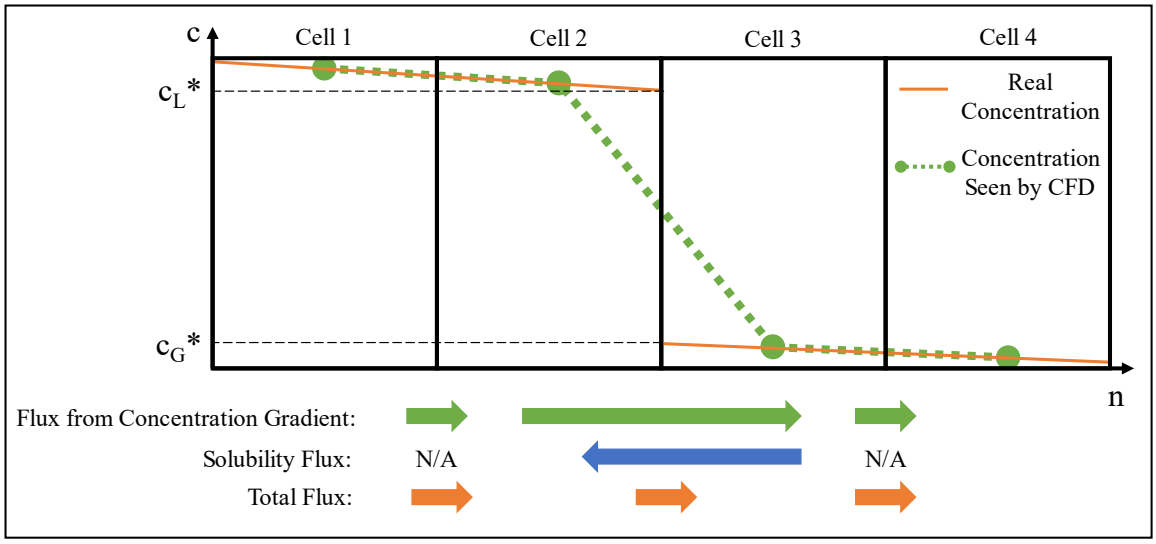

Figure 2-2: Graphical example of an adjusted flux approach.

Adjusted flux terms often rely on a quantification of the interface's presence, commonly with the gradient in the liquid volume fraction. Challenging this quantification, gradients in the liquid volume fraction have non-zero values in cells adjacent to interface cells, challenging accurate identifications of the interface (Alke et al., 2009; Soh et al., 2016). Additionally, accurate predictions of the interfacial area are often needed for this approach.

2.2.2. Two-Field Approaches

2.2.2.1.Higbie Penetration Theory

The Higbie penetration theory can predict the liquid-phase mass transfer coefficient and, therefore, the interfacial mass transfer. The mass transfer coefficient (k) relates the molar flux magnitude (j_A) to the concentration difference (Δc_A), considered the driving force for the process (Bird et al., 2007), as Equation (2-3) shows.

$$j_A = k\Delta c_A \tag{2-3}$$

The mass transfer coefficient is often presented through the Sherwood number, which is defined in Equation (2-4) (Bird et al., 2007).

$$Sh = \frac{k\, L_c}{D_m} \tag{2-4}$$

In Equation (2-4), L_c is the characteristic length and D_m is the molecular diffusion coefficient.

The Higbie penetration theory forms the foundation for the majority of liquid-phase mass transfer coefficient models (Dong et al., 2017). This model is based on film flow between a liquid and a gas. In its original form, the Higbie penetration theory is not empirical, having no application-specific parameters involved. This model, shown by Equation (2-5), predicts the liquid-phase mass transfer coefficient for a gas diffusing into a liquid (Higbie, 1935; Sebastia-Saez et al., 2013).

$$k_L = 2\sqrt{\frac{D_m}{\pi \cdot t_{contact}}} \tag{2-5}$$

The contact time between phases, $t_{contact}$, is a key variable in the Higbie penetration theory. Most studies have computed the contact time from the hydrodynamics of the system. As a result, this theory only requires the system's hydrodynamics to predict the interfacial mass transfer.

Sebastia-Saez et al. (2013) analyzed the liquid-phase mass transfer performance of a liquid film contacting a gas while flowing down a simplified structured packing geometry: an inclined, corrugated plate. The Higbie penetration theory predicted the interfacial mass transfer, and the contact time was the distance traveled from the inlet by a liquid fluid element divided by the velocity at the interface. For a system of oxygen absorbing into water, the Sherwood number results fell between the predictions of the Pigford (Emmert and Pigford, 1954), Zogg (1972), and Haroun et al. (2010b) correlations. The authors reported a positive correlation between the Sherwood number and the liquid Reynolds number. For a propane-toluene system, the CFD simulations underpredicted the mass transfer compared to the experimental data in Xu et al. (2009), showing an average error of approximately 50 percent.

Sebastia-Saez et al. (2015a) studied reactive mass transfer in a structured packing on the microscale using CFD. Because the scale of the study was small, the computational domain was a simple inclined plate. The system modeled was CO_2 dissolving into and reacting with an aqueous monoethanolamine (MEA) solution. The Higbie penetration theory provided the liquid-phase mass transfer coefficient, and the contact time for the theory was calculated as the ratio of the distance traveled by a liquid fluid element from the inlet to the CFD-predicted liquid velocity at the interface, as presented in Haroun et al.

(2010b). The interfacial, gas-phase mass transfer resistance was assumed to be low, so it was neglected. A combination of correlations produced the enhancement factor, which was multiplied with the mass transfer coefficient to account for the chemical reaction. The simulations showed larger liquid loads reducing the effect of the chemical reaction. An increased MEA concentration had two counteracting effects on the overall mass transfer. The chemical reaction rate improved, which benefited the overall mass transfer. But the heightened MEA concentration decreased CO_2's molecular diffusion coefficient in the liquid because of the rise in viscosity, reducing the mass transfer coefficient. Lastly, a larger liquid velocity lowered contact times and therefore gave larger mass transfer coefficients.

2.2.2.2.Equilibration at the Interface

Rather than computing the flux across the interface, any cell containing a portion of the interface can be assumed to have its gas and liquid concentrations in thermodynamic equilibrium with each other (Alke et al., 2009; Bothe and Fleckenstein, 2013). This model involves redistributing the diffusing species between the two phases. While this approach does not directly satisfy a continuity of mass fluxes across the interface, it directly ensures mass conservation, which underpins the continuity of mass fluxes boundary condition. This method obtained grid independence earlier than a flux-based approach (Alke et al., 2009). The model has been applied to bubble column studies but has not been tested on structured packings.

2.2.2.3.Calculating Flux with Recasting at the Interface

Another approach calculates the interfacial mass flux by computing the concentration gradient across the interface using Henry's law. While similar to the recasting approach discussed in the Recasting the Concentration Field section, this approach differs in that rescaling is only used to compute the concentration gradient across the interface; as a result, the bulk fluid movement does not directly influence the interfacial mass transfer. This approach has shown promise for bubble systems (Alke et al., 2010, 2009; Banerjee, 2008; Bothe and Fleckenstein, 2013; Fleckenstein and Bothe, 2015; Hayashi et al., 2014; Hayashi and Tomiyama, 2011; Soh et al., 2017) despite the intrinsic challenge to this method of accurately predicting the interfacial area (Alke et al., 2009).

2.2.2.4.Other Approaches

Other approaches have been used in the literature which could be compatible with structured packing studies although they do not fall into a unifying category.

Sebastia-Saez et al. (2015b) investigated the mass transfer in structured packings using a mesoscale, REU approach for an oxygen-water system. Symmetry boundary conditions were implemented on the left and right faces of the system rather than the periodic boundary conditions applied in typical REU approaches. The gas-phase velocity was neglected due to its assumed small effect on the overall mass transfer. The authors did not directly predict the interfacial mass transfer in this study; instead, the authors applied mass transfer rates calculated in their earlier, MEA-CO_2, micro-scale study (Sebastia-Saez et al., 2015a) to reduce the computational expense of the simulations. In the micro-scale study, the Higbie penetration model predicted the interfacial mass transfer, and the interfacial, gas-phase mass transfer resistance was neglected because that phase was pure.

On a bubble column system, Ganguli and Kenig (2011) satisfied Henry's law and mass flux continuity by including the two conditions as liquid-phase and gas-phase source terms, respectively, in the species convection-diffusion equations. Large prefactors to the equilibrium conditions guaranteed the solver would fulfill the boundary conditions. The modified convection-diffusion equations for the liquid and gas are duplicated in Equations (2-6) and (2-7) below.

$$\frac{\partial c_G}{\partial t} + \mathbf{v} \cdot \nabla c_G = \nabla \cdot \left(D_{G,m} \nabla c_G\right) + C_1 \left(D_{L,m} \frac{\partial c_L}{\partial n} - D_{G,m} \frac{\partial c_G}{\partial n}\right) \tag{2-6}$$

$$\frac{\partial c_L}{\partial t} + \mathbf{v} \cdot \nabla c_L = \nabla \cdot \left(D_{L,m} \nabla c_L\right) + C_2 \left(c_L - \frac{c_G}{He}\right) \tag{2-7}$$

In these equations, $\mathbf{v}$ is the velocity vector, t represents time, C_1 and C_2 are modeling coefficients to ensure the boundary conditions are enforced, n is the direction coordinate normal to the interface, and $D_{G,m}$ and $D_{L,m}$ are the molecular diffusion coefficients in the gas and liquid phases, respectively.

Rieks and Kenig (2018a, 2018b) enforced Henry's law through an iterative scheme. Henry's law was adapted by taking the time derivative of both sides of the equation. The mass exchange between phases was adjusted until this modified Henry's law relationship held. Only cells at the interface received this treatment, and the approach was tested in simple, non-structured-packed systems.

Several studies have been conducted for non-structured-packed systems where equilibrium and mass conservation boundary conditions are enforced through an iterative procedure (Falcone et al., 2018; Haelssig et al., 2010; Weber et al., 2017). In this approach,

the interfacial boundary conditions were treated as additional equations to be solved by the CFD code.

Due to thin concentration boundary layers that can form in the liquid-phase, often too thin to be resolved with current computational resources, models have been implemented to predict the concentration profile on scales smaller than the grid. In some cases, these subgrid-scale models can provide the concentration gradient near the interface (Alke et al., 2010; Gründing et al., 2016; Weiner and Bothe, 2017). This gradient can inform the interfacial mass flux prediction (Gründing et al., 2016; Weiner and Bothe, 2017). This approach has yet to be applied to structured packing systems.

If the gas-liquid interface in structured packings can be modeled as gas bubbles contacting a continuous liquid phase, the Rayleigh-Plesset equation can predict the interfacial mass transfer. This analytical equation models the growth or shrinkage of a spherical bubble in an incompressible fluid. This approach has been tested on a two-dimensional structured packing system (Xu et al., 2019).

2.2.3. Comparison of Single-Field and Two-Field Approaches

Both single-field and two-field approaches have benefits and challenges. For a comparison between the two methods, the reader is directed to Deising et al. (2016). For both approaches, capturing the concentration gradient in the liquid film is an immense challenge. In some situations, the boundary layer can be on the order of micrometers for physical mass transfer (Falcone et al., 2018). These thin boundary layers require fine meshes and, therefore, substantial computational resources. While computational resources continue to increase, curbing the challenge associated with these fine meshes, innovative strategies are necessary to overcome these challenges.

2.2.4. Summary of Interfacial Mass Transfer Approaches

Many interfacial mass transfer methodologies show promise for application to structured packing systems. The one-field approach of Haroun et al. (2010a) has shown particular promise and has sparked significant interest and further developments in the literature (Deising et al., 2016; Marschall et al., 2012; Hill et al., 2018). This methodology by Haroun et al. (2010a) was designed for systems with a concentration field approximately continuous across the gas-liquid interface. Structured packing chemical systems with a small concentration jump at the interface are often liquid-film controlled, which differs from typical structured packing chemical systems where the majority of the mass transfer resistance is often in the gas phase (Erasmus, 2004; Lautenschleger et al., 2015; Schpigel and Meier, 1994). The methodology of Hill et al. (2018) is more compatible with chemical systems having mass transfer resistances in both phases, but its compatibility with commercial CFD software is uncertain.

To predict the interfacial mass transfer in typical structured packing systems, models are needed that can handle larger concentration discontinuities at the gas-liquid interface. In particular, models are needed that are designed for an interfacial concentration jump of several orders of magnitude. To be accessible to industrial researchers, the models must be compatible with commercial CFD software.

2.3. PREDICTIVE INTRAPHASE MASS TRANSFER APPROACHES

Multiple approaches to model intraphase mass transfer in CFD exist, many of which have been used in previous studies for structured packings. Turbulence presents a major difficulty in the prediction of mass transfer because eddies in turbulent flows mix the components. CFD simulations must either resolve all eddies to predict the mass transfer

completely or utilize a mass transfer model that accounts for turbulence. The following sections summarize studies used to investigate intraphase mass transfer in structured packings with computational fluid dynamics. Table 2-4, Table 2-5, and Table 2-6 present the methods and findings of the papers reviewed.

Author(s)	*Year*	*Mass Transfer Method*	*Mass Transfer Experimental Validation*	*Mass Transfer Results*
Hodson et al. & Hodson	1997	Heat/mass transfer analogy	Yes	5-17% increase in heat transfer from simulations on novel packing; 10% more theoretical stages per meter from experiments
Van Gulijk	1998	Tracer phase dispersion	No	Transversal dispersion coefficient
Higler et al.	1999	Tracer phase dispersion from coating layer on packing surface	Yes	Axial dispersion coefficient underpredicted by a factor of 50; Liquid-phase Sherwood number
Van Baten et al.	2001	Tracer phase dispersion	Yes	Good agreement for radial dispersion coefficient; Order of magnitude error for axial dispersion coefficient
Van Baten & Krishna	2001	Tracer phase dispersion from coating layer on packing surface	No	Liquid-phase mass transfer coefficient
Van Baten & Krishna	2002	Tracer phase dispersion from coating layer on packing surface	No, but compared to Graetz solution (Janssen and Warmoeskerken, 1991)	Good agreement with Graetz solution for Sherwood number in an empty tube; Questionable liquid-phase trends
Erasmus	2004	See reference	Yes	Good agreement with experiments for gas-phase mass transfer coefficient
Egorov et al.	2005	Molecular diffusion coefficient	No	Mass fraction profiles
Haghshenas Fard et al.	2007	Imposed dispersion coefficient	Yes	HETP error of 9% with respect to experimental; Error 20% lower than the combination of the Rocha-Bravo-Fair model (Rocha et al., 1996) and Gualito et al. (1997)
Wen et al.	2007	Turbulent diffusion coefficient; Tracer phase in center of packing	No	Mass fraction profiles
Khosravi Nikou et al.	2008	See reference	Yes (cited Haghshenas Fard et al. (2007))	12.9% error for HETP
Khosravi Nikou & Ehsani	2008	See reference	Yes (cited Haghshenas Fard et al. (2007))	7.9-13.5% error for HETP, depending on turbulence model

Table 2-4: Summary of structured packing intraphase mass transfer studies.

Author(s)	*Year*	*Mass Transfer Method*	*Mass Transfer Experimental Validation*	*Mass Transfer Results*
Chen et al.	2009	Turbulent diffusion coefficient	Yes (cited Chen et al. (2004) and Chen (2006))	25.4% error for HETP
Xu et al.	2009	Molecular diffusion coefficient	Yes (cited Paschke et al. (2009))	7.5% error for the outlet mole fraction
Haroun et al.	2010	Direct numerical simulation	No, but compared to Brian et al. correlation (1961)	Enhancement factor matches correlation; Agreement between mass transfer methods for liquid-phase Sherwood number
Dai et al.	2012	Molecular diffusion coefficient	Yes	Liquid-phase mass transfer coefficients
Haroun et al.	2012	Direct numerical simulation	No	Good agreement between mass transfer methods for the liquid-phase Sherwood number
Rahimpour et al.	2013	Molecular diffusion coefficient	Not for structured packings	Mass fraction plots along column length
Sebastia-Saez et al.	2013	See reference	Limited for propane-toluene (used Paschke et al. (2009)); Comparison to Pigford (Emmert and Pigford, 1954), Zogg (1972), and Haroun et al. (2010b) correlations for oxygen-water	~50% error for propane-toluene outlet mass fraction; Same order of magnitude for Sherwood number in oxygen-water system
Sun et al.	2013	Molecular diffusion coefficient	Yes	Approximate average errors of 16% and 25% for inclined plate and baffled plate respectively
Zhang et al.	2013	Turbulent diffusion coefficient	Yes (cited (Zhang et al., 2011))	Less than 10% average deviation for mass transfer coefficients
Lautenschleger et al.	2015	Molecular diffusion coefficient	No; For traditional packings, compared to the Delft model (Olujić et al., 1999)	For mass transfer coefficient, good agreement below flooding and decent agreement above flooding
Sebastia-Saez et al.	2015a	See reference	Not for mass transfer (cited Sebastia-Saez et al. (2014))	Liquid-phase mass transfer coefficients
Sebastia-Saez et al.	2015b	Used mass source term calculated from earlier, micro-scale work	Not for mass transfer (cited Sebastia-Saez et al. (2014))	N/A

Table 2-5: Summary of structured packing intraphase mass transfer studies (continued).

Author(s)	*Year*	*Mass Transfer Method*	*Mass Transfer Experimental Validation*	*Mass Transfer Results*
Haroun & Raynal	2016	Chilton-Colburn heat/mass transfer analogy	Yes, Wang (2012) experimental data and Brunazzi correlation (Brunazzi and Paglianti, 1997)	10% deviation for gas-phase mass transfer compared to experimental data
Dong et al.	2017	Direct numerical simulation; Turbulent diffusion coefficient	No, but compared to predictions from Sebastia-Saez et al. (2015a), Haroun et al. (2012), and Henriques de Brito et al. (1992)	Good agreement between mass transfer methods for liquid-phase mass transfer coefficient; Matches correlations for the liquid-phase mass transfer coefficient
Olenberg et al.	2018	Molecular diffusion coefficient	No	Gas-phase mass transfer coefficient for various geometries
Sotoodeh et al.	2018	See reference	Yes, combination of Agirre Arisketa (2010) experimental data and process simulations	10% deviation for mole fraction data compared to process simulation predictions
Yu et al.	2018	Molecular diffusion coefficient	No	Concentration profiles and HETP
Amini et al.	2019	See reference	Yes	Mass fraction profiles; 20.45% error for HETP
Dietze	2019	Molecular diffusion coefficient	No, but validated method for a flat plate with the Higbie penetration theory (Higbie, 1935)	Contour plots; time-averaged rate of convection plots
Hill et al.	2019	Direct numerical simulation	No, but claim the HETP prediction is consistent with empirical values	Contour plots; HETP
Xu et al.	2019	Molecular diffusion coefficient	Yes, Wang et al. (2018, 2017) experimental data	Liquid-phase mass transfer coefficients
Basha et al.	2020	See reference	No	Percentage of species removed
Manh et al.	2020	See reference	Yes	Mass fraction profiles; 23% error for HETP
Singh et al.	2020	Molecular diffusion coefficient	Yes	Effective areas
Wang et al.	2020	Turbulent diffusion coefficient	Yes	Gas and liquid Sherwood numbers
Hassanvand et al.	2021	See reference	Yes	Mass fraction profiles; 24% error for HETP

Table 2-6: Summary of structured packing intraphase mass transfer studies (continued).

2.3.1. Direct Numerical Simulation

Arguably the most conceptually simple mass transfer approach, direct numerical simulation (DNS) solves the discretized governing equations for mass transfer without requiring additional closure models. These equations include the convection-diffusion equation that directly describes mass transfer. Because advection also supports mass transfer, the governing equations for flow, the continuity and Cauchy momentum equations, must also be solved. Equation (2-8) and Equation (2-9) present these governing equations for fluid flow in non-discretized form (Deen, 2012).

$$\frac{\partial \rho}{\partial t} + \nabla \cdot (\rho \mathbf{v}) = 0 \tag{2-8}$$

$$\frac{\partial \mathbf{v}}{\partial t} + \rho \mathbf{v} \cdot \nabla \mathbf{v} = \rho \mathbf{g} - \nabla p + \nabla \cdot \boldsymbol{\tau} \tag{2-9}$$

In these equations, $\mathbf{g}$ is the gravity vector, p is the pressure, and $\boldsymbol{\tau}$ is the deviatoric stress tensor. No turbulence models can be implemented when solving the governing equations by DNS. For an accurate prediction with DNS, the simulation must resolve all the turbulent eddies in the system, which exacts a large computational expense.

Haroun et al. (2010b) investigated reactive mass transfer between a gas and liquid in a structured packing through DNS. The physical system investigated was a liquid-phase reaction between CO_2 and a liquid flowing cocurrently down a corrugated structured packing. The use of a two-dimensional computational domain rather than a three-dimensional computational domain reduced the computational expense; additionally, applying a much smaller Schmidt number than typical for the system allowed a coarser

mesh to capture the key process phenomena. The Schmidt number is the ratio of momentum diffusivity to mass diffusivity and is defined according to Equation (2-10) (Bird et al., 2007).

$$Sc = \frac{\nu_m}{D_m} \tag{2-10}$$

In this equation, ν_m is the molecular kinematic viscosity. The smaller Schmidt number simplification was necessary because the mass transfer length scale is smaller than the hydrodynamic length scale by a factor of the Schmidt number's square root, severely challenging mass transfer simulations (Alke et al., 2010). From the simulations, the calculated Sherwood number was highest at locations where the packing walls projected furthest into the gas flow due to higher velocities at the interface. Flow down a corrugated geometry provided higher mass transfer than for flow down a flat plane. The authors reported the DNS results showed good agreement with the Higbie penetration theory for the liquid-phase Sherwood number, and the enhancement factor matched the trend predicted by Brian et al. (1961), though no quantitative comparison was provided for either result. For the interfacial mass transfer prediction, the authors included an adjusted flux term, as discussed in the Adjusted Flux Term section. The contact time for the Higbie penetration theory, which was outlined in the Higbie Penetration Theory section, was the ratio of the distance along the interface from the inlet to the velocity at the interface.

Haroun et al. (2012) investigated the effect of recirculation in the troughs of a corrugated structured packing using a two-dimensional, DNS approach. For the interfacial mass transfer, the local mass transfer coefficient was computed with the concentration

gradient and with a derived solubility flux, as described in the Adjusted Flux Term section. The mass transfer coefficient was used to calculate the local Sherwood number. For low liquid Reynolds numbers, the liquid film followed the wall's shape as it flowed downward. But for larger Reynolds numbers, a recirculation region formed in the troughs of the packing, which affected mass transfer by altering the gas-liquid interface. The authors reported good agreement with the Higbie model for the liquid-phase Sherwood number when using the ratio of the distance traveled by a fluid between periodic contact points of corrugation to the velocity at the interface as the contact time, although no quantitative comparison was given. Using the CFD data, the authors crafted a correlation for the contact time that included recirculation effects.

Hill et al. (2019) estimated the performance of a structured packing with simulations of REUs. The direct numerical simulation approach accounted for the turbulence-aided mass transfer. The system simulated was a nitrogen-oxygen mixture at total reflux. With the assumption that the mass transfer did not affect the hydrodynamic prediction, the hydrodynamic flow prediction for a smaller section of packing was mapped to 11 mass-transfer sections, increasing both the effective height of packing simulated for the mass transfer prediction and the amount of chemical separation performed by the packing. The material properties for the system were assumed to be constant for the system. The simulations predicted an HETP of 110 mm, which the authors claim is consistent with empirical values, although no quantitative comparison metric was provided. An adjusted flux term as described in the Adjusted Flux Term section handled the interfacial mass transfer.

Dong et al. (2017) implemented DNS in addition to a turbulent diffusion coefficient approach, as described in the Turbulent Diffusion Coefficient section.

2.3.2. Molecular Diffusion Coefficient

For cases where no turbulence-aided mass transfer exists, such as simulations of laminar flow, the molecular diffusion coefficient and Fick's first law (Bird et al., 2007) can capture the mass transfer (in conjunction with the flow profile). Equation (2-11) presents Fick's first law for mass transfer.

$$\mathbf{j}_A = -D_m \nabla c_A \tag{2-11}$$

In this equation, $\mathbf{j}_A$ is the diffusive flux for chemical species A, D_m is the molecular diffusion coefficient for chemical species A, and c_A is the concentration for chemical species A. While this approach is rigorous and easy to implement, the laminar flow requirement often limits its application.

Dietze (2019) studied the effect of adding corrugations to a flat plate and of imposing waves to the flow profile. The domain was two dimensional, and species transfer occurred in the liquid phase. The liquid Reynolds number for the simulations was 15. A constant concentration in the liquid at the gas-liquid interface was assumed, corresponding to a negligible gas-phase resistance. Waves were found to significantly enhance species transfer. Sinusoidal corrugations exhibited a similar trend, as the length to achieve an equivalent rate of convection decreased by 30 percent with the addition of sinusoidal corrugations. The rate of convection is the total amount of species being carried down the

plate by the liquid at a given distance along the plate. Corrugations produced ripples in the film, which increased interfacial surface area, and, when waves were present, enhanced liquid mixing. The Higbie penetration theory (Higbie, 1935) validated the species transfer results for a flat plate, and the author reported good agreement, although no quantitative metric was offered.

Yu et al. (2018) designed a novel, wave-like structured packing and tested its performance with both simulations and experiments. The channels for the packing were curvilinear rather than extending in a straight direction like for traditional structured packing. The system of interest was oxygen desorbing from water into air. The Higbie penetration theory governed the interfacial mass transfer, and the gas-phase mass transfer resistance was neglected when calculating the interfacial mass transfer. The contact time was the ratio of the falling film length to the liquid velocity at the interface. The authors suggested surface texture effects were significant based on simulation results showing the dissolved oxygen concentration was 6-20 percent higher for packings with a smooth surface versus a rough surface, depending on the liquid Reynolds number. Compared to Mellapak 125X, which had the same specific area as the novel packing, experimental results showed approximately 5 percent and 10 percent decreases in HETP for the smooth surface packing and rough surface packing, respectively. The experimental results and simulation results were not compared.

To study mass transfer, Xu et al. (2009) simplified the hydrodynamics in structured packing geometry to film flow. A smooth plate served as the support for the film, and the liquid phase was assumed to be laminar. The Higbie penetration theory served as the interfacial mass transfer methodology in the three-dimensional simulation, computing the

liquid mass transfer coefficients. The ratio of the interfacial length to the velocity at the interface provided the contact time. The system studied was pure propane absorbing into toluene. Waves in the liquid film were found to increase the mass transfer rate due to the increased interfacial area. These waves were not symmetric, suggesting that three-dimensional simulations are essential for structured packing studies. The authors reported a good agreement with experimental data from Paschke et al. (2009) for the outlet fraction of propane in toluene, achieving an error of 7.46 percent.

Sun et al. (2013) studied mass transfer in simplified structured packing geometries: an inclined plate and multibaffled plate, which had a series of alternatingly oriented inclined plates. In both experiments and two-dimensional CFD simulations, isopropanol desorbed from water into air. The simulation included Marangoni effects because of the high surface tension gradient within the isopropanol-water system. The Higbie penetration theory provided the means to compute the interfacial mass transfer, and the contact time was the ratio of the length of the film to the velocity at the interface. The penetration theory predicted both the liquid-phase and the gas-phase mass transfer coefficients, an unusual application because the penetration theory was developed solely for the liquid phase and assumed negligible resistance in the gas phase (Higbie, 1935). The low gas and liquid Reynolds numbers (below 400) in the system supported the approach in part. The multibaffled plate showed a markedly superior mass transfer performance compared to the inclined plate. This improvement stemmed from an enhanced renewal rate and more direction changes, which were closely related to the formation of vortices in the gas phase. For the concentration difference of isopropanol, the inclined plate and multibaffled plate

simulation results had approximate average errors of 16 percent and 25 percent respectively, relative to experimental values.

Egorov et al. (2005) expanded the work on mass transfer in KATAPAK-S packings using REUs. The process simulated was CO_2 desorption from water in KATAPAK-S packing. The k-ε turbulence model aided the gas-phase simulation prediction. Solutions to the partial differential equations governing mass transfer supported the simulation (Kenig, 2018). Solving the partial differential equations governing mass transfer while simultaneously using a Reynolds-averaged Navier-Stokes (RANS) approach, such as the k-ε model, requires a closure model to account for turbulence-aided mass transfer, which was not reported in the manuscript (Fox, 2003). The analysis produced mass fraction profiles of CO_2 in both phases.

Dai et al. (2012) conducted experiments and CFD simulations to characterize catalytic structured packings. The chemical system was oxygen desorption from water. The k-ε model predicted turbulence, while a molecular diffusion coefficient handled the mass transfer predictions. When a RANS turbulence model is employed, a closure model is needed for the mass transfer predictions (Fox, 2003); no closure model was discussed in the study. Both the experiments and the simulations produced volumetric mass transfer coefficients, which are the product of the mass transfer coefficient and the effective interfacial area. The CFD predictions were approximately three times larger than the experimental data. As part of a packing geometry investigation, the channel inclination angle, packing height, and ratio of reaction to separation regions were varied, and trends in the pressure drop and volumetric mass transfer coefficient were revealed.

Rahimpour et al. (2013) simplified the geometry of a structured packing to a series of inclined wetted wall columns. The wetted wall columns' diameter matched the hydraulic diameter of the packing channels. When flow in the structured packing would exhibit an abrupt direction change, such as when a channel terminates, complete mixing of the phases was assumed. The distance between these complete mixing points determined the lengths of the inclined wetted wall columns. Both phases were assumed to be laminar, allowing a molecular diffusion coefficient to fully predict the intraphase mass transfer. A two-dimensional CFD model predicted the flow in the inclined wetted wall columns and the rate of mass transfer across the interface. The absorption of CO_2 and H_2S into aqueous mixtures of diethanolamine (DEA) and methyl diethanolamine (MDEA) was simulated, and the average mole fraction through the column was predicted. No validation was presented for the structured packing predictions.

Lautenschleger et al. (2015) conducted CFD simulations on a novel structured packing and optimized it for minimal pressure drop while maintaining the mass transfer performance. The authors reported the mass transfer was described by the convection-diffusion equation, suggesting only the molecular diffusion coefficient was implemented. The authors used the realizable k-ε turbulence model, which requires a closure model to predict mass transfer (Fox, 2003); no closure model was mentioned in this study. The process modeled was reactive absorption of H_2S from N_2 into an aqueous NaOH solution. Since the mass transfer resistance for this process was assumed to be dominated by the gas phase, the authors simulated single-phase gas flow through the novel packing as well as through Sulzer BX and Montz B1 packings using the REU method. The inlet and outlet concentrations produced the overall mass transfer coefficient via the height-of-a-transfer-

unit/number-of-transfer-units (HTU/NTU) method. The CFD simulations showed mass transfer trends in the packing stemming from the flow profiles. For the traditional packings, the authors reported good agreement between the predictions by the Delft model (Olujić et al., 1999) for the mass transfer coefficients and the CFD results up to the loading point, although the deviation not specified. After the loading point, the deviation between the Delft model and the simulation increased to 18 percent. Optimization of the novel packing successfully reduced the pressure drop while maintaining the mass transfer performance.

Olenberg et al. (2018) crafted a novel packing by placing twisted tape inserts inside a traditional structured packing. The system of interest was the reactive absorption of H_2S into an NaOH aqueous solution from a H_2S/N_2 gas phase. The mass transfer resistance was assumed to reside entirely in the gas phase, similar to the method by Lautenschleger et al. (2015). The authors report that solutions to the convection-diffusion equation predicted the mass transfer, and the realizable k-ε model accounted for turbulence. The authors did not indicate the use of a closure model for turbulent mass transfer in the study. The inlet and outlet concentrations led to the gas-phase mass transfer coefficient, as described by Lautenschleger et al. (2015). After simulating different twisted tape geometries, the authors identified a design expected to have a significant pressure drop reduction and a similar mass transfer performance compared to a traditional packing having the same specific surface area. No experimental validation of the mass transfer performance was discussed.

Xu et al. (2019) investigated the impact of waves on the mass transfer in films on a zigzag column, a simplification of structured packings, as well as in a wetted wall column. The zigzag column was a piece of corrugated sheet metal with an inclination angle of 0°. For both the wetted wall column and the zigzag column, two-dimensional simulations were

conducted on a wavy film caused by an oscillating inlet velocity. All flow was countercurrent, and a molecular diffusion coefficient supported the CFD mass transfer predictions. The Rayleigh-Plesset equation, as described in the Other Approaches interfacial mass transfer section, governed the interfacial mass transfer. To validate their CFD model, the authors reported the CFD mass transfer coefficient predictions for a wetted wall column matched experimental data within 20 percent. These validation simulations were for the absorption of N_2O into aqueous MEA solvents. Eddies in the zigzag column were reported to enhance the mass transfer compared to a wetted wall geometry. As the liquid viscosity increased, the mass transfer coefficient decreased for both geometries and for both uniform and wavy film flow. The higher mass transfer for wavy flows was most prominent at lower viscosities, which the authors attributed to the presence of eddies.

Singh et al. (2020) predicted the volumetric mass transfer coefficients for Mellapak 250Y and used the predictions to estimate the effective interfacial area. The chemical system was CO_2 absorption into caustic solution and aqueous monoethanolamine (MEA). The physical system had three stacked REUs with a 2 mm gap between packing sheets. The Haroun interfacial mass transfer model (Haroun et al., 2010a, 2010b) was reportedly used for the interfacial mass transfer predictions, but the Haroun flux term was not included in the mass transfer equation, suggesting that a continuous concentration profile was assumed at the gas-liquid interface. The mass transfer coefficient was predicted by the Pohorecki and Moniuk model (1988) and was used in conjunction with the predicted volumetric mass transfer coefficient to estimate the effective interfacial area. A source term accounted for the reaction of CO_2, and this source term was tuned to experimental data.

The CFD-predicted effective areas were compared to experimental data, and the authors reported good agreement, although no qualitative comparison was provided.

2.3.3. Heat Transfer / Mass Transfer Analogy

The similarity between the diffusion of heat and the diffusion of chemicals is well-established. Researchers have used heat transfer as a proxy for mass transfer because advection and diffusion underpin both transport phenomena.

Hodson (1997) and Hodson et al. (1997) studied the mass transfer in structured packings using CFD heat transfer simulations. The heat transfer served as a representation of the mass transfer due to easier CFD implementation. The single-phase simulations revealed trends in the transport properties for the packing, such as locations of highest heat transfer. The results of the studies led to improvements in the packing design, producing a 5 to 17 percent increase in heat transfer efficiency within the simulations. Mass transfer experimental results for a chlorobenzene/ethylbenzene system showed approximately 10 percent more theoretical stages per meter for the novel packing than for Tianjin Mellapak packing with the same specific surface area; however, the pressure drop also increased by approximately 70 percent for F-factors higher than 2 $\sqrt{\text{Pa}}$.

Haroun and Raynal (2016) investigated H_2S migrating from N_2 to react with aqueous NaOH in a structured packing REU. Because the reaction was fast, the liquid-phase mass transfer resistance was assumed to be negligible. The gas-liquid interface was modeled as coinciding with the packing walls. Heat transfer from the packing walls was simulated, and the resultant temperature distribution provided the mass transfer coefficient for the system through the Chilton-Colburn heat/mass transfer analogy. The results were

compared to the experimental data of Wang (2012) and the correlation from Brunazzi and Paglianti (1997) for the gas-phase mass transfer. The CFD prediction had a relative deviation of less than 10 percent relative to the experimental data from Wang (2012) but had a relative deviation of approximately 25 percent at high Reynolds numbers compared to the Brunazzi (1997) correlation.

2.3.4. Tracer Phase Dispersion

The Sherwood number compares convective to diffusive mass transfer effects (Sebastia-Saez et al., 2013). In situations with large Sherwood numbers, diffusive mass transfer effects are negligible. The mass transfer occurring in these contexts, therefore, primarily depends on the convective flow field. Researchers have used this characteristic to simplify the mass transfer predictions. After obtaining converged hydrodynamic results for a system, a tracer phase with identical properties to the bulk phase is inserted into the simulation system, and the phase's spreading reveals the mass transfer performance for the system. This approach does not directly account for turbulent mixing. If a turbulence model is used in the system, then a closure model is required (Fox, 2003).

Van Gulijk (1998) modeled the transversal (horizontal) dispersion coefficient for catalytic distillation through packing channels. A dispersion coefficient reveals the spreading of the fluid as it moves through the structure. Turbulence was predicted with the k-ε model, but no closure model for turbulent mixing was included. After simulating the single-phase velocity field, the transversal dispersion coefficient was calculated by inserting a tracer phase into the device. The previously determined velocity field was used to predict the movement of the tracer through the packing. The outlet tracer concentration

data were fit to a dispersed plug flow model, allowing the dispersion coefficient to be calculated. The transversal dispersion coefficient was approximately forty times larger than for beds with random packing, revealing much better radial spreading for structured packings.

Higler et al. (1999) used CFD and experiments to study liquid-phase mass transfer in KATAPAK-S catalytic structured packing. Simulations only accounted for the liquid flow. At channel intersections, mixing could occur. The mass transfer properties were determined by simulating a constant coating of tracer on the surface of the packing and monitoring the outlet flow composition. The CFD simulations underpredicted axial dispersion coefficients by a factor of fifty compared to experimental values. The Sherwood number based on the hydraulic diameter was independent of the Reynolds number and structure size. When the simulated geometry had a channel intersection, the mass fraction of tracer increased by five orders of magnitude, leading to the conclusion that mixing at channel intersections dominates mass transfer. This result was a forerunner to the REU approach established by Petre et al. (2003).

Van Baten et al. (2001) advanced the work of van Gulijk (1998), studying both the axial and radial dispersion coefficients in a KATAPAK-S structure. The studies only simulated aqueous liquid flow. In both experiments and simulations, a salt tracer solution was introduced at the top of the packing and tracked. The predicted axial dispersion coefficient was an order of magnitude lower than experimental data, which the authors attributed to modeling simplifications. For the radial dispersion coefficient, the authors reported good agreement between the KATAPAK-S experimental results and the CFD results, although no quantitative comparison metric was provided.

Similar to their previous work, van Baten and Krishna (2001) used CFD to study liquid-phase mass transfer in KATAPAK-S structures. The authors simulated the flow of water and found the average liquid-phase mass transfer coefficient after covering the surface of the KATAPAK-S structure with tracer in the simulation and measuring the tracer mass flow at the outlet. The authors reported that the flow profiles contained within the intersection for two channels encompasses all mass transfer effects in the structure, validating the findings of Higler et al. (1999). The mass transfer coefficient was forty percent larger than the corresponding value for a packed tube without intersections.

Continuing their research of KATAPAK-S structures, van Baten and Krishna (2002) used CFD to study the mass transfer coefficients for both phases. The liquid flow and the gas flow were simulated independently. By artificially covering the surface of the structure with a tracer component and measuring the outlet flow composition, the total uptake of tracer was measured for each phase. This value paired with the packing surface area allowed the overall mass transfer rate, and therefore the mass transfer coefficient, to be found. The authors reported that the intersections between open channels quadrupled the gas-phase mass transfer relative to an empty tube; however, compared to catalyst bale packings, the overall performance was not significantly improved, where the Subawalla correlation (Subawalla et al., 1997) predicted the catalyst bale performance. The CFD-predicted gas and liquid Sherwood numbers agreed well with the Graetz solution (Janssen and Warmoeskerken, 1991) in an empty, circular tube, although no quantitative comparison metric was provided. Some of the trends for the liquid-phase mass transfer were questionable according to the authors.

2.3.5. Turbulent Diffusion Coefficient

Analogous to the turbulent eddy viscosity, the turbulent diffusion coefficient supplements the molecular diffusion coefficient by accounting for the additional mass transfer due to turbulence. Equation (2-12) shows the modified diffusive mass transfer flux after the inclusion of the turbulent diffusion coefficient.

$$\mathbf{j}_A = -(D_m + D_T)\nabla c_A \tag{2-12}$$

In this expression, $\mathbf{j}_A$ is the diffusive flux for chemical species A, D_m is the molecular diffusion coefficient, D_t is the turbulent diffusion coefficient, and c_A is the concentration for chemical species A. Although the turbulent diffusion coefficient can be presented alone, it is often embedded within the turbulent Schmidt number (Sc_t), given by Equation (2-13) (Zhang et al., 2013).

$$Sc_t = \frac{\mu_T}{\rho D_T} \tag{2-13}$$

In this equation, μ_T is the turbulent viscosity. Researchers have frequently employed models for the turbulent diffusion coefficient in simulations, such as the $\overline{c'^2} - \varepsilon_c$ model (Chen et al., 2009; Dong et al., 2017; Yu and Yuan, 2017). Alternatively, a constant turbulent Schmidt number can be assumed, making a direct analogy between turbulent momentum transfer and turbulent mass transfer.

Wang et al. (2020) performed a catalytic structured packing geometry study to determine the impact of geometric packing parameters on the hydrodynamic and mass transfer performance. Air and water served as the gas and liquid phases, respectively. The

baseline (BSL) k-ω model predicted turbulent effects on the flow field, and a constant turbulent Schmidt number of 0.7 predicted turbulent effects on the mass transfer performance. Four packing parameters were varied: the channel base length, the channel inclination angle, the channel height, and the area ratio of the structured packing section to the catalysis section. Gas and liquid Sherwood number correlations, developed with the CFD predictions, matched experimental data to average error of 8 percent.

Dong et al. (2017) studied the liquid-phase mass transfer in a structured packing using DNS and the $\overline{c'^2} - \varepsilon_c$ turbulent diffusion coefficient model. Both DNS and the renormalization group (RNG) k-ε model predicted the effects of turbulence in an REU. The molecular diffusion coefficient captured the mass transfer for DNS, but a turbulent diffusion coefficient predicted turbulence-aided mass transfer for the k-ε model. The system of interest was the reactive absorption of CO_2 into an aqueous NaOH solution. A liquid volume fraction of 0.2 served as the separation between cells classified as a liquid or a gas based on a comparison to the model by Tsai et al. (2011). The simulation did not directly resolve the reaction; instead, the reaction was instantaneous, and the chemical product CO_3^{2-} provided insight into the reaction. The authors employed an enhancement factor for the chemical reaction. A differential contactor calculation approach produced the average liquid-phase mass transfer coefficient. Similar results were reported between the two simulation methods (DNS and a turbulent diffusion coefficient) for the liquid-phase mass transfer coefficient. Significant mixing was found to occur near contact points between sheets. The concentration gradient was largest near the interface, leading to the conclusion that the mass transfer resistance primarily resided near the interface. According

to the authors, the results for the liquid-phase mass transfer coefficient agreed reasonably well with the following three models, although no quantitative comparison was presented:

- The Higbie penetration theory with the contact time being the ratio of the distance traveled by a fluid element from the inlet to the velocity at the interface, as used by Sebastia-Saez et al. (2015a)
- The Higbie penetration theory with a correlation from Haroun et al. (2012) for the contact time
- An empirical correlation from Henriques de Brito et al. (1992) for the liquid-phase mass transfer coefficient

Wen et al. (2007) studied species dispersion in Flexipac 3Y packing. The k-ε model accounted for turbulence, and the turbulent diffusion coefficient predicted the turbulence-aided mass transfer. For the species dispersion, the authors inserted a tracer phase (CO_2) into the air system at the center of the packing and simulated the dispersion of the tracer. The tracer phase was continuously supplied at the center of the packing. Mass fraction profiles through the vapor-liquid contactor resulted from the study.

Chen et al. (2009) investigated the hydrodynamics and mass transfer performance of two-phase flow in a structured packing using the REU method. The repeating unit consisted of four channels producing four crisscrossing sections. The turbulent mass transfer was modeled with a turbulent diffusion coefficient, which was produced by the $\overline{c'^2} - \varepsilon_c$ model. Experimental results for Mellapak 350Y structured packing were taken from Chen et al. (2004) and Chen (2006). An n-butane/iso-butane mixture was used for both experimental and CFD studies. The height equivalent to a theoretical plate (HETP) for the system was calculated from the simulation data, as well as being predicted from the

Gualito model (Gualito et al., 1997). The results for the HETP had a 25.4 percent error, with the CFD results often overestimating the mass transfer performance. The CFD model more accurately predicted the mass transfer efficiency than the Gualito model (Gualito et al., 1997). Mass transfer coefficients from the Rocha-Bravo-Fair model (Rocha et al., 1996) and the Gualito model (Gualito et al., 1997) predicted the interfacial mass transfer, an approach discussed in the Hybrid CFD and Semi-Empirical Models section.

Zhang et al. (2013) studied the local mass transfer coefficient using CFD for the vapor deposition of ammonia in JKB-250Y structured packing. With the assumption that the deposition process was fast, the gas phase dominated the mass transfer resistance. A turbulent Schmidt number modeled the turbulence-aided mass transfer; however, the modeling of this turbulent Schmidt number was not outlined. Four turbulence models supported the simulations: the standard k-ε model and three low-Re k-ε models. The Lam-Bremhorst low-Re-k-ε model provided the best match to experimental mass transfer coefficient data from the authors' previous work (Zhang et al., 2011). Qualitatively, the CFD analysis captured trends in the experimental results, including regions of higher mass transfer. Quantitatively, the calculated mass transfer coefficients had an average error below 10 percent compared to the experimental data.

Erasmus (2004) studied gas-phase mass transfer for a structured packing in both experiments and simulations. The author indicated the use of a turbulent Schmidt number. Three-dimensional simulations were performed for a gas-phase, naphthalene-air system. The studied region was seven REUs in series. For the computational studies, the gas-liquid interface coincided with the packing surface, simplifying the simulations to a single-phase system. Mass transfer coefficients were calculated using the inlet and outlet concentrations

for each REU. The results showed a negligible difference between the BSL and k-ω turbulence models. The CFD results were reported to match the experimental gas-phase mass transfer coefficient if the REU contained entrance and exit regions to establish the flow field; no quantitative comparison was provided. The results showed approximately constant mass transfer coefficients between the seven REUs, suggesting only one REU was necessary to predict the mass transfer for the packing.

2.3.6. Summary of Intraphase Mass Transfer Approaches

A variety of predictive intraphase mass transfer methodologies exist. While DNS offers the most reliable predictions, the computational expense limits its application for many structured packing systems. The turbulent diffusion coefficient approach has shown significant promise, despite a limited number of studies employing the method. More research is needed to test this methodology for structured packing systems. For purely laminar conditions, the simple molecular diffusion coefficient approach is promising, although ensuring a negligible impact of turbulent effects on the mass transfer predictions may require a more sophisticated approach.

Regarding structured packing studies, the impact of traditional structured packings' geometry on their performance remains largely unstudied, particularly their mass transfer performance. A deeper understanding of this consideration is especially important for continued structured packing innovation, where changes to a structured packing's design are applied to improve the chemical separation or decrease the pressure drop. Research on this topic should consider both the gas and liquid phases, both the hydrodynamic and mass transfer performances, and turbulent effects.

2.4. HYBRID CFD AND SEMI-EMPIRICAL MODELS

Mass transfer coefficients from experiments or semi-empirical models can predict the performance of structured packings in conjunction with CFD. As discussed in Appendix A: Semi-Empirical Models, the semi-empirical models often require the packing geometry, fluid flow rates, and the properties of the fluids. In return, the models predict the mass transfer coefficients and interfacial area. CFD algorithms can treat the concentration in interfacial cells as the bulk concentration, under the assumption that the concentration boundary layer is much smaller than the size of the cell. Using the estimated mass transfer coefficients and interfacial area, CFD can adjust the interfacial concentrations, while simultaneously enforcing Henry's law, to ensure the interfacial mass fluxes in the two phases agree ("Simcenter STAR-CCM+ 2019.3.1 Theory Guide," 2019). CFD code often accepts the mass transfer coefficients through Sherwood numbers ("Simcenter STAR-CCM+ 2019.3.1 Theory Guide," 2019). While the semi-empirical models predict the interfacial mass transfer rates, CFD tracks the movement of the species within each phase.

Haghshenas Fard et al. (2007) studied the mass transfer of a methanol/isopropanol mixture in MELLADUR 450Y ceramic structured packing and validated the results with experimental studies. The F-factors for the tests were small, ranging up to 0.4 $\sqrt{\text{Pa}}$. The Rocha-Bravo-Fair model (Rocha et al., 1996) gave the mass transfer coefficients, and the Onda correlation (Onda et al., 1968) supplied the effective interfacial area. Total reflux experimental data validated the simulation results. The HETP results showed a good match between the experimental and simulated systems, achieving a 9.15 percent average relative error. The average HETP error for the CFD results was approximately 20 percent lower than for the combination of the Rocha-Bravo-Fair model (Rocha et al., 1996) and the Gualito et al. (1997) model, which overpredicted the HETP.

Khosravi Nikou et al. (2008) studied hydrodynamics, mass transfer, and heat transfer for a structured packing. The RNG k-ε model predicted the impact of turbulence on the hydrodynamics. The Delft model provided the liquid and gas mass transfer coefficients (Olujić, 2002). The packing material was Flexipac 1Y, and the process simulated was methanol-isopropanol distillation at total reflux. The F-factors simulated were low, having a maximum F-factor of only 0.4 $\sqrt{\text{Pa}}$. The overall mass transfer performance was quantified with the HETP. For gas velocities larger than 0.1 $\sqrt{\text{Pa}}$, the CFD model underpredicted the HETP compared to experimental values from Haghshenas Fard et al. (2007). The error for the CFD HETP results was 12.9 percent.

Khosravi Nikou and Ehsani (2008) studied hydrodynamics, heat transfer, and mass transfer in Flexipac 1Y packing. The system investigated was methanol/isopropanol flow at steady state using four different turbulence models: k–ε, RNG k–ε, k–ω, and the BSL k–ω model. No closure model for turbulence-aided intraphase mass transfer was discussed. The Rocha-Bravo-Fair model (Rocha et al., 1996) and Gualito et al. (1997) provided the mass transfer coefficients, and the Onda correlation (Onda et al., 1968) modeled the effective interfacial area. The simulated F-factors were relatively small, having a maximum F-factor of only approximately 0.4 $\sqrt{\text{Pa}}$. Experimental values came from Haghshenas Fard et al. (2007). The error compared to experimental values for the k–ε models' HETP was 50 percent larger than for the k–ω models' HETP. The authors concluded that the k–ω and BSL models provided significantly more accurate results compared to the two k–ε models. Overall, the simulations slightly overpredicted the mass transfer performance with errors between 7.9 and 13.5 percent.

Sotoodeh et al. (2018) investigated reactive distillation systems using CFD, including mass transfer occurring in structured packings. The system of interest was ethanol and butanal reacting to form water and 1,1-diethoxy butane. The reaction occurred in Katapak SP-11 and SP-12, both of which had catalyst containers and corrugated sheets. A modified Delft model for catalytic structured packings (Behrens, 2006) predicted the liquid-phase mass transfer coefficient, and the Onda correlation provided the effective interfacial area. The authors neglected the gas-phase mass transfer resistance in the simulations, and the BSL turbulence model supported the flow predictions. Validation data came from a combination of the experimental data from Agirre Arisketa (2010) and process simulations. The CFD methodology predicted trends in the experimental mass fraction profiles and exhibited a relative error of less than 10 percent.

Amini et al. (2019) examined the mass transfer performance of a novel gauze packing through both simulations and experiments. The system was a mixture of isopropanol and methanol in PACK-2100 packing. The standard k-ω turbulence model predicted turbulence. Mass transfer coefficients from the Rocha-Bravo-Fair model predicted the interfacial mass transfer. The error for the CFD simulation predictions for HETP compared to experimental values was 20.45 percent, with the simulations underpredicting the HETP. The authors attributed the error for the CFD simulations to the assumption of uniform liquid distribution in the column.

Basha et al. (2020) predicted the flow distribution in Mellapak 250Y and also the mass transfer performance. In the simulations, the solvent Selexol absorbed CO_2 from a N_2 stream. The large eddy simulation (LES) model predicted turbulent effects on the flow profile. The Rocha-Bravo-Fair model (Rocha et al., 1996) and the Onda correlation (Onda

et al., 1968) predicted the mass transfer coefficients and effective area, accounting for the interfacial mass transfer. The percentage of CO_2 removed by the system was reported as the number of orifices in the liquid distributor varied. No experimental validation was performed for the mass transfer predictions.

Manh et al. (2020) investigated the performance of novel wire gauze structured packing with a specific packing area of 860 m^2/m^3. A methanol-isopropanol mixture served as the chemical system for the mass transfer evaluation, the standard k-ω model predicted turbulent effects on the fluid mechanics, and the Rocha-Bravo-Fair model predicted the interfacial mass transfer. The simulation HETP predictions exhibited a 23 percent average difference from experimental results, as the predictions often underestimated the HETP. The authors attributed the error to the assumption of uniform liquid distribution.

Hassanvand et al. (2021) studied the performance of a novel wire gauze structured packing with a high specific packing area of 1300 m^2/m^3. The chemical system simulated was a mixture of isopropanol and methanol. The standard k-ω turbulence model accounted for turbulence. The Rocha-Bravo-Fair model predicted the mass transfer coefficients and therefore the interfacial mass transfer. The HETP predictions differed from experimental data by 24 percent on average.

2.4.1. Summary of Hybrid CFD and Semi-Empirical Models

While CFD can implement semi-empirical models to predict the performance of structured packings, the semi-empirical models can predict the performance of traditional structured packings on their own. Additionally, semi-empirical models are often

incompatible with novel structured packing designs, limiting the range of application using this approach. To guide structured packing innovation, fully predictive methodologies are essential.

Chapter 3: Structured Packing Geometry Study for Gas-Phase Performance Using Computational Fluid Dynamics

3.1. INTRODUCTION

The transport phenomena occurring inside structured packings are still unclear, and this lack of insight hampers efforts to improve the packings. The phenomena in the gas phase are especially critical since a high percentage of the mass transfer resistance is often in that phase (Erasmus, 2004; Lautenschleger et al., 2015). Moreover, a limited amount of work has been done on varying structured packings' geometry to improve their performance. To address these issues, this research effort focused on the effects of turbulence on the gas-phase mass transfer performance in structured packings. Additionally, this chapter presents a CFD investigation of traditional structured packing geometries considering both hydrodynamics and mass transfer. Using experimental data from a pilot-scale distillation column, a robust turbulent mass transfer methodology was identified, tested, and validated. With the validated methodology, the structured packing geometry was varied while analyzing both hydrodynamic and mass transfer performances. The mass transfer system used for the simulations was the gas-film-controlled case of SO_2 absorption into caustic solution.

3.2. CFD BACKGROUND

3.2.1. Hydrodynamics

The Simcenter STAR-CCM+ 2019.3.1 CFD software was utilized in this study. The software numerically solved the governing equations for the conservation of mass and conservation of momentum, with the continuity equation describing the conservation of mass for fluid flow (Bird et al., 2007; "Simcenter STAR-CCM+ 2019.3.1 Theory Guide," 2019).

$$\frac{\partial \rho}{\partial t} + \nabla \cdot (\rho \mathbf{v}) = 0 \tag{2-8}$$

Equation (3-1) ensured conservation of momentum for Newtonian, incompressible fluids ("Simcenter STAR-CCM+ 2019.3.1 Theory Guide," 2019).

$$\frac{\partial (\rho \mathbf{v})}{\partial t} + \nabla \cdot (\rho \mathbf{v} \otimes \mathbf{v}) = -\nabla \cdot (p\mathbf{I}) + \nabla \cdot \left((\mu_m + \mu_T)(\nabla \mathbf{v} + (\nabla \mathbf{v})^{\mathbf{T}}) \right) \tag{3-1}$$

The pressure in this equation combines hydrostatic and static contributions. The hydrodynamic and mass transfer solvers used second-order schemes for convection. The steady-state performance was predicted by the segregated flow solver, utilizing the SIMPLE algorithm, and the fluid was assumed to have a constant density and be isothermal. For the turbulent viscosity, μ_T, a turbulence model capable of accurately predicting the hydrodynamic performance was essential. Since both laminar and turbulent conditions could exist in structured packings, the turbulence model should provide accurate

predictions in both flow regimes (Duss, 2013). Previous investigation has indicated the lag elliptic-blending k-ε turbulence model with all-y+ wall treatment meets the requirement, showing the most accurate friction factor predictions for pipe flow out of 12 Reynolds-averaged Navier-Stokes (RANS) turbulence and one control model (Macfarlan et al., 2021).

3.2.2. Mass Transfer

A passive scalar model was used to predict the mass transfer performance of structured packings. This model inhibits the mass transfer solution from affecting the hydrodynamics solution, which is relevant when the diffusing species is dilute. The governing equation for the passive scalar model is shown in Equation (3-2).

$$\frac{\partial(\rho x_A)}{\partial t} + \nabla \cdot (\rho x_A \mathbf{v}) = -\nabla \cdot \mathbf{j}_A + S_A \tag{3-2}$$

The diffusive flux, $\mathbf{j}_A$, had contributions from molecular diffusion and from turbulence.

$$\mathbf{j}_A = -\rho(D_m + D_T)\nabla x_A \tag{3-3}$$

The turbulent diffusion coefficient was predicted by a constant turbulent Schmidt number, forming a direct analogy between turbulent mass transfer and turbulent momentum transfer (Fox, 2003; Wang et al., 2020; Zhang et al., 2013).

$$Sc_T = \frac{\nu_T}{D_T} = \frac{\mu_T}{\rho\, D_T} = 0.7 \qquad (3\text{-}4)$$

Turbulent eddies cause increased viscous effects in the system, but the eddies also support the mixing of species in a system (Pope, 2000). Since the same physical phenomenon affects both the hydrodynamics and the mass transfer, the analogy between the hydrodynamics and the mass transfer is physically reasonable.

For the molecular diffusion coefficient, a value of 0.125 cm^2/s was used. This value was predicted by the Massman model (Massman, 1998) for atmospheric pressure and a temperature of 22°C, which approximately matched the experimental conditions in Macfarlan et al. (2021).

3.3. CFD RESULTS

3.3.1. Pipe Flow

Following the work of van Baten and Krishna (2002), the gas-phase mass transfer in a wetted-wall column was first simulated, which served as a test of the mass transfer approach. Building on the efforts of Erasmus (2004), Lautenschleger et al. (2015), Haroun and Raynal (2016), and Olenberg et al. (2018), the liquid film was assumed to be infinitely thin, so the gas-liquid interface coincided with the pipe walls. The process simulated was SO_2 scrubbing by reaction with concentrated aqueous NaOH. The liquid-phase reaction was fast enough that the SO_2 concentration at the gas-liquid interface was assumed to be zero. Table 3-1 displays the physical properties for the system. The pipe was 4 cm in

diameter and 2 m in length, as shown in Figure 3-1. The two pipe ends had periodic boundary conditions, and the specified mass flow rate through those faces yielded a Reynolds number of 5,000. The base cell size was 4 mm, and 16 prism layers covered the pipe walls. The simulation progressed until the hydrodynamic solution converged.

Molecular Dynamic Viscosity, μ_m (Pa-s)	**Density, ρ (kg/m^3)**	**Molecular Diffusion Coefficient, D_m (cm^2/s)**
1.84e-5	1.195	0.125

Table 3-1: Physical properties.

The converged hydrodynamic solution was the starting point for the mass transfer simulations. After the hydrodynamic predictions converged, the periodic boundary conditions were replaced with a velocity inlet boundary condition at the entrance and pressure outlet boundary condition at the end. The converged hydrodynamic profile, namely the velocity and the turbulence quantities (turbulent kinetic energy, turbulent dissipation rate, and reduced stress function), supplied the conditions at the new velocity inlet condition. The reduced stress function is a turbulence quantity for the lag elliptic-blending k-ε turbulence model representing the wall-normal stress component ("Simcenter STAR-CCM+ 2019.3.1 Theory Guide," 2019). The inlet mass fraction of SO_2 was 55.28 ppm to be consistent with the experimental conditions in Macfarlan et al. (2021). The SO_2 mass fraction at the walls was zero, corresponding to a complete reaction with NaOH. The SO_2 mass fraction at the outlet was numerically calculated from the flow profile inside the pipe. In the event of backflow at a pressure outlet, a mass fraction is required. A mass fraction of zero was specified, although no backflow was detected in any pipe flow simulation. The mixing-cup mass fraction of SO_2 quantified the remaining amount of SO_2

at various cross-sections along the pipe length. The mixing-cup mass fraction is the average mass fraction weighted with the velocities on the cross-section, and it better depicted the average mass fraction in the flow exiting the pipe than a simple surface average because it accounted for the varied mass fluxes at different radial positions.

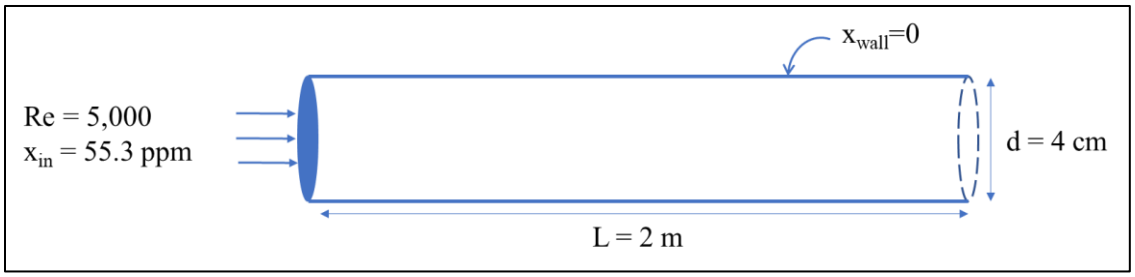

Figure 3-1: Configuration for mass transfer in pipe flow simulations.

A mesh sensitivity analysis was conducted for the base cell size as well as the number of prism layers, the latter being critical to resolve the thin concentration boundary layer. Starting from the original case, halving the base cell size did not alter the mass transfer prediction, as Table 3-2 shows. Similarly, a 50 percent increase in the number of prism layers did not change the mass fraction predictions. Therefore, the mesh was fine enough to capture the relevant mass transfer phenomena.

Base Cell Size (mm)	Prism Layers	Outlet Mixing-Cup Mass Fraction (ppm)
4	16	23.5
2	16	23.5
4	24	23.5

Table 3-2: Mesh sensitivity study for pipe-flow mass transfer simulations.

The pipe flow simulation results validated the CFD mass transfer methodology. The mass-fraction profiles from the pipe flow simulations are plotted in Figure 3-2. Multiple semi-empirical models validated the accuracy of the results. Figure 3-2 plots predictions from the Sherwood correlation (Gilliland and Sherwood, 1934), McCarter correlation (McCarter and Stutzman, 1959), and Spedding correlation (Spedding and Jones, 1988) for the mass fraction along the length of the pipe. The simulation results resided between the predictions from the various models. The excellent agreement with the semi-empirical data confirmed the ability of the turbulent Schmidt number approach to account for turbulent mass transfer effects.

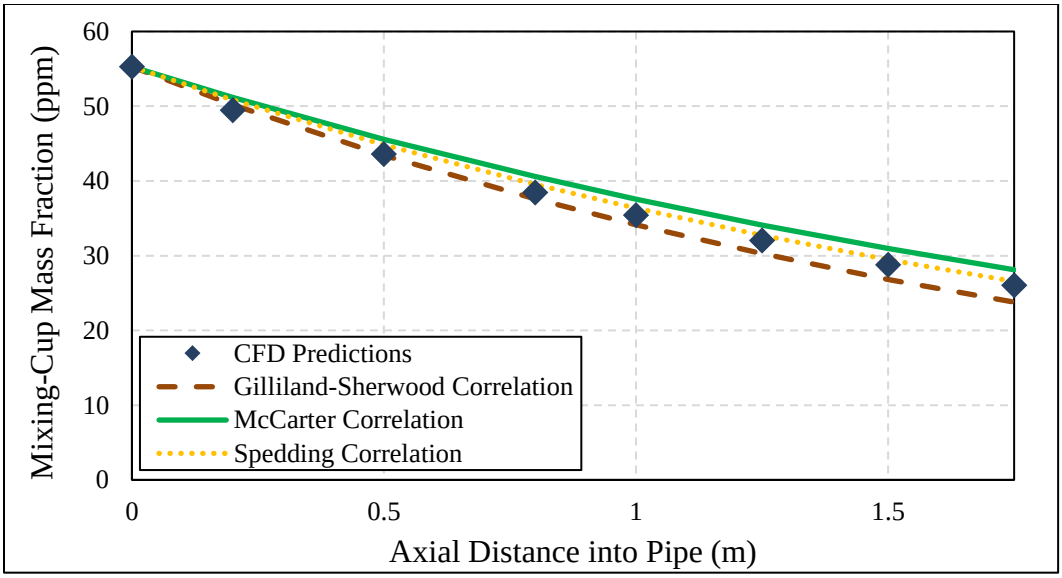

Figure 3-2: Empirical correlation and CFD mass transfer predictions for SO_2 scrubbing in a wetted-wall column with a Reynolds number of 5,000.

3.3.2. Single REU

Utilizing the methods developed and validated in previous sections, the hydrodynamic and mass transfer performances in a structured packing system were simulated through the use of a representative elementary unit (REU). An REU captures the repeating geometry of a structured packing and is effectively the building block of a structured packing, as shown in Figure 1-3. Multiple researchers have shown promising results for using an REU's CFD performance to predict the performance of the structured packing as a whole (Basden, 2014; Erasmus, 2004; Lautenschleger et al., 2015; Petre et al., 2003).

To validate the mass transfer methods on a structured packing system, the hydrodynamic and mass transfer performance of a Mellapak 250Y REU was simulated. Table 3-3 shows the dimensions of the REU (Petre et al., 2003), and Figure 3-3 illustrates the channel dimensions in the REU. Building on the efforts of Erasmus (2004), Lautenschleger et al. (2015), Haroun and Raynal (2016), and Olenberg et al. (2018), the liquid film was assumed to be infinitely thin so the gas-liquid interface coincided with the packing surface.

Channel Inclination Angle, α (°)	**Channel Base Length, b (mm)**	**Channel Height, h (mm)**	**Channel Side Length, s (mm)**	**REU Height, H (mm)**
45	24.1	11.9	17.0	34.1

Table 3-3: Dimensions of a Mellapak 250Y REU.

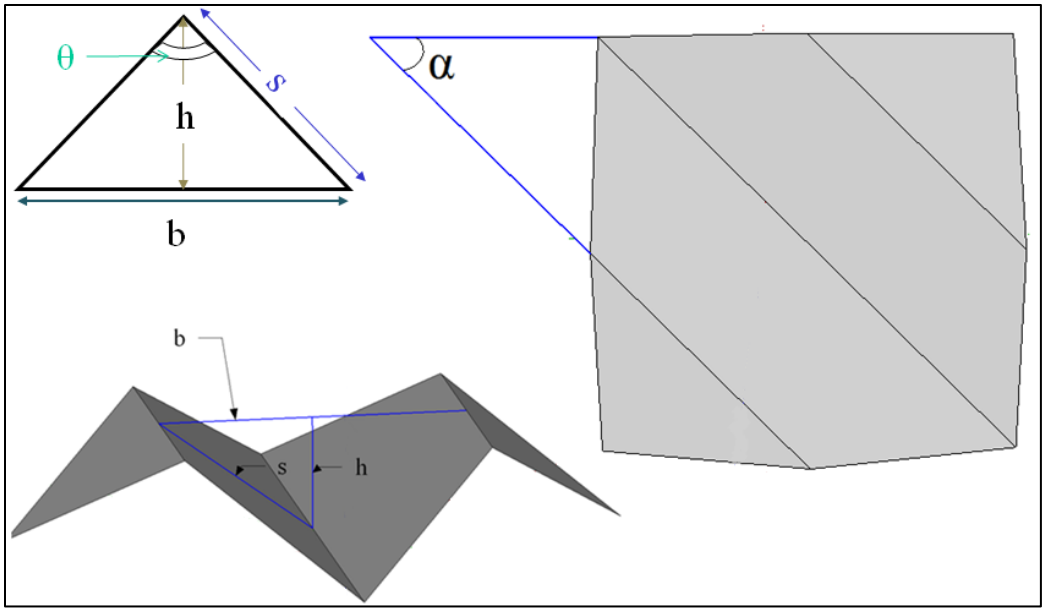

Figure 3-3: Structured packing parameters (Basden, 2014).

The chemical system was dilute SO_2 diffusing from air into caustic solution, as was performed experimentally by Macfarlan et al. (2021). The physical properties for the system are listed in Table 3-1. The left and right sides of the REU had periodic boundary conditions, as did the top and bottom surfaces. Additionally, between the top and bottom surfaces, a pressure drop was imposed, driving the gas upward. The front and back of the REU, which correspond to the packing surface, had no-slip boundary conditions. As the simulation developed, the F-factor of the flow through the top surface was monitored. The F-factor is a measure of the vapor flow rate, where the F-factor is defined according to Equation (3-5) (Olujić et al., 2004).

$$F_G = v_{G,s}\sqrt{\rho_G} \tag{3-5}$$

For systems with a specified pressure drop, when the F-factor and the mass flow rate through the top surface changed by less than 0.1 percent over the last 200 iterations, the hydrodynamic portion of the simulation completed. Some simulations demonstrated an oscillatory convergence not meeting the criteria previously described. Phan et al. (2020) determined that a transitional flow regime can cause non-traditional convergence when utilizing the lag elliptic-blending k-ε turbulence model with all-y+ wall treatment. In those oscillatory-converged situations, the simulation was ended when the F-factor matched the average F-factor from the last 1,000 iterations. For systems with a specified gas velocity, imposed by setting the mass flow rate between the top and bottom periodic boundary conditions, the hydrodynamic solution converged when the total pressure drop across the system changed by less than 0.01 percent over the last 500 simulations. For oscillatory-converged cases, the simulation ended when the pressure drop or F-factor (whichever was the dependent variable) matched its values from the past 1,000 iterations. The lag elliptic-blending k-ε turbulence model with all-y+ wall treatment predicted turbulent effects.

After obtaining and recording the hydrodynamic results, the REU's mass transfer performance was simulated. The segregated flow velocity solver, lag k-ε turbulence model solver, and k-ε turbulent viscosity solver were frozen, inhibiting the velocity or turbulent properties from further change during subsequent stages of analysis. The top and bottom periodic boundary conditions were removed, with the bottom boundary condition becoming a velocity inlet condition and the top boundary condition becoming a pressure outlet condition. At the velocity inlet condition, the SO_2 mass fraction was 55.28 ppm to correspond with the experimental conditions of Macfarlan et al. (2021). Consistent with the experiments, the NaOH solution in the liquid was assumed to be concentrated and the

reaction of SO_2 with NaOH was assumed to be fast, so any SO_2 contacting the liquid was instantly consumed. In the simulation, this condition corresponded to a SO_2 mass fraction of zero at the walls of the REU. The mass fraction of SO_2 at the exit was determined by the flow profile in the REU. A mass fraction must be specified in the event of backflow at a pressure outlet, and a mass fraction of 0 was provided. The mass transfer coefficient was calculated using the SO_2 efflux from the system with Equation (3-6).

$$k_G = \frac{Q}{A_i} \cdot \ln\left(\frac{x_{SO_2,i} - \overline{x_{SO_2,in}}}{x_{SO_2,i} - \overline{x_{SO_2,e}}}\right) \tag{3-6}$$

The average mass transfer coefficient, k_G, is defined as the local mass transfer coefficient averaged over the height of the system (Seader et al., 2011), as Equation (3-7) shows.

$$k_G \equiv \frac{1}{Z_2 - Z_1}\int_{Z_1}^{Z_2} k\, dZ \tag{3-7}$$

Equation (3-8) defines the local mass transfer coefficient, k (Seader et al., 2011).

$$N_A \equiv k A_i \Delta c_A \tag{3-8}$$

The mass transfer portion of the simulation completed when both the mixing-cup SO_2 mass fraction at the outlet as well as the mass transfer coefficient changed by less than 0.01 percent over the last 500 iterations. Analogous to the hydrodynamic case, if a

simulation demonstrated an oscillatory convergence, the simulation ended when the SO_2 mass fraction matched the average value from the past 1,000 iterations.

A mesh sensitivity study ensured the system's mesh was fine enough for the REU system. As the mesh had both prism layer cells and core, polyhedral cells, the two cell types were evaluated independently. Starting with a base cell size of 0.3 mm, 12 prism layers, and a 0.6 mm thick prism layer region, the number of prism layers was varied by 50 percent between cases to determine the number of prism layers necessary to adequately capture the near-wall effects. As shown in Figure 3-4, the mass transfer coefficient and the F-factor for the system remained relatively constant between meshes with at least 12 prism layers. Therefore, 12 prism layers were sufficient. Next, the base cell size was evaluated, with the size varying by 50 percent between each case. Figure 3-5 shows a similar F-factor and mass transfer coefficient resulting from base cell size meshes less than 0.45 mm. Therefore, a 0.45 mm base cell size with 12 prism layers captured the relevant phenomena sufficiently, including the mass fraction gradients, as Figure 3-6 depicts. It should be noted that, for the 1 Pa pressure drop imposed between the top and bottom faces, oscillatory convergence was observed for the hydrodynamic portion of the simulations.

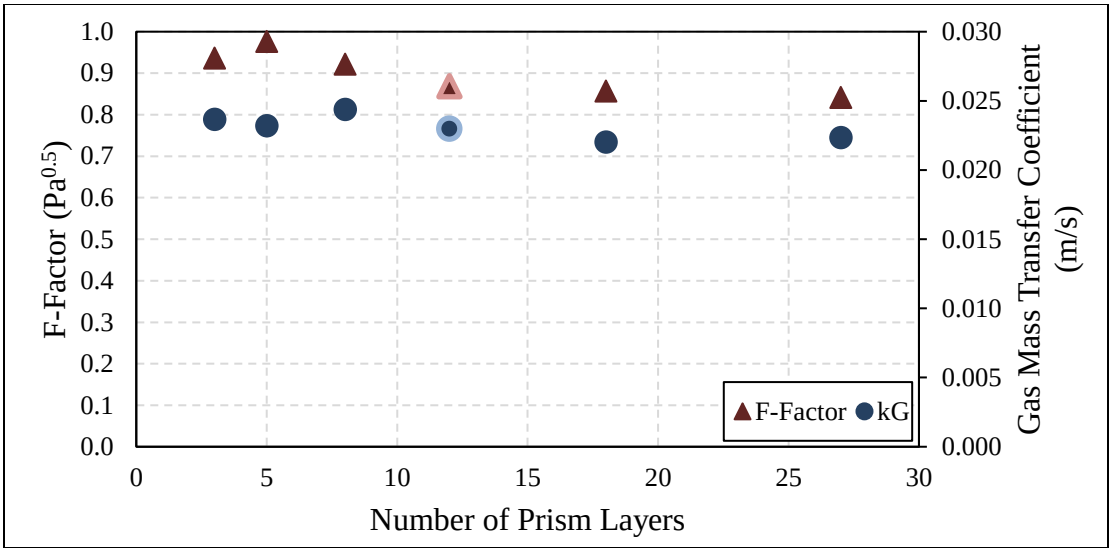

Figure 3-4: Mesh sensitivity study for the effect of the number of prism layers on both the hydrodynamics and mass transfer with the selected core mesh size highlighted.

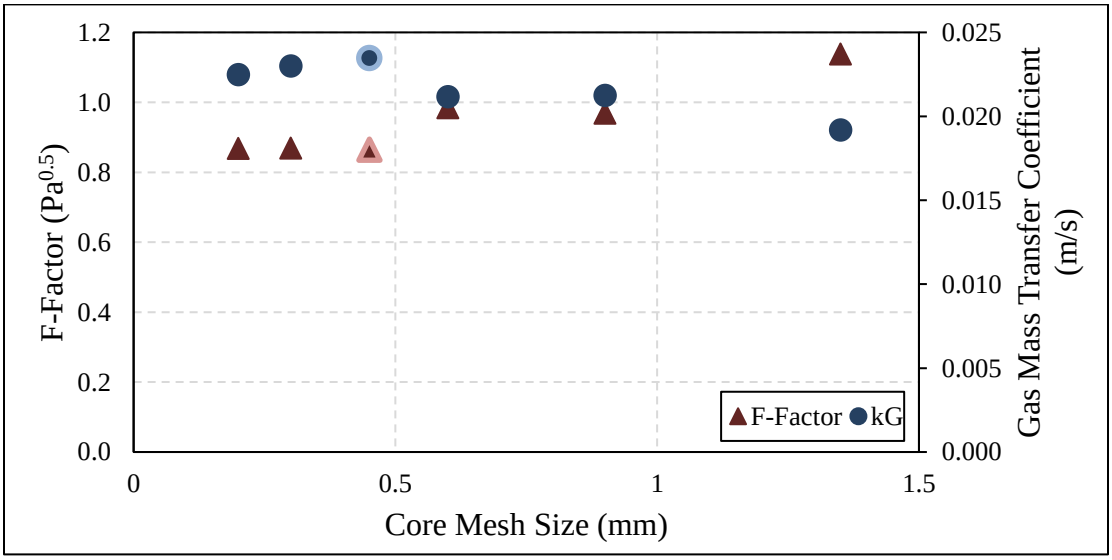

Figure 3-5: Mesh sensitivity study for the effect of the core mesh size on both the hydrodynamics and mass transfer with the selected core mesh size highlighted.

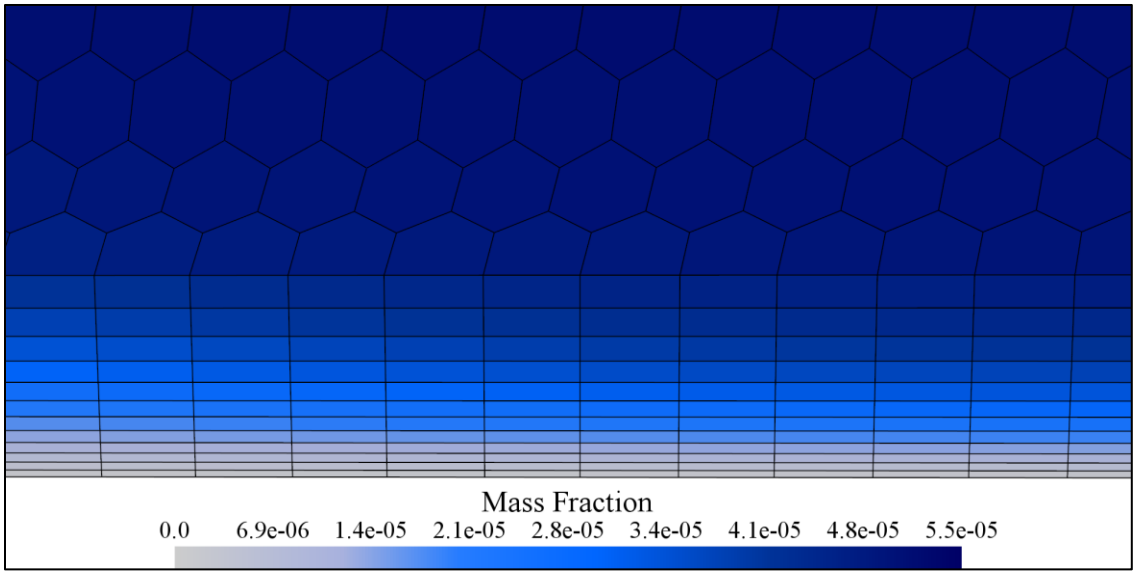

Figure 3-6: Mass fraction gradients captured by mesh.

The mass transfer predictions from the CFD simulations agreed with the experimental data. Simulations were conducted for pressure drops ranging from 14.7 to 249 Pa/m between the top and bottom faces. Figure 3-7 shows the mass transfer coefficients predicted by the simulations as a function of the F-factor. Experimental data from the Separations Research Program at the University of Texas at Austin are also included in Figure 3-7 (Macfarlan et al., 2021). Semi-empirical models for predicting the mass transfer performance of structured packings are plotted as well. The CFD predictions show strong agreement with the experimental data, both quantitatively and qualitatively. Quantitatively, the CFD predictions showed an absolute average deviation (AAD) of five percent. Qualitatively, the CFD predictions showed a similar trend to the experimental data, increasing as the F-factor grew. Together, the quantitative and qualitative agreement with the experimental data validated the CFD methodology.

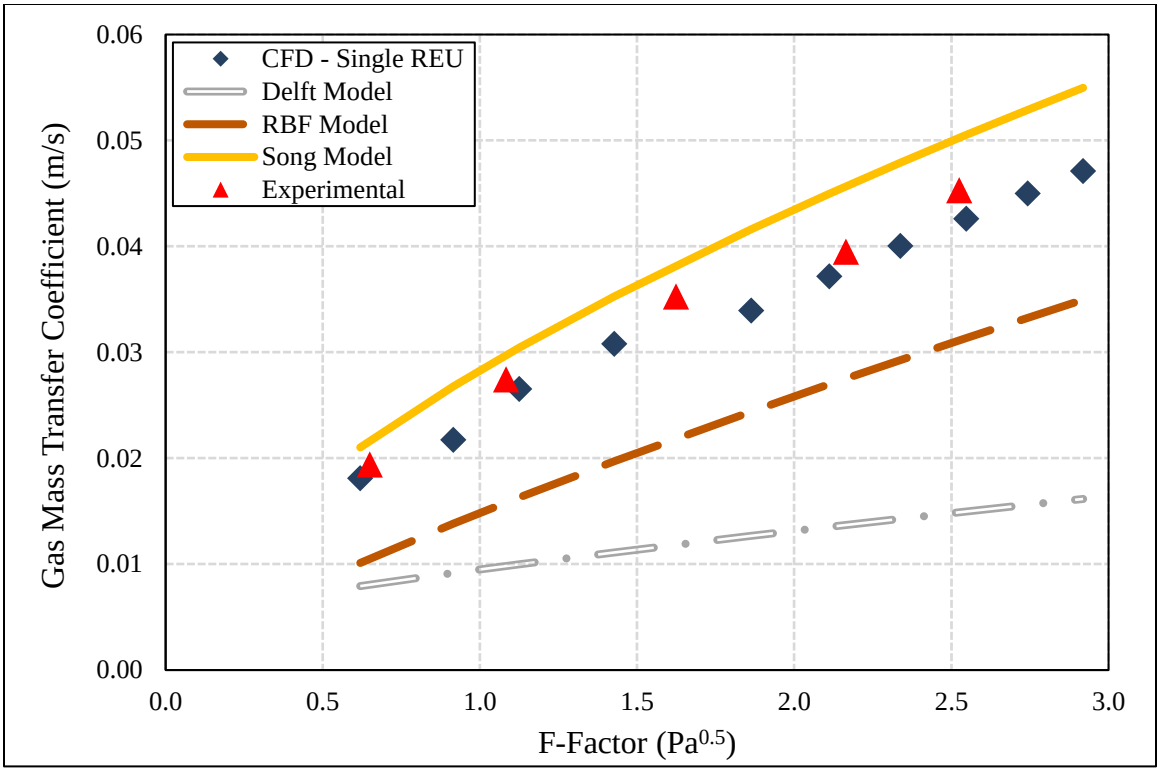

Figure 3-7: CFD SO_2 absorption results in Mellapak 250Y compared to experimental data and semi-empirical correlations: the Delft model, the Rocha-Bravo-Fair (RBF) model, and the Song model.

The following three semi-empirical models were compared to the CFD predictions: the Delft model (Dejanović et al., 2011; Olujić, 2019; Olujić et al., 2012, 2004; Olujić and Seibert, 2014), the Rocha-Bravo-Fair model (Rocha et al., 1996), and the Song model (Song, 2017). All three of these models were developed using large experimental databases from pilot-scale or larger columns. In the Rocha-Bravo-Fair model, the liquid velocity was set to zero to match the simulation conditions, effectively the limit of extremely low liquid flow, simplifying the gas Sherwood number prediction to the form in Equation (3-9). The predictions for the mass transfer coefficient significantly varied. The mass transfer coefficients predicted by the simulations reside within the predictions from the semi-

empirical models, showing marginal agreement between the semi-empirical models and the current CFD approach and validating the simulation results.

$$\mathrm{Sh_G} = \frac{k_G s}{D_{G,m}} = 0.054 \left(\frac{v_{G,effective} \rho_G s}{\mu_{G,m}} \right)^{0.8} \left(\frac{\mu_{G,m}}{D_{G,m} \rho_G} \right)^{0.33} \quad (3\text{-}9)$$

The simulations revealed that the crimps in the structured packing significantly impacted the mass transfer. For an F-factor of 0.92 $\sqrt{\text{Pa}}$, Figure 3-8 shows the mass fraction of SO_2 on the plane between the two packing sheets. As the gas traveled upward, the mass fraction of SO_2 in the gas dropped noticeably after the gas crossed each crimp in the structured packing. The driving factor for this increased mass transfer was the higher average velocity in the region near the packing crimps. As Figure 3-9 demonstrates, the speed of the gas in the core of the channel was larger than the speed near the packing surface. This trend stemmed from the no-slip boundary condition at the packing surface. The higher velocity produced more turbulence, which increased the turbulence-aided mass transfer. Figure 3-10 demonstrates this effect, highlighting the relatively large value for the turbulent diffusion coefficient in the region near the packing crimps despite only a relatively low F-factor of 0.92 $\sqrt{\text{Pa}}$. At the same F-factor, the turbulent diffusion coefficient was also relatively large in the bulk gas flow, as Figure 3-11 shows. Lastly, Figure 3-12 shows the local mass transfer coefficient on the surface of the packing, and the local mass transfer coefficient values are noticeably higher near the structured packing crimp that projects into the flow. The trends in Figure 3-12 further highlight the importance of the structured packing crimps on the gas-phase mass transfer performance.

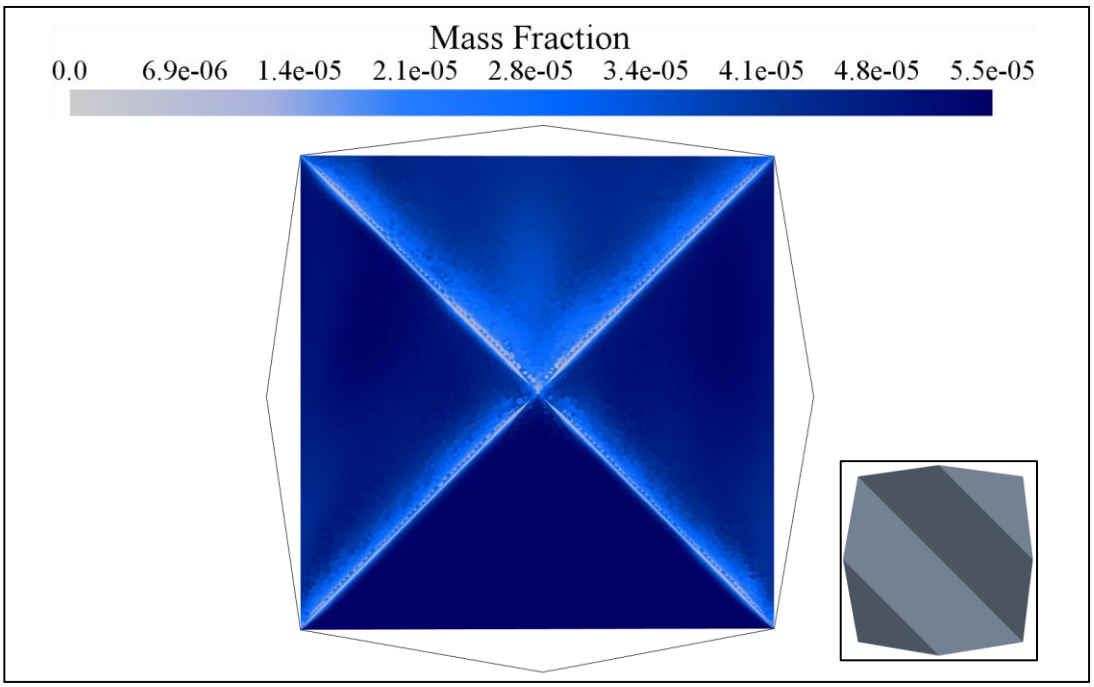

Figure 3-8: SO_2 mass fraction on plane between packing sheets for an F-factor of 0.92 $Pa^{0.5}$; insert shows section of REU.

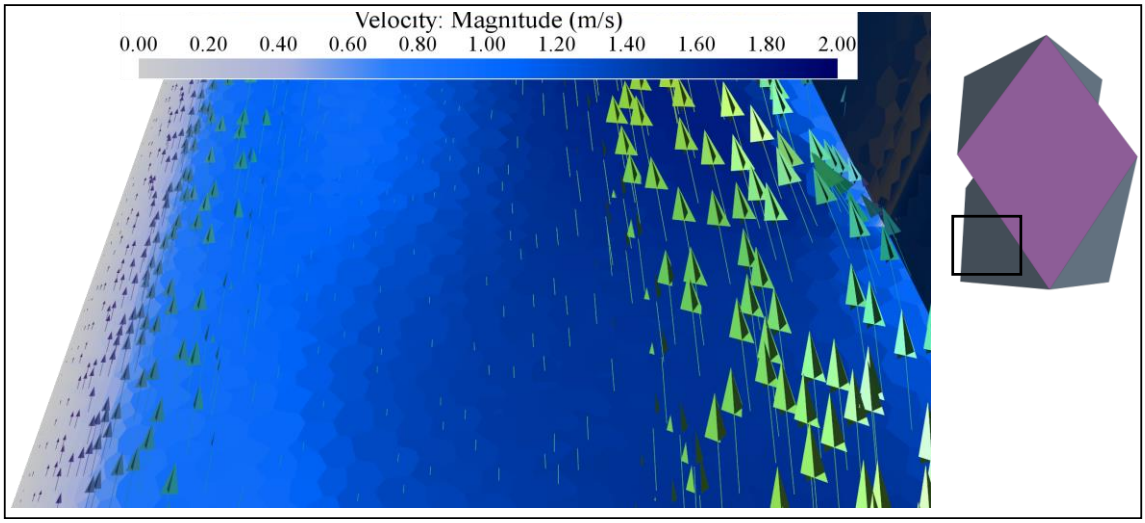

Figure 3-9: Velocity magnitude in REU for an F-factor of 0.92 $Pa^{0.5}$, revealing larger velocity magnitudes near the center of the structured packing channel; insert shows the region of the REU captured.

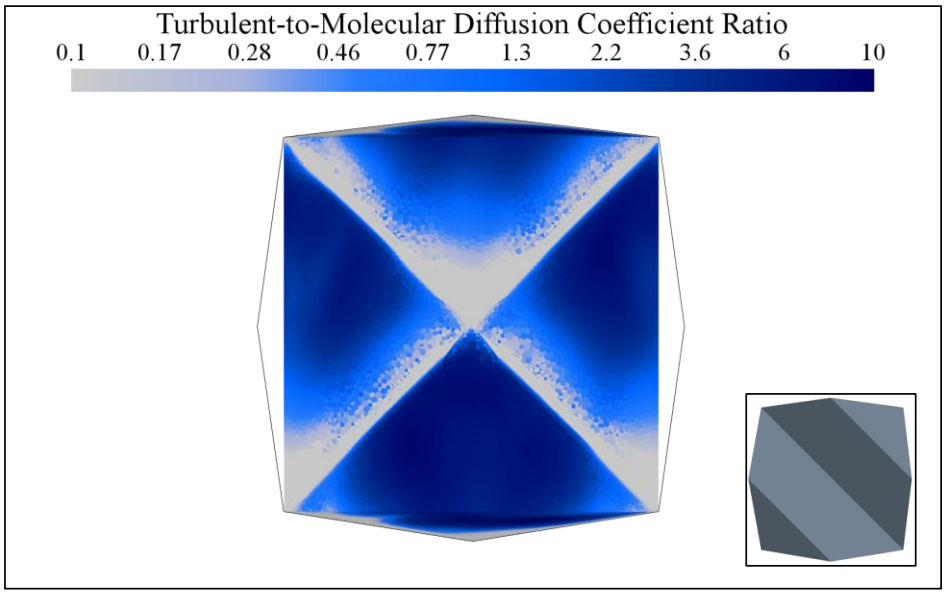

Figure 3-10: Turbulent-to-molecular diffusion coefficient ratio on plane between packing sheets for an F-factor of 0.92 $Pa^{0.5}$; insert shows region of REU.

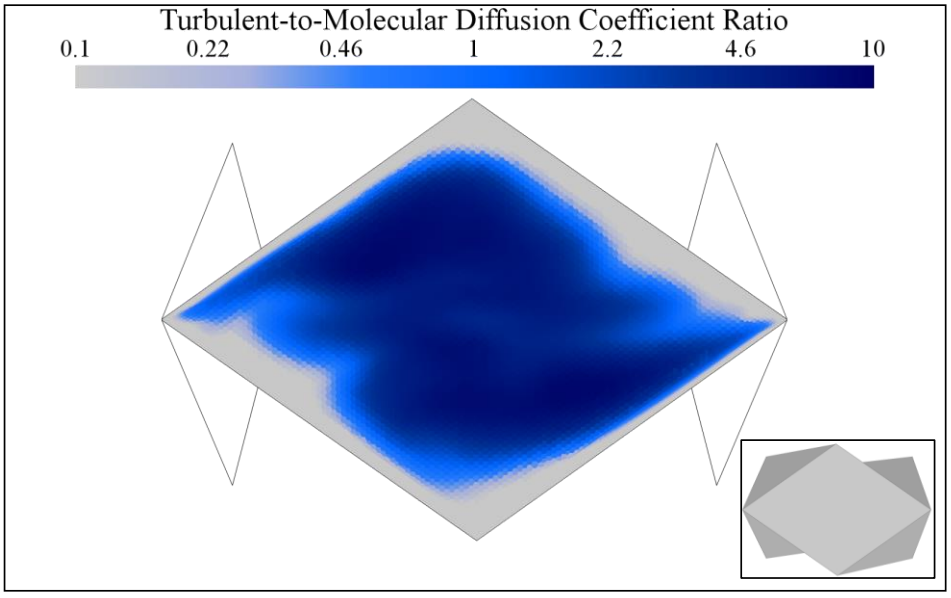

Figure 3-11: Turbulent-to-molecular diffusion coefficient ratio on top surface of REU for an F-factor of 0.92 $Pa^{0.5}$; insert shows region of REU.

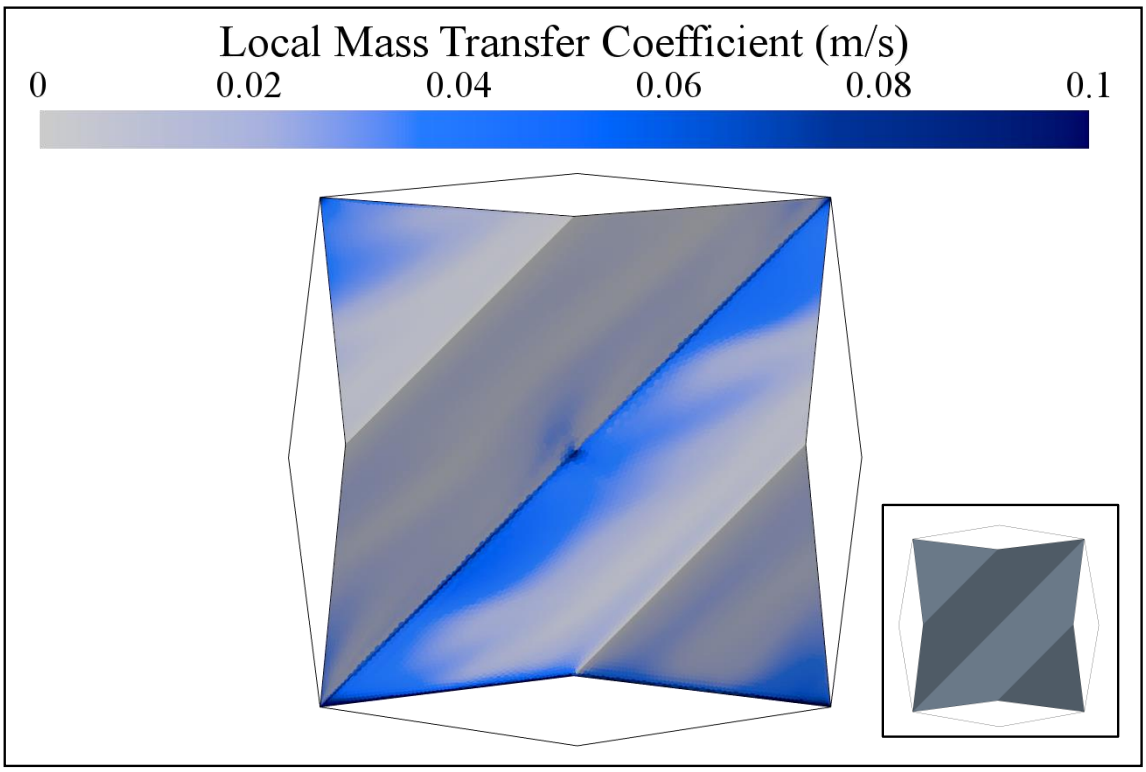

Figure 3-12: Local mass transfer coefficient on back surface of REU for an F-factor of 0.92 $Pa^{0.5}$; insert shows region of REU.

3.3.3. Stacked REU

Simulations in a multiple-REU system tested the impact of periodic boundary conditions as well as the frozen-flow-field mass transfer methodology on the mass transfer prediction. A single REU with periodic boundary conditions between the top and bottom surfaces could potentially change the velocity profile and change the prediction of the REU's mass transfer performance. Additionally, not simulating the hydrodynamics and mass transfer simultaneously could alter the CFD predictions. An REU system with

multiple REUs in the vertical direction removed the top/bottom periodic boundary condition and eliminated the independent simulation of the hydrodynamics and mass transfer.

A system with eight REUs was simulated, as shown in Figure 3-13. The meshing conditions of the stacked REU system matched the meshing conditions in the single REU system. The bottom of the system had a specified, uniform velocity and a specified SO_2 mass fraction. The left and right surfaces of the REUs had periodic boundary conditions, and the front and back of the REUs, corresponding to the packing surface, had no-slip conditions. The bottommost four REUs served as an entrance region, developing the flow into its steady-state profile. To measure the mass transfer coefficient, the target REU's packing surface had a specified mass fraction of zero. In REUs where the mass transfer performance was not being simulated, the packing walls had zero flux conditions for the diffusing species. Only a single REU's mass transfer performance was measured at a time. The physical properties of the system matched the conditions in Table 3-1. The velocity specified on the bottom surface was 2.31 m/s, which gave an F-factor of 2.53 $\sqrt{\text{Pa}}$, matching the most turbulent case in the experiments of Macfarlan et al. (2021).

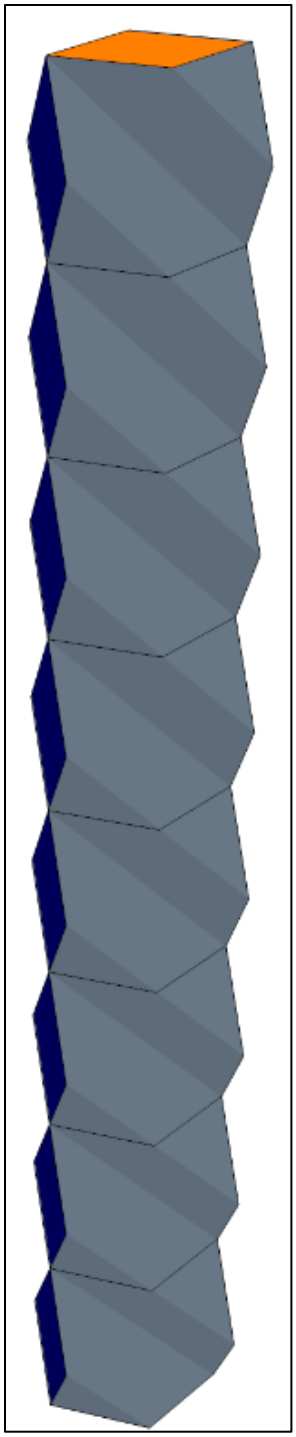

Figure 3-13: Simulated system of eight stacked REUs.

To ensure the entrance region was long enough, the pressure drop and the mass transfer coefficient in the topmost REUs of the system were measured. Figure 3-14 shows the pressure drop across each REU, measured by the difference in the relative total pressure's surface average between the top and bottom surfaces of each REU. The REUs before the fifth REU from the bottom showed significant variation in the pressure drop, due to the undeveloped flow. For the last four REUs, the pressure drop became more consistent. From the trends in Figure 3-14, four REUs effectively develop the flow field. To ensure four REUs provided a long enough entrance region for the mass transfer prediction, the mass transfer performances for the fifth, sixth, seventh, and eighth REUs from the bottom were simulated. Although the velocity and other hydrodynamic solvers remained on, the mass transfer performance in each REU was simulated individually by only applying the interfacial mass transfer condition to the targeted REU. Figure 3-15 plots the mass transfer coefficients for each REU and shows a similar mass transfer performance for the four topmost REUs. Therefore, four REUs sufficiently developed the flow, and only a system of five REUs was simulated in the following analysis. The prediction for the mass transfer coefficient in the fifth REU negligibly changed between the eight REU system and the five REU system.

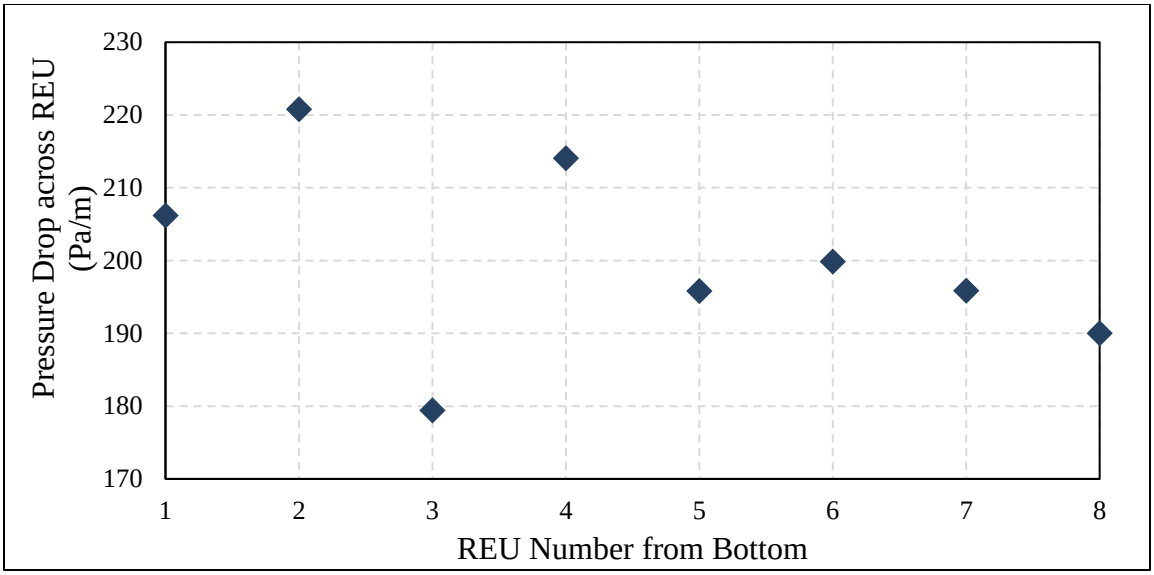

Figure 3-14: Pressure drop across each REU in an eight REU system for an F-factor of 2.53 $Pa^{0.5}$.

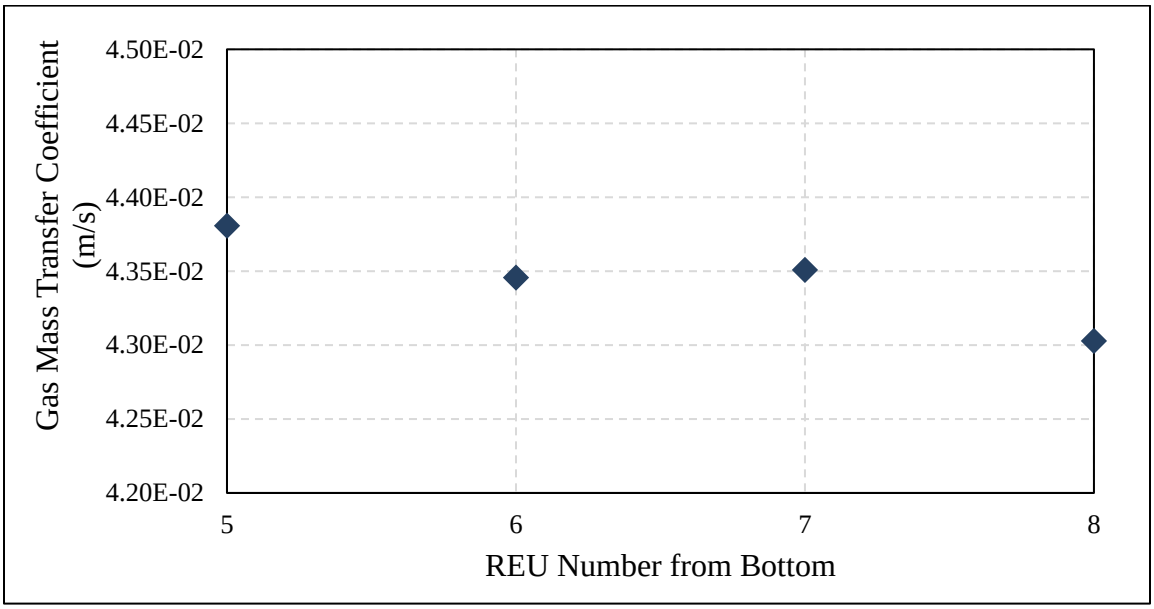

Figure 3-15: Gas mass transfer coefficient for topmost, developed REUs in an eight REU system for an F-factor of 2.53 $Pa^{0.5}$.

When the F-factor ranged from 0.65 to 2.8 $\sqrt{Pa}$, the mass transfer coefficient increased, as Figure 3-16 shows. This increase directly resulted from the high gas-phase velocities, which enhanced mixing. Figure 3-16 also contains the experimental data and the predictions from the semi-empirical correlations. Qualitatively, the multiple-REU results matched the experimental data and the single REU predictions. Quantitatively, for the cases matching the experimental F-factors, the absolute average deviation (AAD) was three percent compared to the experimental values, showcasing the agreement between the experimental data and both CFD approaches. Additionally, the agreement between the CFD approaches revealed the periodic boundary conditions and the mass transfer approach with a single REU did not significantly alter the mass transfer prediction. Therefore, the top and bottom periodic boundary conditions did not impair the predictions, and neither did the asynchronous predictions for the hydrodynamics and mass transfer.

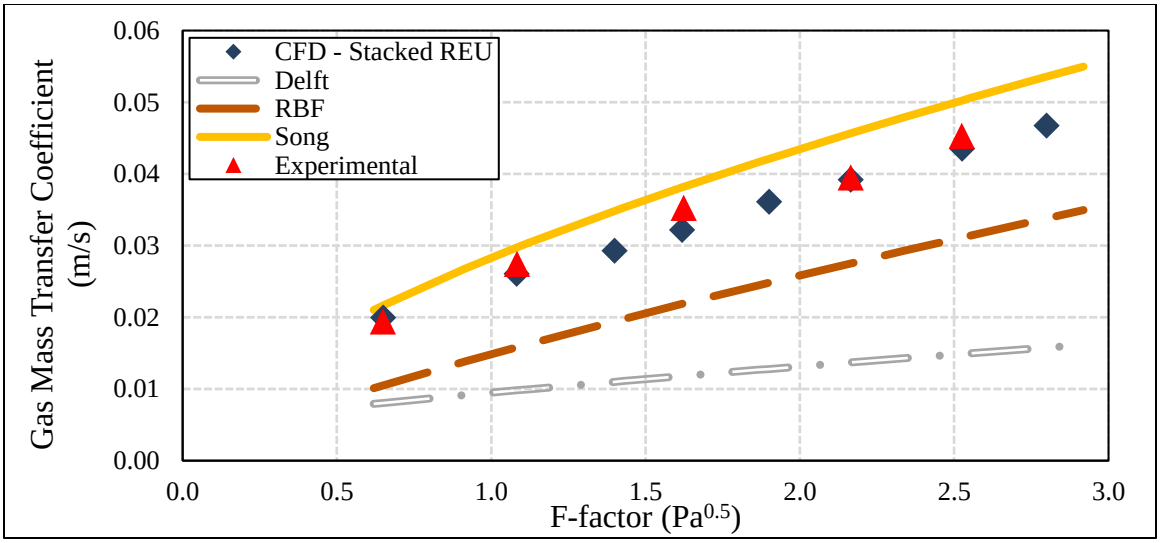

Figure 3-16: CFD SO_2 absorption results in a five-REU system compared to experimental data and semi-empirical correlations: the Delft model, the Rocha-Bravo-Fair (RBF) model, and the Song model.

3.3.4. Packing Geometry Investigation

To identify packing geometries exhibiting low pressure drop but large mass transfer rates, three parameters fundamental to traditional structured packing geometries were systematically varied. The three fundamental parameters were the specific packing area, the channel inclination angle, and the channel opening angle, which are illustrated in Figure 3-3. Basden (2014) also identified these three variables for a hydrodynamic packing geometry study. The specific packing area (A_P), channel inclination angle (α), and channel opening angle (θ) are related to the channel side length (s), channel base length (b), and channel height (h), assuming perfectly sharp channel crimps (Basden, 2014; Petre et al., 2003).

$$b = \frac{4}{A_P \cos\left(\frac{\theta}{2}\right)} \tag{3-10}$$

$$s = \frac{4}{A_P \sin(\theta)} \tag{3-11}$$

$$h = \frac{2}{A_P \sin\left(\frac{\theta}{2}\right)} \tag{3-12}$$

The height of an REU is also related to the three fundamental variables through Equation (3-13).

$$H = \frac{4}{A_P \cos(\alpha) \cos\left(\frac{\theta}{2}\right)} \tag{3-13}$$

From the baseline 250Y case, the channel opening angle varied from 60° to 120° while the other two variables remained constant. Likewise, with the specific packing area and the channel opening angle constant at their values for 250Y, the channel inclination angle varied from 30° to 90°. Note that Equation (3-13) does not apply to the case with α=90° because the height of the vertical channel would be infinite; instead, the REU for the α=90° case had a height of 10 cm. Lastly, the specific packing area changed from 109 to 517 m^2/m^3 while the channel inclination angle and opening angle remained fixed at their values for 250Y. Table 3-4 summarizes the geometries simulated. Note the 109, 236, and 517 m^2/m^3 cases corresponded to 125Y, 250Y, and 500Y packings, according to Tsai (2010).

Specific Packing Area, A_P (m^2/m^3)	**Channel Inclination Angle, α (°)**	**Channel Opening Angle, θ (°)**
Baseline Case		
236	45	90.7
Varying θ		
236	45	60
236	45	75
236	45	105
236	45	120
Varying α		
236	30	90.7
236	60	90.7
236	75	90.7
236	90	90.7
Varying A_p		
109	45	90.7
350	45	90.7
517	45	90.7

Table 3-4: Geometries tested for the gas-phase packing geometry study.

To ensure a valid hydrodynamic comparison between packings, two options were possible: first, the F-factor could remain constant between the packing simulations, and the pressure drop would change; or second, the pressure drop could remain constant, allowing the F-factor to vary. Both alternatives were conducted for this study. For each case, the simulations predicted the mass transfer coefficient and accounted for any changes in interfacial area between cases.

3.3.4.1.Constant F-Factor

Some industrial scenarios require a constant F-factor while the packing type change. For example, for CO_2 absorption from flue gas, the power plant fixes the gas flow rate in the system. For a given column diameter and gas density, this constant flow rate implies a specified F-factor as well. From a hydrodynamic standpoint, a superior packing would diminish the pressure drop across the vapor-liquid contactor, resulting in lower power consumption and capital cost from blower operation. This analysis seeks to identify packing geometries exhibiting lower pressure drop while simultaneously maintaining or improving the mass transfer performance.

For the constant F-factor packing geometry study, an F-factor of 1.83 $\sqrt{\text{Pa}}$ was used, which was approximately the median F-factor from Figure 3-16. This F-factor also matched the conditions studied by Green et al. (2007). The difference between the total pressure's surface average at the top and bottom of the REU served as the pressure drop.

Figure 3-17 shows both the pressure drop and the mass transfer coefficient as the channel opening angle varied. An opening angle of approximately 90° maximized both the pressure drop and the mass transfer coefficient. As discussed by Basden (2014), an angle

greater than 90° shrinks the vortex which forms in the center of the channel; an angle less than 90° reduces the gas-gas friction at the channel intersection. The mass transfer coefficient demonstrated a trend similar to the pressure drop. This trend stemmed from the heightened turbulence, which increased mixing but also pressure losses. The similar trend in the pressure drop and the mass transfer revealed a tradeoff between hydrodynamic and mass transfer performances.

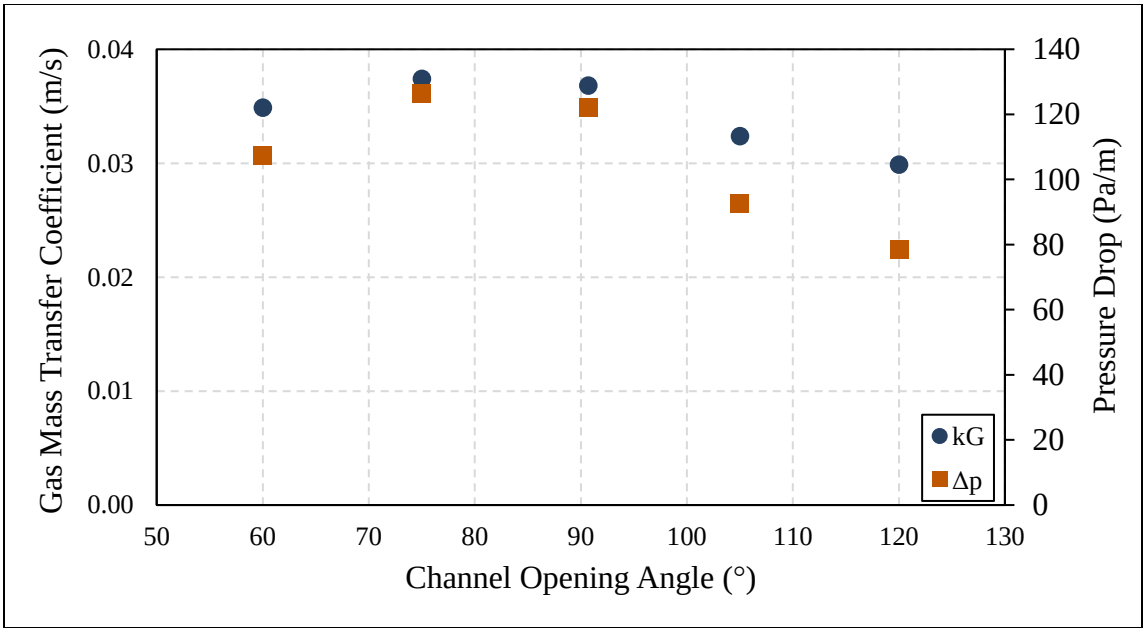

Figure 3-17: Gas mass transfer coefficient and pressure drop versus channel opening angle for SO_2 absorption with a constant F-factor of 1.83 $Pa^{0.5}$, specific packing area of 236 m^2/m^3, and channel inclination angle of 45°.

Figure 3-18 plots the pressure drop and the mass transfer coefficient as the channel inclination angle changed. Both the mass transfer coefficient and the pressure drop decreased as the inclination angle increased. The pressure drop shrank due to the decreased gas-gas friction at the channel intersection. Additionally, since the F-factor depends on the

vertical component of the gas' velocity, horizontal gas flow diminished as the channels became more vertically aligned. Horizontal flow raises the effective gas velocity and thus the pressure drop. Unfortunately, this reduction in gas-gas friction and horizontal flow also impaired the mass transfer performance. Higher gas flow rates and more gas-gas friction supported turbulence-aided mass transfer, so the elimination of those quantities undercut the mass transfer. However, the rates of decrease for the pressure drop and the mass transfer were not equal. The pressure drop exhibited an exponential-decay-like trend while the mass transfer coefficient decreased approximately linearly. Taking advantage of these trends, a channel inclination angle between 45° and 60° would significantly improve the hydrodynamic performance while only modestly impairing the mass transfer performance. These two channel inclination angles are the most common configurations in industrial structured packings, likely due to these trends.

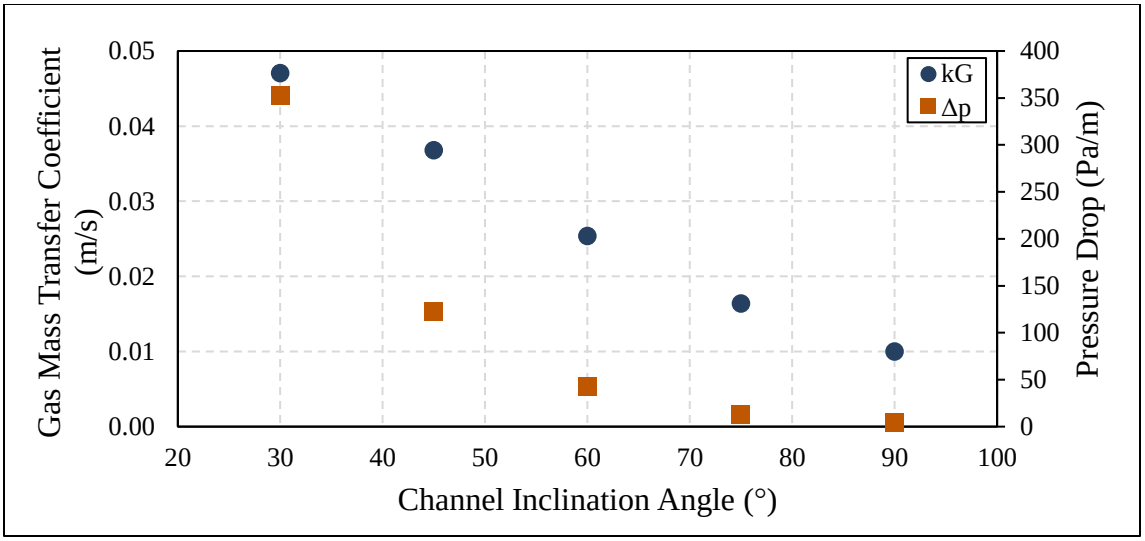

Figure 3-18: Gas mass transfer coefficient and pressure drop versus channel inclination angle for SO_2 absorption with a constant F-factor of 1.83 $Pa^{0.5}$, specific packing area of 236 m^2/m^3, and channel opening angle of 90.7°.

Lastly, Figure 3-19 shows the pressure drop and the mass transfer coefficient rising as the specific packing area increased. As the specific packing area rose while the F-factor remained constant, the cross-sectional area inside the channel decreased. The smaller channels forced the gas flow closer to the no-slip walls on average, causing higher velocity gradients and more friction. The greater frictional effects as the specific packing area increased produced higher pressure drops. Additionally, as the physical distance between the bulk flow and the walls shrank, the concentration gradient increased. This steeper gradient improved the mass transfer and the mass transfer coefficient. Once again, a tradeoff appeared between the hydrodynamic performance and the mass transfer performance. Improving the performance of one transport phenomenon detrimentally affected the other.

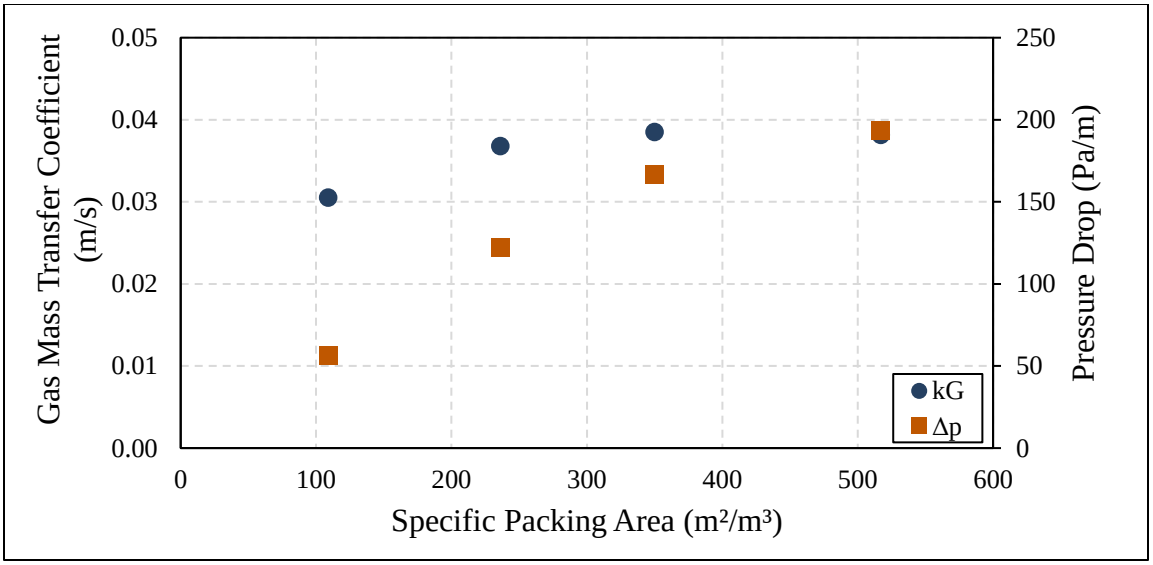

Figure 3-19: Gas mass transfer coefficient and pressure drop versus specific packing area for SO_2 absorption with a constant F-factor of 1.83 $Pa^{0.5}$, channel inclination angle of 45°, and channel opening angle of 90.7°.

The increase in interfacial area coupled with the increase in the mass transfer coefficient led to a markedly improved mass transfer performance as the specific packing area rose. Since the liquid film was assumed to be infinitely thin with complete wetting of the liquid on the packing surface, any change to the specific packing area in the system directly correlated with a change in the gas-liquid interfacial area. The mass transfer resistance was entirely in the gas phase, so the outlet SO_2 concentration allowed for prediction of the gas height of a transfer unit (HTU_G) with Equation (3-14).

$$HTU_G = \frac{H}{NTU_G} = \frac{H}{\ln\left(\overline{x_{SO_2,in}} \Big/ \overline{x_{SO_2,e}}\right)} \tag{3-14}$$

HTU is a common measurement of mass transfer performance in a vapor-liquid contactor because it reflects the efficiency of the gas-liquid contacting (Seader et al., 2011). Figure 3-20 reveals the trend in the HTU_G as A_P scaled. The HTU_G shrank significantly from the lowest to highest A_P, reflecting the combined impact of the mass transfer coefficient and interfacial area enhancements.

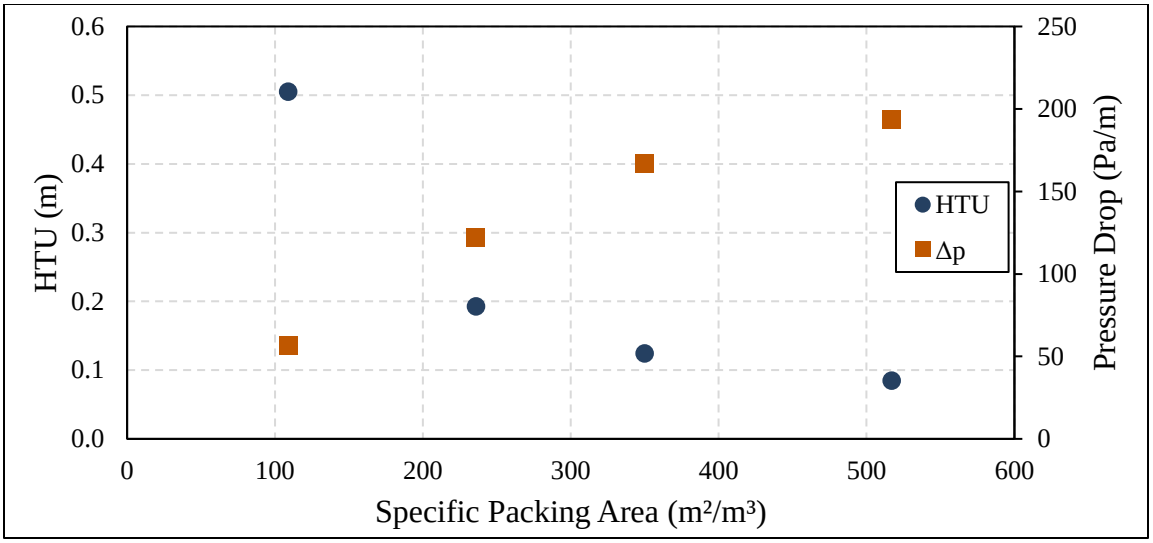

Figure 3-20: HTU_G and pressure drop versus specific packing area for SO_2 absorption with a constant F-factor of 1.83 $Pa^{0.5}$, channel inclination angle of 45°, and channel opening angle of 90.7°.

Trends in Figure 3-17, Figure 3-18, and Figure 3-19 highlight the importance of considering both the hydrodynamic performance as well as the mass transfer performance when improving packings. From only the pressure drop trend, Figure 3-18 suggests the performance of a vapor-liquid contactor would improve as the inclination angle increases to 90°. However, implementing that strategy would significantly impair the mass transfer performance, possibly causing the chemical separation in the vapor-liquid contactor to miss purity requirements. Similar problems occur when only using the pressure drop trends in Figure 3-17 and Figure 3-19. Conversely, only using the mass transfer predictions could misrepresent the performance of a structured packing geometry. To improve or optimize a packing geometry properly, hydrodynamic predictions (such as pressure drop) must be paired with mass transfer predictions to provide an accurate and holistic depiction of the packing's performance.

3.3.4.2.Constant Pressure Drop

In some situations, the pressure drop across the column is the driving condition for the column operation. For example, in vacuum distillation like an ethylbenzene-styrene process, the pressure drop can significantly affect the column operation because the operating pressure is low. A higher pressure drop by the packing results in a higher boiling point in the reboiler, which can polymerize the styrene and foul the column (Welch, 2001). Therefore, the pressure drop must be carefully monitored when designing an ethylbenzene-styrene column. As another example, trayed columns are often converted to columns with a structured packing to increase the throughput of the system. By increasing the column's throughput, the F-factor would change. For these types of scenarios, a constant pressure drop through the packing would be more relevant than a constant F-factor while changing the packing geometry.

To account for these situations, another packing geometry study was conducted while holding the pressure drop across the structured packing at 100 Pa/m and measuring the F-factor. All other conditions matched the conditions in the previous packing geometry simulations.

Figure 3-21 shows the mass transfer coefficient and the F-factor as the channel inclination angle increased until the structured packing channels were vertically aligned. From a hydrodynamic perspective, the F-factor increased as the channels became more vertical, resulting from less gas-gas friction at the channel intersections as well as fewer obstacles inhibiting the gas flow in the vertical direction. The exponential increase in the F-factor gave an improvement in the mass transfer coefficient, as the high vapor flow rates enhanced the gas-phase mixing. However, even though the mass transfer coefficient improved, the chemical separation provided by the packing system worsened as the

inclination angle increased, as Figure 3-22 demonstrates. Although the mass transfer coefficient increased as the channels became more vertical and the gas traveled faster, the mass transfer rates could not keep pace with the increased throughput. The SO_2 remaining in the flow at the top of the REU increased with the inclination angle, signifying a worse chemical separation in the system.

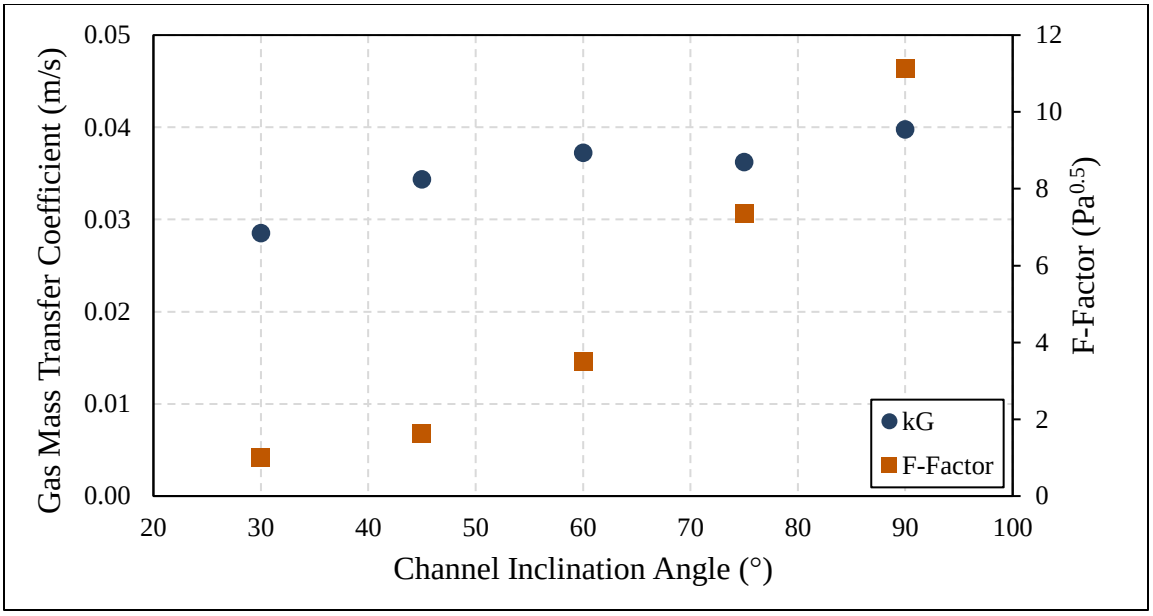

Figure 3-21: Gas mass transfer coefficient and F-factor versus channel inclination angle for SO_2 absorption with a constant pressure drop of 100 Pa/m, specific packing area of 236 m^2/m^3, and channel opening angle of 90.7°.

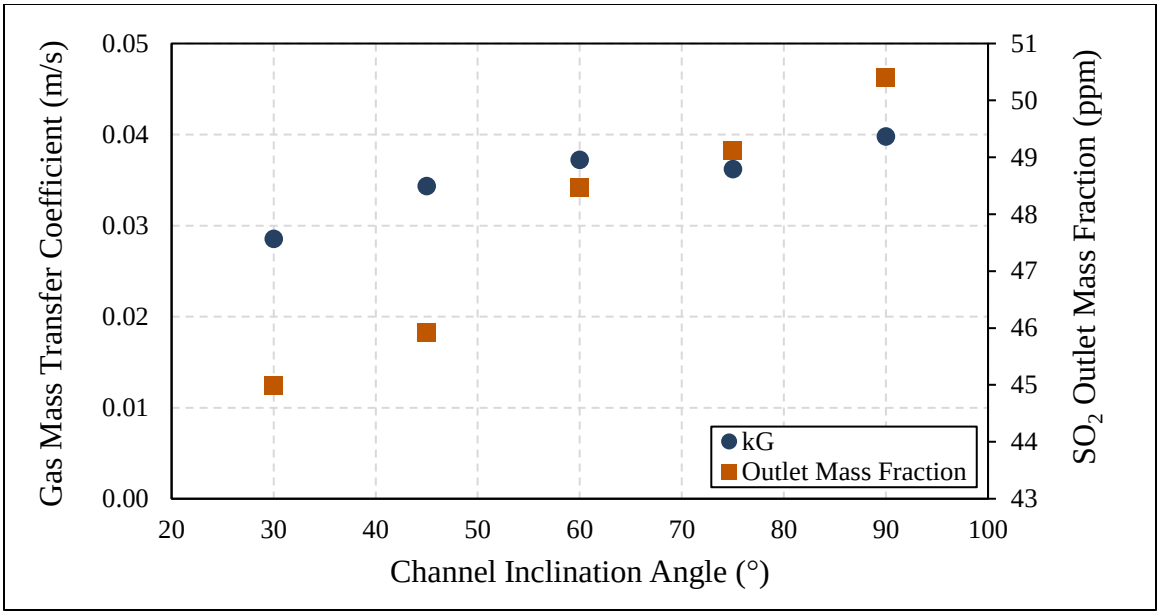

Figure 3-22: Gas mass transfer coefficient and SO_2 mixing-cup mass fraction versus channel inclination angle for SO_2 absorption with a constant pressure drop of 100 Pa/m, specific packing area of 236 m^2/m^3, and channel opening angle of 90.7°.

Because the vapor throughput in the system changed with a constant pressure drop approach, a better performance metric for the mass transfer in the system is the HTU_G, rather than the mass transfer coefficient. The HTU_G shows a macroscopic perspective of the mass transfer performance and accounts for the purity produced by the process, which is essential to ensure a column's products satisfy purity specifications. Figure 3-23 shows the HTU_G rising with the inclination angle, suggesting a worse chemical separation and supporting the trends in Figure 3-22. Similar trends between the HTU_G and F-factor are evident, again reflecting the tradeoff between mass transfer and hydrodynamic performances.

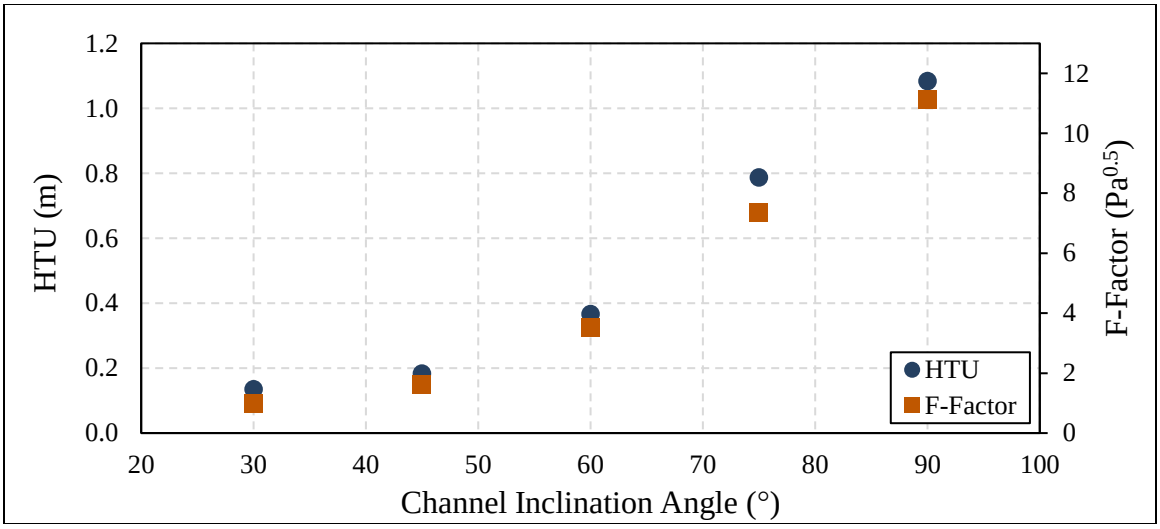

Figure 3-23: HTU_G and F-factor versus channel inclination angle for SO_2 absorption with a constant pressure drop of 100 Pa/m, specific packing area of 236 m^2/m^3, and channel opening angle of 90.7°.

The channel opening angle was varied from 60° to 120°, and the mass transfer coefficient and the F-factor were monitored, as Figure 3-24 shows. The F-factor increased as the channel opening angle deviated from 90°. As discussed earlier, the frictional losses due to turbulence were maximized when the channel opening angle was around 90°. Those frictional losses caused the depression in the F-factor. The mass transfer performance exhibited little dependence on the channel opening angle, although a slight maximum was predicted around an angle of 90°. In Figure 3-25, the HTU_G was maximized around an opening angle of 90°. Like the trends in Figure 3-23, a strong correlation existed between the HTU_G and the F-factor, originating from the impact of turbulent eddies.

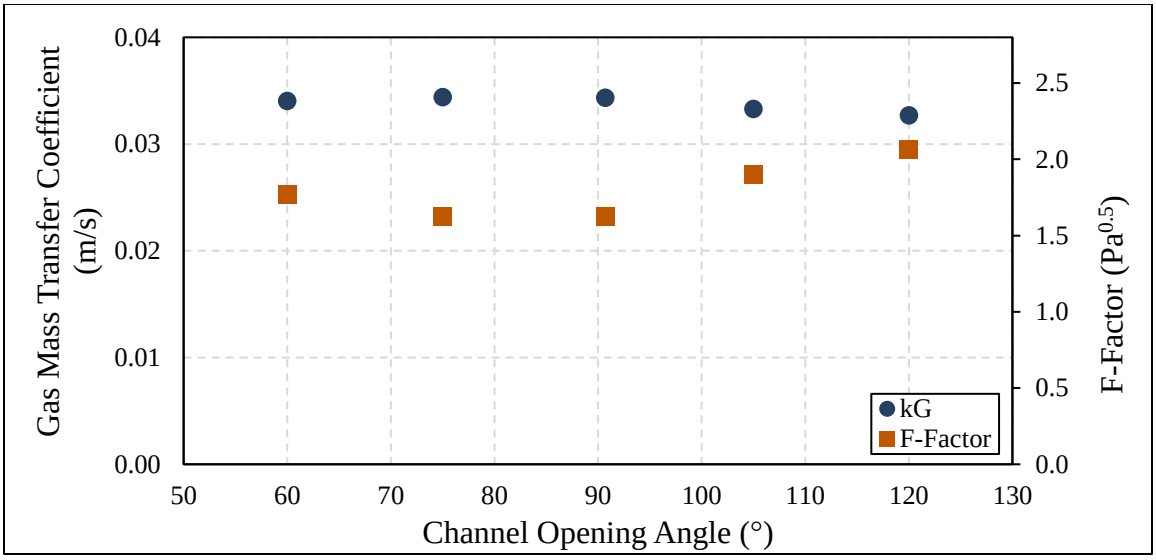

Figure 3-24: Gas mass transfer coefficient and F-factor versus channel opening angle for SO_2 absorption with a constant pressure drop of 100 Pa/m, specific packing area of 236 m²/m³, and channel inclination angle of 45°.

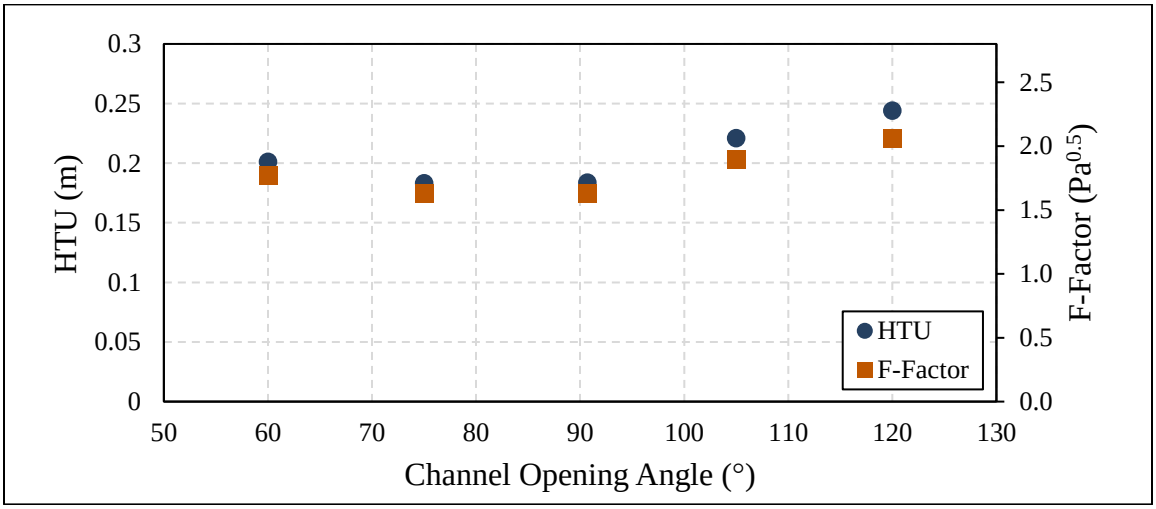

Figure 3-25: HTU_G and F-factor versus channel opening angle for SO_2 absorption with a constant pressure drop of 100 Pa/m, specific packing area of 236 m²/m³, and channel inclination angle of 45°.

Lastly, the specific packing area varied from 109 to 517 m^2/m^3. As presented in Figure 3-26, when the area increased, the F-factor dropped, a result of the gas' closer proximity to the packing walls. The higher shear stress caused more friction and slowed the flow. The closer proximity of the flow to the walls also produced higher gradients for mass transfer; however, the slower flow impaired the gas-phase mixing. The net result of the two factors was an approximately constant mass transfer coefficient as the specific area increased. However, the increase in interfacial area significantly improved the HTU_G, as Figure 3-27 shows.

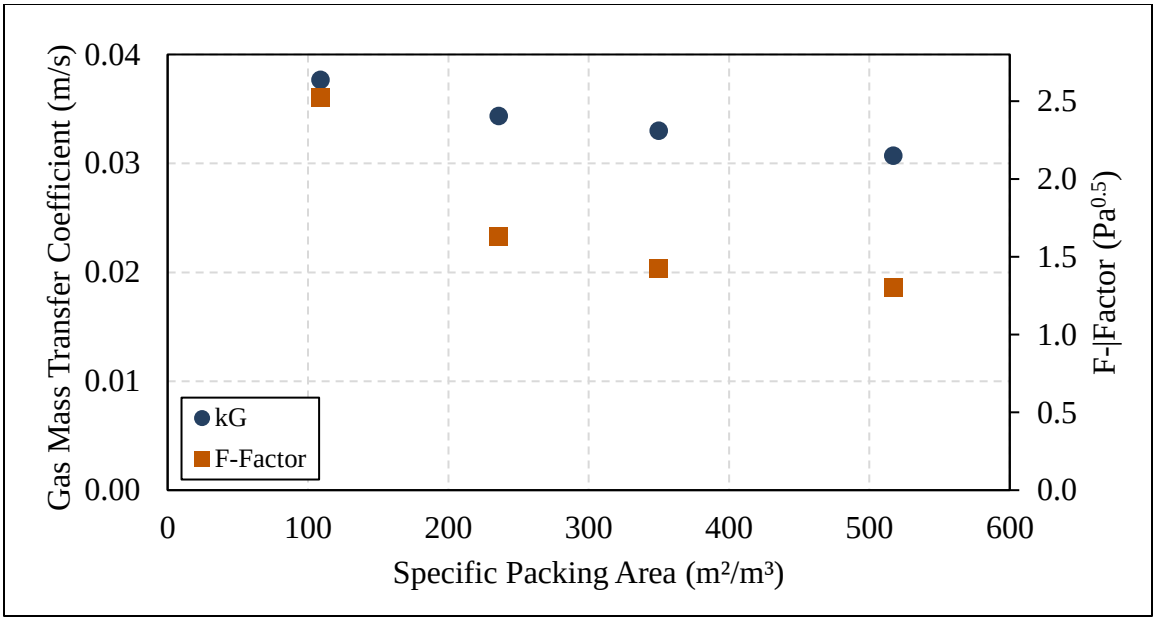

Figure 3-26: Gas mass transfer coefficient and F-factor versus specific packing area for SO_2 absorption with a constant pressure drop of 100 Pa/m, channel inclination angle of 45°, and channel opening angle of 90.7°.

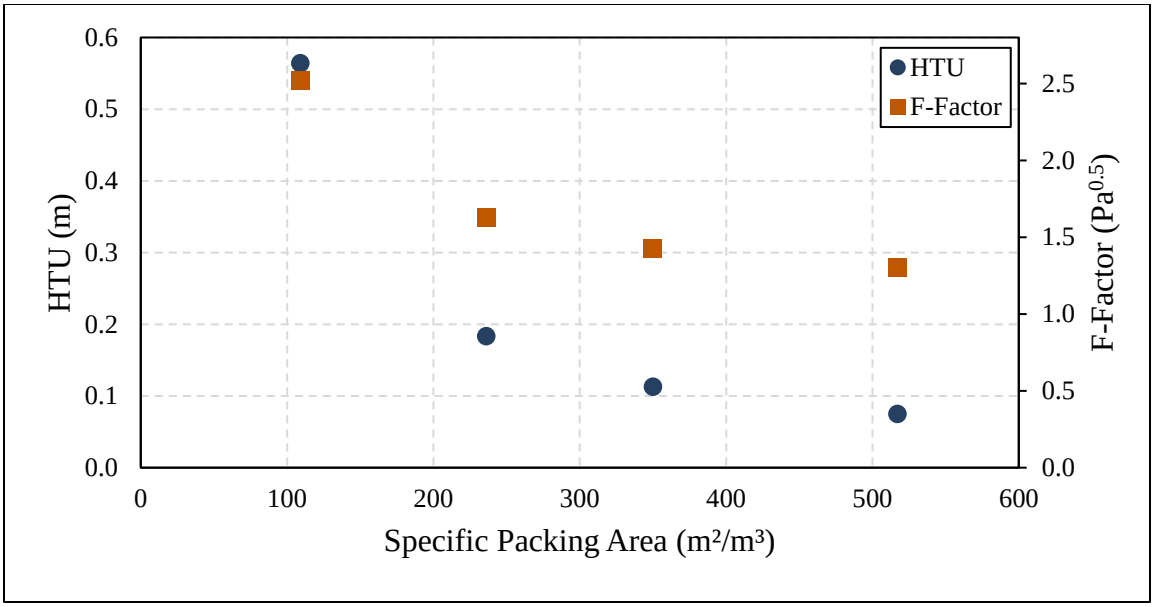

Figure 3-27: HTU_G and F-factor versus specific packing area for SO_2 absorption with a constant pressure drop of 100 Pa/m, channel inclination angle of 45°, and channel opening angle of 90.7°.

3.4. CONCLUSIONS

This study investigated structured packing geometry using a mass transfer methodology validated across multiple systems. The effects of turbulence on the gas-phase mass transfer were carefully investigated. A constant turbulent Schmidt number approach enabled the accurate hydrodynamic turbulence model to predict the turbulence-aided mass transfer. Pipe flow simulations tested and validated this methodology before implementation in structured packing simulations. An SO_2 scrubbing process was simulated in Mellapak 250Y, and the simulations agreed well with experimental data, having an absolute average deviation (AAD) of five percent. The CFD predictions were

within the range of several semi-empirical correlations developed on pilot-scale or larger columns, further validating the CFD results.

The stacked REU system provided further support for the validity of the single-REU mass transfer approach. The stacked REU system showed periodic boundary conditions on horizontal faces can reduce computational expense and still provide high fidelity predictions. Additionally, the efforts confirmed the asynchronous hydrodynamic and mass transfer prediction methodology provides results as accurate as the synchronous prediction methodology. The strong agreement between the experimental data and the stacked REU system, shown by the three percent error, further revealed the ability of CFD to accurately predict the gas-phase mass transfer performance.

The packing geometry studies revealed trends as the channel opening angle, channel inclination angle, and specific packing area varied. A tradeoff between the mass transfer and hydrodynamic performances was observed. Considering both the constant-pressure-drop and constant-F-factor approaches, this study advised the use of a geometry with a channel opening angle of 60°, channel inclination angle of 50°, and a specific packing area of 517 m^2/m^3. The analysis predicted this geometry would provide high mass transfer rates and a good chemical separation while enabling a satisfactory pressure drop. While other configurations might reduce the pressure drop, the diminished mass transfer performance would outweigh improvements to the hydrodynamic performance. This analysis only considered the gas-phase phenomena, so effects such as liquid maldistribution, flooding, and liquid-phase mass transfer resistance were not considered. The analysis also assumed the liquid forms a thin film over the entire packing surface, and

the validity of this assumption is uncertain for high specific packing areas. Additionally, the packing geometry was varied without regard for capital cost.

Chapter 4: Structured Packing Geometry Study for Liquid-Phase Performance Using Computational Fluid Dynamics

4.1. INTRODUCTION

Many questions remain regarding the transport phenomena occurring inside structured packings, particularly regarding the hydrodynamics and mass transfer. Without a complete understanding of these phenomena, efforts to improve packings are hampered. The transport phenomena in the liquid phase is particularly important for environmental purposes, as many carbon dioxide capture systems exhibit large mass transfer resistances in the liquid phase (Dong et al., 2017; Sebastia-Saez et al., 2015a; Song et al., 2018). Efforts to improve the liquid-phase performance by changing the packing geometry are limited in the literature. To address these needs, this study investigated the influence of a structured packing's shape on its liquid-phase performance with CFD, including both the hydrodynamic and mass transfer performances. The impact of turbulence on the liquid-phase performance was also considered.

After describing the CFD methodology and the mesh sensitivity analysis, this paper discusses the hydrodynamic validation of the simulations using three key variables: the liquid holdup, the liquid flow angle, and the Fanning friction factor. The mass transfer predictions were subsequently validated with experimental data and several high-fidelity models. Building on the validation for the hydrodynamics and mass transfer, the structured packing geometry was varied, and the hydrodynamic and mass transfer performance of the liquid-phase was quantified during that process.

4.2. CFD METHODOLOGY

4.2.1. Hydrodynamics

The CFD software for this study was Simcenter STAR-CCM+ version 2019.3.1. In this software, the continuity equation ensured the conservation of mass (Bird et al., 2007; "Simcenter STAR-CCM+ 2019.3.1 Theory Guide," 2019).

$$\frac{\partial \rho}{\partial t} + \nabla \cdot (\rho \mathbf{v}) = 0 \tag{2-8}$$

Equation (3-1) below ensured conservation of momentum for the Newtonian, incompressible fluid in the CFD software ("Simcenter STAR-CCM+ 2019.3.1 Theory Guide," 2019).

$$\frac{\partial (\rho \mathbf{v})}{\partial t} + \nabla \cdot (\rho \mathbf{v} \otimes \mathbf{v}) = -\nabla \cdot (p\mathbf{I}) + \nabla \cdot \left((\mu_m + \mu_T)(\nabla \mathbf{v} + (\nabla \mathbf{v})^{\mathbf{T}}) \right) \tag{3-1}$$

The pressure in this equation has contributions from both hydrostatic and static sources. The segregated flow solver with the SIMPLE algorithm predicted the steady-state behavior with a second-order scheme for convection. The fluid had a constant density and was isothermal. The lag elliptic-blending k-ε turbulence model with all-y+ wall treatment predicted the turbulent viscosity, μ_T. For fully laminar flows, the turbulent viscosity would be negligible.

4.2.2. Mass Transfer

The passive scalar model simulated the mass transfer performance in CFD. The mass transfer predictions with this model do not impact the hydrodynamic predictions, which is relevant for dilute systems where the small magnitude of mass transfer causes an insignificant change in the flow field. The governing equation for the passive scalar model is below ("Simcenter STAR-CCM+ 2019.3.1 Theory Guide," 2019).

$$\frac{\partial(\rho x_A)}{\partial t} + \nabla \cdot (\rho x_A \mathbf{v}) = -\nabla \cdot \mathbf{j}_A + S_A \tag{3-2}$$

Molecular and turbulent diffusion contributed to the diffusive flux, as Equation (3-3) shows.

$$\mathbf{j}_A = -\rho(D_m + D_T)\nabla x_A \tag{3-3}$$

The turbulent diffusion coefficient was predicted by a constant turbulent Schmidt number, forming a direct analogy between turbulent mass transfer and turbulent momentum transfer (Fox, 2003; Wang et al., 2020; Zhang et al., 2013).

$$Sc_T = \frac{\nu_T}{D_T} = \frac{\mu_T}{\rho\, D_T} = 0.7 \tag{3-4}$$

The constant turbulent Schmidt number approach established a direct analogy between the momentum transfer and the mass transfer. A second-order scheme accounted for convection.

4.3. CFD SETUP AND RESULTS

The chemical system simulated in this study was toluene desorption from water into air. This system is liquid-film controlled for mass transfer, where the toluene entering the gas phase is quickly swept away (Song et al., 2018). Table 4-1 presents the physical properties of the liquid. The value of the molecular diffusion coefficient was based on the prediction by the Wilke-Chang model, which was relevant for the dilute system simulated (Wilke and Chang, 1955).

Molecular Dynamic Viscosity, μ_m (Pa-s)	**Density, ρ (kg/m^3)**	**Molecular Diffusion Coefficient, D_m (m^2/s)**
1.14e-3	999.4	7.2e-10

Table 4-1: Physical properties of the liquid.

To reduce computational expense, a representative elementary unit (REU) approach was employed. As Figure 1-3 depicts, an REU captures the geometry of the structured packing while also utilizing the repeating pattern to reduce the system's size. Several studies have successfully used this approach to predict the performance of an entire structured packing bed (Basden, 2014; Dong et al., 2017; Hill et al., 2019; Petre et al., 2003; Said et al., 2011). Table 3-3 shows the dimensions of a Mellapak 250Y REU (Petre et al., 2003), and Figure 3-3 illustrates the dimensions (Basden, 2014).

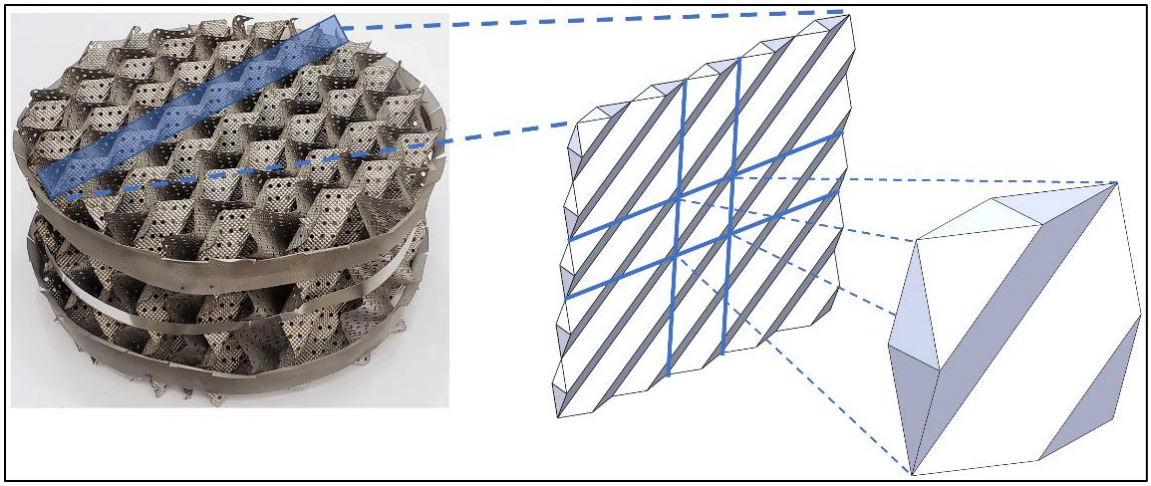

Figure 1-3: Sample representative elementary unit (REU) geometry.

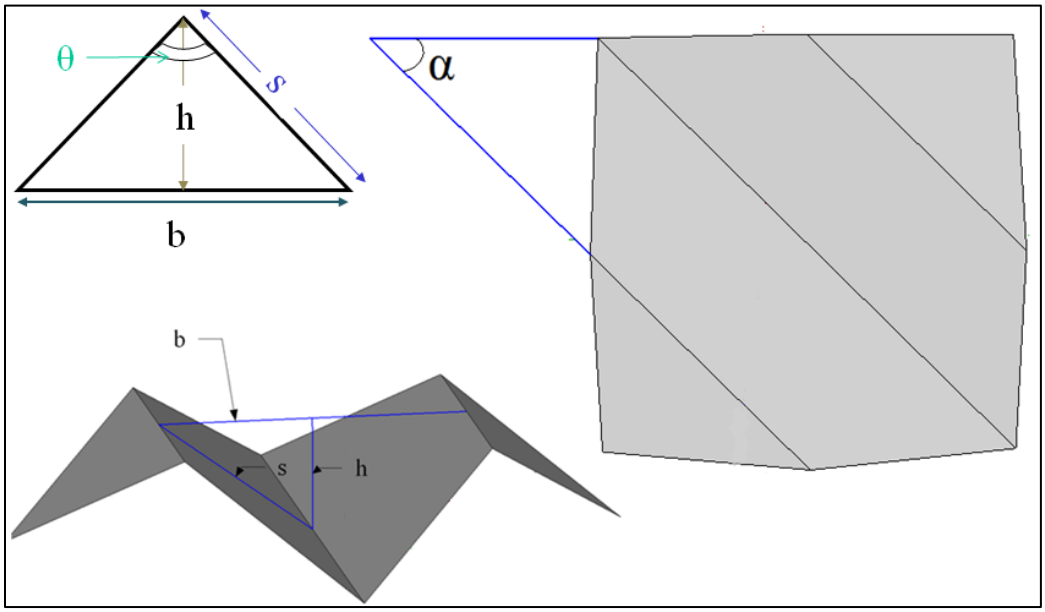

Figure 3-3: Structured packing parameters (Basden, 2014).

Channel Inclination Angle, α (°)	Channel Base Length, b (mm)	Channel Height, h (mm)	Channel Side Length, s (mm)	REU Height, H (mm)
45	24.1	11.9	17.0	34.1

Table 3-3: Dimensions of a Mellapak 250Y REU.

Previous studies have successfully predicted the mass transfer in structured packings by simplifying the system to only simulate a single phase (Erasmus, 2004; Haroun and Raynal, 2016; Lautenschleger et al., 2015; Olenberg et al., 2018). With reasonable assumptions regarding the location of the gas-liquid interface, the complex, multiphase system could be simplified to obtain predictions for the mass transfer in gas-film-controlled systems. Building on this work, a standard REU was modified to simulate only the liquid phase.

Previous research has suggested that the liquid travels through the packings as a film on the packing surface (Fair et al., 2000; Green et al., 2007; Rocha et al., 1996, 1993). At high liquid flow rates, the gas-liquid interfacial area approaches the surface area of the packings, suggesting that the liquid film covers the entire packing surface (Green et al., 2007; Macfarlan et al., 2021; Olujic, 1997; Olujić et al., 2004; Tsai et al., 2011). In this study, the liquid was assumed to cover the entire packing surface and have a constant film thickness, allowing a structured packing to be further simplified by creating an REU for just the liquid phase. This liquid representative elementary unit (LREU) has the same structure as the original REU, but the core of the REU where the gas would reside was removed, as Figure 4-1 shows. This removal leaves a constant film thickness on the surface of the packing where the liquid can flow. The film thickness in the LREU was adjusted to control the liquid flow rate through the packing. The removal of the gas phase in the REU

allowed only the liquid to be simulated in CFD. Xie et al. (2021) reported success using a similar approach for liquid films flowing vertically. The shell feature in SOLIDWORKS 2019 converted the REU geometry into the LREU geometry.

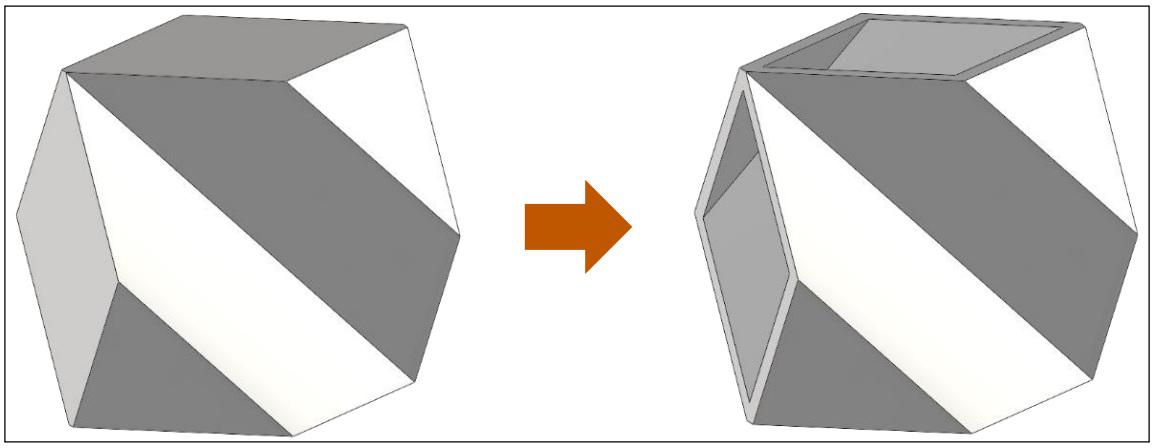

Figure 4-1: Removal of core to convert an REU into a liquid REU (LREU).

In this study, an asynchronous approach to predict the hydrodynamic and mass transfer performance was conducted. This research project previously demonstrated that, for cases with a dilute diffusing species, the converged velocity and pressure field can be frozen and subsequently used to predict the mass transfer performance without impairing the predictions' accuracy. A similar approach was utilized in this portion of the study, where the predicted steady-state hydrodynamic performance informed the mass transfer simulations.

Hydrodynamics boundary conditions reflecting film flow conditions were imposed in the LREU. At the packing surface, the flow experienced a no-slip boundary condition. At the gas-liquid interface, a symmetry boundary condition was used to impose a lack of shear stress, which is a common assumption in inclined plate film theory (Bird et al., 2007).

Periodic boundary conditions existed between the left and right faces, along with a 0 Pa pressure difference. Periodic boundary conditions also existed between the top and bottom surfaces, and a pressure drop was imposed to account for the typical gas-phase pressure drop in structured packings as well as the hydrostatic pressure difference in the system. The gas-phase pressure drop contribution was 118 Pa/m. Regarding the hydrostatic pressure drop, Simcenter STAR-CCM+ automatically included the hydrostatic pressure drop for the liquid, but, in typical film flow conditions, the pressure in the liquid phase corresponds to the pressure in the gas phase. Because air exhibits a much smaller hydrostatic pressure drop than water, the hydrostatic pressure drop automatically imposed by Simcenter STAR-CCM+ had to be removed through the specified pressure drop. The specified pressure drop was calculated according to Equation (4-1) below. The hydrodynamic portion of the simulation converged when the mass flow through the bottom of the LREU changed by less than 0.01 percent over the last 500 iterations.

$$p_{bottom} - p_{top} = \left(118 \frac{Pa}{m}\right) H - \rho_L g H \tag{4-1}$$

After the hydrodynamic prediction converged, the mass transfer was subsequently simulated. During this process, the segregated flow solver and, for cases with a turbulence model, the lag elliptic blending k-ε turbulence solver were frozen, inhibiting the velocity and pressure fields from evolving further. The periodic boundary conditions between the top and bottom surfaces were removed and replaced with a velocity inlet boundary condition at the top surface and a pressure outlet condition at the bottom surface. At the velocity inlet, the toluene mass fraction was 1.49e-4. The mass fraction of toluene at the

outlet was computed using the flow profile and diffusive mass transfer predictions within the system. In the event of backflow at the outlet, a mass fraction of 0 was specified, although no backflow was observed. At the gas-liquid interface, a wall boundary condition replaced the symmetry boundary condition, allowing the mass fraction at the gas-liquid interface to be specified. Toluene desorption from water into air is a liquid-film-controlled process, as the toluene is quickly swept away after reaching the gas phase, leading to a negligible toluene concentration at the gas-liquid interface. To reflect this process, the mass fraction of toluene at the gas-liquid interface was 0 during the mass transfer section of the simulations. The mass transfer portion of the simulation converged when the mixing-cup mass fraction of toluene at the exit as well as the mass transfer coefficient changed by less than 0.01 percent over the last 1,000 iterations. As previously described in this work, the mixing-cup mass fraction better reflects the mass flow of the species through a cross-section because it accounts for different mass fluxes at different locations on the cross-section. The mass transfer coefficient was computed using a differential contactor approach, as Equation (4-2) shows.

$$k_L = \frac{Q}{A_i} \cdot \ln\left(\frac{x_{toluene,i} - \overline{x_{toluene,in}}}{x_{toluene,i} - \overline{x_{toluene,e}}}\right) \tag{4-2}$$

The average liquid mass transfer coefficient is the liquid mass transfer coefficient averaged over the height of the system (Seader et al., 2011).

$$k_L = \frac{1}{Z_2 - Z_1} \int_{Z_1}^{Z_2} k \, dZ \tag{4-3}$$

Equation (3-8) defines the local mass transfer coefficient, k (Seader et al., 2011).

$$N_A \equiv kA_i\Delta c_A \tag{3-8}$$

4.3.1. Mesh Sensitivity and Turbulence Modeling

A mesh sensitivity analysis was performed for the LREU system to ensure the mesh was fine enough to capture all relevant phenomena. For this analysis, the liquid mass transfer coefficient and the liquid flow rate were the observed variables, ensuring independence for both the hydrodynamics and the mass transfer. The mesh resolution near the gas-liquid interface and near the packing surface was critical in order to capture key concentration and velocity gradients, respectively. The application of prism layer cells on both the packing surface and the gas-liquid interface enabled high resolution in those locations. The advancing layer mesher produced these prism layer cells, the polyhedral mesher produced the core mesh, and the laminar solver was used. The core mesh underwent five optimization cycles to improve its quality. The film thickness in this analysis was 0.3 mm, which reflects a typical liquid holdup measured by Green et al. (2007). The first parameter changed was the number of prism layers at the wall to ensure the velocity gradients were captured. Figure 4-2 shows the results of this analysis for the fluid mechanics and the mass transfer. The predicted liquid flow rate and liquid mass transfer coefficient were slightly lower for the case without prism layers. Therefore, the analysis revealed that 3 prism layers on the structured packing surface captured the physics.

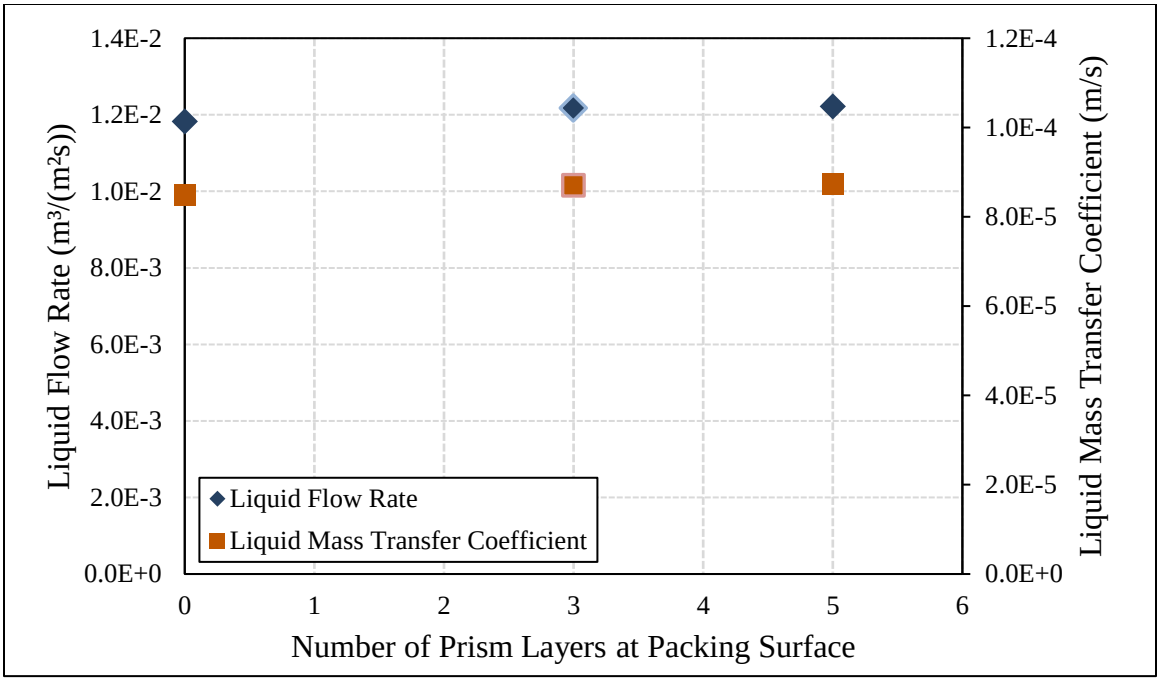

Figure 4-2: Mesh sensitivity study for the number of prism layers at the structured packing surface, with the liquid flow rate and liquid mass transfer coefficient serving as the performance metrics for the hydrodynamics and mass transfer, respectively; results for the selected mesh condition are outlined.

The number of prism layers at the gas-liquid interface was also varied to ensure the concentration boundary layer was sufficiently captured. The number of prism layers varied from four to 13, and the liquid flow rate and the liquid mass transfer coefficient were observed. Figure 4-3 shows the results of this analysis for the hydrodynamics and the mass transfer. The liquid flow rate exhibited little change from altering the mesh fineness at the gas-liquid interface. This negligible change stemmed from the lack of a significant velocity gradient at the interface. The liquid mass transfer coefficient changed significantly between cases with less than seven prism layers at the interface. From the relative change in the

variables, 10 prism layers at the gas-liquid interface sufficiently captured the mass fraction gradient.

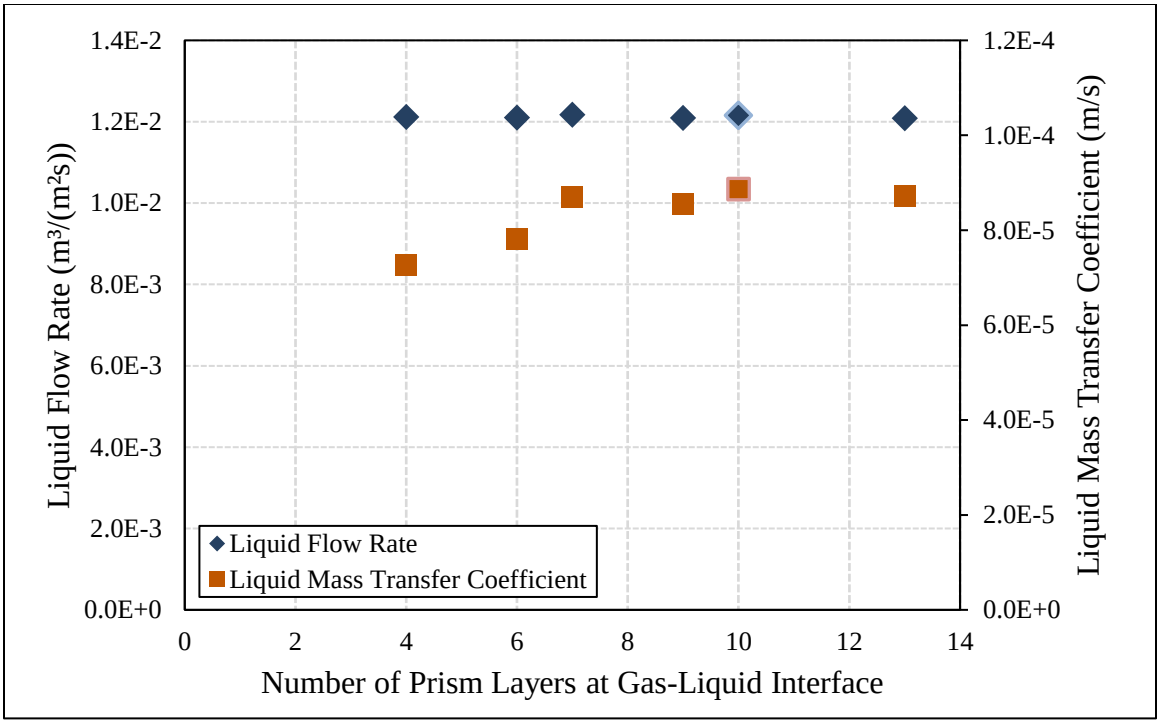

Figure 4-3: Mesh sensitivity study for the number of prism layers at the gas-liquid interface, with the liquid flow rate and liquid mass transfer coefficient serving as the performance metrics for the hydrodynamics and mass transfer, respectively; results for the selected mesh condition are outlined.

Previous research has indicated that both laminar and turbulent flow conditions can exist in structured packings (Duss, 2013; Phan et al., 2020). Turbulence models have been used in previous studies when simulating the mass transfer in the liquid phase (Chen et al., 2009; Dong et al., 2017). However, other modeling efforts have neglected turbulent effects in the liquid phase (Olujić et al., 2004; Xu et al., 2009), which align with inclined plate film theory (Bird et al., 2007).

To account for any turbulence present in the system, the lag elliptic-blending k-ε turbulence model with all-y+ wall treatment predicted turbulent effects in the LREU. This turbulence model provides accurate predictions for laminar up to turbulent conditions typical in structured packing systems (Macfarlan et al., 2021; Phan et al., 2020). A constant turbulent Schmidt number predicted turbulent effects on the mass transfer, which has shown promise in previous structured packing investigations (Wang et al., 2020; Zhang et al., 2013).

The impact of turbulence was analyzed for a case with a 0.3 mm film thickness. Table 4-2 shows the key performance predictions when using the turbulence model as well as when using the laminar model. The predictions negligibly changed for the fluid mechanics, suggesting turbulence was not relevant. The predicted turbulent-to-molecular viscosity ratio highlights this finding. This ratio reveals the relative importance of turbulence on the hydrodynamics, with a value of unity suggesting equal importance between molecular and turbulent viscosities. Figure 4-4 shows the turbulent-to-molecular viscosity ratio at the gas-liquid interface, where inclined plate film theory predicts the largest velocity to occur. The ratio was largest just below the contact point, where the liquid films on the packing surfaces cross. Overall, the turbulent-to-molecular viscosity ratio in the LREU was small, with a maximum turbulent-to-molecular viscosity ratio of 8.6e-4 and an average ratio of 4.6e-8. As the turbulent viscosity is the primary product of k-ε turbulence models, this small ratio resulted in the inconsequential impact of turbulence on the hydrodynamic predictions and implied laminar flow conditions in the liquid.

	Laminar Model	Turbulence Model
Liquid Flow Rate, $m^3/(m^2s)$	0.0122	0.0122
Mixing-Cup Mass Fraction at Outlet	1.41e-4	1.41e-4
Liquid Mass Transfer Coefficient, m/s	8.89e-5	8.85e-5

Table 4-2: Performance variables for a Mellapak 250Y LREU when using a turbulence model and when using a laminar model.

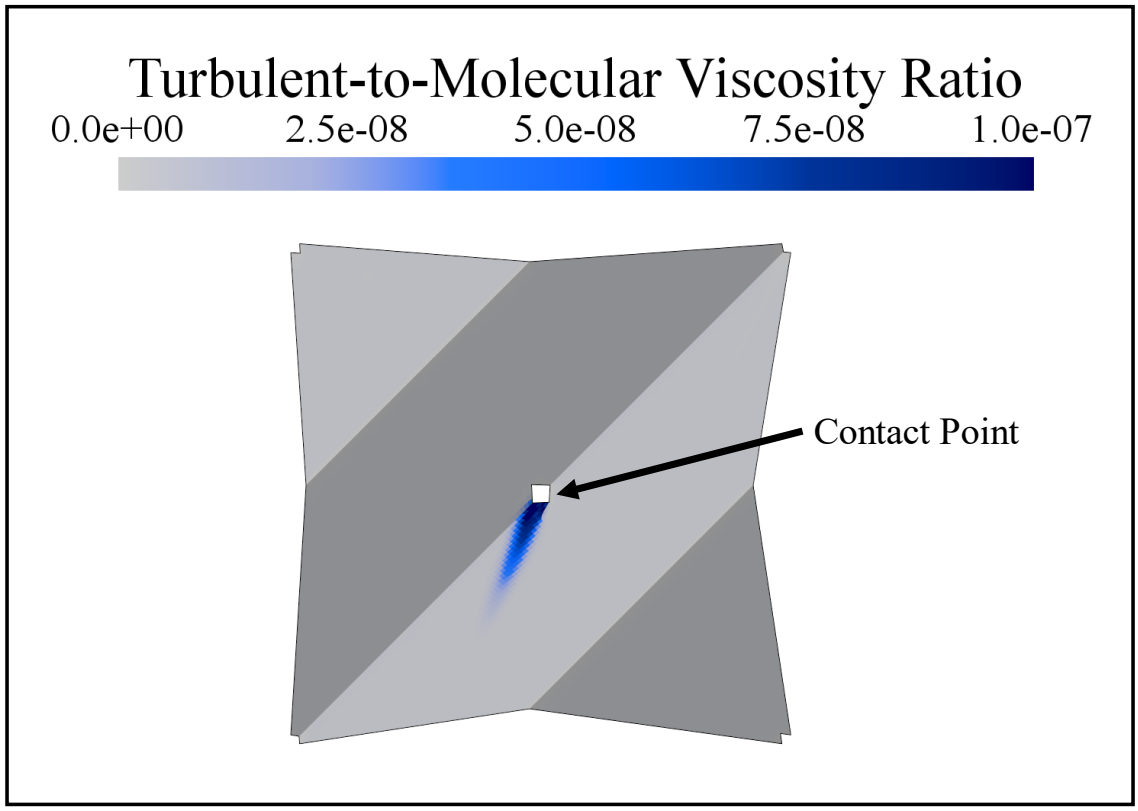

Figure 4-4: Low turbulent-to-molecular viscosity ratio at the gas-liquid interface suggesting laminar flow for an LREU with a 0.3 mm film thickness, with a maximum ratio occurring below the contact point due to film-film interactions.

The impact of turbulence on the mass transfer was also analyzed. Table 4-2 reveals a negligible change in the mass transfer performance metrics between the laminar and

turbulent cases. The turbulent-to-molecular diffusion coefficient ratio illustrates the negligible impact of turbulence on the mass transfer. This ratio represents the relative importance of turbulence on mass transfer compared to molecular diffusion. Figure 4-5 displays the turbulent-to-molecular diffusion coefficient ratio at the gas-liquid interface. As with the viscosity ratio, the largest turbulent-to-molecular diffusion coefficient ratio occurred below the contact point due to the crossing liquid films. Overall, the impact of turbulence on the mass transfer was small in the LREU, with a 6.6e-4 maximum turbulent-to-molecular diffusion coefficient ratio and an average ratio of 9.5e-8 in the system. Due to the negligible impact of turbulence demonstrated above, the laminar model was used in subsequent analysis to reduce computational expense.

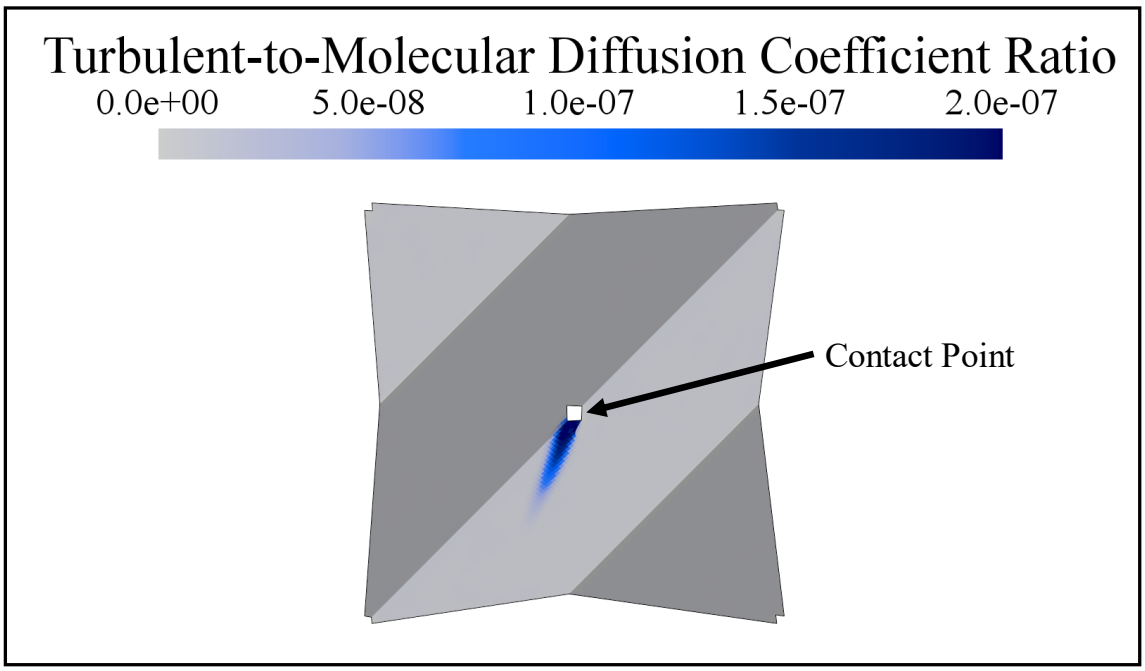

Figure 4-5: Low turbulent-to-molecular diffusion coefficient ratio at the gas-liquid interface for an LREU with a 0.3 mm film thickness, showing a negligible impact of turbulence on the mass transfer.

4.3.2. LREU Validation for Hydrodynamics

To ensure the CFD predictions accurately predicted the phenomena in structured packings, the hydrodynamic and the mass transfer performances were validated. For the hydrodynamics, three validation parameters were employed: the liquid holdup, the liquid flow angle, and the friction factor.

4.3.2.1.Liquid Holdup

Figure 4-6 shows the liquid holdup predicted by CFD as well as the liquid film thickness as a function of the liquid flow rate through the packing. The liquid flow rate through the system was predicted to increase as the film became thicker. This trend stemmed from the increased cross-sectional area for the liquid to travel through the column as well as the liquid being further away from the no-slip boundary condition on the packing surface. The liquid holdup also increased as the film became thicker. The liquid holdup was calculated by comparing the volume of the LREU to the volume of the REU. The increase in the liquid holdup was caused by the increased volume the liquid utilized in the system for larger flow rates.

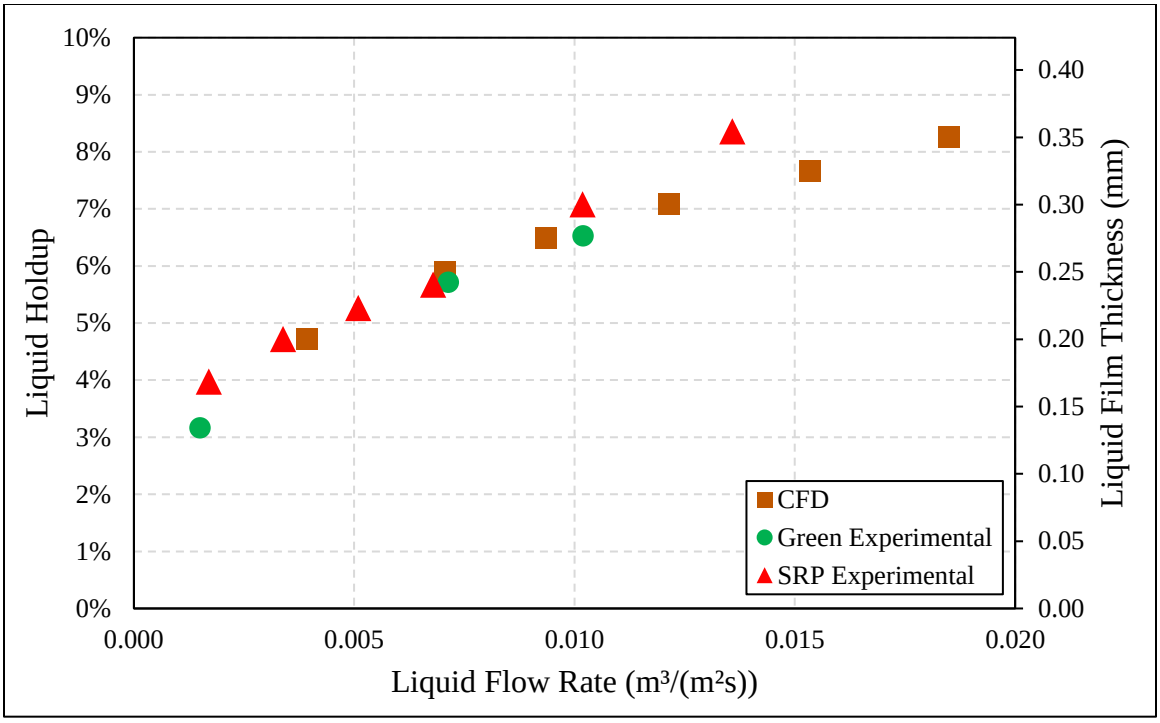

Figure 4-6: CFD predictions and experimental data from Green et al. (2007) and the Separations Research Program (SRP) for liquid holdup in Mellapak 250Y; Corresponding film thickness for the liquid holdup also shown, assuming a constant film thickness.

The predicted flow rates for the corresponding liquid holdups compared favorably to the experimental data reported by Green et al. (2007). Green et al. (2007) conducted computed tomography (CT) analysis to capture the liquid inside Mellapak 250Y, and traditional liquid holdup measurements from the Separation Research Program (SRP) were also reported in the study for comparison. Figure 4-6 has plots of both experimental data sets compared to the CFD prediction. Only experimental data from the preloading regime were included to align with the simulated conditions. Green et al. (2007) reported regions near the packing joints having a higher liquid holdup than the middle of the structured packing element, where the LREU is most relevant, so only CT liquid holdup data from

the bulk of the packing were included in Figure 4-6. The traditional experimental measurements from the SRP reflected the liquid holdup of the entire packed bed. The CFD predictions showed excellent qualitative agreement with the CT measurements, increasing at a similar rate as the liquid flow rate. The CFD and CT data also showed excellent quantitative agreement, exhibiting an absolute average deviation (AAD) of six percent (using linear interpolation of the experimental data to obtain consistent liquid flow rates). Similarly, the traditional liquid holdup data from the SRP showed strong qualitative and quantitative agreement with the CFD predictions, having an AAD of five percent. Overall, the SRP measurements were slightly higher than the CFD data, likely due to the inclusion of the liquid holdup near the packing joints.

4.3.2.2.Liquid Flow Angle

The liquid flow angle, β, describes the direction that the liquid moves relative to the column's axis as it travels down the packing. Based on the definition of the flow angle in Figure 4-7, the term describes the relative amount of horizontal flow in the system. A larger flow angle correlates with greater horizontal liquid movement. For a given film thickness and superficial liquid flow rate, the liquid flow angle can change the effective velocity of the liquid film. The effective velocity of the liquid film at the gas-liquid interface has been tied to higher liquid mass transfer coefficients, so the flow angle can significantly impact the performance of the packed system (Haroun et al., 2012; Sebastia-Saez et al., 2014).

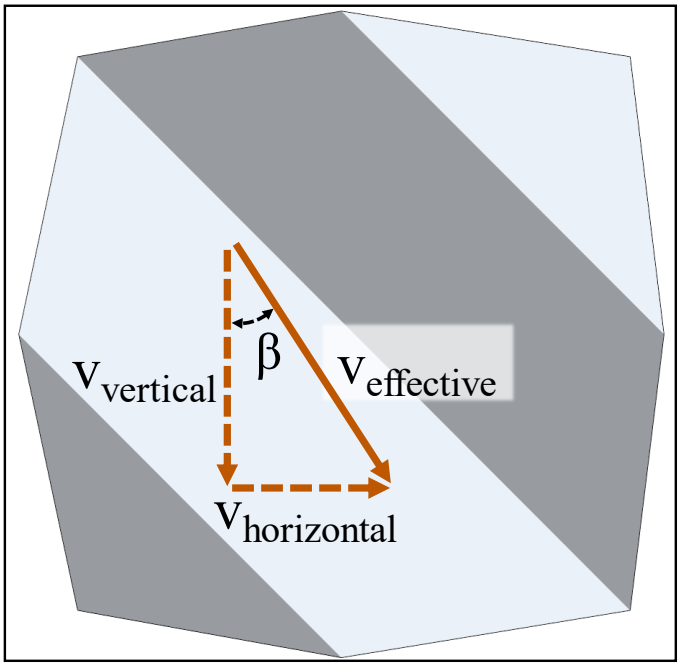

Figure 4-7: Liquid flow angle, β, which is a measure of the fluid's horizontal movement.

Zogg (1973) developed an analytical expression for the flow angle on structured packings. This model assumes the liquid travels down the steepest direction on the surface of the packings under the force of gravity. The equation developed by Zogg, shown in Equation (4-4), includes influences from both the channel opening angle, θ, as well as the channel inclination angle, α. The Delft model also predicts the liquid flow angle, which is presented in Equation (4-5) (Olujić et al., 2004). Like the Zogg equation, the prediction from the Delft model shows a dependence on the channel inclination angle and channel opening angle.

$$\tan\left(90° - \beta_{Zogg}\right) = \frac{\cot(90° - \alpha)}{\sin\left[\tan^{-1}\left(\frac{\cos(90° - \alpha)}{\tan\left(\frac{\theta}{2}\right)}\right)\right]} \tag{4-4}$$

$$90° - \beta_{Delft} = \tan^{-1}\left[\frac{\cos(90° - \alpha)}{\sin(90° - \alpha)\cos\left(\tan^{-1}\left(\frac{b}{2h}\right)\right)}\right] \tag{4-5}$$

Through trigonometry identities, the Zogg prediction can be simplified to the form shown in Equation (4-6) below. The Delft model prediction can also be simplified and rewritten in terms of the channel opening angle, as Equation (4-7) depicts.

$$\beta_{Zogg} = \sin^{-1}(\cos\theta\cos\alpha) \tag{4-6}$$

$$\beta_{Delft} = \cot^{-1}\left[\frac{\cot(90° - \alpha)}{\cos\left(\frac{\theta}{2}\right)}\right] \tag{4-7}$$

In the CFD simulations, the liquid flow angle was computed using the predicted liquid effective velocity and the vertical velocity, as shown by Equation (4-8).

$$\beta_{CFD} = \cos^{-1}\left(\frac{V_{vertical}}{V_{effective}}\right) \tag{4-8}$$

Figure 4-8 plots the predictions for the volume-averaged liquid flow angle as the liquid flow rate increased. A relatively constant value was predicted by the simulations.

The CFD predictions showed strong agreement with the analytical expression developed by Zogg (1973), especially at lower flow rates. At higher flow rates, a slight deviation from the Zogg prediction was observed, which resulted from increased inertial effects. As the liquid flow rate increased, the liquid film could less readily change directions when it passed over the packing crimps. The Zogg expression assumed gravity would determine the liquid flow direction, but the greater inertia caused a slower transition after each packing crimp. However, the discrepancy between the CFD and Zogg liquid flow angle predictions was small, even at high liquid flow rates, with an overall AAD of 0.58 percent. The CFD flow angle predictions showed a stronger agreement with the Zogg analytical expression than the Delft model, and the AAD between the Delft and CFD predictions was 14.6 percent. Qualitatively, the CFD predictions agreed with the observations of Fair et al. (2000), where the liquid was noted to travel down the surface of the packing at a steeper angle than the channel inclination angle.

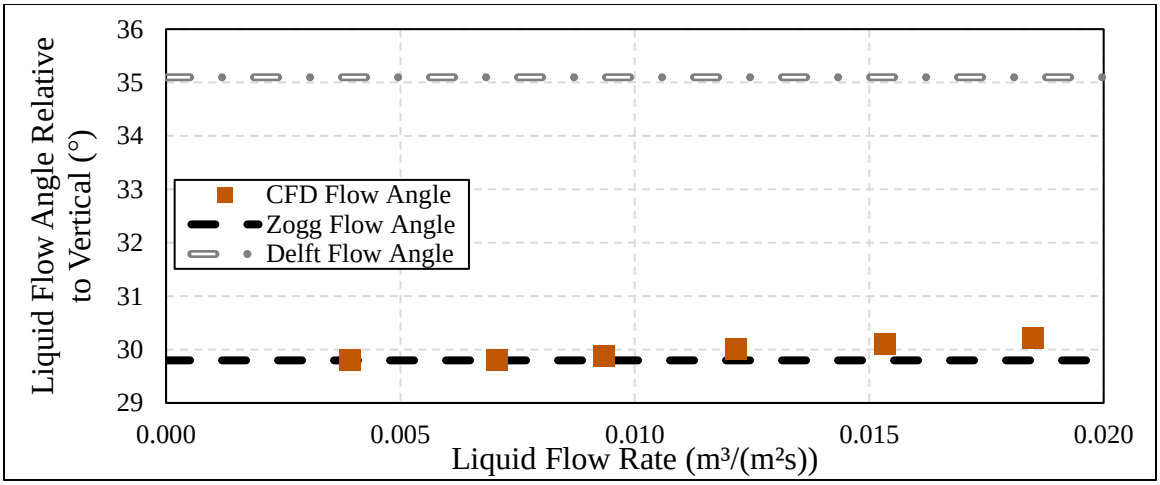

Figure 4-8: Volume-averaged CFD liquid flow angle predictions for Mellapak 250Y versus the liquid flow rate, along with predictions for the flow angle from Zogg (1973) and the Delft model (Olujić et al., 2004).

4.3.2.3.Friction Factor

To provide an additional comparison source for the CFD hydrodynamic predictions, the Fanning friction factors in the CFD simulations were compared to the friction factors predicted from inclined plate film theory. The Fanning friction factor is a measure of the system's resistance to the flow, representing the shear stress at the no-slip surface to the average kinetic energy of the fluid, as Equation (4-9) demonstrates. For an infinitely wide and tall inclined plate, inclined plate film theory predicts the average film velocity shown in Equation (4-10) and an average shear stress on the inclined plate shown by Equation (4-11) (Bird et al., 2007). Combining Equations (4-9), (4-10), and (4-11), Equation (4-12) shows the Fanning friction factor for liquid film flow on an inclined plate (Bird et al., 2007).

$$f = \frac{\left|\tau_{\text{wall,avg}}\right|}{\frac{1}{2}\rho v_{\text{avg}}^2} \tag{4-9}$$

$$v_{\text{avg}} = \frac{\rho g \delta^2 \cos(\beta)}{3\mu_m} \tag{4-10}$$

$$\tau_{\text{wall,avg}} = \rho g \delta \cos(\beta) \tag{4-11}$$

$$f_{\text{inclined plate}} = \frac{18\mu_m^2}{\rho^2 g \delta^3 \cos(\beta)} \tag{4-12}$$

The Fanning friction factor was also predicted in CFD. The friction factors for the simulations were calculated using Equation (4-9), and Figure 4-9 compares the CFD

predictions to the predictions from Equation (4-12). For the liquid flow angle in Equation (4-12), the analytical expression by Zogg was utilized, shown in Equation (4-6).

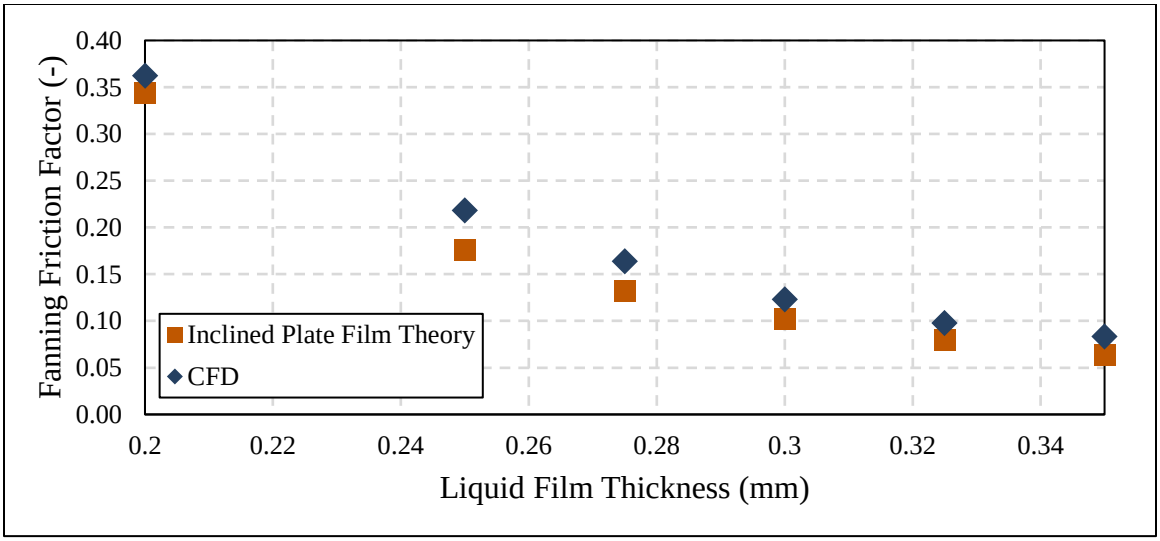

Figure 4-9: Friction factor predictions from inclined plate film theory and CFD.

Both the CFD simulations and the inclined plate film theory predicted a decrease in the friction factor as the film became thicker. This trend resulted from the higher liquid flow rate and liquid velocity. As the liquid traveled faster through the system, the kinetic energy of the fluid increased, producing a larger denominator in Equation (4-9). The friction factor predictions from CFD were consistently higher than the corresponding predictions from inclined plate film theory. This trend was due to the packing crimps. As the liquid traveled over each packing crimp in the CFD simulations, the fluid had to change directions, which slowed the fluid's movement. The slower flow for the LREU caused a smaller denominator in Equation (4-9) and produced a higher friction factor. These direction changes at the packing crimps were absent from the inclined plate case. Despite

the difference in geometry between the inclined plate and the LREU, a decent agreement for the Fanning friction factor was observed, with an AAD of 20.9 percent. This agreement, in conjunction with the liquid holdup and liquid flow angle comparisons, validated the hydrodynamic LREU predictions from CFD.

4.3.3. LREU Validation for Mass Transfer

The liquid mass transfer coefficient was the observed variable for the LREU mass transfer validation. The CFD predictions were compared to the experimental mass transfer data for toluene desorption from water into air in Mellapak 250Y reported by Song (2017). In addition to the CFD simulations, the liquid mass transfer coefficient was also predicted by several industry-accepted correlations: the Billet and Schultes model (Billet and Schultes, 1999; Schultes, 2018), the Delft model (Dejanović et al., 2011; Olujić, 2019; Olujić et al., 2012, 2004; Olujić and Seibert, 2014), the Rocha-Bravo-Fair (RBF) model (Rocha et al., 1996), and the Song model (Song et al., 2018). All four of these models were developed on pilot-scale or larger columns, making their predictions more comparable to industrial scales. Additionally, all of these models utilized large experimental databases, a critical factor to develop high-fidelity correlations (Erasmus, 2004). To align with typical experimental conditions for toluene desorption studies, the gas F-factor in the RBF model calculations was 2 $\sqrt{\text{Pa}}$. Figure 4-10 shows the liquid mass transfer coefficient predictions from CFD and from the correlations.

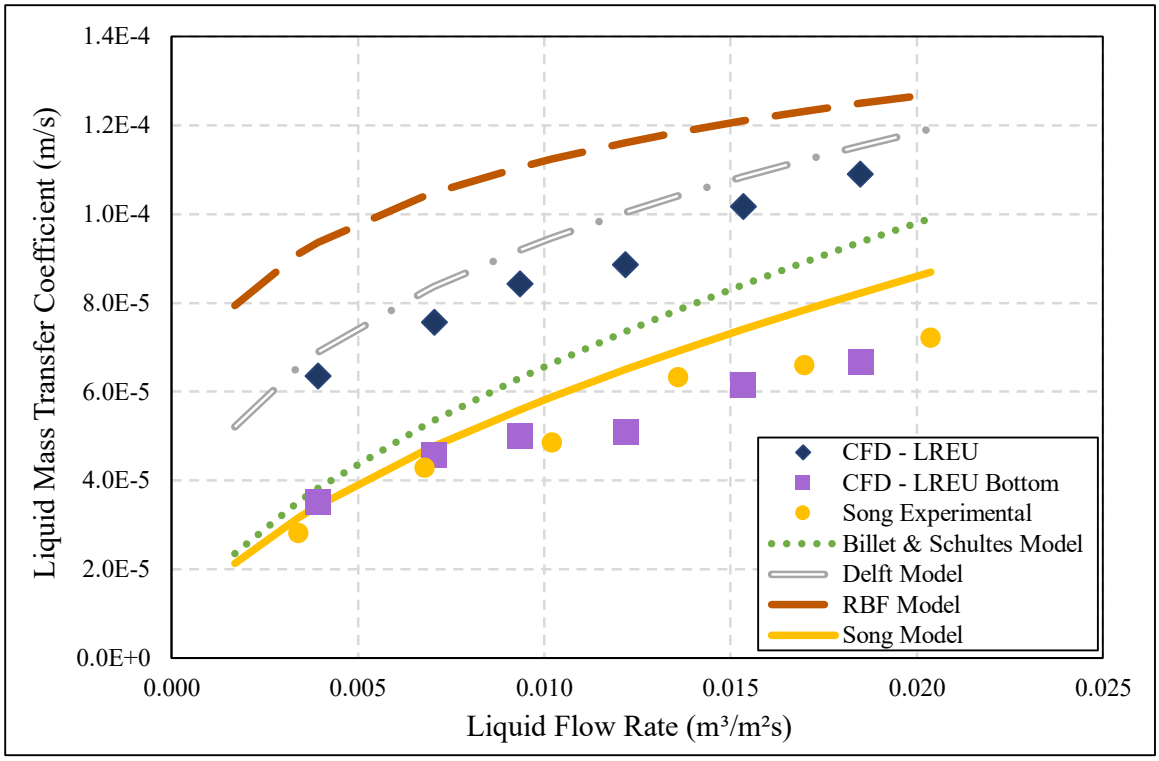

Figure 4-10: Predictions of the liquid mass transfer coefficient for toluene desorption in Mellapak 250Y from CFD, the Billet & Schultes model, the Delft model, the Rocha-Bravo-Fair model, and the Song model.

The CFD simulations predicted an increase in the liquid mass transfer coefficient as the liquid film became thicker and more liquid passed through the system. This trend resulted from the higher flow rates, which improved surface renewal in the system, and was supported by the experimental data and the correlations. The correlations exhibited some variation in their predictions. The CFD predictions were approximately in the center of the predictions from the high-fidelity correlations, adding validity to the mass transfer predictions using the LREU approach.

Figure 4-11 shows the local mass transfer coefficient at the gas-liquid interface in the LREU, calculated according to Equation (3-8). As shown in the figure, higher mass

transfer coefficients occurred near the top of the LREU. These higher values stemmed from the uniform mass fraction imposed at the top of the LREU, which caused large concentration gradients at the gas-liquid interface. To capture the LREU's performance in the absence of these entrance effects, the local mass transfer coefficient was averaged across the bottom half of the LREU, and the predictions were plotted in Figure 4-10. The predictions from the bottom half of the LREU had excellent agreement with the experimental data from Song (2017), showing an AAD of approximately eight percent (linearly interpolating the experimental data to ensure matching liquid flow rates).

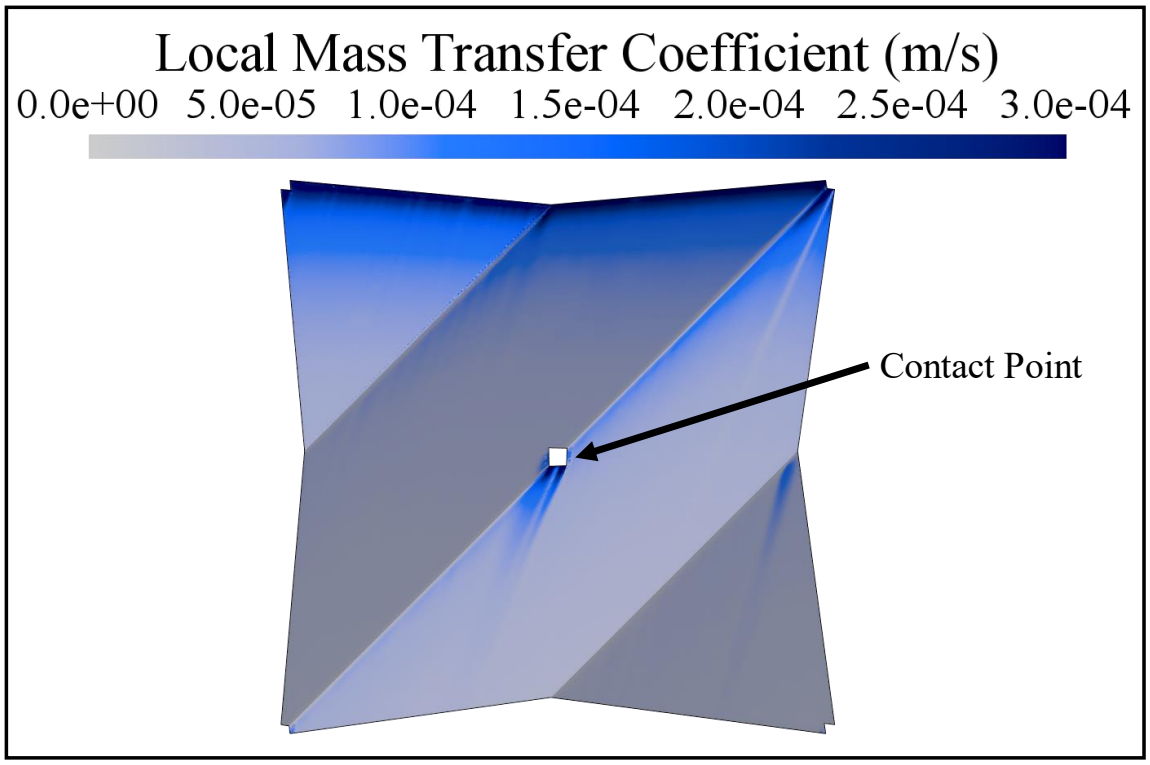

Figure 4-11: Predicted local mass transfer coefficient at the gas-liquid interface for Mellapak 250Y with a film thickness of 0.275 mm, showing high values near the top of the LREU where the toluene was inserted into the system.

4.3.4. Structured Packing Geometry Investigation

A geometry investigation of structured packings was conducted to determine the impact of a packing's geometry on the liquid-phase performance. Two fundamental parameters for structured packing geometry were systematically and independently varied: the channel opening angle and the channel inclination angle. In addition to the earlier work in this research project, Basden (2014) previously changed these variables while investigating the gas-phase performance of structured packings. During this process, Mellapak 250Y served as the baseline condition, and the specific packing area was held constant at 236 m^2/m^3 during this process. The channel base length, channel side length, and channel height can be calculated with the channel opening angle, channel inclination angle, and the specific packing area through Equations (3-10), (3-11), and (3-12).

$$b = \frac{4}{A_P \cos\left(\frac{\theta}{2}\right)} \tag{3-10}$$

$$s = \frac{4}{A_P \sin(\theta)} \tag{3-11}$$

$$h = \frac{2}{A_P \sin\left(\frac{\theta}{2}\right)} \tag{3-12}$$

Following the previous work in this research effort, the channel inclination angle changed from 30° to 120° with 15° increments. Similarly, the channel opening angle varied from 60° to 120° with increments of approximately 15°. Table 4-3 lists the structured packing geometries simulated. For the channel inclination angle of 90°, the LREU geometry reduced to a liquid film traveling down a vertical, almost-square pipe. The

system's geometry did not constrain the height of the system in this case, so a height of 10 cm was used, as performed earlier in this research effort.

Specific Packing Area, A_P (m^2/m^3)	**Channel Inclination Angle, α (°)**	**Channel Opening Angle, θ (°)**
Baseline Case		
236	45	90.7
Varying θ		
236	45	60
236	45	75
236	45	105
236	45	120
Varying α		
236	30	90.7
236	60	90.7
236	75	90.7
236	90	90.7

Table 4-3: Geometries tested for LREU packing geometry study.

To ensure an appropriate comparison between cases, the liquid flow rate in all cases was 0.010 $m^3/(m^2s)$. This flow rate was approximately the average flow rate in Figure 4-10 and also matched conditions studied by Green et al. (2007). To enforce this flow rate in the LREU, the mass flow rate for the periodic boundary conditions between the top and bottom faces of the LREU was specified. The liquid film thickness was adjusted until the absolute total pressure drop between the top and bottom faces was between 100 and 425 Pa/m, a range typically observed experimentally for irrigated gas-phase pressure drops in structured packings. A surface average was used to calculate the pressure. The hydrodynamic portion of the simulations converged when the absolute total pressure drop

changed by less than 0.001 percent over the last 500 iterations, and the mass transfer portion of the simulations had the same convergence criteria as described for the Mellapak 250Y case. The base mesh for all cases had 6 prism layers at the packing surface and 18 prism layers at the gas-liquid interface. This base mesh was finer than necessary according to the mesh sensitivity case for the 0.3 mm film thickness Mellapak 250Y case to ensure mesh independence as the geometry changed. For each case, the average liquid flow angle in the LREU and the average mass transfer coefficient in the bottom half of the LREU were observed.

4.3.4.1.Channel Inclination Angle Variation

The channel inclination angle was the first term varied. Figure 4-12 plots the predicted volume-averaged liquid flow angle and mass transfer coefficient as the inclination angle changed. The prediction by the Zogg equation, shown in Equation (4-6), is also presented for comparison. As the channel inclination angle increased, the simulations predicted smaller flow angles, implying a decreased amount of horizontal flow. This trend was reasonable because the channels became more vertical with a larger channel inclination angle, which allowed the liquid to travel in a more downward direction as it followed the packing surface under the force of gravity. The Zogg equation predicted a similar trend, adding validity to observed trend. The predicted flow angle and the Zogg prediction showed strong agreement, exhibiting an AAD of 0.34 percent for channel inclination angles less than 90°. The percent deviation for the 90° case was undetermined because the Zogg equation predicted a flow angle of 0°, but the CFD and Zogg predictions differed by less than 0.05°.

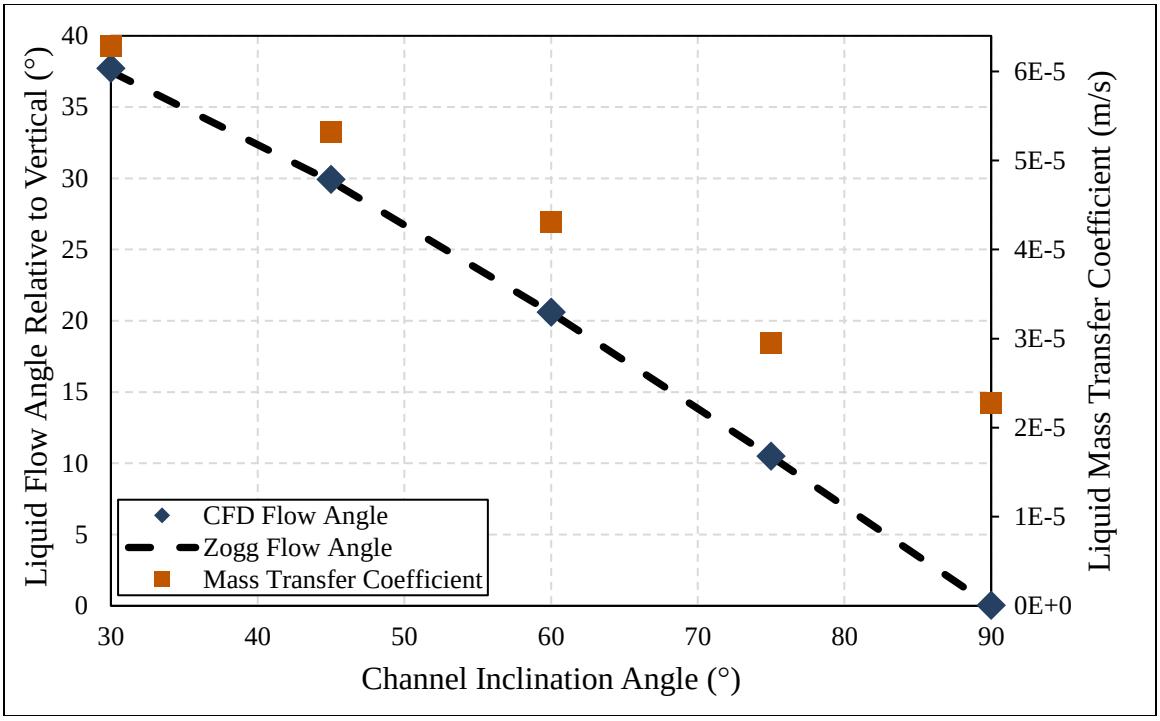

Figure 4-12: Liquid mass transfer coefficients predictions from CFD and volume-averaged liquid flow angle predictions from CFD, compared against predictions from Zogg (1973), as the channel inclination angle varied.

Figure 4-12 also shows the liquid mass transfer coefficient increasing as the channel inclination angle diminished. This trend resulted from the increased horizontal flow, as described by the flow angle predictions. When the liquid crossed a crimp in the packing, the steepness of the packing sheet remained constant, as predicted by Equation (4-6). However, the liquid had to change the direction it moved horizontally to continue sliding down the steepest direction on the packing surface. This horizontal change in direction produced liquid upheaval and surface renewal, which improved the mass transfer performance. As the channel inclination angle approached 90°, the film approached a condition without a direction change, evidenced in Figure 4-12 by the flow angle

approaching 0°. This trend resulted in the liquid mass transfer coefficient exhibiting an asymptote as the structured packing channels become vertical, aligning with a condition where the film does not experience direction changes. The observed importance of the crimps aligned with the work of Sun et al. (2013), who reported liquid film direction changes markedly improving the mass transfer performance.

To demonstrate the liquid upheaval after the liquid crossed the packing crimp, Figure 4-13 presents the local mass transfer coefficient in the system and further reveals the importance of the packing crimps. For a channel inclination angle of 30°, the regions just below each packing crimp showed a noticeably higher local mass transfer coefficient. This region of higher mass transfer resulted from the horizontal direction change, which caused surface renewal. As the liquid was overturned, toluene in the bulk liquid phase drew closer to the gas phase, where it desorbed and could be swept away by the gas phase.

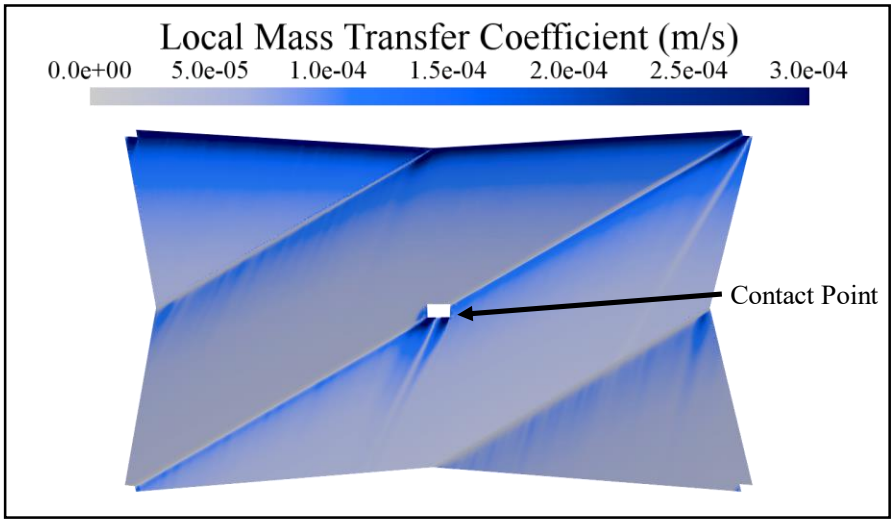

Figure 4-13: Predicted local mass transfer coefficient at the gas-liquid interface for a channel inclination angle of 30°, showing high values near packing crimps due to liquid upheaval.

The direction change from the packing crimps impacted the hydrodynamic performance in addition to the mass transfer performance. Figure 4-14 presents the velocity magnitude on the gas-liquid interface for a channel inclination angle of 30°. Near each crimp in the structured packing, the liquid velocity decreased. The direction change of the film caused this slowdown in the system. While a slower liquid film impairs the mass transfer performance, as Figure 4-10 demonstrates, the benefit of the liquid upheaval in the system typically outweighed this penalty in the LREU. Figure 4-14 also shows streaks of lower velocity on the gas-liquid interface. These streaks were wakes formed by the contact points between structured packing sheets. Wake formation in laminar flow conditions has been previously reported for flow past cylinders (Rajani et al., 2009; Vyas et al., 2020; Zdravkovich, 1990). The streaks caused by the wakes in Figure 4-14 produced similar trends in the local mass transfer coefficient profile in Figure 4-13.

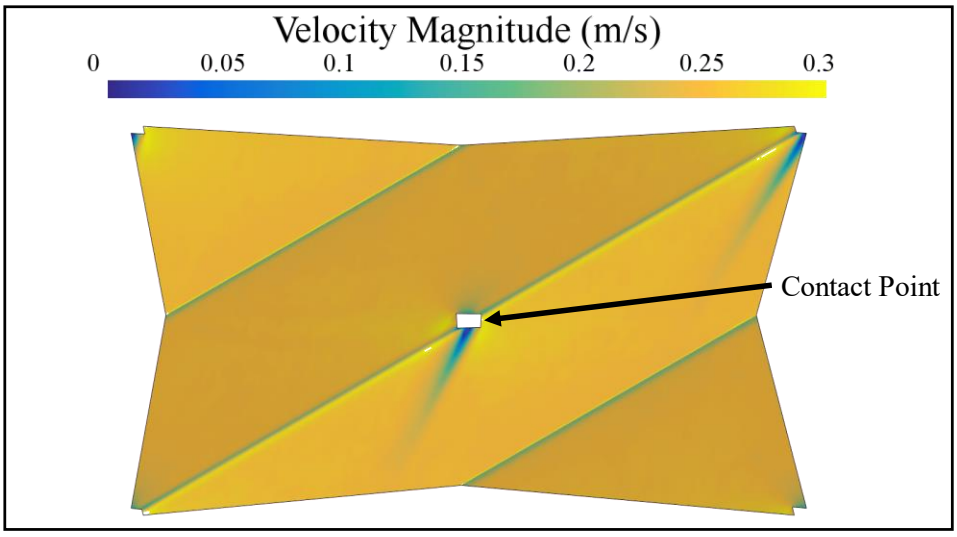

Figure 4-14: Predicted liquid speed at the gas-liquid interface for a channel inclination angle of 30°, showing slower speeds both near packing crimps due to direction changes and below the contact point due to wake formation.

For comparison to the 30° channel inclination angle case in Figure 4-13, Figure 4-15 presents the local liquid mass transfer coefficient for a channel inclination angle of 75°. This 75° case had the largest inclination angle while still exhibiting flow crossing structured packing crimps. The local mass transfer coefficient in Figure 4-15 is lower than the corresponding term in Figure 4-13 both after the structured packing crimps as well as below the contact point between the structured packing sheets. The local mass transfer coefficient after the packing crimps was lower because of the smaller flow angle, which produced a less significant direction change and less upheaval of the liquid. The flow angle was also responsible for the smaller local mass transfer coefficient below the contact point. Because of the relatively small amount of horizontal flow in the 75° case, the two liquid films on the packing surfaces which merged near the contact point had similar flow directions. The similar flow directions caused less liquid upheaval, bringing fewer toluene molecules near the gas-liquid interface.

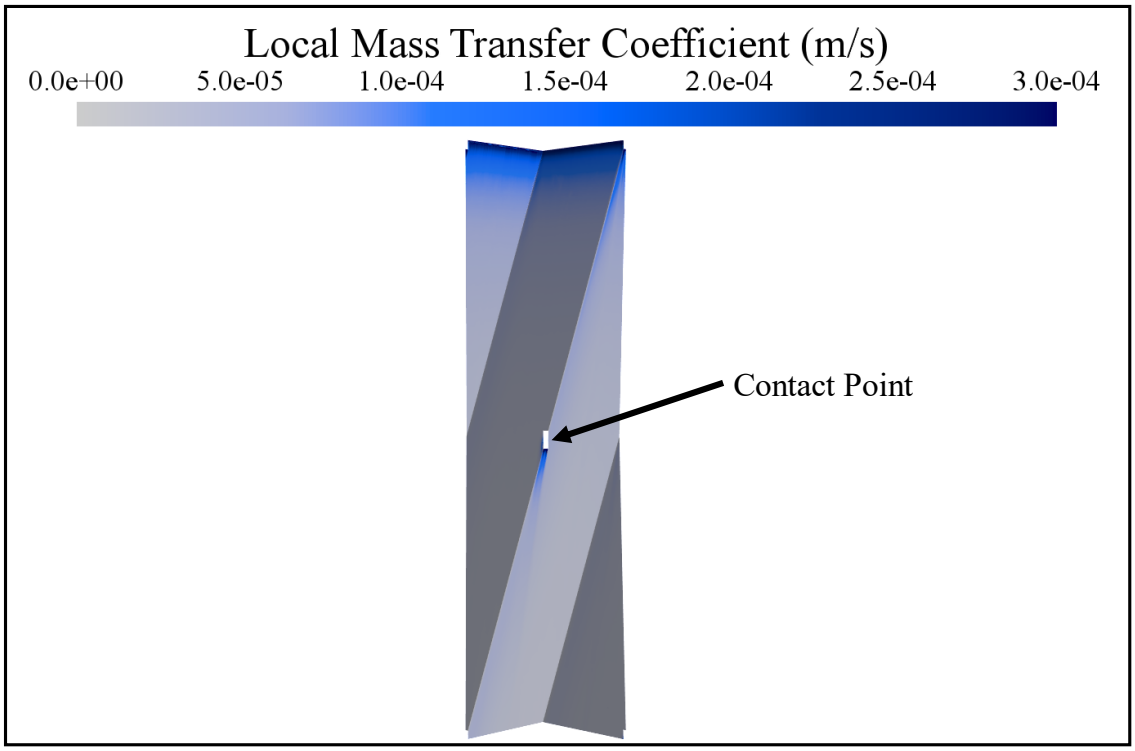

Figure 4-15: Predicted local mass transfer coefficient at the gas-liquid interface for a channel inclination angle of 75°, showing lower values compared to the 30° channel inclination angle LREU due to smaller direction changes.

4.3.4.2.Channel Opening Angle Variation

Figure 4-16 plots the volume-averaged liquid flow angle predictions from the CFD simulations versus the channel opening angle. As the channel became more open, the flow angle decreased, implying a decreased amount of horizontal flow. This trend resulted from the decreased barriers to the flow that the channel crimps imposed. As the channel opening angle increased, the structured packing sheets became flatter, which offered a more vertical path to the liquid. This observed trend was also predicted by the Zogg equation, which is

plotted in Figure 4-16. The CFD predictions for the flow angle again showed strong agreement with Equation (4-6), having an AAD of 0.33 percent as the geometry changed.

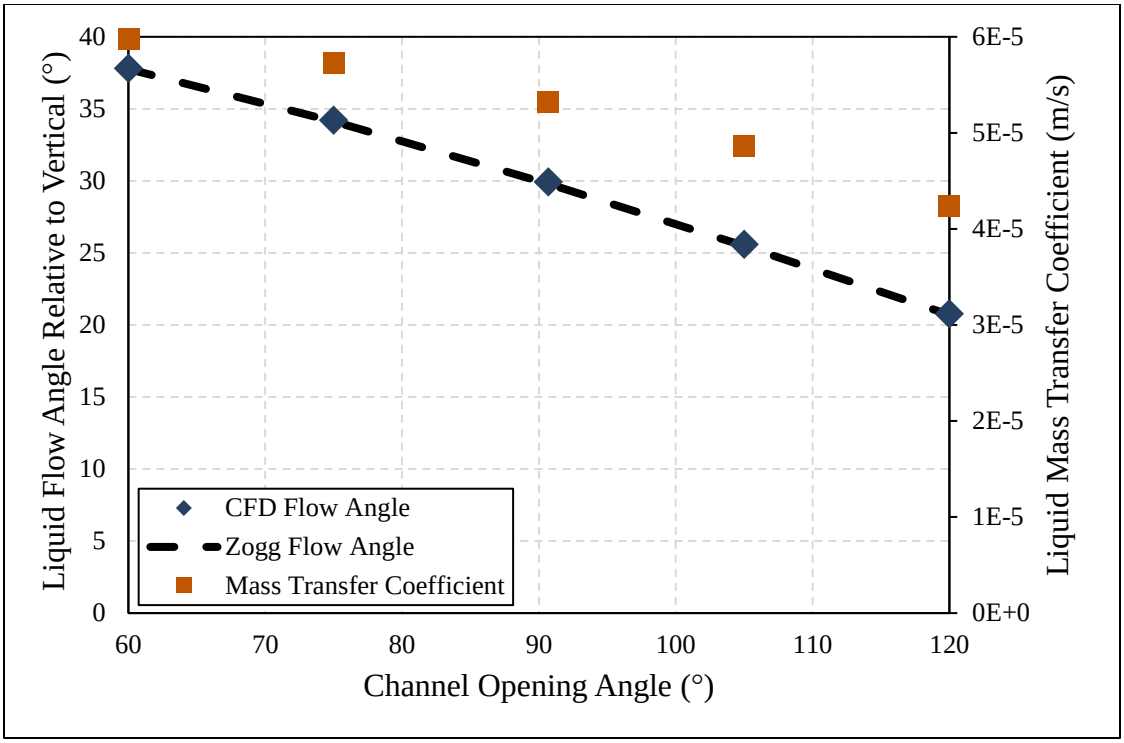

Figure 4-16: Liquid mass transfer coefficients predictions from CFD and volume-averaged liquid flow angle predictions from CFD, compared against predictions from Zogg (1973), as the channel opening angle varied.

Figure 4-16 also revealed the dependence of the liquid mass transfer coefficient on the channel opening angle. As the channel opened, the mass transfer coefficient decreased. This trend stemmed from the decreased amount of horizontal flow, as revealed by the smaller flow angle. The smaller amount of horizontal flow resulted in smaller direction changes when the liquid passed each crimp in the structured packings. The diminished

direction changes produced less liquid upheaval and surface renewal, impairing the mass transfer performance.

Figure 4-17 demonstrates the increase in mass transfer across the packing crimps for the 60° channel opening angle case. Similar to the trends in Figure 4-13, the local mass transfer coefficient in regions just below the structured packing crimps showed a much higher mass transfer rate for small channel opening angles. The sharper channel opening angle caused a greater direction change for the liquid film in the 60° case compared to the 90.7° case, resulting in improved mass transfer.

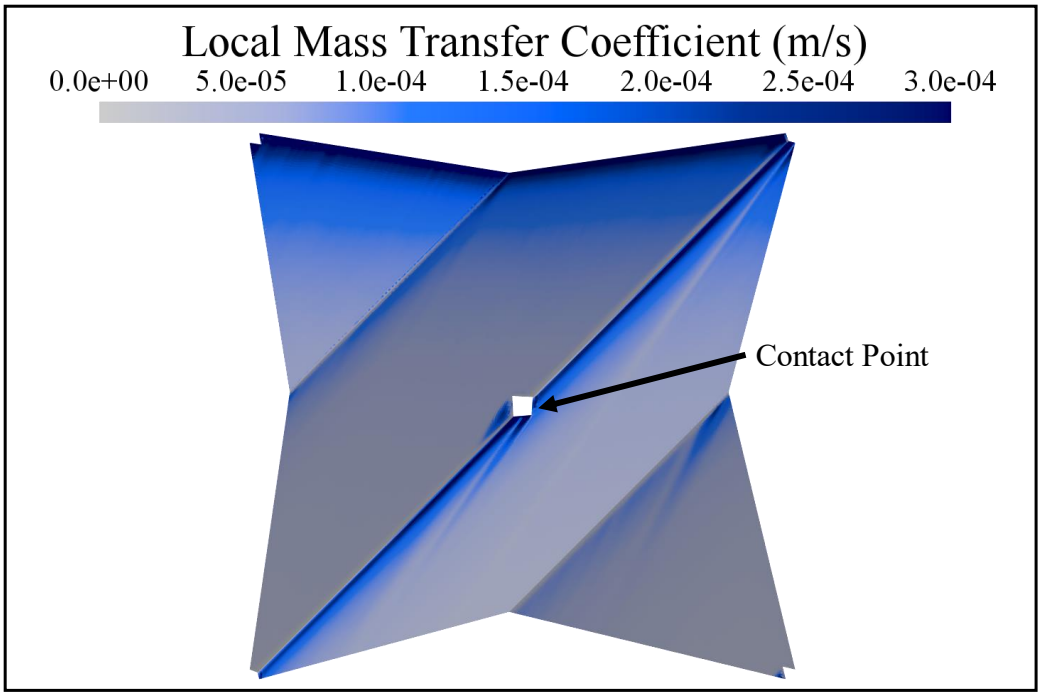

Figure 4-17: Predicted local mass transfer coefficient at the gas-liquid interface for a channel opening angle of 60°, showing higher values near packing crimps due to direction changes.

Contrasting with the trends in Figure 4-17, Figure 4-18 showed a negligible increase in the mass transfer performance after the structured packing crimps for a channel opening angle of 120°. Because the structured packing sheets were flatter in this case, the liquid film could travel more vertically and less horizontally, which caused a smaller direction change across each crimp in the structured packing.

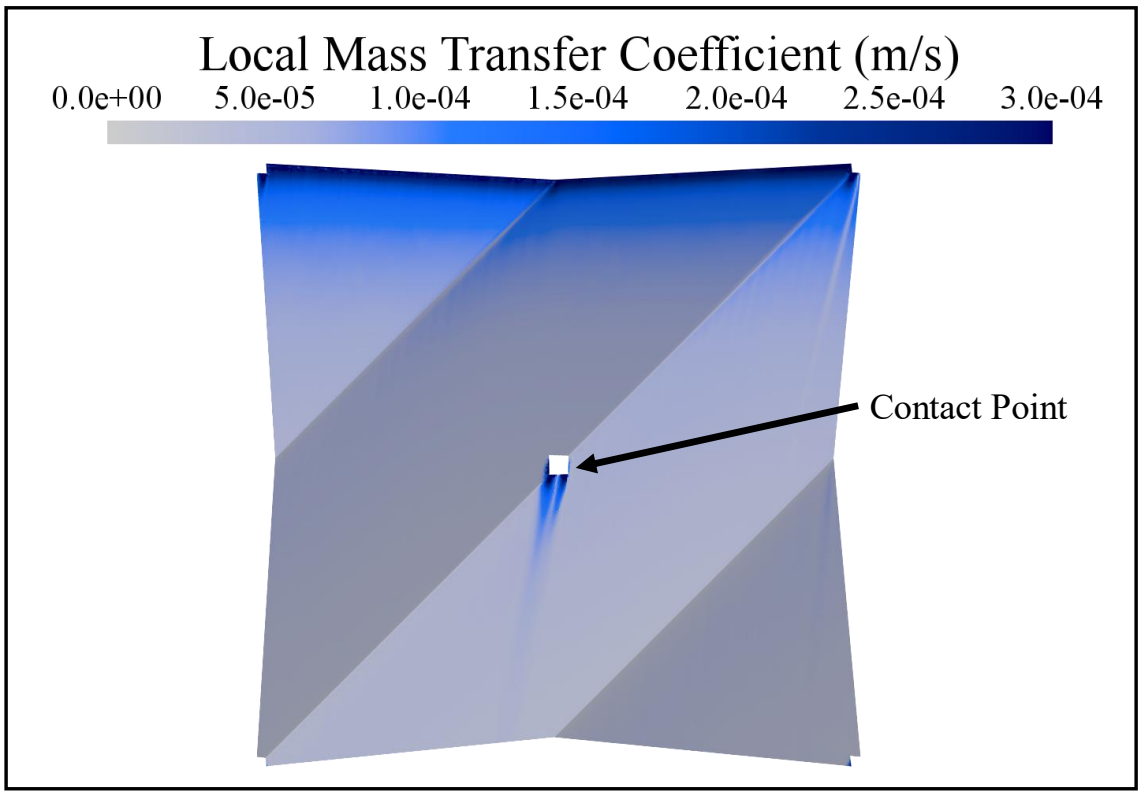

Figure 4-18: Predicted local mass transfer coefficient at the gas-liquid interface for a channel opening angle of 120°, showing lower values near packing crimps compared to the 60° channel opening angle LREU due to smaller direction changes.

4.4. CONCLUSIONS

In this study, the dependence of the liquid phase's performance on the structured packing geometry was investigated. The study employed a representative elementary unit (REU) approach to reduce computational expense, but the system was simplified to create a liquid representative elementary unit (LREU), with the liquid having a constant film thickness. Increasing the liquid film thickness produced a larger liquid flow rate through the LREU, and the liquid holdup for a given liquid flow rate showed strong agreement with two experimental datasets reported by Green et al. (2007), with an absolute average deviation (AAD) of approximately six percent. The liquid flow angle was predicted with the CFD simulations, and the calculated values showed strong agreement with the analytical expression developed by Zogg (1973), having an AAD of 0.58 percent across a range of liquid flow rates. The friction factor for the LREU was compared to the friction factor from inclined plate film theory, and a good qualitative agreement was observed across several liquid flow rates. The quantitative agreement was acceptable, showing an AAD of 20.9 percent, and the discrepancy resulted from direction changes at the packing crimps, which are absent in inclined plate film theory.

The mass transfer performance for the system was predicted for toluene desorption from water. This system is liquid-film controlled, allowing the gas-phase mass transfer to be neglected. The average liquid mass transfer coefficient was calculated using a differential contactor approach, and the predicted values were within the range of four high-fidelity semi-empirical models. Additionally, the average liquid mass transfer coefficient in the bottom half of the LREU showed strong agreement with experimental data from Song (2017), with an AAD of eight percent further validating the mass transfer methodology.

The packing geometry investigation highlighted the importance of the liquid flow angle on liquid-phase performance. When the channel inclination angle or the channel opening angle varied, configurations resulting in a higher liquid flow angle produced larger liquid mass transfer coefficients. This superior mass transfer performance in the liquid resulted from direction changes at the structured packing crimps, which caused upheaval in the liquid. Trends in the local liquid mass transfer coefficient supported this observation, with markedly improved mass transfer occurring directly below the structured packing crimps. Trends revealed during the packing geometry investigation suggested smaller channel opening angles and smaller inclination angles would improve the liquid mass transfer performance.

The results of this analysis highlight the importance of capturing the surface renewal at the structured packing crimps and at the contact point between structured packing sheets. Neglecting this surface renewal could significantly impair performance predictions, including by modeling the liquid film in structured packings as simple film flow down an inclined plate.

Chapter 5: A Volume-of-Fluid Methodology for Interfacial Mass Transfer

5.1. INTRODUCTION

To fully predict the mass transfer in structured packings, the mass transfer across the gas-liquid interface must be considered. This capability will enable the simulation of chemical systems with mass transfer resistances in both phases. While many methodologies have been developed in the last two decades to predict interfacial mass transfer, most models are only applicable for a small concentration jump across the interface. This study developed a new interfacial mass transfer model capable of handling a concentration jump of multiple orders of magnitude across the interface, made possible by tracking the mass fraction rather than the concentration. The model was implemented in commercial CFD software.

A chemical species thermodynamic preference to reside in one phase over another phase creates a concentration jump at the interface and leads to spurious mass transfer fluxes across the interface in CFD. As illustrated in Figure 2-2, a jump in concentration between the two phases can lead CFD solvers to observe a large concentration gradient and predict a large mass flux across the interface, even at thermodynamic equilibrium. To counteract this spurious interfacial flux, Haroun et al. (2010a) proposed the application of a flux to counter this spurious diffusion generated by the concentration jump. This supplemental solubility flux uses Henry's law to negate the concentration gradient flux at thermodynamic equilibrium, as Figure 2-2 demonstrates. Equation (5-1) presents the model by Haroun et al. (2010a) for the solubility flux, which was developed from the convection-diffusion governing equation for mass transfer, shown in Equation (5-2). Deising et al. (2016) provided a thorough discussion on the mathematical underpinnings of the model.

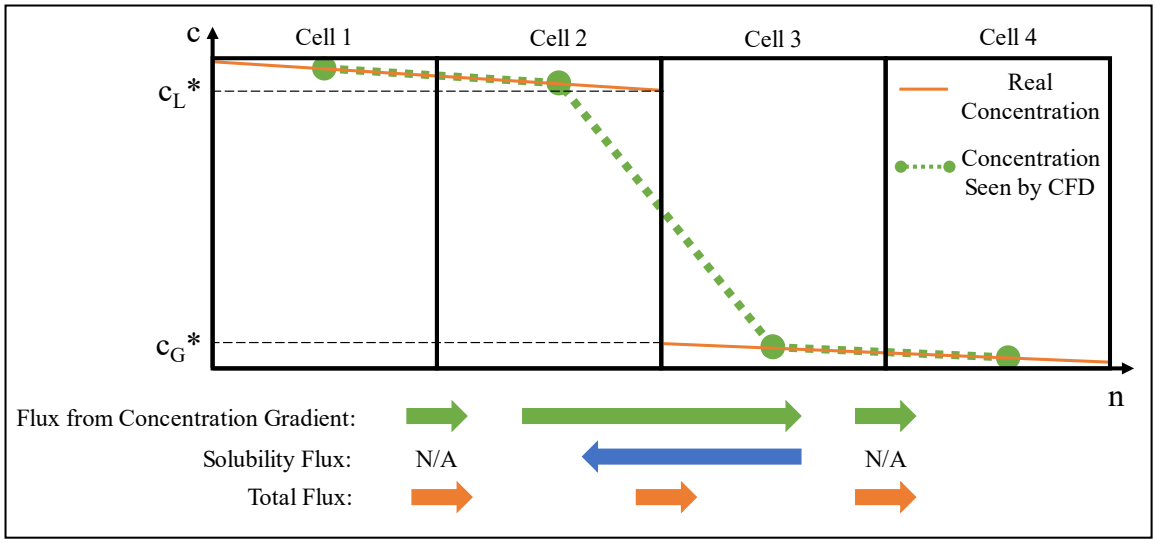

Figure 2-2: Graphical example of an adjusted flux approach.

$$\frac{\partial c_A}{\partial t} + \nabla \cdot (c_A \mathbf{v}) = \nabla \cdot \left(D_A \nabla c_A + \mathbf{\Phi}_{A,Sol}\right) + S_A \tag{5-1}$$

$$\frac{\partial c_A}{\partial t} + \nabla \cdot (c_A \mathbf{v}) = \nabla \cdot \left(D_{A,m} \nabla c_A\right) + S_A \tag{5-2}$$

Equation (5-3) defines the solubility flux, $\mathbf{\Phi}_{A,Sol}$.

$$\mathbf{\Phi}_{A,Sol} \equiv -D_A \frac{c_A(1 - He_A)}{\omega_L + He_A \omega_G} \nabla \omega_L \tag{5-3}$$

In this equation, ω_L represents the liquid volume fraction. Additionally, He_A represents the Henry's law constant describing the concentration jump of the chemical species between the two phases, as demonstrated in the equation below.

$$He_A \equiv \frac{c_G{}^*}{c_L{}^*} \tag{5-4}$$

For systems with an equal concentration in the two phases, the Henry's constant would equal one. Under these conditions, the magnitude of the solubility flux would be zero, causing the solubility flux to effectively turn off. Deviations from a Henry's constant equal to unity create a non-zero solubility flux. For these deviations from unity, the solubility flux can become large in magnitude, due to the sharp gas-liquid interface causing a large value for $\nabla\omega_L$.

As explained by Yang et al. (2020), large magnitudes of the diffusive flux and the solubility flux cause numerical challenges. For a system at thermodynamic equilibrium, the two terms should cancel each other, but even miniscule percent differences can still alter the mass transfer prediction due to the fluxes' large magnitude. Numerical instabilities have been reported in studies using a solubility flux approach, possibly the cause of many previous investigations having a Henry's constant within an order of magnitude of unity, which limits the magnitude of the solubility flux (Haroun et al., 2010a; Yang et al., 2020). Unfortunately, this limitation reduces the number of chemical systems that can be investigated, especially since systems in this range of Henry's constants are often liquid-film controlled (Linek et al., 1998; Liss and Slater, 1974). Many systems exhibit He_A<0.1 or conditions where the gas-phase has significant mass transfer resistance. For example, packed columns often have the majority of the mass transfer resistance in the gas phase (Arwikar and Sandall, 1980; Erasmus, 2004; Lautenschleger et al., 2015; Schpigel and Meier, 1994).

In this study, to model gas-phase controlled processes, an interfacial mass transfer model was developed by adjusting the Haroun et al. (2010a) model. Rather than tracking a concentration field, a mass fraction field was simulated. Due to the difference in densities between the two phases, often with the liquid-to-gas density ratio on the order of 10^3, this approach is conducive to systems with He_A on the order of 10^{-3}.

5.2. CFD METHODOLOGY

5.2.1. Hydrodynamic Methodology

Simcenter STAR-CCM+ 2021.1.1 served as the CFD software. In this software, the continuity equation ensured conservation of mass (Bird et al., 2007; "Simcenter STAR-CCM+ 2021.1.1 Theory Guide," 2021).

$$\frac{\partial \rho}{\partial t} + \nabla \cdot (\rho \mathbf{v}) = 0 \tag{2-8}$$

Equation (5-5) below ensured momentum was conserved in the system ("Simcenter STAR-CCM+ 2021.1.1 Theory Guide," 2021). The pressure in this equation combines the hydrostatic and static pressure. A second-order scheme was implemented for convection, and a first-order scheme was implemented for temporal discretization.

$$\frac{\partial (\rho \mathbf{v})}{\partial t} + \nabla \cdot (\rho \mathbf{v} \otimes \mathbf{v}) = -\nabla \cdot (p\mathbf{I}) + \nabla \cdot \left(\mu_{\text{effective}} \left(\nabla \mathbf{v} + (\nabla \mathbf{v})^{\mathbf{T}} \right) \right) \tag{5-5}$$

For laminar flow, $\mu_{effective}$ is simply the molecular dynamic viscosity. At the gas-liquid interface, the continuum surface force (CSF) model applied surface tension. This model, reproduced in Equation (5-6) below, converts the surface tension force into a volumetric force in cells containing a portion of the interface. The HRIC method predicted the location of the gas-liquid interface.

$$\mathbf{f}_{CSF} = -\sigma \nabla \cdot \left(\frac{\nabla \omega_L}{|\nabla \omega_L|} \right) \nabla \omega_L \tag{5-6}$$

The volume of fluid (VOF) model predicted the liquid volume fraction through the following equation.

$$\frac{\partial \omega_L}{\partial t} + \nabla \cdot (\omega_L \mathbf{v}) = 0 \tag{5-7}$$

This model scales physical properties according to the relative volume of each phase present in the cell, as demonstrated below for the viscosity.

$$\mu_m = \mu_{L,m} \omega_L + \mu_{G,m} \omega_G \tag{5-8}$$

5.2.2. Mass Transfer Methodology

A VOF mass fraction can be defined according to Equation (5-9) below using the mixture density and concentration, as suggested by Hill et al. (2018).

$$x_A \equiv \frac{c_A}{\rho_{mix}} \tag{5-9}$$

Using this definition, the Haroun et al. (2010a) model in Equation (5-1) can be rewritten in terms of mass fractions, as Equation (5-10) shows.

$$\frac{\partial \rho_{mix} x_A}{\partial t} + \nabla \cdot (\rho_{mix} x_A \mathbf{v}) = \nabla \cdot \left(D_A \nabla (\rho_{mix} x_A) + \mathbf{\Phi}_{A,Sol} \right) + S_A \tag{5-10}$$

For multiphase systems, the mixture density is not constant but can change spatially due to the different material properties of the two phases. With this consideration, Equation (5-11) expands the diffusive flux term.

$$\begin{aligned} \frac{\partial \rho_{mix} x_A}{\partial t} + \nabla \cdot (\rho_{mix} x_A \mathbf{v}) \\ = \nabla \cdot \left(\rho_{mix} D_A \nabla x_A + x_A D_A \nabla \rho_{mix} + \mathbf{\Phi}_{A,Sol} \right) + S_A \end{aligned} \tag{5-11}$$

The gradient of the density can be reformulated in terms of ω_L using the properties of VOF.

$$x_A D_A \nabla \rho_{mix} = x_A D_A \nabla \left(\rho_L \omega_L + \rho_G (1 - \omega_L) \right) = x_A D_A (\rho_L - \rho_G) \nabla \omega_L \tag{5-12}$$

This flux term can be combined with the solubility flux term in Equation (5-3) while also using the mass fraction definition in Equation (5-9).

$$\begin{aligned} \mathbf{\Phi}_{A,new} &= x_A D_A \nabla \rho_{mix} + \mathbf{\Phi}_{A,Sol} \\ &= x_A D_A \left((\rho_L - \rho_G) - \frac{\rho_{mix} (1 - He_A)}{\omega_L + He_A \omega_G} \right) \nabla \omega_L \end{aligned} \tag{5-13}$$

Combining Equations (5-11) and (5-13) gives the final form of the model in Equation (5-14).

$$\frac{\partial \rho_{mix} x_A}{\partial t} + \nabla \cdot (\rho_{mix} x_A \mathbf{v}) = \nabla \cdot (\rho_{mix} D_A \nabla x_A) + \nabla \cdot \left(x_A D_A \left((\rho_L - \rho_G) - \frac{\rho_{mix}(1 - He_A)}{\omega_L + He_A \omega_G} \right) \nabla \omega_L \right) + S_A \quad (5\text{-}14)$$

The additional flux term has two sources of contributions, as Equation (5-13) shows. One contribution comes from the interfacial concentration jump of the diffusing species between the two phases. Haroun et al. (2010a) previously elucidated this concentration jump contribution. The other contribution, presented in this study, stems from the difference in densities between the two phases. With this second contribution, the interfacial mass transfer model computes the interfacial diffusive flux solely based on the mass fraction gradient, superficially independent of any density differences. Overall, the entire interfacial mass transfer model reframes the mass transfer prediction by tracking the mass fraction rather than the concentration.

When $He_A = \rho_G/\rho_L$, the additional flux term equals zero, producing the standard convection-diffusion equation in Equation (5-2). This condition results in a mass fraction field that is continuous across the interface. This baseline value for the Henry's constant is approximately three orders of magnitude lower than the baseline value for the original Haroun et al. (2010a) model, depending on the densities of the phases simulated. It should be noted that applying the strategy used in the steps above to the interfacial mass transfer models developed by Marschall et al. (2012) and Deising et al. (2016) does not reproduce the convection-diffusion equation when $He_A = \rho_G/\rho_L$.

The interfacial mass transfer model was implemented in the commercial CFD software through the passive scalar model. This model inhibits the mass transfer predictions from affecting the hydrodynamic predictions, which aligns with the conditions of a dilute diffusing chemical species. The passive scalar model is shown in Equation (5-15) below ("Simcenter STAR-CCM+ 2021.1.1 Theory Guide," 2021).

$$\frac{\partial(\rho x_A)}{\partial t} + \nabla \cdot (\rho x_A \mathbf{v}) = \rho D_A \nabla x_A + S_{A,CFD} \tag{5-15}$$

The interfacial mass transfer model was included in this model as a source term using the field functions in Simcenter STAR-CCM+. By implementing the model as a source term, the chemical species was created or destroyed in each cell rather than directly being moved between cells. The amount of the species created in each cell was equal to the net flux into the cell specified by the additional flux term.

$$S_{A,CFD} = \nabla \cdot \boldsymbol{\Phi}_{A,new} \tag{5-16}$$

Equation (5-17) presents the harmonic average of the molecular diffusion coefficient employed for the molecular diffusion contribution, as recommended by previous studies (Deising et al., 2016; Haroun et al., 2012, 2010a; Yang et al., 2020).

$$D_A = \frac{D_{L,m} D_{G,m}}{D_{G,m} \omega_L + D_{L,m} \omega_G} \tag{5-17}$$

5.3. Model Validation with One-Phase Mass Transfer Resistance, Two-Dimensional System

The interfacial mass transfer model is mathematically identical to the model by Haroun et al. (2010a), which has already been rigorously validated. For validation of the model's new formulation, a two-dimensional system was employed, similar to the system used by Losher et al. (2020). Shown in Figure 5-1, this system was 10 cm long and 1 cm tall. The top and bottom of the system had no shear stress. This condition was applied with a symmetry boundary condition. The top and bottom surfaces inhibited any flux of material for the diffusing species. The top half of the system had air, and the bottom half had water. This condition was enforced during initialization and with the liquid volume fraction at the inlet. The system was assumed to be laminar. A uniform velocity of 1 m/s was imposed on the left surface for both the gas and the liquid, and the flow was cocurrent. A pressure outlet was imposed on the right surface. The pressure at the pressure outlet automatically accounted for the hydrostatic pressure of the gas since the reference density was specified to match the gas density. However, the specified pressure on the bottom half of the exit had to account for the hydrostatic pressure of the liquid, as Equation (5-18) shows. The diffusing species entered with the water at a mass fraction of 0.0001 and desorbed into the air. The air entering the system did not have any of the diffusing species.

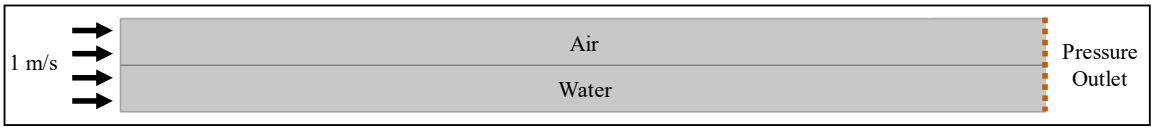

Figure 5-1: Simulated two-dimensional system for validation, with cocurrent flow, a velocity of 1 m/s specified for both phases at the left face, a pressure outlet boundary condition on the right face, air in the top half of the system, and water in the bottom half of the system.

$$P_{e,bottom} = (\rho_L - \rho_G)g\zeta \tag{5-18}$$

As explained by Losher et al. (2020), this system reduces to a simple one-dimensional problem from a Lagrangian perspective, where the distance from the inlet correlates to the contact time between phases. Equation (5-19) shows the analytically derived local mass transfer coefficient at the gas-liquid interface for this system (Welty et al., 2015).

$$k_G = \sqrt{\frac{D_{G,m}}{\pi\, t_{contact}}} \tag{5-19}$$

Equation (3-8) defines the local mass transfer coefficient.

$$N_A \equiv kA_i\Delta c_A \tag{3-8}$$

Equation (5-19) requires a dilute diffusing species, the concentration penetration depth to not reach the top surface of the system, and a constant gas-phase concentration at the gas-liquid interface.

Table 5-1 shows the material properties for the simulated system. This chemical system corresponded to water and air, with dilute ammonia migrating between phases. The simulated Henry's constant was larger than the experimental value of approximately 6.7e-4 to provide easier implementation of the interfacial mass transfer model (Sander, 2015). The molecular diffusion coefficient for the liquid was also set artificially high to eliminate the mass transfer resistance in the liquid. This simplification ensured a constant gas-phase

concentration at the gas-liquid interface, aligning the simulated conditions with the system for Equation (5-19).

	Liquid	Gas
Density (kg/m^3)	998.2	1.195
Dynamic Viscosity (Pa-s)	0.0010	1.84e-5
Surface Tension (N/m)	0.0728	
Molecular Diffusion Coefficient (m^2/s)	1	2.27e-5
Henry's Constant (-)	0.0012	

Table 5-1: Material properties for simulated chemical system with gas-film-controlled mass transfer.

5.3.1. Two-Dimensional System, One-Phase Resistance Mesh Sensitivity Analysis

A mesh sensitivity analysis was performed to ensure the mesh captured all relevant physics. Simcenter STAR-CCM+ created the mesh for the system using the quadrilateral mesher with curvature and proximity refinement. The software also used the prism layer mesher near the gas-liquid interface to provide a finer mesh and also ensure cell faces parallel to the gas-liquid interface, both of which helped capture the concentration gradients. The thickness of each prism layer increased by 5 percent compared to the previous layer's thickness, and the total thickness of the prism layer region in each phase was 0.4 cm. The baseline mesh for this analysis had 40 prism layers in each phase at the gas-liquid interface and a base cell size of 600 μm. The observed parameter was the average gas mass transfer coefficient from 1 cm away from the inlet to 1 cm away from the outlet. This section was chosen to avoid any effects from the boundary conditions. The CFD software calculated the gas mass transfer coefficient using the mass flux at the interface

and Equation (3-8). During this mesh sensitivity analysis, a time step was chosen to ensure the average Courant number in the system and at the interface was less than 0.5 over the course of the simulation. Each time step had 10 iterations. The simulations converged when the average gas mass transfer coefficient changed by less than 0.1 percent over the last 500 time steps.

First, the base cell size was repeatedly halved, and the average gas mass transfer coefficient was observed. Figure 5-2 shows the results of this analysis. The difference in predictions between a base cell size of 300 μm and 150 μm was only 0.04 percent, so a base cell size of 300 μm adequately captured the relevant physics.

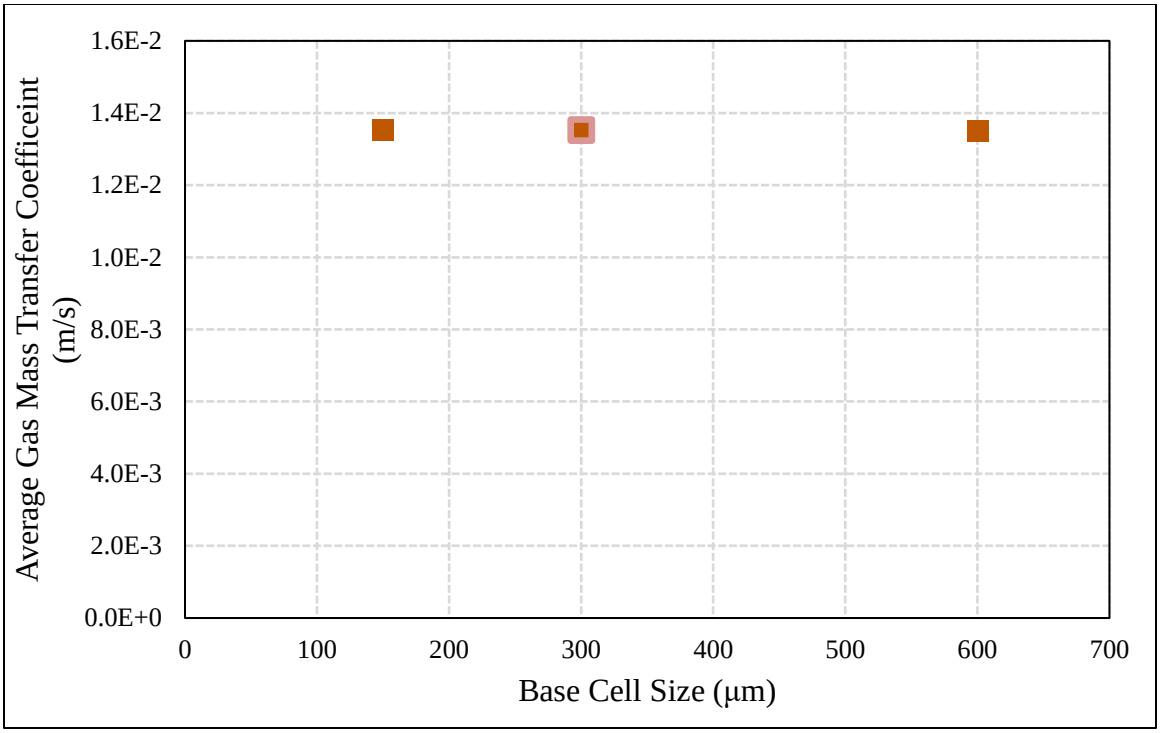

Figure 5-2: Mesh sensitivity study of the base cell size on the average gas mass transfer coefficient for a two-dimensional, gas-film-controlled system, with the final mesh condition outlined.

Figure 5-3 illustrates the impact of the base cell size on the mesh. The base cell size adjusted the width of the prism layer cells (in the direction parallel to the gas-liquid interface) as well as the fineness in all directions for non-prism-layer cells.

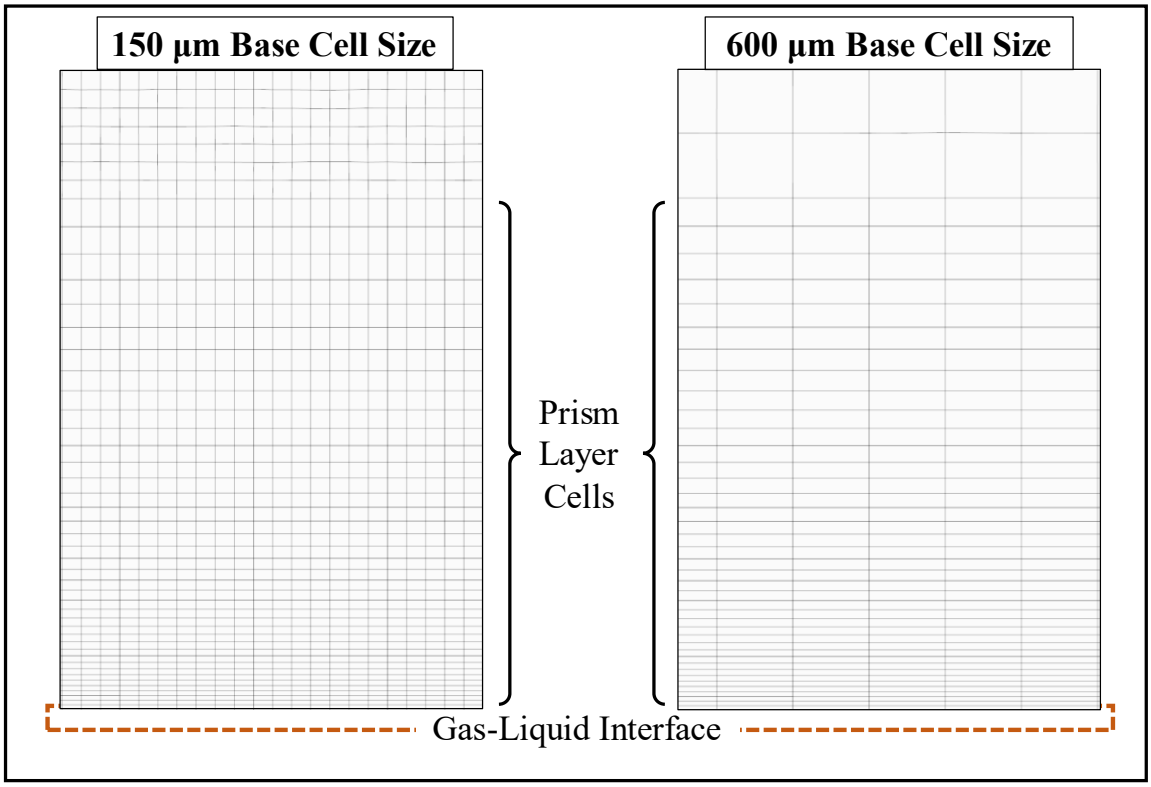

Figure 5-3: Impact of the base cell size on the mesh, as shown for the gas-phase region of the two-dimensional system, with the mesh symmetric across the gas-liquid interface.

After changing the base cell size, the number of prism layers at the interface was modified. Starting with 40 prism layers in each phase at the interface, the number of prism layers was varied, with the number of prism layers doubling between cases. Figure 5-4 displays the results of the mesh sensitivity study. Because the predicted average gas mass

transfer coefficient changed by 0.3 percent between cases with 40 and 80 prism layers per phase, 40 prism layers sufficiently captured the relevant mass transfer phenomena.

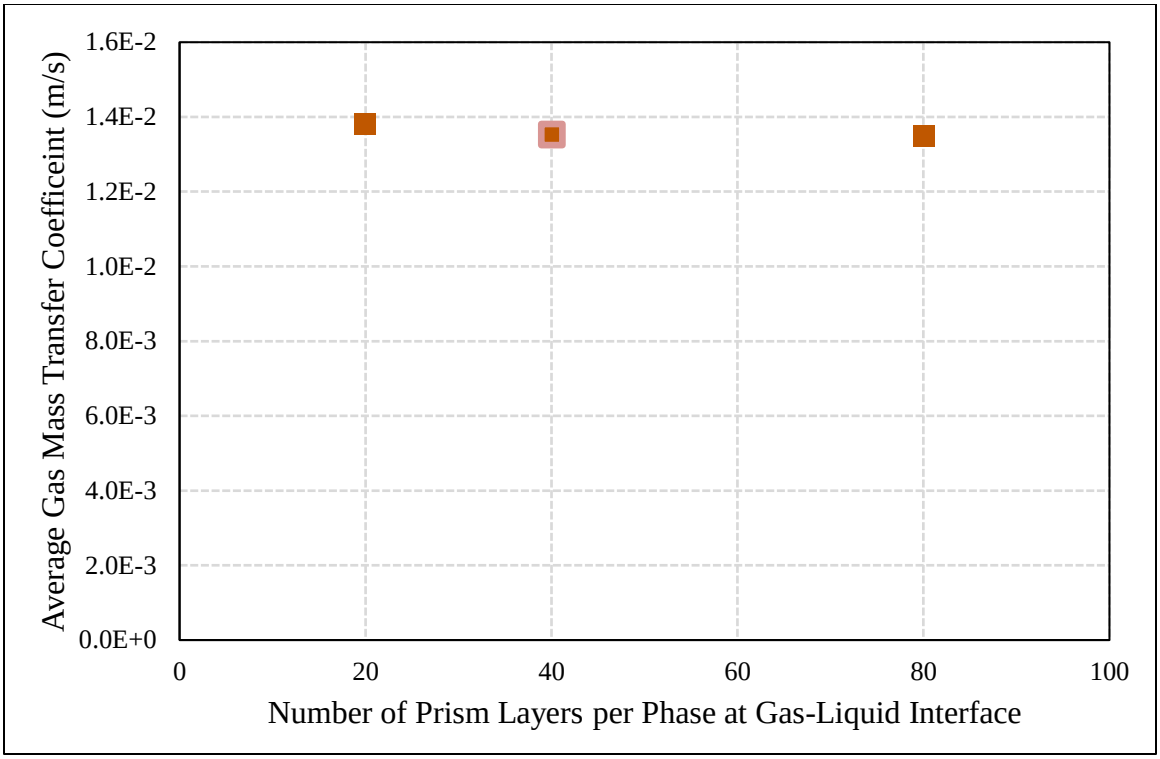

Figure 5-4: Mesh sensitivity study of the number of prism layers per phase on the average gas mass transfer coefficient for a two-dimensional, gas-film-controlled system, with the final mesh condition outlined.

Figure 5-5 demonstrates the impact of the number of prism layers on the mesh. As the number of prism layers increased, the non-prism-layer cells were unchanged, but the fineness of the prism layer cells increased in the direction perpendicular to the gas-liquid interface. The fineness in this direction was key to capture the concentration gradients from the mass transfer process.

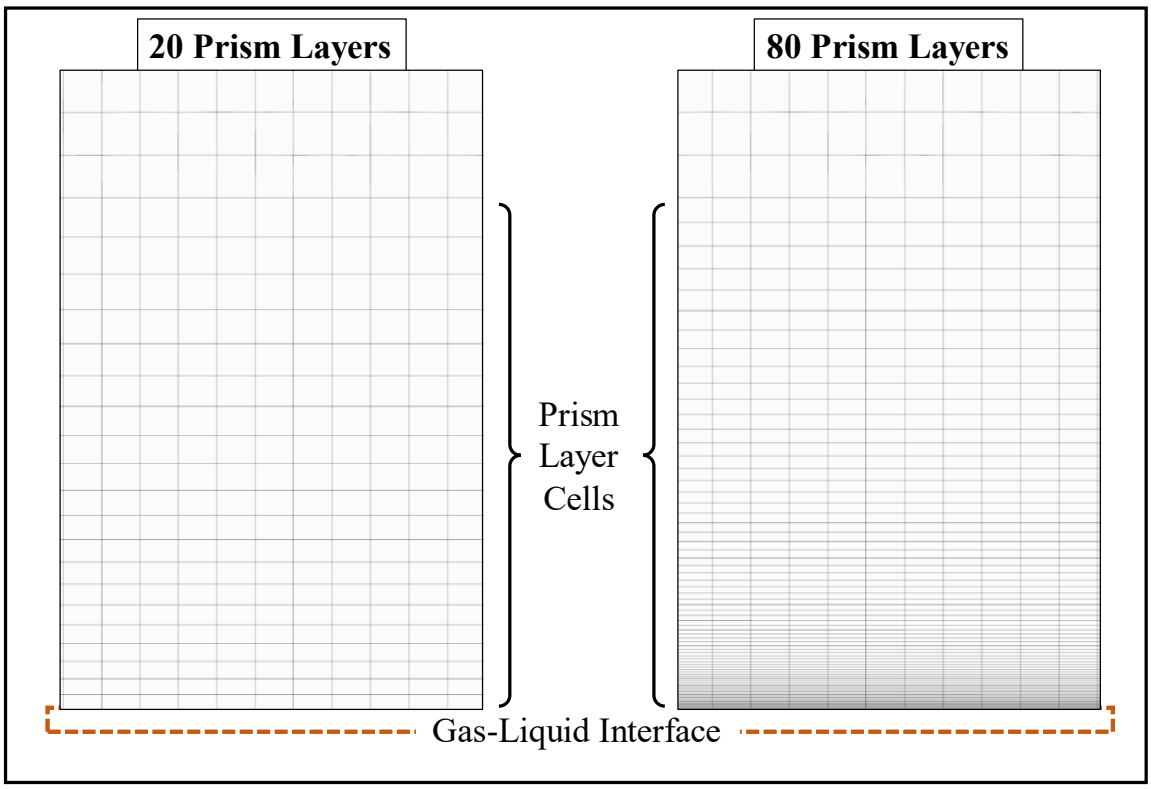

Figure 5-5: Impact of the number of prism layers on the mesh, as shown for the gas-phase region of the two-dimensional system, with the mesh symmetric across the gas-liquid interface.

5.3.2. Two-Dimensional System, One-Phase Resistance Validation

To validate the interfacial mass transfer model, the predicted gas mass transfer coefficients were compared to the analytical solution shown in Equation (5-19). The local gas mass transfer coefficient exhibited excellent agreement with the analytical solution, as the absolute average deviation (AAD) for the CFD predictions was 0.87 percent. Figure 5-6 presents the predicted mass fraction profile in the system. The mass transfer penetration depth did not reach the top surface of the system, meeting the theory's requirements.

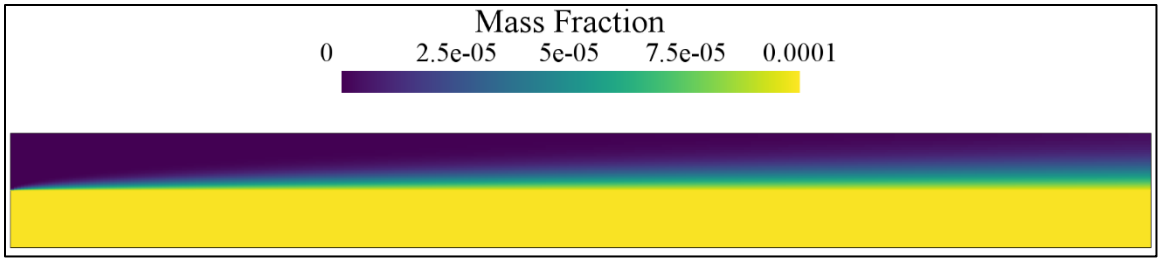

Figure 5-6: Predicted ammonia mass fraction field in two-dimensional system, with the mass fraction penetration depth not reaching the top boundary condition.

Figure 5-7 shows the predicted local mass transfer coefficient for the gas phase over the entire two-dimensional system. The gas mass transfer coefficient near the inlet was large. This trend stemmed from large mass transfer gradients, as the gas entering the system had no ammonia present. Figure 5-6 shows the large mass fraction gradient at the gas-liquid interface near the inlet. This large gradient provided a significant driving force for diffusion and produced a large local mass transfer coefficient. As the ammonia had time to diffuse into the gas-phase, the mass transfer gradient became smoother. This smaller gradient, shown near the exit in Figure 5-6, provided a smaller driving force for the diffusion of the species. The reduction in diffusion decreased the local mass transfer coefficient when moving away from inlet, producing the trend in Figure 5-7. According to Equation (5-19), if the two fluids had an infinite amount of time to interact and exchange ammonia, the local mass transfer coefficient would approach zero, due to a negligible gradient and therefore a vanishing driving force for diffusion.

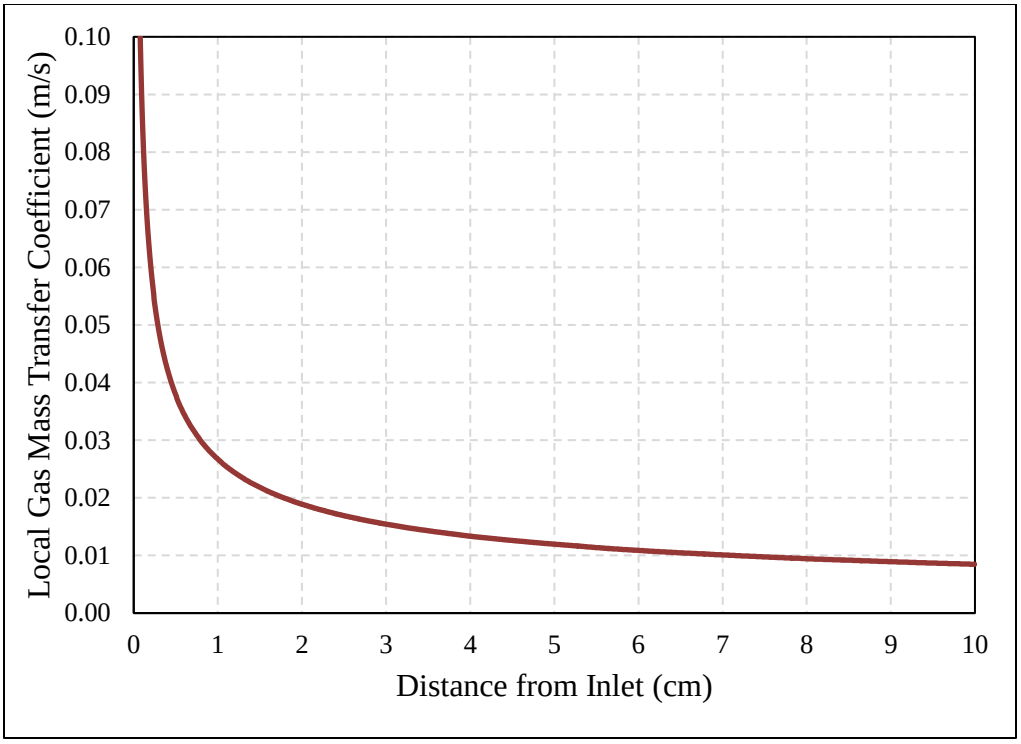

Figure 5-7: Local gas mass transfer coefficient predicted by CFD versus the distance from the inlet.

5.4. MODEL VALIDATION WITH TWO-PHASE MASS TRANSFER RESISTANCE, TWO-DIMENSIONAL SYSTEM

The interfacial mass transfer model was tested on a system with mass transfer resistances in both phases. To ensure resistance in the liquid phase, the liquid molecular diffusion coefficient was set to a value consistent for ammonia in water. All other physical properties as well as the system setup matched the conditions in the gas-phase-controlled system. Table 5-2 presents the material properties for the simulated system having mass transfer resistance in both phases. In parallel with the gas-phase-controlled case, the two-

dimensional simulations converged when the average interfacial mass flux from 1 cm away from the inlet to 1 cm away from the outlet changed by less than 0.1 percent over the last 500 time steps.

	Liquid	Gas
Density (kg/m³)	998.2	1.195
Dynamic Viscosity (Pa-s)	0.0010	1.84e-5
Surface Tension (N/m)	0.0728	
Molecular Diffusion Coefficient (m²/s)	1.51×10^{-9}	2.27e-5
Henry's Constant (-)	0.0012	

Table 5-2: Material properties for the simulated chemical system with mass transfer resistance in both phases.

5.4.1. Two-Dimensional System, Two-Phase Resistance Mesh Sensitivity Analysis

Due to the change in physical properties from the gas-film-controlled system, the previous mesh might not capture the relevant transport phenomena sufficiently. To ensure a sufficient mesh, a second mesh sensitivity study was performed. First, the base mesh size was repeatedly halved, and the average gas mass transfer coefficient in the middle 8 cm was observed. Figure 5-8 shows the results of this analysis. Between a base cell size of 75 μm and 40 μm, the average gas mass transfer coefficient only changed by 0.47 percent. From these trends, a base cell size of 75 μm sufficient captured the relevant physics in the system.

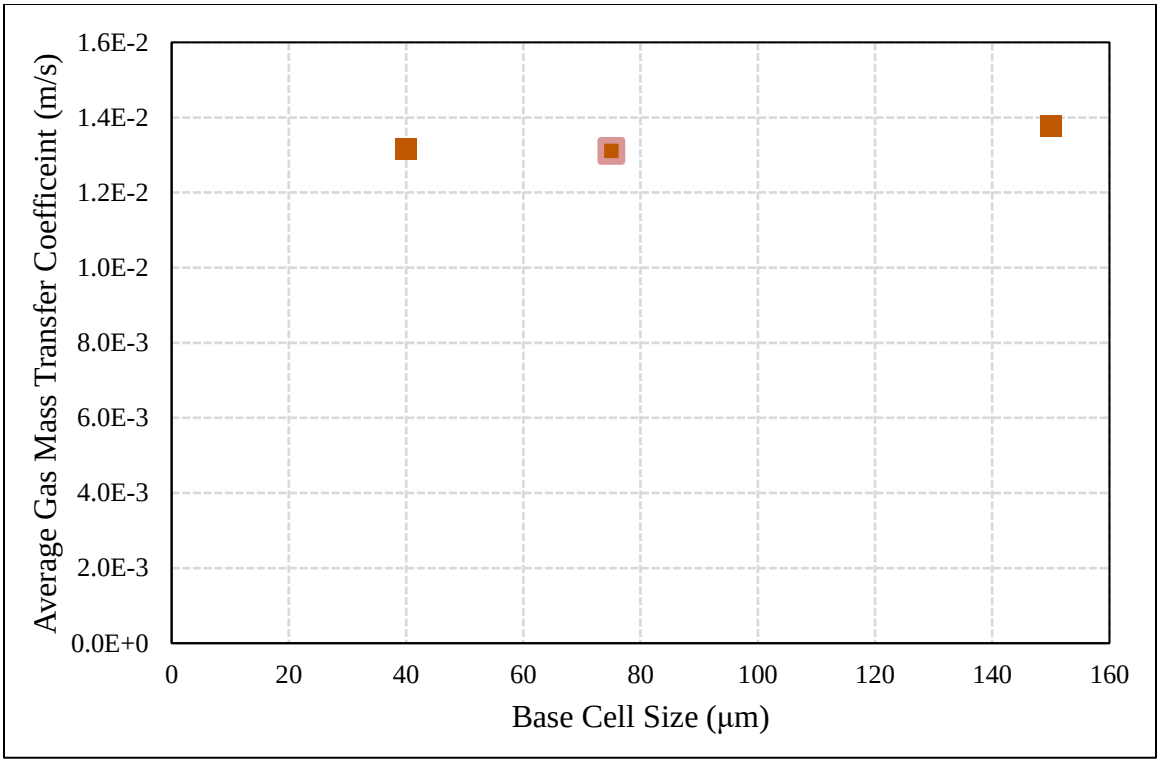

Figure 5-8: Mesh sensitivity study of the base cell size on the average gas mass transfer coefficient for a two-dimensional system with mass transfer resistance in both phases, with the final mesh condition outlined.

Next, the number of prism layers at the interface was repeatedly increased by 50 percent, and the average gas mass transfer coefficient in the middle 8 cm was observed. Figure 5-9 presents the predicted gas mass transfer coefficients. The difference in predictions between the 60 and 90 prism layer cases was 0.46 percent. The number of prism layers was increased to 135, and the average gas mass transfer coefficient only changed by 0.21 percent. This small change in predictions between the final three cases suggested that 60 prism layers in each phase at the gas-liquid interface were sufficient.

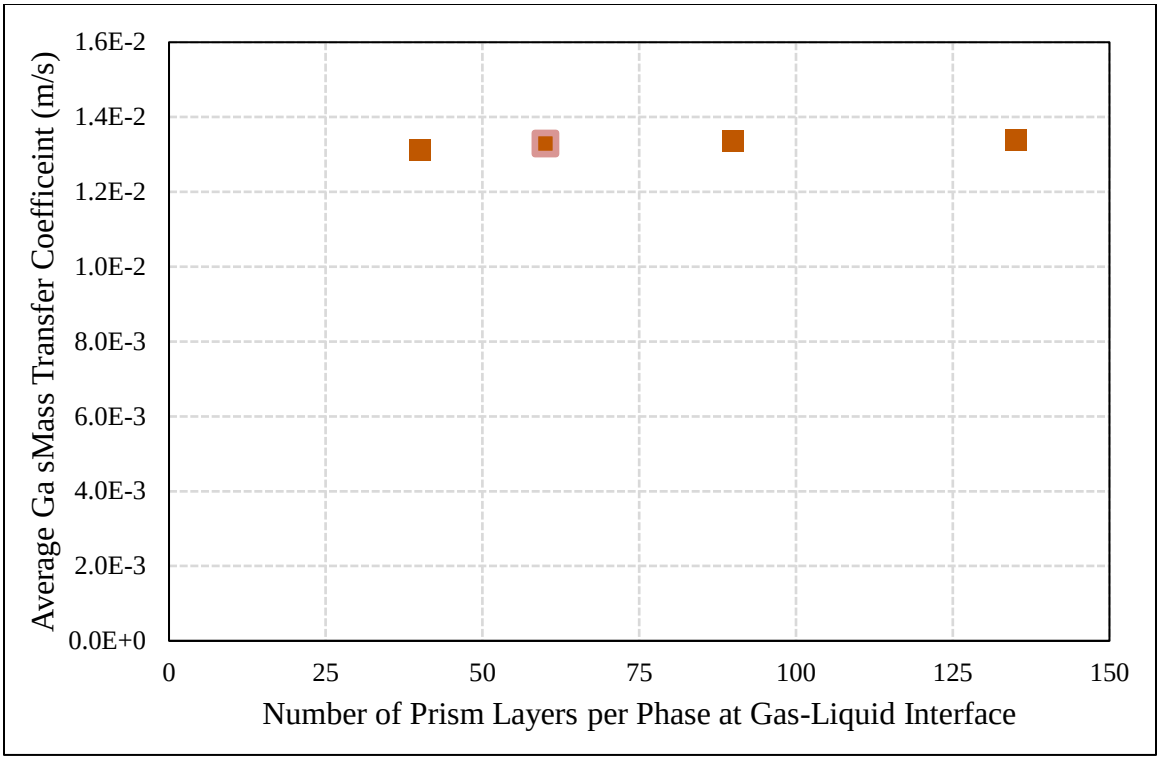

Figure 5-9: Mesh sensitivity study of the number of prism layers per phase on the average gas mass transfer coefficient for a two-dimensional system with mass transfer resistance in both phases, with the final mesh condition outlined.

Overall, a significantly finer mesh was required for the case with mass transfer resistances in both phases than for the gas-film-controlled case. The sharp concentration gradient in the liquid phase required this finer mesh. As Equation (5-20) shows, to satisfy mass conservation across the interface, the interfacial mass flux in the gas and the interfacial mass flux in the liquid must be equal in magnitude. Because the molecular diffusion coefficient in the liquid was multiple orders of magnitude lower than the corresponding value in the gas, as Table 5-2 indicates, a much steeper gradient was necessary in the liquid to produce the same mass transfer. This steeper gradient provided

additional driving force for the mass transfer to overcome the smaller molecular diffusion coefficient. For future studies with this two-dimensional system, the mesh for the case with mass transfer resistances in both phases is recommended, as the mesh captured the relevant physics in both the gas and liquid phases and the computational expense for the two-dimensional system was relatively low.

$$\frac{N_{A,i}}{A_i} = -D_{L,m}\frac{\partial c_{A,L}}{\partial n}\bigg|_{interface} = -D_{G,m}\frac{\partial c_{A,G}}{\partial n}\bigg|_{interface} \tag{5-20}$$

5.4.2. Two-Dimensional System, Two-Phase Resistance Validation

The predicted gas mass transfer coefficients were compared to the analytical solution shown in Equation (5-19). Although both phases had mass transfer resistances, the gas-phase mass fraction of ammonia at the interface was only about 10 percent lower than for the gas-film-controlled case. Additionally, the mass fraction showed little variation as the distance from the inlet increased, as Figure 5-10 demonstrates. Figure 5-11 plots the predicted gas mass transfer coefficients through the system. The predicted values showed excellent agreement with the analytical solution, having an AAD of 0.68 percent.

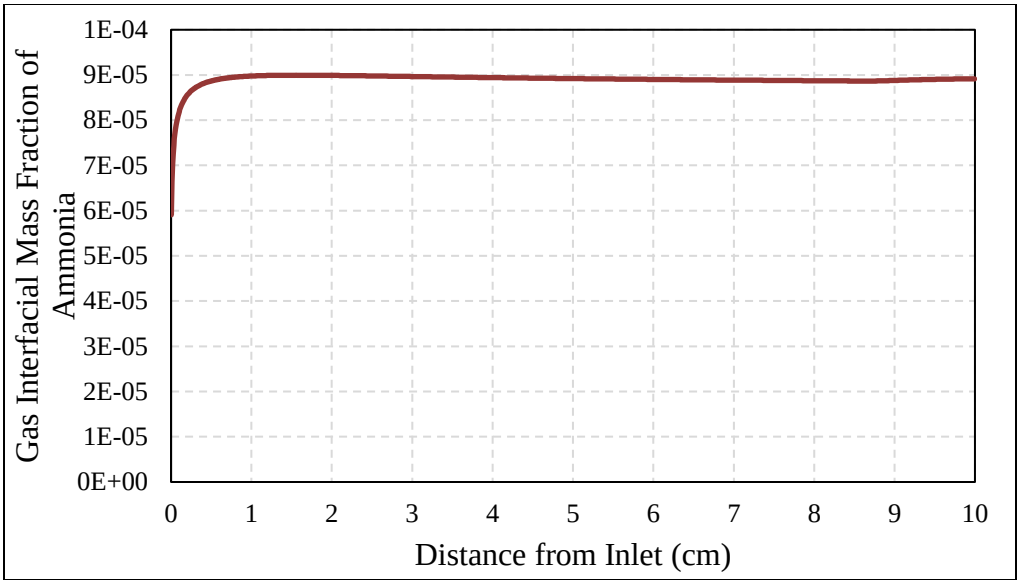

Figure 5-10: Ammonia gas mass fraction at the interface for the two-dimensional system with mass transfer resistances in both phases.

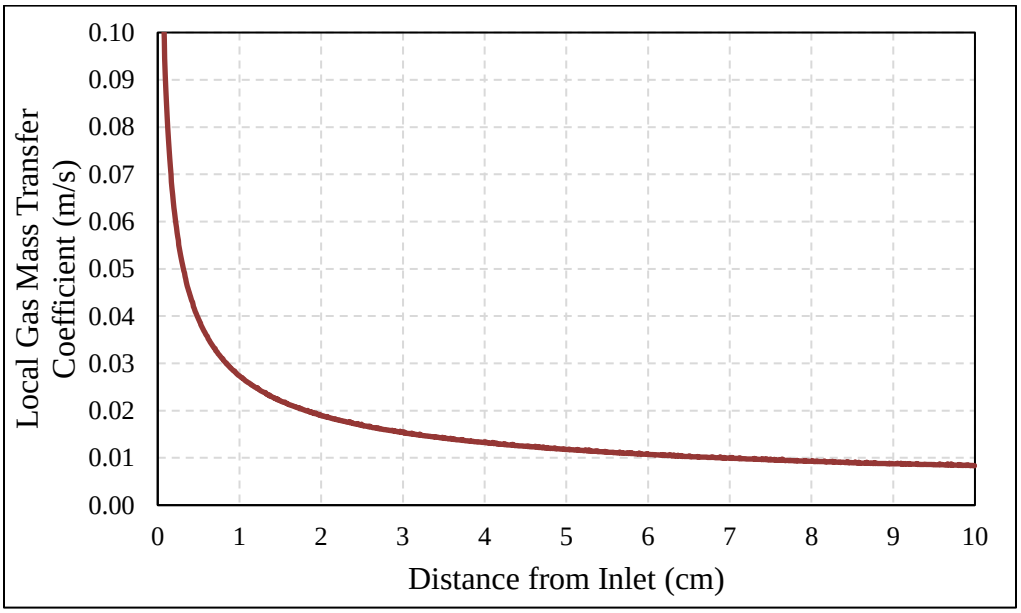

Figure 5-11: Local gas mass transfer coefficient versus the distance from the inlet.

Additional cases were simulated with Henry's constants not equal to 0.0012, but limitations in Simcenter STAR-CCM+ inhibited convergence. For the system simulated, a Henry's constant of 0.0012 corresponded to a continuous mass fraction across the interface, causing the magnitude of $\mathbf{\Phi}_{\mathrm{A,new}}$ to be small. For Henry's constants above or below 0.0012, the magnitude of $\mathbf{\Phi}_{\mathrm{A,new}}$ increased, and accurate gradient predictions were essential. The gradients in the software's field functions are computed at the center of a cell rather than the face between cells. This difference in location meant that slight differences in the computed gradients between two cells could occur, as Figure 5-12 illustrates. At the gas-liquid interface where the liquid volume fraction and possibly the diffusing species have sharp gradients, even a miniscule percent discrepancy between the two cells can result in large differences in fluxes predicted by the model. The difference in computed flux terms caused a lack of mass conservation and a lack of convergence. Nevertheless, in the simulations, a jump in concentration of multiple orders of magnitude was still enforced, as shown in Figure 5-13. Additionally, a discontinuity in the mole fractions at the interface occurred. For the air-water system, the interfacial ratio of the gas mole fraction to liquid mole fraction for ammonia was 1.6.

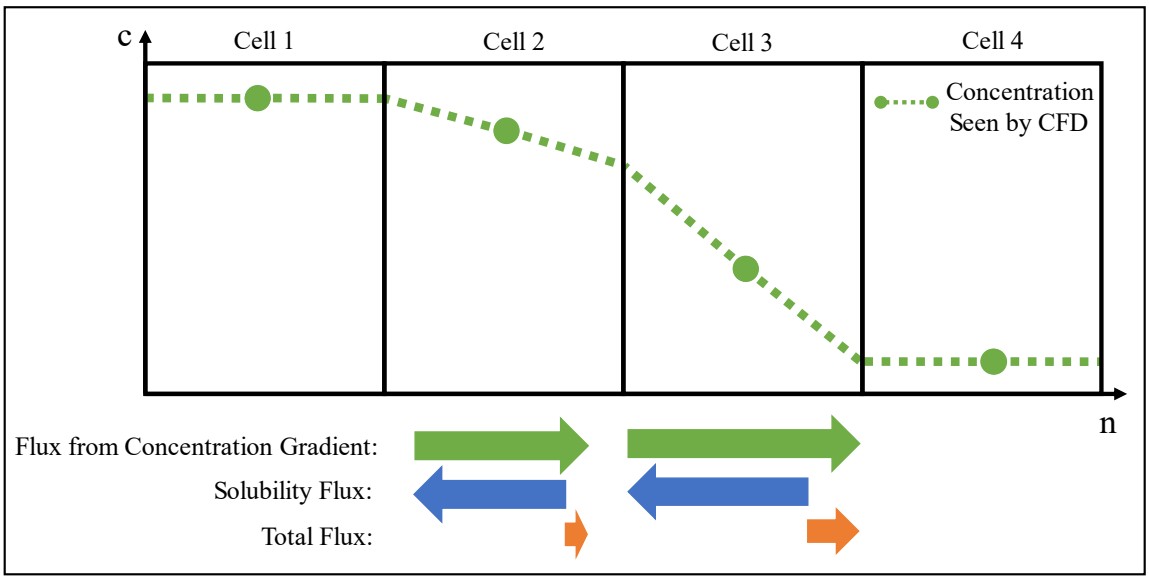

Figure 5-12: Mass not conserved due to flux calculations at computational cell centers rather than cell faces.

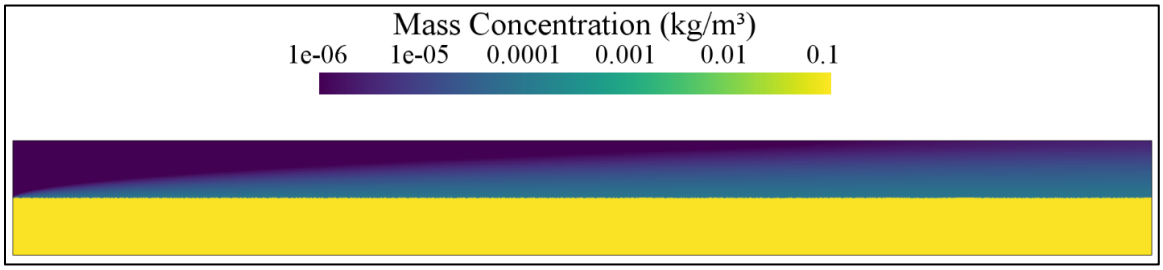

Figure 5-13: Predicted ammonia mass concentration in the two-dimensional system, with a jump in concentration of multiple orders of magnitude.

5.5. Interfacial Mass Transfer Model in Turbulent Conditions

Turbulence is present in many systems where interfacial mass transfer occurs. To obtain accurate predictions for these systems, both turbulence-aided mass transfer and

interfacial mass transfer processes must be predicted. For example, the gas-phase flow through structured packings is often turbulent, but interfacial mass transfer also occurs between the gas and liquid in the system.

Multiple alternatives exist to account for turbulence in CFD simulations. Direct numerical simulation is the most straightforward approach, as Equation (5-14) can be directly applied. However, this methodology is extremely computationally expensive, which limits the applicability of the methodology for industrial-scale problems. To model hydrodynamic turbulent effects, a Reynolds-averaged Navier-Stokes (RANS) approach is common. This approach splits variables into a time-averaged quantity and a fluctuating quantity, the latter of which results from turbulent eddies. A similar approach can be conducted for the concentration, as Equation (5-21) demonstrates.

$$c = \langle c \rangle + c' \tag{5-21}$$

In this equation, $\langle c \rangle$ represents the time-averaged quantity, while c' is the fluctuating quantity due to turbulence. Implementing the time-averaging approach to the convection-diffusion equation and employing a gradient-diffusion hypothesis results in Equation (5-22) (Fox, 2003; Pope, 2000).

$$\frac{\partial \langle c_A \rangle}{\partial t} + \nabla \cdot (\langle c_A \rangle \langle \mathbf{v} \rangle) = \nabla \cdot \left(\left(D_{A,m} + D_T \right) \nabla \langle c_A \rangle \right) + \langle S_A \rangle \tag{5-22}$$

This equation is identical to the convection-diffusion equation in Equation (5-2), except time-averaged quantities are employed and the molecular diffusion coefficient is

supplemented with a turbulent diffusion coefficient term. Using this equation as the starting point for the interfacial mass transfer model produces a similar formulation, except time-averaged quantities must be used and the diffusion coefficient for each phase must include the turbulent diffusion coefficient. The final mass transfer model for turbulent systems is shown in Equation (5-23).

$$\frac{\partial \rho_{mix}\langle x_A\rangle}{\partial t} + \nabla\cdot(\rho_{mix}\langle x_A\rangle\langle \mathbf{v}\rangle) = \nabla\cdot(\rho_{mix}D_{effective}\nabla\langle x_A\rangle) + \nabla\cdot\left(\langle x_A\rangle D_{effective}\left((\rho_L-\rho_G)-\frac{\rho_{mix}(1-He_A)}{\omega_L+He_A\omega_G}\right)\nabla\omega_L\right)+\langle S_A\rangle \tag{5-23}$$

In this equation, the diffusion coefficient is defined according to Equation (5-24), where a harmonic average was used, in parallel with Equation (5-17).

$$D_{effective} = \frac{(D_{L,m}+D_{L,T})(D_{G,m}+D_{G,T})}{(D_{G,m}+D_{G,T})\omega_L+(D_{L,m}+D_{L,T})\omega_G} \tag{5-24}$$

A constant turbulent Schmidt number predicted the turbulent diffusion coefficient for each phase, as Equations (5-25) and (5-26) show. This approach forms a direct analogy to the hydrodynamic turbulence predictions and has shown promise in previous studies (Wang et al., 2020; Zhang et al., 2013).

$$Sc_{L,T} = \frac{\nu_{L,T}}{D_{L,T}} = \frac{\mu_T}{\rho_L D_{L,T}} = 0.7 \tag{5-25}$$

$$Sc_{G,T} = \frac{\nu_{G,T}}{D_{G,T}} = \frac{\mu_T}{\rho_G D_{G,T}} = 0.7 \tag{5-26}$$

The lag elliptic-blending k-ε turbulence model with all-y+ wall treatment accounted for the effects of turbulence on the hydrodynamics. This model predicts the turbulent dynamic viscosity, which supplemented the molecular dynamic viscosity as Equation (5-27) shows.

$$\mu_{effective} = \mu_m + \mu_T \tag{5-27}$$

5.5.1. Application of Interfacial Mass Transfer Model to Turbulent Structured Packing System

To test the interfacial mass transfer methodology in turbulent conditions and in a three-dimensional system, ammonia absorption from air into water inside Mellapak 250Y structured packing was simulated. Table 5-2 presents the material properties for this system, and the contact angle was 0°, following the findings of Basden (2014). The simulated packing had a 2 mm crimp radius and no gap between packing sheets, reflecting the typical geometry of the packing. The REU for this packing was built by first creating a REU with sharp packing crimps in SOLIDWORKS 2019. This REU had a specific packing area of 236 m^2/m^3 channel inclination angle of 45°, and a channel opening angle of 90.7°. The crimps were rounded with the fillet feature in SOLIDWORKS 2019, which caused a gap to form between packing sheets, as Figure 5-14 shows. The packing sheets were then brought back together to ensure no gap existed between the packing sheets.

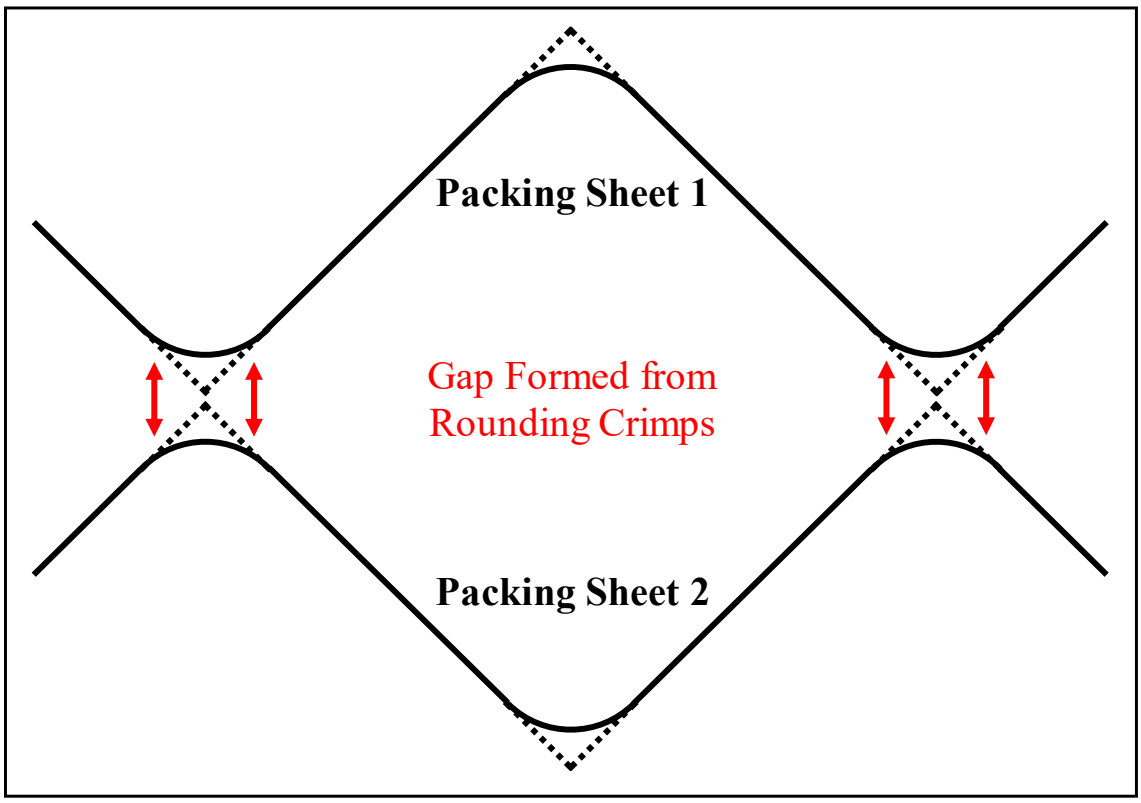

Figure 5-14: Gap formation between structured packing sheets caused by rounding packing crimps.

As proposed by Basden (2014) and later used by Singh et al. (2020), a stacked REU approach was utilized. As Figure 5-15 depicts, three REUs composed the center of the system, and entrance regions were included above and below the REUs to develop the flow. The entrance regions were both 30 mm tall in the vertical direction, excluding the 5-mm-long gas inlet regions on the bottom entrance region. The left and right sides of the REUs had periodic boundary conditions, while the front and back of the REUs had wall conditions. In the top entrance region, liquid was supplied through the opening indicated in Figure 5-16. Except for the liquid inlet, the front and back of the entrance regions were

walls. The gas and liquid outlets, indicated in Figure 5-16 and Figure 5-17, respectively, were pressure outlet conditions, and a pressure drop of 20 Pa was assigned between the gas and liquid outlets. On this bottom boundary condition, the liquid could exit the system, but gas could also enter the system through backflow, driven by the pressure difference through the system. Gas also entered through the five gas inlets shown in Figure 5-17, where the velocity was 10 m/s. For gas entering the structured packing system at the bottom of the system, the ammonia mass fraction was 0.0001. For the liquid entering at the top of the system, no ammonia was present, and the specified speed at the liquid inlet was 0.044 m/s. In the event of backflow at the gas outlet, the fluid was specified as gas with no ammonia present. The time step in the simulations was chosen to keep the average Courant number at the interface below 0.5 and the average Courant number in the entire system below 0.8. Each time step had 4 iterations. The gas and liquid flow rates through the structured packing system were measured at the top of the target REU, and the pressure drop was measured across the target REU. The target REU was the central REU, as Figure 5-15 shows.

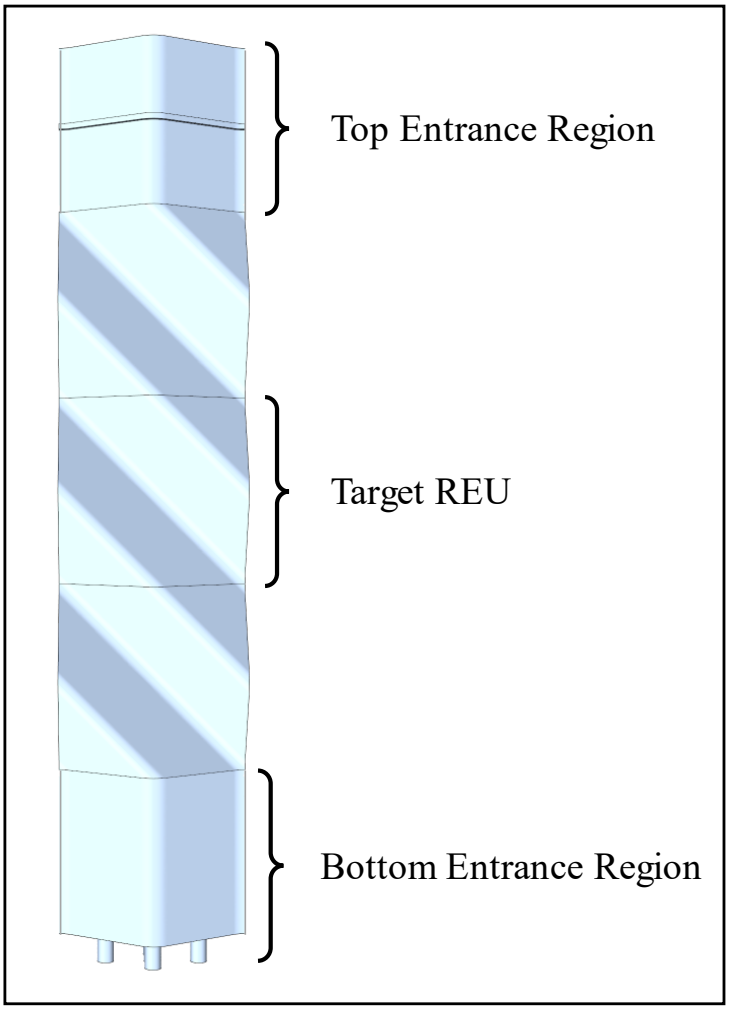

Figure 5-15: Structured packing system simulated, consisting of three representative elementary units (REUs) and entrance regions at both the top and bottom of the system to develop the flow.

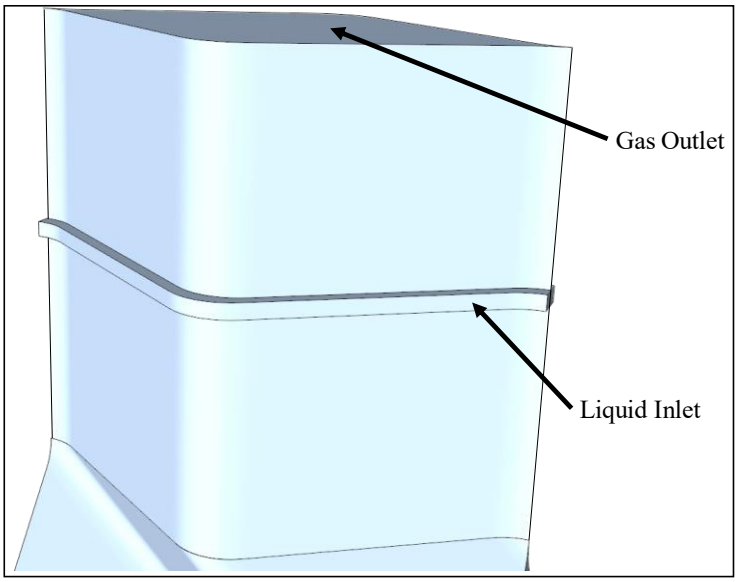

Figure 5-16: Top entrance region of structured packing system, having a liquid inlet for each packing sheet and a gas outlet.

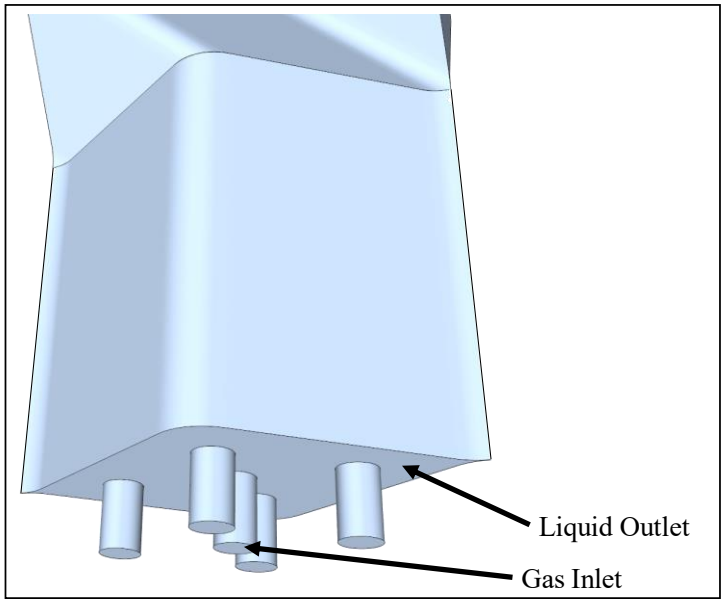

Figure 5-17: Bottom entrance region of structured packing system, having five gas inlets and one liquid outlet.

Both hydrodynamic and mass transfer performance metrics were observed during the structured packing simulations. The performance metrics for the hydrodynamics were the pressure drop across the central REU in the system, the F-factor (defined in Equation (3-5)) for the gas flow rate, and the liquid flow rate. For the mass transfer performance, the gas overall number of transfer units (NTU_{OG}) for the central REU was observed. The NTU_{OG} was calculated according to Equation (5-28). A mixing-cup average was used for the mass fractions to better describe the chemical makeup of the flows entering and exiting the REU. Fluid with $\omega_L > 0.5$ was deemed liquid, while fluid with $\omega_G > 0.5$ was deemed gas. The time-averaged NTU_{OG} over the last 4,000 iterations provided a representative value of the variable, smoothing out any temporary fluctuations. When this average NTU_{OG} changed by less than 1 percent over the last 200 iterations and at least one second of flow was simulated, the simulation converged.

$$F_G = v_{G,s}\sqrt{\rho_G} \tag{3-5}$$

$$NTU_{OG} = \frac{\ln\left(\frac{a-1}{a}\frac{x_{G,bottom} - \frac{\rho_L}{\rho_G}He_A x_{L,top}}{x_{G,top} - \frac{\rho_L}{\rho_G}He_A x_{L,top}} + \frac{1}{a}\right)}{(a-1)/a} \tag{5-28}$$

In Equation (5-28), a is the absorption factor, which Equation (5-29) defines.

$$a = \frac{\dot{M}_L}{\left(He_A \frac{\rho_L}{\rho_G}\right)\dot{M}_G} \tag{5-29}$$

5.5.2. Mesh Sensitivity Analysis for Structured Packing System

To ensure the mesh captured all relevant physics, a mesh sensitivity analysis was performed. The baseline mesh had a base cell size of 1.35 mm. When moving away from the structured packing surface, each prism layer's thickness increased by 5 percent compared to the previous cell's thickness. The baseline mesh had 25 prism layers at the packing surface, and the total thickness of the prism layers was 0.6 mm. First, the base cell size was repeatedly decreased by a third to determine the predictions' dependence on the mesh parameter. Figure 5-18 presents the gas-phase hydrodynamic results from the base cell size mesh sensitivity analysis, considering both the F-factor and the pressure drop. For the liquid-phase hydrodynamics, Figure 5-19 plots the liquid flow rate versus the base cell size. All three hydrodynamic values were relatively constant for a base cell size of less than 0.6 mm. For the mass transfer results, Figure 5-20 shows the NTU_{OG} as the base cell size varied. As with the hydrodynamic performance, the mass transfer performance showed little change for cases with a base cell size of at most 0.6 mm. Based on the trends in Figure 5-18, Figure 5-19, and Figure 5-20, a base cell size of 0.6 mm was used.

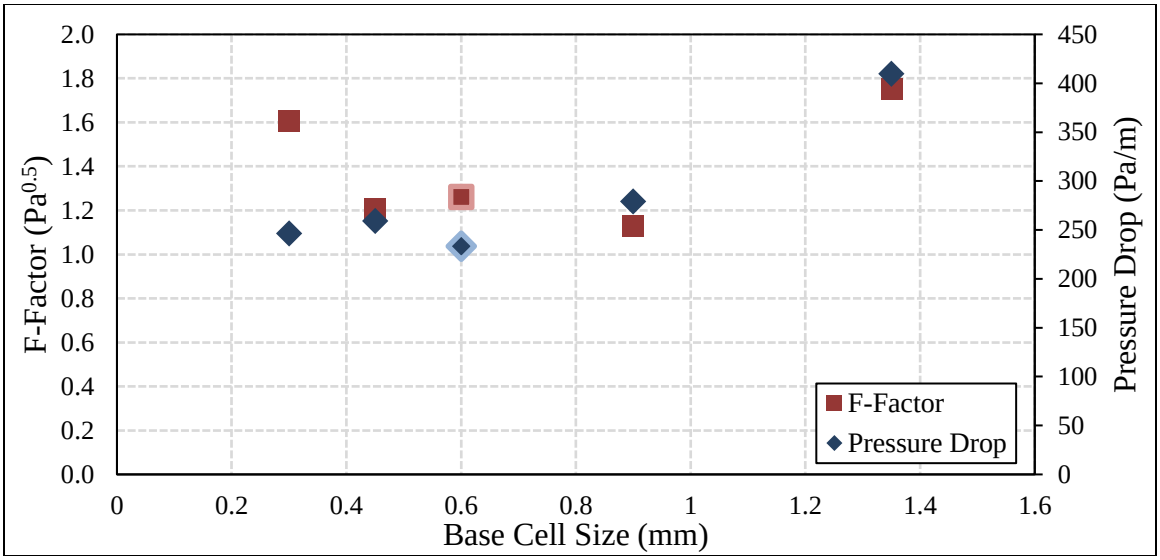

Figure 5-18: Gas-phase hydrodynamic predictions from the base cell size mesh sensitivity analysis for the structured packing system, with the final mesh conditions outlined.

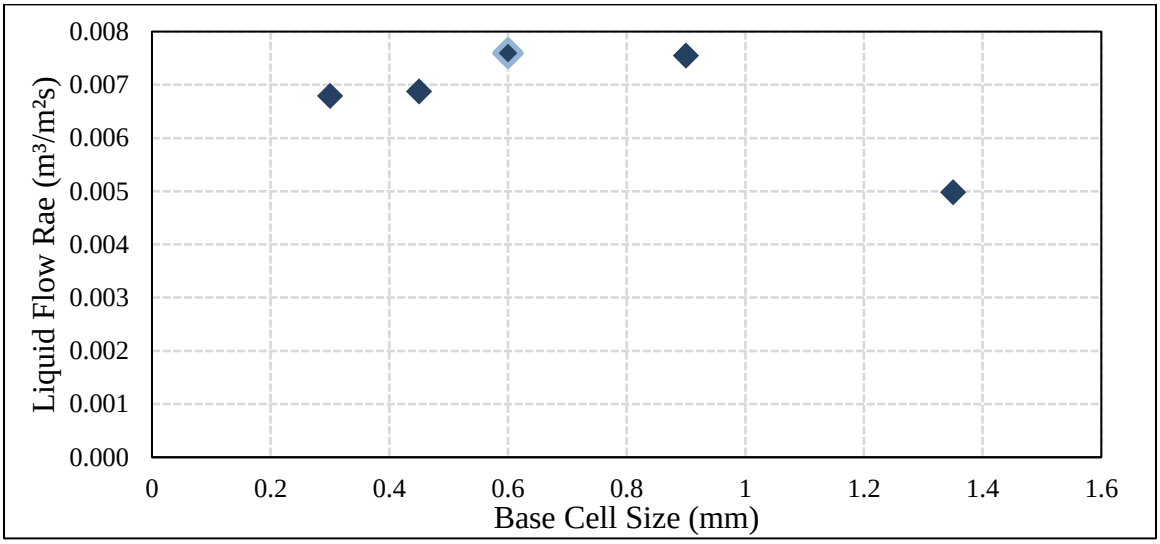

Figure 5-19: Liquid-phase hydrodynamic predictions from the base cell size mesh sensitivity analysis for the structured packing system, with the final mesh conditions outlined.

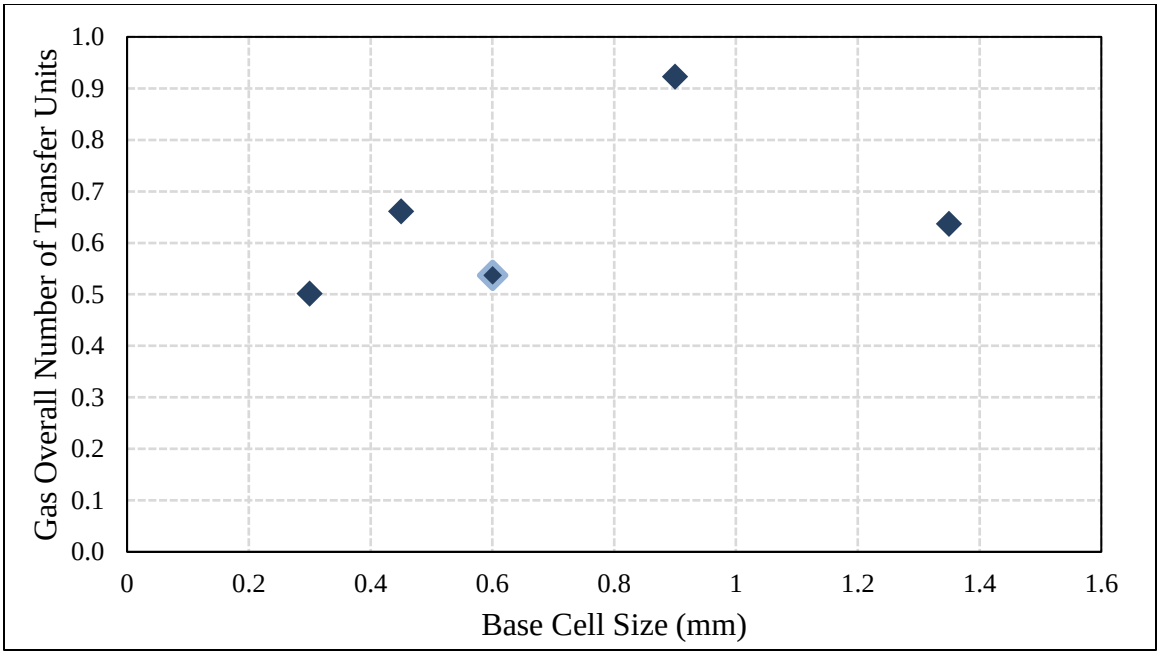

Figure 5-20: Mass transfer predictions from the base cell size mesh sensitivity analysis for the structured packing system, with the final mesh conditions outlined.

Due to the importance of the phenomena at the gas-liquid interface, where sharp concentration gradients can occur, an additional mesh sensitivity study was conducted for the number of prism layers. The number of prism layers was varied, and both the hydrodynamic and the mass transfer performances were observed. Figure 5-21 presents the gas-phase hydrodynamic results from the analysis, plotting both the F-factor and the pressure drop. The predicted gas hydrodynamic performance showed little change for at least 60 prism layers. Figure 5-22 plots the predicted liquid flow rate as the number of prism layers increased, and Figure 5-23 shows the mass transfer predictions from the analysis. From the trends in Figure 5-21, Figure 5-22, and Figure 5-23, 60 prism layers were used in subsequent analysis. For future studies with this multiphase structured

packing system, a mesh with at least 60 prism layers and a base cell size of at most 0.6 mm is recommended.

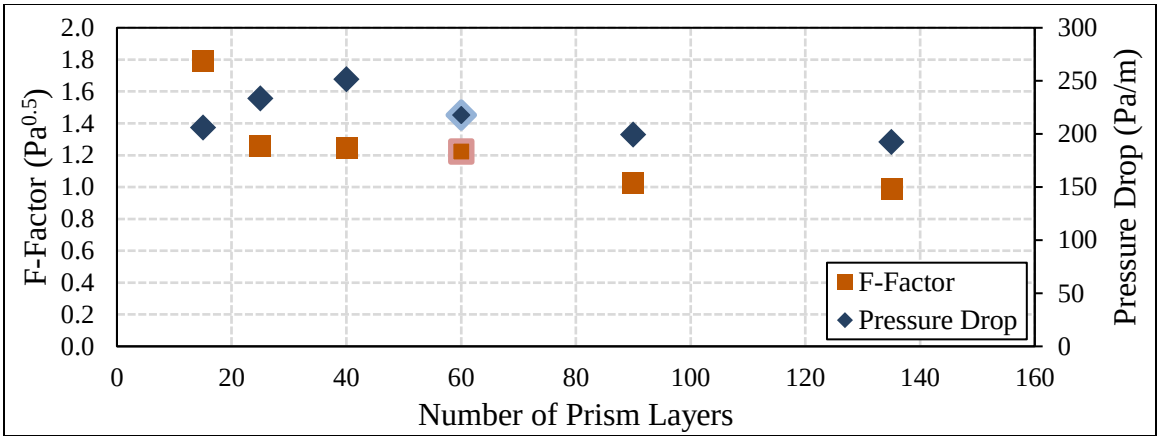

Figure 5-21: Gas-phase hydrodynamic predictions from the mesh sensitivity analysis for the number of prism layers, with the final mesh conditions for the structured packing system outlined.

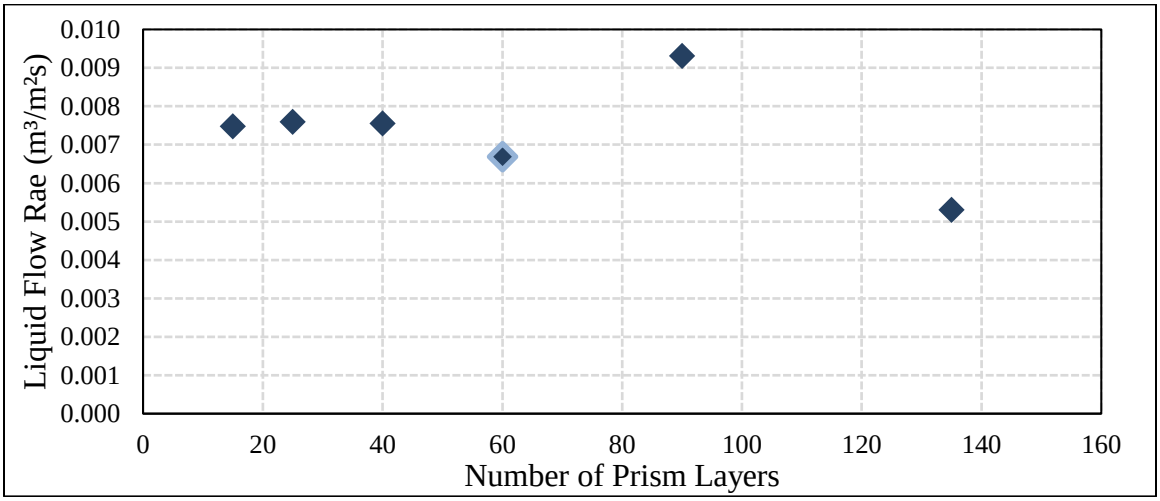

Figure 5-22: Liquid-phase hydrodynamic predictions from the mesh sensitivity analysis for the number of prism layers, with the final mesh conditions for the structured packing system outlined.

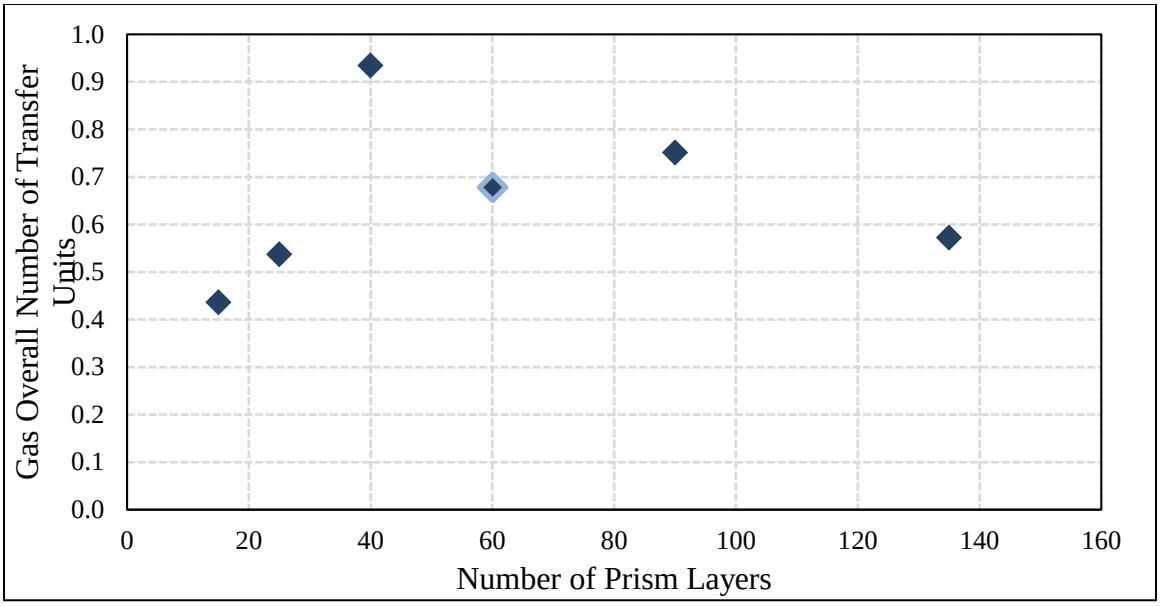

Figure 5-23: Mass transfer predictions from the mesh sensitivity analysis for the number of prism layers, with the final mesh conditions for the structured packing system outlined.

5.5.3. Simulation Results for Structured Packing System

Figure 5-24 shows the liquid volume fraction through the system on the plane vertically bisecting the REUs. The simulations predicted the liquid to reside near the packing surface, especially near the contact point between packing sheets. The trends for the liquid volume fraction in the bottom REU and the middle REU were similar, suggesting the entrance region near the top of the system sufficiently developed the liquid film.

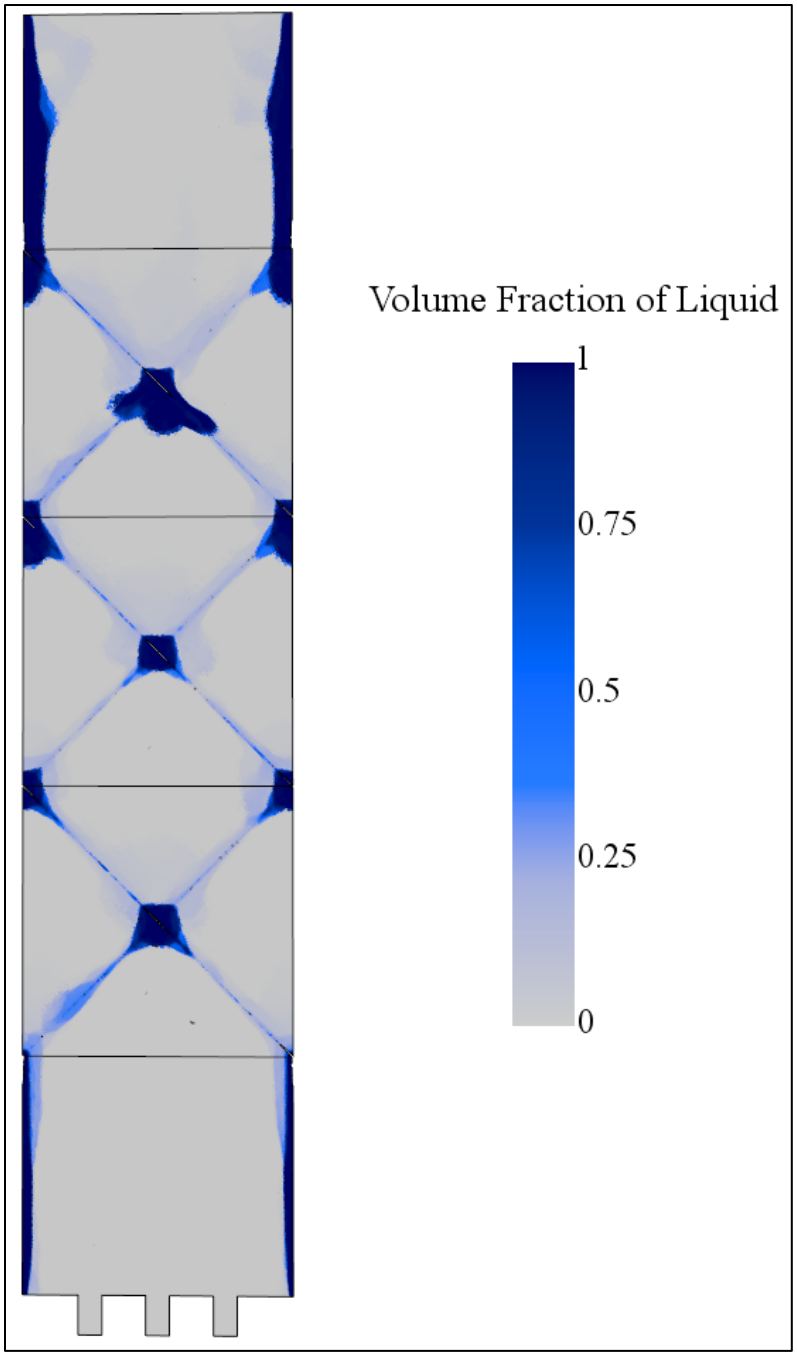

Figure 5-24: Predicted liquid volume fraction in the structured packing system on the plane between packing sheets.

Figure 5-25 shows the ammonia mass fraction profile in the structured packing system. Mass fraction gradients are present near the gas-liquid interface, which served as the driving force for the diffusion of ammonia from the gas into the liquid. The mass fraction of ammonia in the gas phase was larger near the bottom than the top, which resulted from the absorption of ammonia from the gas into the liquid.

As demonstrated for the two-dimensional system, a jump in concentration of three orders of magnitude was predicted at the gas-liquid interface. Figure 5-26 shows the concentration profile through the system, which confirms the ability of the interfacial mass transfer model with the turbulence modification to handle large jumps in concentration at the gas-liquid interface.

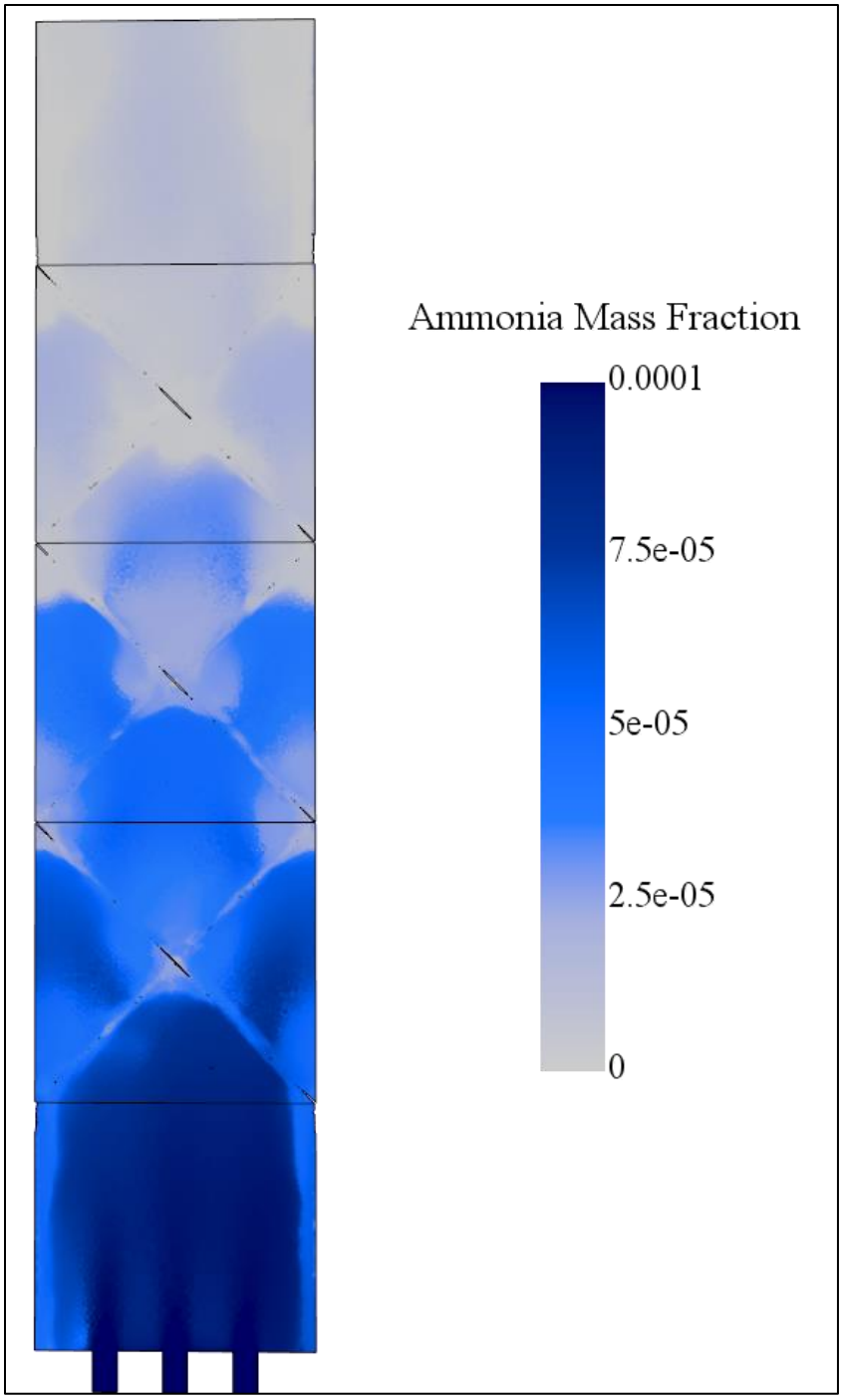

Figure 5-25: Predicted ammonia mass fraction profile in the structured packing system on the plane between packing sheets.

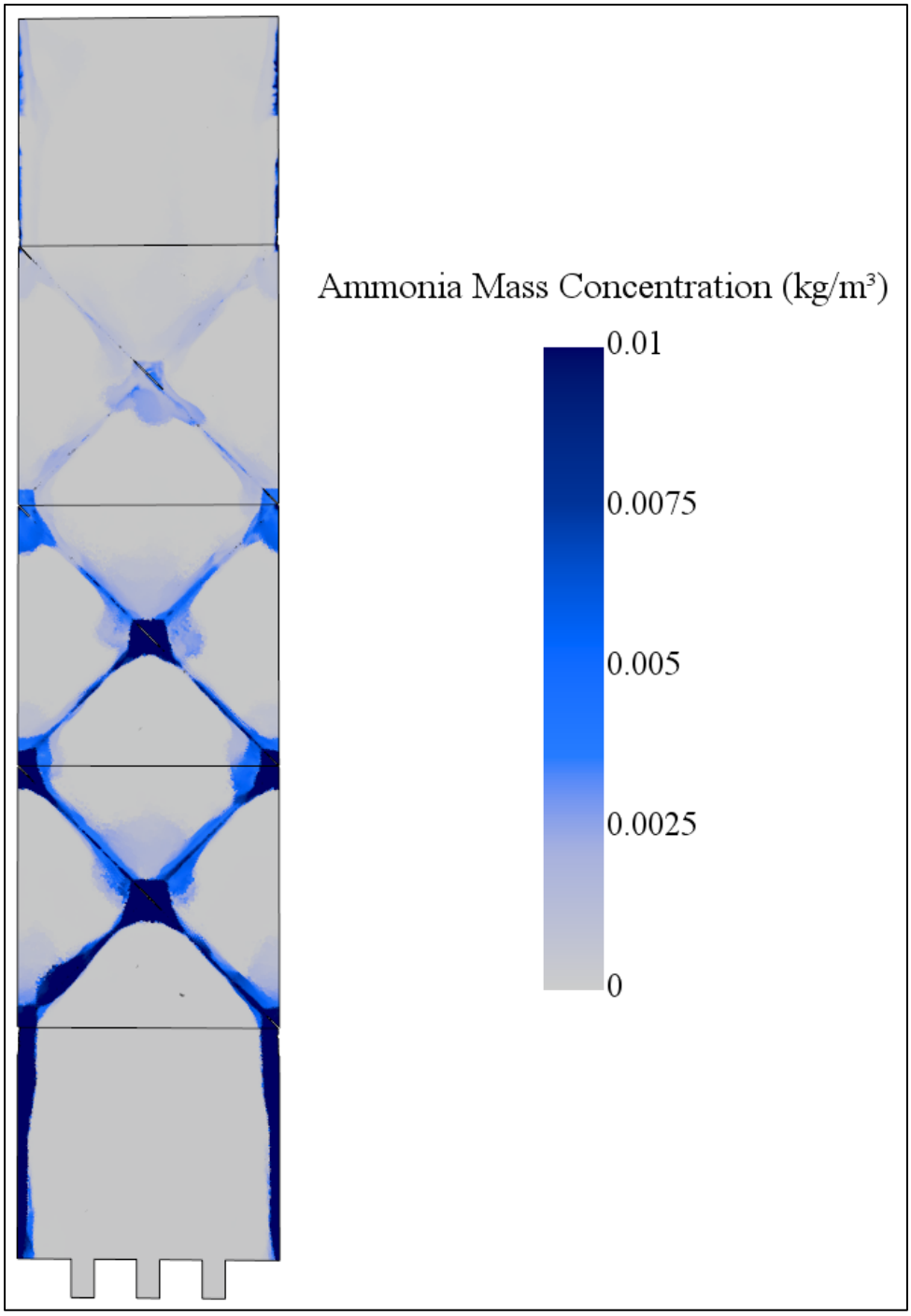

Figure 5-26: Predicted ammonia concentration profile for the middle REU in the structured packing system on the plane between packing sheets.

5.6. CONCLUSIONS

This study presented a novel interfacial mass transfer model for computational fluid dynamics (CFD). The model is applicable for volume-of-fluid (VOF) simulations. Building on the work of Haroun et al. (2010a), this model tracks the mass fraction of the diffusing species rather than the concentration, which enables a concentration jump of multiple orders of magnitude across the gas-liquid interface. Compared to the model by Haroun et al. (2010a), an additional contribution was provided for the difference in densities between the two fluids. A Henry's constant accounts for the concentration jump of the diffusing species between the two phases. The interfacial mass transfer model was implemented using commercial CFD code.

The model was validated on a simple two-dimensional system, which had an analytical solution. The simulation predictions showed an absolute average deviation (AAD) of less than one percent compared to the solution. A concentration jump of three orders of magnitude across the interface was demonstrated. A system with the mass transfer resistance primarily in one phase as well as a system with mass transfer resistance in both phases were tested.

The interfacial mass transfer model was adapted for systems with turbulent flow. A time-averaging treatment of the concentration field produced a model compatible with Reynolds-averaged Navier-Stokes (RANS) turbulence models. The interfacial mass transfer model for turbulent conditions was demonstrated on a structured packing system, with a turbulent diffusion coefficient accounting for the effects of turbulence on the mass transfer.

Future work includes implementing the interfacial mass transfer model with a face-based additional flux calculation. Calculations of material fluxes between two

computational cells at their shared face would support mass conservation. With this calculation scheme, chemical systems could be tested with a larger variety of Henry's constants.

Chapter 6: Conclusions and Recommendations

This research effort focused on predicting the mass transfer performance of vapor-liquid contactors equipped with structured packings by using computational fluid dynamics (CFD). Using a representative elementary unit (REU) simplification, this computational approach predicted the mass transfer in all three types of chemical systems: a gas-film-controlled system, a liquid-film-controlled system, and a system with mass transfer resistance in both phases. For each type of chemical system, good agreement was observed between the CFD predictions and either experimental data, semi-empirical correlations, or analytical solutions. Multiple novel CFD mass transfer methodologies were developed as part of this process.

The ultimate motivation for the structured packing simulations was to improve the mass transfer performance of structured packings. A robust CFD methodology to predict the transport phenomena in structured packings could provide valuable guidance for packing innovation, such as identification of locations having high mass transfer rates and low pressure losses. Such observations would likely inspire modifications to structured packing geometry and lead to improved performance of vapor-liquid contactors. Additionally, a robust CFD methodology would be conducive to rapid prototyping, allowing packing design iterations to be conducted computationally rather than experimentally, which could lower financial obstacles and accelerate the innovation process. These improved structured packing designs would reduce the energy consumption of vapor-liquid contactors, lowering operating costs associated with energy usage and decreasing emissions associated with power production.

As computational resources continue to become cheaper and easier to access, CFD research efforts will likely become more commonly used in the future. The uptick in CFD

structured packing and interfacial mass transfer studies in the past two decades provides evidence for this trend. Recent research has shown promise for simulating the mass transfer within a phase (intraphase mass transfer) in structured packings using CFD, and methodologies for predicting interfacial mass transfer have significantly improved over the last decade. Current commercial CFD software can accurately predict the intraphase mass transfer in structured packings. Predictive interfacial mass transfer methodologies have been implemented on structured packing systems using user-created CFD software, although continued research is necessary to implement the methodologies in commercial CFD software.

6.1. SUMMARY

The conclusions for this research effort are divided into three sections. The first section discusses the gas-film-controlled system, including the setup, results, and primary findings. The second section reviews similar topics for the liquid-film-controlled system. Lastly, the system with mass transfer resistances in both phases is summarized.

6.1.1. Gas-Film-Controlled System

A methodology to account for turbulence-aided, intraphase mass transfer was identified and tested using pipe flow simulations. This intraphase mass transfer methodology was a turbulent diffusion coefficient predicted with a constant turbulent Schmidt number. A constant turbulent Schmidt number forms an analogy between the impact of turbulence on hydrodynamics and its impact on mass transfer. The turbulent

diffusion coefficient supplements the molecular diffusion coefficient. The chemical system simulated was the reactive absorption of SO_2 from air into aqueous sodium hydroxide, and the film of liquid on the pipe wall was assumed to be infinitely thin so the gas-liquid interface coincided with the wall. The CFD predictions for the SO_2 mass fraction along the pipe length fell within the range of predictions from three semi-empirical correlations, validating the intraphase mass transfer methodology.

An asynchronous approach was implemented to simulate the hydrodynamics and mass transfer in a structured packing REU. For these structured packing simulations, the hydrodynamics were first predicted, then the velocity field was frozen and the mass transfer was simulated. The chemical system simulated was the reactive absorption of SO_2 into aqueous sodium hydroxide. As assumed with the pipe flow simulations, the liquid film was assumed to be infinitely thin so the gas-liquid interface coincided with the surface of the packing, simplifying the simulation to gas-only flow. The simulations predicted the gas-phase mass transfer coefficient over a range of F-factors, and the simulations matched experimental data to an average absolute deviation (AAD) of five percent. The predictions also showed good agreement with three semi-empirical models.

To test the validity of the asynchronous hydrodynamic and mass transfer predictions, a system of stacked REUs was also simulated with a synchronous approach. This stacked REU system removed the periodic boundary conditions on the top and bottom of the REU through the inclusion of multiple REUs in the vertical direction. The stacked REU system exhibited an AAD of three percent compared to the experimental data and displayed good agreement with the semi-empirical models as well. The similar predictions

between the asynchronous and synchronous approaches showed that both approaches can provide accurate predictions of the gas-phase mass transfer performance.

The validated CFD mass transfer methodology was applied to a structured packing geometry study. Three fundamental parameters of traditional structured packing geometry were independently and systematically varied: the channel opening angle, the channel inclination angle, and the specific packing area. While each parameter varied, the other parameters were held constant at their values for Mellapak 250Y. Two conditions were considered during this analysis as the packing geometry changed: a case with a constant F-factor and a case with a constant pressure drop. For both conditions, a tradeoff was seen between the hydrodynamic and mass transfer performances.

Simulations of the gas-film-controlled system uncovered many trends in the gas-phase performance. A constant turbulent Schmidt number can accurately account for turbulent effects on mass transfer, although a high-fidelity hydrodynamic turbulence model is essential. Turbulence was found to have a large impact on the gas-phase mass transfer performance in structured packings. Asynchronous predictions of the mass transfer and hydrodynamics can be as accurate as a synchronous approach, and the asynchronous approach requires significantly less computational expense due to the need for only one REU. Higher mass transfer coefficients were predicted near the packing crimps projecting into the channel, which resulted from the higher gas speeds in that region. From the geometry investigation, the hydrodynamics and the mass transfer performances exhibited a tradeoff, where improving one performance metric often impaired the other performance metric. Considering both the hydrodynamic and mass transfer results from the geometry investigation, a structured packing geometry with a specific packing area of 517 m^2/m^3, a

channel inclination angle near 50°, and a channel opening angle of 60° gave the best gas-phase performance.

6.1.2. Liquid-Film-Controlled System

The liquid-phase performance in a structured packing system was simulated using a simplified REU geometry. This simplified geometry was created by removing the regions of the REU far from the packing surface, creating a liquid REU (LREU) with a constant film thickness. The chemical system simulated was toluene desorption from water. An asynchronous methodology produced the hydrodynamic and mass transfer predictions. During the hydrodynamic portion of the simulations, the gas-liquid interface was modeled as having no shear stress, while during the mass transfer portion of the simulations, any toluene reaching the interface was instantly removed. The film thickness controlled the liquid flow rate through the system. The pressure drop across the LREU matched the typical pressure drop in the gas phase during vapor-liquid contactor operation.

Three different variables over a range of liquid flow rates validated the hydrodynamic predictions. First, the liquid holdup showed strong agreement with both traditional liquid holdup experimental measurements and computed tomography (CT) experimental data, having AADs of five and six percent, respectively. Second, the liquid flow angle had an AAD of 0.58 percent compared to an analytical expression by Zogg (1973) and a 14.6 percent AAD compared to the Delft semi-empirical model. Third, the liquid friction factor had an AAD of 20.9 percent compared to inclined plate film theory, with the deviation resulting from the lack of direction changes in the theory. The validation

provided by these three variables showed that the LREU approach accurately predicted the liquid-phase hydrodynamics.

Experimental data and semi-empirical model predictions of the liquid mass transfer coefficient validated the LREU mass transfer modeling. The mass transfer coefficient was compared to four different semi-empirical models over a range of liquid flow rates. The CFD predictions were within the range of the semi-empirical models, supporting the mass transfer predictions. Additionally, the average liquid mass transfer coefficient in the bottom half of the LREU showed excellent agreement with experimental data from Song (2017), having an eight percent average deviation.

Using the validated LREU approach, a structured packing geometry investigation was performed for the liquid-phase performance. Two fundamental parameters of traditional structured packing geometry were independently and systematically varied: the channel inclination angle and the channel opening angle. While each angle changed, the other angle and the specific packing area matched their values for Mellapak 250Y.

When either the channel inclination angle or the channel opening angle increased, the liquid film traveled less horizontally. Trends in the liquid flow angle indicated this decrease in horizontal flow, which resulted from the decreased barriers to flow as the angles increased. The analytical expression by Zogg (1973) validated these trends, showing an AAD of 0.34 percent for the CFD predictions during the channel inclination angle variation and an AAD of 0.33 percent during the channel opening angle variation.

The liquid flow angle had a large impact on the liquid mass transfer coefficient. As the channel inclination angle or the channel opening angle decreased, the predicted mass transfer coefficient increased. This trend stemmed from the increased horizontal flow,

which caused larger direction changes when the liquid film crossed each packing crimp. These larger direction changes near packing crimps caused more liquid upheaval, which improved the mass transfer performance.

Several general trends resulted from the simulations of the liquid-film-controlled system. The simulations predicted turbulence to have a negligible impact on both the hydrodynamic and mass transfer predictions for the liquid phase, indicating laminar flow. The novel LREU methodology accurately predicted the hydrodynamic and mass transfer performance. From the packing geometry investigation, smaller channel inclination angles and channel opening angles increased the liquid mass transfer coefficients due to larger direction changes at the packing crimps. The predicted importance of these direction changes discourages modeling the liquid film in structured packings as flow down an inclined plate, which is a common simplification in previous CFD studies.

6.1.3. System with Mass Transfer Resistances in Both Phases

A novel interfacial mass transfer model was developed that is applicable for simulations of structured packing performance. This interfacial mass transfer model can simulate a jump in concentration of multiple orders of magnitude across the gas-liquid interface, which frequently occurs in structured packing chemical systems. Similar in form to the interfacial mass transfer model for a concentration field developed by Haroun et al. (2010a), the model in this study differs from the Haroun model by tracking the mass fraction of the diffusing species rather than its concentration, allowing for a large jump in concentration to be simulated. To account for a potential concentration jump of the

diffusing species between the two phases, the model adds an additional flux term to the convection-diffusion equation, which is a governing equation for mass transfer.

The interfacial mass transfer model was tested on a system with the mass transfer resistance only in the gas phase. The two-dimensional system had a uniform velocity profile, and an analytical solution was available. After conducting a thorough mesh sensitivity analysis, the average mass transfer coefficient from the CFD simulations was predicted as a function of the distance into the system. The predictions showed excellent agreement with the analytical solution, exhibiting an AAD of 0.87 percent.

The interfacial mass transfer model was also tested on a system with mass transfer resistances in both phases. The physical system and the flow profile matched the previous case, but the liquid molecular diffusion coefficient was smaller, increasing the mass transfer resistance in that phase. Another mesh sensitivity study was performed, and the system required a finer mesh than the previous case's mesh due to the sharp concentration gradient in the liquid phase near the gas-liquid interface. Although the analytical solution used for the previous case is only valid for a constant mass fraction at the gas-liquid interface, the approximately constant mass fraction at the interface enabled the analytical solution to be employed. The CFD predictions showed excellent agreement with the analytical solution, having an AAD of 0.68 percent.

The interfacial mass transfer model was adapted to be applicable in simulations of turbulent flow, including when a Reynolds-averaged Navier-Stokes (RANS) hydrodynamic turbulence model is used. A turbulent diffusion coefficient accounted for turbulent effects on the mass transfer performance, and a constant turbulent Schmidt number predicted the value of the turbulent diffusion coefficient. The turbulent interfacial

mass transfer model was demonstrated for a structured packing system of Mellapak 250Y. These simulations employed a stacked REU approach. The chemical system was ammonia absorption into water from air. The analysis predicted the overall gas number of transfer units (NTU_{OG}).

In general, the multiphase simulations illustrated the application of the novel interfacial mass transfer model. This model could handle a concentration jump of multiple orders of magnitude, which was proven on a two-dimensional system. For simulations involving a RANS approach to account for turbulence, the mass transfer model was adapted for time-averaged quantities and included a turbulent diffusion coefficient. Similar to the laminar flow simulation, this approach produced a concentration jump of multiple orders of magnitude in a structured packing system. This interfacial mass transfer model was implemented in commercial CFD code.

6.2. RECOMMENDATIONS FOR FUTURE STUDIES

Multiple opportunities for further research exist for structured packing studies with CFD. Some of these opportunities build on the methodologies and results found in this research project, including the single-phase and multiphase simulations. Other opportunities are new avenues not explored in this study.

6.2.1. Single-Phase Simulation Opportunities

For both the gas-phase REU approach and the LREU approach, sharp packing crimps were employed, which have been used in many previous structured packing

simulations (Basden, 2014; Haroun et al., 2012, 2010b; Larachi et al., 2003; Petre et al., 2003; Wang et al., 2020; Zhang et al., 2013). However, perfectly sharp crimps likely oversimply the geometry of structured packings. Instead, rounded packing crimps could better reflect the geometry of typical structured packing geometry. The multiphase simulations in this study employed rounded crimps, but a performance comparison between rounded packing crimps and sharp packing crimps could reveal interesting trends, particularly for the liquid-phase performance.

Continuing the liquid-phase packing geometry study, varying the specific packing area could provide additional insight into the impact of the packing geometry on the liquid-phase performance. The analysis performed in this study did not include this parameter. While varying the specific packing area, any validation sources (such as semi-empirical models or experimental data) should have gas flow rates low enough to ensure pre-loading conditions, ensuring consistency with the assumption of no shear stress at the gas-liquid interface.

Building on both the gas and liquid packing geometry study, an optimization of structured packing geometry could provide significant guidance to structured packing designers. This analysis could include changing multiple packing parameters simultaneously using a factorial design strategy. The objection function for this study could consider economic factors, such as structured packing material cost, operating cost, and capital cost due to the size of equipment needed to produce the desired chemical separation.

For the liquid phase, a stacked LREU system could add validity to the asynchronous simulation strategy for the mass transfer and the hydrodynamics. This study considered a stacked REU system for the gas-phase performance, but a parallel study for an LREU

system could rigorously validate the asynchronous methodology. This stacked LREU system could be similar to the stacked REU system, with periodic boundary conditions on the left and right faces, wall conditions at the packing surface, a velocity inlet condition at the top of the system, and a pressure outlet condition at the bottom of the system. The gas-liquid interface could have a slip-wall boundary condition, satisfying both the lack of shear stress for the hydrodynamics but also a Dirichlet boundary condition for the mass transfer.

6.2.2. Multiphase Simulation Opportunities

Consistent calculations of the additional flux term between computational cells could provide a more robust methodology for interfacial mass transfer predictions. Many of the commonly employed interfacial mass transfer models include an additional flux term to the convection-diffusion equation to account for the concentration jump. Due to the large values typically involved in these additional flux terms for the concentration gradient and the volume fraction gradient, even small residuals can significantly alter the mass transfer predictions. For the calculations of fluxes between cells in CFD software like Simcenter STAR-CCM+, significant care is taken to accurately compute these gradients and to ensure mass is conserved when moving material. For fluxes between cells, calculations at cell faces rather than at cell centers help ensure mass conservation. By guaranteeing the value of the flux between two computational cells is calculated at the same location, an identical flux value is predicted for both cells. The field functions in Simcenter STAR-CCM+ calculate the source terms at the cell center, which causes mass conservation challenges. User code might be necessary to compute these flux terms with a face-based approach in Simcenter STAR-CCM+. Alternatively, other CFD software packages may allow user-

specified additional flux terms. Accurate and consistent calculations of the additional flux terms could improve predictions of the interfacial mass transfer for chemical systems with a variety of concentration jumps between the two phases. Accurate predictions of the interfacial mass transfer could greatly support packing innovation, as that transport phenomenon is a key prediction for the overall performance of structured packings. Predicting this interfacial mass transfer with commercial code could aid future efforts, as commercial CFD code is commonly used in industry.

A CFD analysis of packing surface treatment could aid packing designers. Although structured packings often have surface treatment, such as perforations or artificial roughness, significant research remains to uncover the impact of these treatments on mass transfer. Due to its ability to predict small-scale phenomena, CFD could provide significant insight not available through experimental methods.

CFD simulations on computed tomography (CT) scans could reveal the mass transfer at structured packing joints and near the column walls. CT scans of structured packings offer a realistic depiction of structured packing geometry, including packing crimps, perforations, and wiper bands. CFD simulations of these CT scans could better represent the mass transfer performance of structured packings. In particular, a limited amount of research has been conducted on the mass transfer near packing joints and near wall gaps. Because the geometry in these regions is different than the geometry in the core of a structured packing element, the mass transfer performance might differ as well.

6.2.3. Other Opportunities

Other opportunities for further research on structured packings exist with potential application to single-phase and multiphase simulations. For example, including heat transfer in the simulations could enable different temperatures in different regions of the structured packings to be predicted, which could result in varied material properties throughout the system. A constant turbulent Prandtl number could predict the intraphase heat transfer, in analogy to the constant turbulent Schmidt number. Experimental temperature profiles could provide an additional validation source for CFD simulations, in addition to observed chemical separation or pressure drop performances.

CFD simulations of non-dilute systems could also be relevant to structured packing designers. While dilute systems are common in absorption and stripping chemical processes, distillation processes often have non-dilute diffusing species. Significant evaporation and condensation often occur, which can change flow patterns. Additionally, for non-dilute systems, the high mass transfer rates can alter the flow field and the hydrodynamic predictions. CFD could potentially predict these effects, but more research on the topic is necessary.

Further validation analysis could verify trends in this study. For both the gas-phase and liquid-phase geometry studies, the CFD predictions were compared to experimental data for the baseline Mellapak 250Y case. To further validate the CFD predictions, experimental data for geometries different than Mellapak 250Y could be compared to the CFD predictions. Additionally, the multiphase structured packing simulations remain to be compared to experimental data.

6.3. CONCLUSION

Previous research has shown that computational fluid dynamics can provide useful insight into the operation of vapor-liquid contactors equipped with structured packings. This insight can guide packing designs and streamline packing innovation, as the computational approach is conducive to rapid prototyping and can predict small-scale phenomena that are difficult to measure experimentally. Improved packing designs can lower the energy usage and expense associated with chemical separations.

The capabilities of CFD simulations have expanded significantly in the past two decades. Approaches have been established to simulate the performance of structured packings, including of the intraphase mass transfer. Several methodologies have been developed for predicting the interfacial mass transfer, as well. This work applied intraphase mass transfer methodologies and coupled them with new simulation strategies to investigate the impact of structured packing geometry on the gas and liquid mass transfer performances. A new interfacial mass transfer model was also developed that can handle concentration jumps of multiple orders of magnitude across the interface. The methodologies developed in this study and the trends identified can aid packing designers and future CFD studies.

Many opportunities exist for continued research on structured packings using CFD. For single-phase studies, the performance of rounded crimps could be compared to the performance of sharp crimps. Varying the specific packing area could provide additional insight into the impact of the packing geometry on the liquid-phase performance. Using the approach and the data from both geometry studies, the geometry of structured packings could be optimized. Simulations of stacked LREUs could provide additional support for the asynchronous hydrodynamic and mass transfer simulation approach. For the

multiphase simulations, calculation of the interfacial mass transfer term at computational cell faces could enable simulations of more chemical systems. The effect of surface treatment on the structured packings could be predicted with CFD simulations. The mass transfer approaches could be tested on computed tomography scans of structured packings in order to include packing joints and wall effects. For both single-phase and multiphase simulations, heat transfer could be predicted, and the mass transfer methodologies in this study could be adapted for non-dilute systems. These areas for further study represent just a few of the potential opportunities to uncover the transport phenomena in structured packings using CFD.

Computational fluid dynamics simulations have already provided significant insight into the mass transfer in structured packings. As new methodologies continue to be developed and tested, better predictions of the transport phenomena in these column internals will likely become feasible. Significant opportunity remains to improve vapor-liquid contactors using this computational approach.

Appendix A: Semi-Empirical Models

The Rocha-Bravo-Fair model is a common semi-empirical approach to estimate the performance of structured packings. For the gas-side mass transfer coefficient, the model uses a correlation developed for wetted-wall columns (Rocha et al., 1996). Equation (A-1) shows this correlation.

$$\frac{k_G s}{D_{G,m}} = 0.054 \left(\frac{(v_{G,effective} + v_{L,effective}) \rho_G s}{\mu_{G,m}} \right)^{0.8} \left(\frac{\mu_{G,m}}{D_{G,m} \rho_G} \right)^{0.33} \quad \text{(A-1)}$$

In Equation (A-1), $v_{G,effective}$ and $v_{L,effective}$ represent the gas and liquid effective velocities, respectively, which are defined according to Equations (A-2) and (A-3) (Rocha et al., 1996).

$$v_{G,effective} = \frac{v_{G,s}}{\epsilon \, (1 - \psi_L) \sin \alpha} \quad \text{(A-2)}$$

$$v_{L,effective} = \frac{v_{L,s}}{\epsilon \, \psi_L \sin \alpha} \quad \text{(A-3)}$$

A modified Higbie penetration theory predicts the liquid-side mass transfer coefficient (Rocha et al., 1996), as Equation (A-4) shows.

$$k_L = 2 \sqrt{\frac{0.9 D_{L,m} v_{L,effective}}{\pi \, s}} \quad \text{(A-4)}$$

The interfacial area in the Rocha-Bravo-Fair model stems from the Shi and Mersmann correlation (1985), which Equation (A-5) presents.

$$\frac{a_{effective}}{a_p} = C_{enhance} \frac{29.12 \left(\frac{v_{L,s}^2 \rho_L s}{\sigma} \frac{v_{L,s}^2}{s\, g} \right)^{0.15} s^{0.359}}{\left(\frac{v_{L,s} \rho_L s}{\mu_{L,m}} \right)^{0.2} \epsilon^{0.6} (1 - 0.93 \cos\gamma)(\sin\alpha)^{0.3}} \qquad \text{(A-5)}$$

In Equation (A-5), $C_{enhance}$ is a surface enhancement coefficient. Gualito et al. (1997) adapted this correlation to better fit data from high pressure operating conditions, and Equation (A-6) shows the modified correlation for sheet metal packings.

$$\frac{a_{effective}}{a_p} = C_{enhance} \frac{29.12 \left(\frac{v_{L,s}^2 \rho_L s}{\sigma} \frac{v_{L,s}^2}{s\, g} \right)^{0.15} s^{0.36}}{\left(\frac{v_{L,s} \rho_L s}{\mu_{L,m}} \right)^{0.2} \epsilon^{0.6} (1 - 0.93 \cos\gamma)(\sin\alpha)^{0.3}} \left(\frac{1.2}{1 + 0.2 e^{\left(\frac{30 v_{L,s}}{2 v_{L,s}} \right)}} \right) \qquad \text{(A-6)}$$

It should be noted that the liquid-side mass transfer coefficient equation in the Gualito model does not have the 0.9 factor in the numerator of the square root.

Another common model in structured packing studies for the interfacial area is the Onda correlation (Onda et al., 1968). This model was developed for random packings, and its application to structured packing is questionable. The Onda correlation implies the wetted surface of the packing pieces is identical to the interfacial area. Equation (A-7) presents the model's prediction of the fraction of packing surface area that is wetted.

$$\frac{a_w}{a_p} = 1 - \exp\left(-1.45\left(\frac{\sigma_{crit}}{\sigma}\right)^{0.75}\left(\frac{\dot{m}_{L,s}}{A_p\mu_{L,m}}\right)^{0.1}\left(\frac{\dot{m}_{L,s}^2 A_p}{{\rho_L}^2 g}\right)^{-0.05}\left(\frac{\dot{m}_{L,s}^2}{\rho_L \sigma A_p}\right)^{0.2}\right) \quad \text{(A-7)}$$

Glossary

a	Absorption factor
A	Area
b	Channel base length
c	Concentration
C	Modeling coefficient
d	Diameter
D	Diffusion coefficient
f	Fanning friction factor
f	Surface tension force vector
F	F-factor
g	Gravitational vector
g	Gravitational acceleration, taken to be 9.80665 m/s^2
h	Channel height
H	Height of an REU or LREU
He	Henry's constant
HTU	Height of a transfer unit
I	Identity matrix
j	Molar flux magnitude
j	Diffusive flux
k	Mass transfer coefficient
L	Length
$\dot{m}$	Mass flow rate per area
$\dot{M}$	Mass flow rate
n	Direction normal to the gas-liquid interface
N	Mass transfer rate
NTU	Number of transfer units
p	Pressure
Q	Volumetric flow rate
s	Channel side length
S	Sum of source terms
t	Time
v	Velocity vector
v	Velocity magnitude
x	Mass fraction
y	Mole fraction

Z	Height
α	Channel inclination angle
β	Liquid flow angle
γ	Contact angle between liquid and solid
δ	Liquid film thickness
ϵ	Void fraction of packing
ζ	Vertical distance from gas-liquid interface
θ	Channel opening angle
μ	Dynamic viscosity
ν	Kinematic viscosity
ρ	Density
σ	Surface tension
τ	Shear stress
$\boldsymbol{\tau}$	Deviatoric stress tensor
$\boldsymbol{\Phi}$	Flux term
ψ	Holdup
ω	Phase volume fraction
Subscripts	
avg	Average value
A	Of or pertaining to species A
bottom	Value near bottom
c	Characteristic value
crit	Critical value
contact	Value pertaining to contact between two fluids
CFD	Value predicted by CFD
CSF	Value predicted by the continuum surface force model
Delft	Value predicted by the Delft model
e	Value at exit
effective	Effective quantity
enhance	Pertaining to surface enhancement
G	Of or pertaining to the gas phase
horizontal	Horizontal component
i	Of or pertaining to the gas-liquid interface
in	Value at inlet
inclined plate	Value from inclined plate film theory

laminar	Of or pertaining to laminar flow conditions
L	Of or pertaining to the liquid phase
m	Molecular quantity
mix	Quantity for a mixture of gas and liquid phases
new	Quantity introduced in this research effort
OG	Overall quantity for the gas phase
P	Of or pertaining to packing
s	Superficial quantity
Sol	Related to solubility
toluene	Of or pertaining to toluene
top	Value at top surface
T	Turbulent quantity
vertical	Vertical component
w	Wetted quantity
wall	Value at wall
Zogg	Value predicted by the Zogg equation
Superscripts	
T	Transpose
$\bar{}$	Mixing cup average
~	Recast value
*	Value at gas-liquid interface
′	Term fluctuating with time due to turbulence
Dimensionless Number Groups	
$Re = \frac{\rho v d}{\mu}$	Reynolds number for pipe flow
$Sc = \frac{\nu_m}{D_{A,m}}$	Schmidt number
$Sc_T = \frac{\mu_T}{\rho D_T}$	Turbulent Schmidt number
$Sh = \frac{k L_c}{D_{A,m}}$	Sherwood number

Bibliography

Agirre Arisketa, I., 2010. Innovative Reaction Systems for Acetal (1,1 Diethoxy Butane) Production from Renewable Sources (PhD Dissertation). University of the Basque Country, Bilbao, Biscay, Spain.

Agrawal, R., Herron, D.M., 2000. Encyclopedia of Separation Science. Encyclopedia of Separation Science.

Alke, A., Bothe, D., Kroeger, M., Warnecke, H.-J., 2009. VOF-based simulation of conjugate mass transfer from freely moving fluid particles. WIT Transactions on Engineering Sciences, Computational Methods in Multiphase Flow V 63, 157–168. https://doi.org/10.2495/MPF090141.

Alke, A., Bothe, D., Kroger, M., Weigand, B., Weirich, D., Weking, H., 2010. Direct numerical simulation of high Schmidt number mass transfer from air bubbles rising in liquids using the Volume-of-Fluid-Method. ERCOFTAC Bulletin 82, 5–10.

Amini, Y., Karimi-Sabet, J., Esfahany, M.N., Haghshenasfard, M., Dastbaz, A., 2019. Experimental and numerical study of mass transfer efficiency in new wire gauze with high capacity structured packing. Separation Science and Technology 54 (16), 2706–2717. https://doi.org/10.1080/01496395.2018.1549076.

Arwikar, K.J., Sandall, O.C., 1980. Liquid phase mass transfer resistance in a small scale packed distillation column. Chemical Engineering Science 35 (11), 2337–2343. https://doi.org/10.1016/0009-2509(80)87012-6.

Banerjee, R., 2008. Turbulent conjugate heat and mass transfer from the surface of a binary mixture of ethanol/iso-octane in a countercurrent stratified two-phase flow system. International Journal of Heat and Mass Transfer 51 (25), 5958–5974. https://doi.org/10.1016/j.ijheatmasstransfer.2008.04.057.

Basden, M.A., 2014. Characterization of Structured Packing via Computational Fluid Dynamics (PhD Dissertation). University of Texas at Austin, Austin, Texas.

Basha, O.M., Wang, R., Gamwo, I.K., Siefert, N.S., Morsi, B.I., 2020. Full-scale CFD modeling of multiphase flow distribution in a packed-bed absorber with structured packing Mellapak 250Y. International Journal of Chemical Reactor Engineering 18 (3), 20190207. https://doi.org/doi:10.1515/ijcre-2019-0207.

Behrens, M., 2006. Hydrodynamics and Mass Transfer of Modular Catalytic Structured Packing. Technische Universiteit Delft.

Billet, R., Schultes, M., 1999. Prediction of mass transfer columns with dumped and arranged packings: Updated summary of the calculation method of Billet and Schultes. Chemical Engineering Research and Design 77 (6), 498–504. https://doi.org/10.1205/026387699526520.

Billet, R., Schultes, M., 1993. Predicting mass transfer in packed columns. Chemical Engineering & Technology 16 (1), 1–9. https://doi.org/10.1002/ceat.270160102.

Bird, R.B., Stewart, W.E., Lightfoot, E.N., 2007. Transport Phenomena, Revised. John Wiley & Sons, Inc., New York.

Boot-Handford, M.E., Abanades, J.C., Anthony, E.J., Blunt, M.J., Brandani, S., Mac Dowell, N., Fernandez, J.R., Ferrari, M.-C., Gross, R., Hallett, J.P., Haszeldine, R.S., Heptonstall, P., Lyngfelt, A., Makuch, Z., Mangano, E., Porter, R.T.J., Pourkashanian, M., Rochelle, G.T., Shah, N., Yao, J.G., Fennell, P.S., 2014. Carbon capture and storage update. Energy Environ. Sci. 7 (1), 130–189. https://doi.org/10.1039/C3EE42350F.

Bothe, D., Fleckenstein, S., 2013. A Volume-of-Fluid-based method for mass transfer processes at fluid particles. Chemical Engineering Science 101, 283–302. https://doi.org/10.1016/j.ces.2013.05.029.

Bothe, D., Koebe, M., Warnecke, H.-J., 2003a. VOF-simulation of the rise behavior of single air bubbles with oxygen transfer to the ambient fluid. Presented at the Conference on Transport Phenomena with Moving Boundaries, Berlin, Germany, pp. 134–146.

Bothe, D., Koebe, M., Wielage, K., Prüss, J., Warnecke, H.-J., 2004. Direct numerical simulation of mass transfer between rising gas bubbles and water, in: Bubbly Flows : Analysis, Modelling, and Calculation. pp. 159–174.

Bothe, D., Koebe, M., Wielage, K., Warnecke, H.-J., 2003b. VOF-simulations of mass transfer from single bubbles and bubble chains rising in aqueous solutions, in: Proceedings of ASME FEDSM'03 4th ASME_JSME Joint Fluids Engineering Conference. Presented at the ASME FEDSM'03 4th ASME_JSME Joint Fluids Engineering Conference, Honolulu, Hawaii, USA, pp. 423–429. https://doi.org/10.1115/FEDSM2003-45155.

Bothe, D., Kroger, M., Alke, A., Warnecke, H.-J., 2009. VOF-based simulation of reactive mass transfer across deformable interfaces. Progress in Computational Fluid Dynamics 9 (6/7), 325–331.

Bothe, D., Kröger, M., Warnecke, H.-J., 2011. A VOF-based conservative method for the simulation of reactive mass transfer from rising bubbles. FDMP 7 (3), 303–316.

Bothe, D., Warnecke, H.-J., 2005. VOF-simulation of rising air bubbles with mass transfer to the ambient liquid, in: 10th Workshop on Proceedings of Transport Phenomena in Two-Phase Flow. pp. 61–72.

Brian, P.L.T., Hurley, J.F., Hasseltine, E.H., 1961. Penetration theory for gas absorption accompanied by a second order chemical reaction. AIChE Journal 7 (2), 226–231. https://doi.org/10.1002/aic.690070212.

Brunazzi, E., Paglianti, A., 1997. Liquid-film mass-transfer coefficient in a column equipped with structured packings. Industrial & Engineering Chemistry Research 36 (9), 3792–3799. https://doi.org/10.1021/ie970045h.

Bumbac, G., Ene, A., Isopescu, R., Toma, A., 2009. Process simulation of reactive distillation in dividing wall column for ETBE synthesis process. Chemical Engineering Transactions 18, 487–492. https://doi.org/10.3303/CET0918079.

Chen, J., 2006. Numerical and Experimental Study of Transport Phenomena in a Structured Packed Column at High Pressure. Tianjin University, Tianjin.

Chen, J., Liu, C., Yuan, X., Yu, G., 2009. CFD simulation of flow and mass transfer in structured packing distillation columns. Chinese Journal of Chemical Engineering 17 (3), 381–388. https://doi.org/10.1016/S1004-9541(08)60220-7.

Chen, J., Tang, Z., Wang, G., Liu, C., Yuan, X., Yu, G., 2004. Performance of Mellapak 350Y corrugated sheet structured packing at elevated pressure. J. Chem. Ind. Eng. (China), 55 (2), 335–336.

Dai, C., Lei, Z., Li, Q., Chen, B., 2012. Pressure drop and mass transfer study in structured catalytic packings. Separation and Purification Technology 98, 78–87. https://doi.org/10.1016/j.seppur.2012.06.035.

Deen, W.M., 2012. Analysis of Transport Phenomena. Oxford University Press.

Deising, D., Marschall, H., Bothe, D., 2016. A unified single-field model framework for Volume-Of-Fluid simulations of interfacial species transfer applied to bubbly flows. Chemical Engineering Science 139, 173–195. https://doi.org/10.1016/j.ces.2015.06.021.

Dejanović, I., Matijašević, L., Jansen, H., Olujić, Ž., 2011. Designing a packed dividing wall column for an aromatics processing plant. Industrial & Engineering Chemistry Research 50 (9), 5680–5692. https://doi.org/10.1021/ie1020206.

Dietze, G.F., 2019. Effect of wall corrugations on scalar transfer to a wavy falling liquid film. Journal of Fluid Mechanics 859, 1098–1128. https://doi.org/10.1017/jfm.2018.851.

Dong, B., Yuan, X.G., Yu, K.T., 2017. Determination of liquid mass-transfer coefficients for the absorption of CO_2 in alkaline aqueous solutions in structured packing using numerical simulations. Chemical Engineering Research and Design 124, 238–251. https://doi.org/10.1016/j.cherd.2017.06.017.

Duss, M., 2013. Packing pressure drop prediction at low operating pressure: Is there anything new? Presented at the Distillation Topical Conference, AIChE Spring Meeting, AIChE, San Antonio, Texas.

Egorov, Y., Menter, F., Klöker, M., Kenig, E.Y., 2005. On the combination of CFD and rate-based modelling in the simulation of reactive separation processes. Chemical

Engineering and Processing: Process Intensification 44 (6), 631–644. https://doi.org/10.1016/j.cep.2003.10.011.

Emmert, R.E., Pigford, R.L., 1954. A study of gas absorption in falling liquid films. Chem. Eng. Prog. 50 (2), 87–93.

Erasmus, A.B., 2004. Mass Transfer in Structured Packing (PhD Thesis). University of Stellenbosch, Stellenbosch.

Fair, J.R., Seibert, A.F., Behrens, M., Saraber, P.P., Olujic, Z., 2000. Structured packing performance—Experimental evaluation of two predictive models. Ind. Eng. Chem. Res. 39 (6), 1788–1796. https://doi.org/10.1021/ie990910t.

Falcone, M., Bothe, D., Marschall, H., 2018. 3D direct numerical simulations of reactive mass transfer from deformable single bubbles: An analysis of mass transfer coefficients and reaction selectivities. Chemical Engineering Science 177, 523–536. https://doi.org/10.1016/j.ces.2017.11.024.

Fernandes, J., Simões, P.C., Mota, J.P.B., Saatdjian, E., 2008. Application of CFD in the study of supercritical fluid extraction with structured packing: Dry pressure drop calculations. The Journal of Supercritical Fluids 47 (1), 17–24. https://doi.org/10.1016/j.supflu.2008.07.008.

Fleckenstein, S., Bothe, D., 2015. A Volume-of-Fluid-based numerical method for multi-component mass transfer with local volume changes. Journal of Computational Physics 301, 35–58. https://doi.org/10.1016/j.jcp.2015.08.011.

Fox, R.O., 2003. Computational Models for Turbulent Reacting Flows. Cambridge University Press, New York.

Francois, M.M., Carlson, N.N., 2013. The global embedded interface formulation for interfacial mass transfer within a volume tracking framework. Computers & Fluids 87, 102–114. https://doi.org/10.1016/j.compfluid.2013.02.016.

Francois, M.M., Carlson, N.N., 2010. The balanced-force volume tracking algorithm and global embedded interface formulation for droplet dynamics with mass transfer, in: ASME 2010 3rd Joint US-European Fluids Engineering Summer Meeting: Volume 1, Symposia – Parts A, B, and C. Presented at the ASME 2010 3rd Joint US-European Fluids Engineering Summer Meeting collocated with 8th International Conference on Nanochannels, Microchannels, and Minichannels, ASME, Montreal, Quebec, Canada. https://doi.org/10.1115/FEDSM-ICNMM2010-31032.

Ganguli, A.A., Kenig, E.Y., 2011. A CFD-based approach to the interfacial mass transfer at free gas–liquid interfaces. Chemical Engineering Science 66 (14), 3301–3308. https://doi.org/10.1016/j.ces.2011.01.055.

Gilliland, E.R., Sherwood, T.K., 1934. Diffusion of vapors into air streams. Ind. Eng. Chem. 26 (5), 516–523. https://doi.org/10.1021/ie50293a010.

Green, C.W., Farone, J., Briley, J.K., Eldridge, R.B., Ketcham, R.A., Nightingale, B., 2007. Novel application of x-ray computed tomography: Determination of gas/liquid contact area and liquid holdup in structured packing. Ind. Eng. Chem. Res. 46 (17), 5734–5753. https://doi.org/10.1021/ie0701827.

Gründing, D., Fleckenstein, S., Bothe, D., 2016. A subgrid-scale model for reactive concentration boundary layers for 3D mass transfer simulations with deformable fluid interfaces. International Journal of Heat and Mass Transfer 101, 476–487. https://doi.org/10.1016/j.ijheatmasstransfer.2016.04.119.

Gualito, J.J., Cerino, F.J., Cardenas, J.C., Rocha, J.A., 1997. Design method for distillation columns filled with metallic, ceramic, or plastic structured packings. Industrial & Engineering Chemistry Research 36 (5), 1747–1757. https://doi.org/10.1021/ie960625z.

Haelssig, J.B., Tremblay, A.Y., Thibault, J., Etemad, S.Gh., 2010. Direct numerical simulation of interphase heat and mass transfer in multicomponent vapour–liquid flows. International Journal of Heat and Mass Transfer 53 (19-20), 3947–3960. https://doi.org/10.1016/j.ijheatmasstransfer.2010.05.013.

Haghshenas Fard, M., Zivdar, M., Rahimi, R., Nasr Esfahani, M., Afacan, A., Nandakumar, K., Chuang, K.T., 2007. CFD Simulation of mass transfer efficiency and pressure drop in a structured packed distillation column. Chemical Engineering & Technology 30 (7), 854–861. https://doi.org/10.1002/ceat.200700011.

Haroun, Y., Legendre, D., Raynal, L., 2010a. Volume of fluid method for interfacial reactive mass transfer: Application to stable liquid film. Chemical Engineering Science 65 (10), 2896–2909. https://doi.org/10.1016/j.ces.2010.01.012.

Haroun, Y., Legendre, D., Raynal, L., 2010b. Direct numerical simulation of reactive absorption in gas–liquid flow on structured packing using interface capturing method. Chemical Engineering Science 65 (1), 351–356. https://doi.org/10.1016/j.ces.2009.07.018.

Haroun, Y., Raynal, L., 2016. Use of computational fluid dynamics for absorption packed column design. Oil & Gas Science and Technology 71 (3).

Haroun, Y., Raynal, L., Legendre, D., 2012. Mass transfer and liquid hold-up determination in structured packing by CFD. Chemical Engineering Science 75, 342–348. https://doi.org/10.1016/j.ces.2012.03.011.

Hassanvand, A., Esmaeili-Faraj, S.H., Moghaddam, M.S., Moradi, R., 2021. Characterization of a new structured packing by computational fluid dynamics. Chemical Engineering & Technology 44 (1), 156–163. https://doi.org/10.1002/ceat.202000237.

Hayashi, K., Hosoda, S., Tryggvason, G., Tomiyama, A., 2014. Effects of shape oscillation on mass transfer from a Taylor bubble. International Journal of Multiphase Flow 58, 236–245. https://doi.org/10.1016/j.ijmultiphaseflow.2013.09.009.

Hayashi, K., Tomiyama, A., 2011. Interface tracking simulation of mass transfer from a dissolving bubble. The Journal of Computational Multiphase Flows 3 (4), 247–261. https://doi.org/10.1260/1757-482X.3.4.247.

Henriques de Brito, M., von Stockar, U., Bomio, P., 1992. Predicting the liquid phase mass transfer coefficient k_L for the Sulzer structured packing Mellapak. Institution of Chemical Engineers Symposium Series 128, B137–B144.

Higbie, R., 1935. The rate of absorption of a pure gas into a still liquid during short periods of exposure. Trans. Am. Inst. Chem. Eng. 31, 365–389.

Higler, A.P., Krishna, R., Ellenberger, J., Taylor, R., 1999. Counter-current operation of a structured catalytically packed-bed reactor: Liquid phase mixing and mass transfer. Chemical Engineering Science 54 (21), 5145–5152. https://doi.org/10.1016/S0009-2509(99)00229-8.

Hill, S., Acher, T., Hoffmann, R., Ferstl, J., Deising, D., Marschall, H., Rehfeldt, S., Klein, H., 2019. Quantifizierung der Trenneffizienz einer strukturierten Packung mittels numerischer Simulation. Chemie Ingenieur Technik 91 (12), 1833–1841. https://doi.org/10/ggj4q3.

Hill, S., Acher, T., Hoffmann, R., Ferstl, J., Deising, D., Marschall, H., Rehfeldt, S., Klein, H., 2018. Numerical simulation of two-phase flow and interfacial species transfer in structured packings. Chemical Engineering Transactions 69, 337–342. https://doi.org/10.3303/CET1869057.

Hodson, J., 1997. Computational Fluid Dynamical Studies of Structured Distillation Packings. University of Aston, Birmingham.

Hodson, J.S., Fletcher, J.P., Porter, K.E., 1997. Fluid mechanical studies of structured distillation packings. Presented at the Distillation and absorption ’97 : a three-day symposium, Institution of Chemical Engineers and the Netherlands Process Technology Foundation e.2, pp. 999–1007.

Janssen, L.P.B.M., Warmoeskerken, M.M.C.G., 1991. Transport Phenomena Data Companion. Delftse Uitgevers Maatschappij, Delft, Holland.

Kenig, E.Y., 2018. Email Correspondence: Mass Transfer Method in 2005 Paper.

Khosravi Nikou, M.R., Ehsani, M.R., 2008. Turbulence models application on CFD simulation of hydrodynamics, heat and mass transfer in a structured packing. International Communications in Heat and Mass Transfer 35 (9), 1211–1219. https://doi.org/10.1016/j.icheatmasstransfer.2008.05.017.

Khosravi Nikou, M.R., Ehsani, M.R., Davazdah Emami, M., 2008. CFD simulation of hydrodynamics, heat and mass transfer simultaneously in structured packing.

International Journal of Chemical Reactor Engineering 6 (1). https://doi.org/10.2202/1542-6580.1763
Kister, H.Z., 1992. Distillation Design. McGraw-Hill.
Kroger, M., Alke, A., Bothe, D., Warnecke, H.-J., 2007. A VOF-based approach for the simulation of reactive mass transfer from rising bubbles, in: Proceedings of 4th International Berlin Workshop on Transport Phenomena with Moving Boundaries. Presented at the 4th International Berlin Workshop on Transport Phenomena with Moving Boundaries, pp. 290–301.
Larachi, F., Petre, C.F., Iliuta, I., Grandjean, B., 2003. Tailoring the pressure drop of structured packings through CFD simulations. Chemical Engineering and Processing: Process Intensification 42 (7), 535–541. https://doi.org/10.1016/S0255-2701(02)00073-9.
Lautenschleger, A., Olenberg, A., Kenig, E.Y., 2015. A systematic CFD-based method to investigate and optimise novel structured packings. Chemical Engineering Science 122, 452–464. https://doi.org/10.1016/j.ces.2014.09.040.
Linek, V., Sinkule, J., Janda, V., 1998. Design of packed aeration towers to strip volatile organic contaminants from water. Water Research 32 (4), 1264–1270. https://doi.org/10.1016/S0043-1354(97)00336-9.
Liss, P.S., Slater, P.G., 1974. Flux of gases across the air-sea interface. Nature 247 (5438), 181–184. https://doi.org/10.1038/247181a0.
Losher, T., Kleiner, T., Hill, S., Sarajlic, N., Rehfeldt, S., Klein, H., 2020. Comparison of the Generalized Species Transfer Model with a two-field approach for interfacial mass transfer. Chemical Engineering & Technology 43 (12), 2576–2582. https://doi.org/10.1002/ceat.202000259.
Macfarlan, L.H., Seibert, A.F., Phan, M.T., Eldridge, R.B., 2021. CFD-based study on structured packing geometry. Chemical Engineering Science 243, 116767. https://doi.org/10.1016/j.ces.2021.116767.
Maes, J., Soulaine, C., 2020. A unified single-field Volume-of-Fluid-based formulation for multi-component interfacial transfer with local volume changes. Journal of Computational Physics 402, 109024. https://doi.org/10/ggdmtw.
Maes, J., Soulaine, C., 2018. A new compressive scheme to simulate species transfer across fluid interfaces using the Volume-Of-Fluid method. Chemical Engineering Science 190, 405–418. https://doi.org/10/gdvmtj.
Manh, T.D., Nam, N.D., Babazadeh, H., Moradi, R., 2020. Computational fluid dynamics characterization of high-capacity structured packing. Chemical Engineering & Technology 43 (9), 1690–1698. https://doi.org/10.1002/ceat.202000060.
Marschall, H., Hinterberger, K., Schüler, C., Habla, F., Hinrichsen, O., 2012. Numerical simulation of species transfer across fluid interfaces in free-surface flows using

OpenFOAM. Chemical Engineering Science 78, 111–127. https://doi.org/10.1016/j.ces.2012.02.034.

Massman, W.J., 1998. A review of the molecular diffusivities of H_2O, CO_2, CH_4, CO, O_3, SO_2, NH_3, N_2O, NO, and NO_2 in air, O_2 and N_2 near STP. Atmospheric Environment 32 (6), 1111–1127. https://doi.org/10.1016/S1352-2310(97)00391-9.

McCarter, R.J., Stutzman, L.F., 1959. Transfer resistance and fluid mechanics. AIChE Journal 5 (4), 502–505. https://doi.org/10.1002/aic.690050418.

Olenberg, A., Reschetnik, W., Kullmer, G., Kenig, E.Y., 2018. Optimization of structured packings using twisted tape inserts. Chemical Engineering Research and Design 132, 1–8. https://doi.org/10.1016/j.cherd.2017.12.036.

Olujić, Ž., 2019. Predicting the pressure drop of corrugated sheet structured packings in deep vacuum applications. Chem. Biochem. Eng. Q. 33 (3), 303–323. https://doi.org/10.15255/CABEQ.2018.1574.

Olujić, Ž., 2002. Delft model- A comprehensive design tool for corrugated sheet structured packings. Presented at the AIChE Spring National Meeting, AIChE, New Orleans, Louisiana.

Olujic, Z., 1997. Development of a complete simulation model for predicting the hydraulic and separation performance of distillation columns equipped with structured packings. Chemical and Biochemical Engineering Quarterly 11 (1), 31–46.

Olujić, Ž., Behrens, M., Colli, L., Paglianti, A., 2004. Predicting the efficiency of corrugated sheet structured packings with large specific surface area. Chem. Biochem. Eng. Q. 18 (2), 89–96. https://doi.org/10.15255/CABEQ.2014.570.

Olujić, Ž., Kamerbeek, A.B., de Graauw, J., 1999. A corrugation geometry based model for efficiency of structured distillation packing. Chemical Engineering and Processing: Process Intensification 38 (4), 683–695. https://doi.org/10.1016/S0255-2701(99)00068-9.

Olujić, Ž., Rietfort, T., Jansen, H., Kaibel, B., Zich, E., Frey, G., Ruffert, G., Zielke, T., 2012. Experimental characterization and modeling of high performance structured packings. Industrial & Engineering Chemistry Research 51 (11), 4414–4423. https://doi.org/10.1021/ie202585t.

Olujić, Ž., Seibert, A.F., 2014. Predicting the liquid phase mass transfer resistance of structured packings. Chem. Biochem. Eng. Q. 28 (4), 409–424. https://doi.org/10.15255/CABEQ.2014.19344.

Onda, K., Takeuchi, H., Okumoto, Y., 1968. Mass transfer coefficients between gas and liquid phases in packed columns. Journal of Chemical Engineering of Japan 1 (1), 56–62. https://doi.org/10.1252/jcej.1.56.

Onea, A., Wörner, M., Cacuci, D.G., 2009. A qualitative computational study of mass transfer in upward bubble train flow through square and rectangular mini-channels.

Chemical Engineering Science 64 (7), 1416–1435. https://doi.org/10.1016/j.ces.2008.11.008.

Onea, A.A., 2006. Numerical simulation of mass transfer with and without first order chemical reaction in two-fluid flows. Universitat Karlsruhe.

Owens, S.A., Perkins, M.R., Eldridge, R.B., Schulz, K.W., Ketcham, R.A., 2013. Computational fluid dynamics simulation of structured packing. Industrial & Engineering Chemistry Research 52 (2), 2032–2045. https://doi.org/10.1021/ie3016889.

Paschke, S., Thiele, R., Repke, J.-U., 2009. Untersuchung des Stoffübergangverhaltens dreiphasig betriebener Fallfilmabsorber. Chemie Ingenieur Technik 81 (3), 297–304. https://doi.org/10.1002/cite.200800130.

Petera, J., Weatherley, L.R., 2001. Modelling of mass transfer from falling droplets. Chemical Engineering Science 56 (16), 4929–4947. https://doi.org/10.1016/S0009-2509(01)00142-7.

Petre, C.F., Larachi, F., Iliuta, I., Grandjean, B.P.A., 2003. Pressure drop through structured packings: Breakdown into the contributing mechanisms by CFD modeling. Chemical Engineering Science 58 (1), 163–177. https://doi.org/10.1016/S0009-2509(02)00473-6.

Phan, M.T., Macfarlan, L.H., Eldridge, R.B., 2020. Advanced modeling for structured packing development - a: Hydraulics, in: 2020 Virtual Spring Meeting and 16th GCPS. Presented at the AIChE Spring Meeting and Global Congress on Process Safety, AIChE.

Pohorecki, R., Moniuk, W., 1988. Kinetics of reaction between carbon dioxide and hydroxyl ions in aqueous electrolyte solutions. Chemical Engineering Science 43 (7), 1677–1684. https://doi.org/10.1016/0009-2509(88)85159-5.

Pope, S.B., 2000. Turbulent Flows. Cambridge University Press, Cambridge.

Rahimpour, M.R., Saidi, M., Baniadam, M., Parhoudeh, M., 2013. Investigation of natural gas sweetening process in corrugated packed bed column using computational fluid dynamics (CFD) model. Journal of Natural Gas Science and Engineering 15, 127–137. https://doi.org/10.1016/j.jngse.2013.10.003.

Rajani, B.N., Kandasamy, A., Majumdar, S., 2009. Numerical simulation of laminar flow past a circular cylinder. Applied Mathematical Modelling 33 (3), 1228–1247. https://doi.org/10.1016/j.apm.2008.01.017.

Raynal, L., Ben Rayana, F., Royon-Lebeaud, A., 2009. Use of CFD for CO_2 absorbers optimum design: From local scale to large industrial scale. Energy Procedia 1 (1), 917–924. https://doi.org/10.1016/j.egypro.2009.01.122.

Raynal, L., Boyer, C., Ballaguet, J.-P., 2004. Liquid holdup and pressure drop determination in structured packing with CFD simulations. The Canadian Journal of Chemical Engineering 82 (5), 871–879. https://doi.org/10.1002/cjce.5450820502.

Rieks, S., Kenig, E.Y., 2018a. Modelling and numerical simulation of coupled transport phenomena with phase change: Mixture evaporation from a rectangular capillary. Chemical Engineering Science 181, 173–185. https://doi.org/10.1016/j.ces.2017.12.023.

Rieks, S., Kenig, E.Y., 2018b. Modelling and numerical simulation of coupled transport phenomena with phase change: Layer evaporation of a binary mixture. Chemical Engineering Science 176, 367–376. https://doi.org/10.1016/j.ces.2017.10.040.

Rocha, J.A., Bravo, J.L., Fair, J.R., 1996. Distillation columns containing structured packings: A comprehensive model for their performance. 2. Mass-transfer model. Ind. Eng. Chem. Res. 35 (5), 1660–1667. https://doi.org/10.1021/ie940406i.

Rocha, J.A., Bravo, J.L., Fair, J.R., 1993. Distillation columns containing structured packings: a comprehensive model for their performance. 1. Hydraulic models. Ind. Eng. Chem. Res. 32 (4), 641–651. https://doi.org/10.1021/ie00016a010.

Said, W., Nemer, M., Clodic, D., 2011. Modeling of dry pressure drop for fully developed gas flow in structured packing using CFD simulations. Chemical Engineering Science 66 (10), 2107–2117. https://doi.org/10.1016/j.ces.2011.02.011.

Sander, R., 2015. Compilation of Henry's law constants (version 4.0) for water as solvent. Atmospheric Chemistry and Physics 15 (8), 4399–4981. https://doi.org/10.5194/acp-15-4399-2015.

Schpigel, L., Meier, W., 1994. Performance characteristics of various types of Mellapak packings (productivity, pressure differential, and deficiency). Chemical and Petroleum Engineering 30 (3), 118–125. https://doi.org/10.1007/BF01147885.

Schultes, M., 2018. Designing CO_2 absorption columns with activated amine solutions. Chemical Engineering Transactions 69, 133–138. https://doi.org/10.3303/CET1869023.

Seader, J.D., Henley, E.J., Roper, D.K., 2011. Separation Process Principles: Chemical and Biochemical Operations. John Wiley & Sons, Inc, Hoboken.

Sebastia-Saez, D., Gu, S., Ranganathan, P., 2014. Volume of fluid modeling of the reactive mass transfer of CO_2 into aqueous amine solutions in structured packed elements at micro-scale. Energy Procedia 63, 1229–1242. https://doi.org/10.1016/j.egypro.2014.11.133.

Sebastia-Saez, D., Gu, S., Ranganathan, P., Papadikis, K., 2015a. Micro-scale CFD modeling of reactive mass transfer in falling liquid films within structured packing materials. International Journal of Greenhouse Gas Control 33, 40–50. https://doi.org/10.1016/j.ijggc.2014.11.019.

Sebastia-Saez, D., Gu, S., Ranganathan, P., Papadikis, K., 2015b. Meso-scale CFD study of the pressure drop, liquid hold-up, interfacial area and mass transfer in structured packing materials. International Journal of Greenhouse Gas Control 42, 388–399. https://doi.org/10.1016/j.ijggc.2015.08.016.

Sebastia-Saez, D., Gu, S., Ranganathan, P., Papadikis, K., 2013. 3D modeling of hydrodynamics and physical mass transfer characteristics of liquid film flows in structured packing elements. International Journal of Greenhouse Gas Control 19, 492–502. https://doi.org/10.1016/j.ijggc.2013.10.013.

Shi, M.G., Mersmann, A., 1985. Effective interfacial area in packed columns. Ger. Chem. Eng. 8, 87–96.

Shilkin, A., Heinen, K., Großmann, C., Lautenschleger, A., Janzen, A., Kenig, E.Y., 2010. On the development of an energy efficient packing for vacuum distillation, in: Distillation Absorption 2010. Presented at the Distillation & Absorption, pp. 653–658.

Sholl, D.S., Lively, R.P., 2016. Seven chemical separations to change the world. Nature 532 (7600), 435–437. https://doi.org/10.1038/532435a.

Simcenter STAR-CCM+ 2019.3.1 Theory Guide, 2019.

Simcenter STAR-CCM+ 2021.1.1 Theory Guide, 2021.

Singh, R.K., Bao, J., Wang, C., Fu, Y., Xu, Z., 2020. Hydrodynamics of countercurrent flows in a structured packed column: Effects of initial wetting and dynamic contact angle. Chemical Engineering Journal 398, 125548. https://doi.org/10.1016/j.cej.2020.125548.

Singh, R.K., Galvin, J.E., Sun, X., 2018. Multiphase flow studies for microscale hydrodynamics in the structured packed column. Chemical Engineering Journal 353, 949–963. https://doi.org/10.1016/j.cej.2018.07.067.

Soh, G.Y., Yeoh, G.H., Timchenko, V., 2017. A CFD model for the coupling of multiphase, multicomponent and mass transfer physics for micro-scale simulations. International Journal of Heat and Mass Transfer 113, 922–934. https://doi.org/10.1016/j.ijheatmasstransfer.2017.06.001.

Soh, G.Y., Yeoh, G.H., Timchenko, V., 2016. An algorithm to calculate interfacial area for multiphase mass transfer through the volume-of-fluid method. International Journal of Heat and Mass Transfer 100, 573–581. https://doi.org/10.1016/j.ijheatmasstransfer.2016.05.006.

Song, D., 2017. Effect of Liquid Viscosity on Liquid Film Mass Transfer for Packings (PhD Thesis). University of Texas at Austin.

Song, D., Seibert, A.F., Rochelle, G.T., 2018. Mass transfer parameters for packings: Effect of viscosity. Ind. Eng. Chem. Res. 57 (2), 718–729. https://doi.org/10.1021/acs.iecr.7b04396.

Sotoodeh, M.M., Zivdar, M., Rahimi, R., 2018. CFD modeling of multiphase flow in reactive distillation column. Chemical Engineering and Processing - Process Intensification 129, 1–9. https://doi.org/10.1016/j.cep.2018.04.034.

Spedding, P.L., Jones, M.T., 1988. Heat and mass transfer in wetted-wall columns: I. Chemical Engineering Journal 37 (3), 165–176. https://doi.org/10/bfpjq6.

Subawalla, H., González, J.C., Seibert, A.F., Fair, J.R., 1997. Capacity and efficiency of reactive distillation bale packing: Modeling and experimental validation. Industrial & Engineering Chemistry Research 36 (9), 3821–3832. https://doi.org/10.1021/ie970050l.

Suess, Ph., Pluss, R.C., Meier, W., Lang, E., 1994. Entwicklung einer neuen Stoffaustausch-Struktur für Rektifizier- und Absorptionskolonnen. Chemie Ingenieur Technik 66 (9), 1254–1255. https://doi.org/10.1002/cite.3306609159

Sun, B., Zhu, M., Liu, B.T., Liu, C.J., Yuan, X., 2013. Investigation of falling liquid film flow on novel structured packing. Industrial & Engineering Chemistry Research 52 (13), 4950–4956. https://doi.org/10.1021/ie302272s.

Tsai, R.E., 2010. Mass Transfer Area of Structured Packing (PhD Thesis). University of Texas at Austin.

Tsai, R.E., Seibert, A.F., Eldridge, R.B., Rochelle, G.T., 2011. A dimensionless model for predicting the mass-transfer area of structured packing. AIChE Journal 57 (5), 1173–1184. https://doi.org/10.1002/aic.12345.

van Baten, J.M., Ellenberger, J., Krishna, R., 2001. Radial and axial dispersion of the liquid phase within a KATAPAK-S® structure: Experiments vs. CFD simulations. Chemical Engineering Science 56 (3), 813–821. https://doi.org/10.1016/S0009-2509(00)00293-1.

van Baten, J.M., Krishna, R., 2002. Gas and liquid phase mass transfer within KATAPAK-S® structures studied using CFD simulations. Chemical Engineering Science 57 (9), 1531–1536. https://doi.org/10.1016/S0009-2509(02)00026-X.

van Baten, J.M., Krishna, R., 2001. Liquid-phase mass transfer within KATAPAK-S® structures studied using computational fluid dynamics simulations. Catalysis Today 69 (1), 371–377. https://doi.org/10.1016/S0920-5861(01)00394-7.

van Gulijk, C., 1998. Using computational fluid dynamics to calculate transversal dispersion in a structured packed bed. Computers & Chemical Engineering 22, S767–S770. https://doi.org/10.1016/S0098-1354(98)00144-6.

Van Winkle, M., 1967. Distillation, Chemical Engineering. McGraw-Hill, Inc.

Vyas, A., Yadav, A., Srivastava, A., 2020. Flow and heat transfer measurements in the laminar wake region of semi-circular cylinder embedded within a rectangular channel. International Communications in Heat and Mass Transfer 116, 104692. https://doi.org/10.1016/j.icheatmasstransfer.2020.104692.

Wang, C., 2012. Measurement of packing effective area and mass transfer coefficients (Quarterly Report). University of Texas at Austin, Austin, Texas.

Wang, C., Xu, Z., Lai, C., Whyatt, G., Marcy, P., Sun, X., 2017. Hierarchical calibration and validation for modeling bench-scale solvent-based carbon capture. Part 1: Non-reactive physical mass transfer across the wetted wall column. Greenhouse Gases: Science and Technology 7 (4), 706–720. https://doi.org/10.1002/ghg.1682.

Wang, C., Xu, Z., Lai, K., Whyatt, G., Marcy, P.W., Sun, X., 2018. Hierarchical calibration and validation framework of bench-scale computational fluid dynamics simulations for solvent-based carbon capture. Part 2: Chemical absorption across a wetted wall column. Greenhouse Gases: Science and Technology 8 (1), 150–160. https://doi.org/10.1002/ghg.1727.

Wang, G.Q., Yuan, X.G., Yu, K.T., 2005. Review of mass-transfer correlations for packed columns. Ind. Eng. Chem. Res. 44 (23), 8715–8729. https://doi.org/10.1021/ie050017w.

Wang, J., Lu, P., Wang, Z., Yang, C., Mao, Z.-S., 2008. Numerical simulation of unsteady mass transfer by the level set method. Chemical Engineering Science 63 (12), 3141–3151. https://doi.org/10.1016/j.ces.2008.03.018.

Wang, Q., Liu, X., Wu, X., Yang, C., Qiu, T., 2020. A multi-scale approach to optimize vapor-liquid mass transfer layer in structured catalytic packing. Chemical Engineering Science 214, 115434. https://doi.org/10.1016/j.ces.2019.115434.

Weber, P.S., Marschall, H., Bothe, D., 2017. Highly accurate two-phase species transfer based on ALE Interface Tracking. International Journal of Heat and Mass Transfer 104, 759–773. https://doi.org/10.1016/j.ijheatmasstransfer.2016.08.072.

Weiner, A., Bothe, D., 2017. Advanced subgrid-scale modeling for convection-dominated species transport at fluid interfaces with application to mass transfer from rising bubbles. Journal of Computational Physics 347, 261–289. https://doi.org/10.1016/j.jcp.2017.06.040.

Weinfeld, J.A., Owens, S.A., Eldridge, R.B., 2018. Reactive dividing wall columns: A comprehensive review. Chemical Engineering and Processing: Process Intensification 123, 20–33. https://doi.org/10.1016/j.cep.2017.10.019.

Welch, V.A., 2001. Cascade Reboiling of Ethylbenzene/Styrene Columns. 6,171,449.

Welty, J.R., Rorrer, G.L., Foster, D.G., 2015. Fundamentals of Momentum, Heat, and Mass Transfer. Wiley.

Wen, X., Akhter, S., Afacan, A., Nandakumar, K., Chuang, K.T., 2007. CFD modeling of columns equipped with structured packings: I. Approach based on detailed packing geometry. Asia-Pacific Journal of Chemical Engineering 2 (4), 336–344. https://doi.org/10.1002/apj.90.

Wilke, C.R., Chang, P., 1955. Correlation of diffusion coefficients in dilute solutions. AIChE Journal 1 (2), 264–270. https://doi.org/10.1002/aic.690010222.

Xie, H., Zong, Y., Shen, L., Dai, G., 2021. Interfacial mass transfer intensification with highly viscous mixture. Chemical Engineering Science 236. https://doi.org/10/gjrbm8.

Xu, Y.Y., Paschke, S., Repke, J.-U., Yuan, J.Q., Wozny, G., 2009. Computational approach to characterize the mass transfer between the counter-current gas-liquid flow. Chemical Engineering & Technology 32 (8), 1227–1235. https://doi.org/10.1002/ceat.200900099.

Xu, Z., Singh, R.K., Bao, J., Wang, C., 2019. Direct effect of solvent viscosity on the physical mass transfer for wavy film flow in a packed column. Ind. Eng. Chem. Res. 58 (37), 17524–17539. https://doi.org/10.1021/acs.iecr.9b01226.

Yang, C., Mao, Z.-S., 2005. Numerical simulation of interphase mass transfer with the level set approach. Chemical Engineering Science 60 (10), 2643–2660. https://doi.org/10.1016/j.ces.2004.11.054.

Yang, L., Peters, E.A.J.F., Fries, L., Harshe, Y.M., Kuipers, J.A.M., Baltussen, M.W., 2020. Direct numerical simulation of mass transfer and mixing in complex two-phase systems using a coupled volume of fluid and immersed boundary method. Chemical Engineering Science: X 5, 100059. https://doi.org/10.1016/j.cesx.2020.100059.

Yu, D., Cao, D., Li, Z., Li, Q., 2018. Experimental and CFD studies on the effects of surface texture on liquid thickness, wetted area and mass transfer in wave-like structured packings. Chemical Engineering Research and Design 129, 170–181. https://doi.org/10.1016/j.cherd.2017.10.035.

Yu, K.-T., Yuan, X., 2017. Introduction to Computational Mass Transfer With Applications to Chemical Engineering. Springer Nature.

Zdravkovich, M.M., 1990. Conceptual overview of laminar and turbulent flows past smooth and rough circular cylinders. Journal of Wind Engineering and Industrial Aerodynamics 33 (1), 53–62. https://doi.org/10.1016/0167-6105(90)90020-D.

Zhang, Y., Zhu, H., Yin, Q., 2011. Experimental study on local mass transfer of structured packing with the method of flow visualization. Chinese Journal of Chemical Engineering 19 (5), 870–875. https://doi.org/10.1016/S1004-9541(11)60067-0.

Zhang, Y.-L., Zhu, H.-M., Yin, Q.-X., 2013. CFD study on the local mass transfer efficiency in the gas phase of structured packing. Chemical Engineering & Technology 36 (7), 1138–1146. https://doi.org/10.1002/ceat.201300097.

Zogg, M., 1973. Stoffaustausch in der Sulzer-Gewebepackung. Chemie Ingenieur Technik 45 (2), 67–74. https://doi.org/10.1002/cite.330450205.

Zogg, M., 1972. Modifizierte Stoffübergangskoeffizienten für bilanzmäßige Stoffübergangsberechnungen an laminaren Rieselfilmen. Chemie Ingenieur Technik 44 (15), 930–936.

Vita

Luke Howard Macfarlan grew up in Siloam Springs, Arkansas as the third of four children. He completed his high school education at Macfarlan Home School, where he was both first and last in his graduating class. He graduated from John Brown University summa cum laude with a double major in chemistry and engineering with a mechanical concentration. He moved to Austin, Texas in 2017 to begin his graduate studies at the University of Texas. During his graduate work, he performed an internship in the Distillation Research and Development division at Praxair Inc. (now Linde Group). He has accepted employment as a Polymer Engineer at Schlumberger.

Permanent email: Luke [DOT] Macfarlan [AT] UTexas [DOT] edu

This dissertation was typed by Luke H. Macfarlan.